UNIVERSITY OF SOUTHAMPTON

FACULTY OF PHYSICAL SCIENCES AND ENGINEERING

Physics and Astronomy

DNA-coated gold nanoparticles for sensing and drug delivery

by

Maria Eleni Kyriazi

Thesis for the degree of Doctor of Philosophy

March 2018

UNIVERSITY OF SOUTHAMPTON

ABSTRACT

FACULTY OF PHYSICAL SCIENCES AND ENGINEERING

Physics and Astronomy

Thesis for the degree of Doctor of Philosophy

DNA-COATED GOLD NANOPARTICLES FOR SENSING AND DRUG DELIVERY

Maria Eleni Kyriazi

In recent years inorganic nanoparticles have been of great scientific interest not only due to the fact that they can be tailored in morphology allowing for the tuning of their optical and electronic properties but also due to their rich surface chemistry. Recent advances in conjugation techniques have allowed for the surface functionalization of nanoparticles with ligands such as synthetic oligonucleotides. This has led to the development of bio-nanomaterials that have been successfully used in applications ranging from bio sensing to the targeted delivery of molecules such as drugs.

This thesis focuses on the design and synthesis of advanced DNA-coated gold nanostructures that can perform the synergistic tasks of sensing and drug delivery in cells.

Gold nanoparticles functionalized with synthetic oligonucleotides were assembled into dimers using copper free click chemistry and were used for the intracellular detection of up to two mRNA targets. Once taken up by

cells they showed great biocompatibility, no significant susceptibility to degradation by nucleases and most importantly excellent specificity towards the mRNA sequence they were designed to detect.

Furthermore, DNA-coated gold nanoparticle dimers were developed into multifunctional nanostructures. In addition to live cell mRNA detection we showed how they could also be designed to deliver up to two chemotherapeutic drugs. By relying on the specificity of the gold nanoparticle dimer towards an mRNA target, cell specific drug delivery was made possible thus demonstrating the synergistic capabilities of this system.

Finally with a view of shedding light on the interaction between DNA-coated gold nanoparticles and cells their intracellular fate including the time point and location of mRNA detection after cellular entry was investigated.

Table of Contents

Table of figures

Table of figures

Table of figures

Table of Tables

Table of schemes

Table of equations

Academic Thesis: Declaration Of Authorship

I, ... please print name

declare that this thesis and the work presented in it are my own and has been generated by me as the result of my own original research.

title of thesis .....

.....

I confirm that:

1. This work was done wholly or mainly while in candidature for a research degree at this University;
2. Where any part of this thesis has previously been submitted for a degree or any other qualification at this University or any other institution, this has been clearly stated;
3. Where I have consulted the published work of others, this is always clearly attributed;
4. Where I have quoted from the work of others, the source is always given. With the exception of such quotations, this thesis is entirely my own work;
5. I have acknowledged all main sources of help;
6. Where the thesis is based on work done by myself jointly with others, I have made clear exactly what was done by others and what I have contributed myself;

7. Delete as appropriate None of this work has been published before submission or Parts of this work have been published as:

Articles in academic press:

1. Kyriazi, Maria-Eleni; Giust, Davide; El-Sagheer, Afaf H.; Lackie, Peter M.; Muskens, Otto L.; Brown, Tom; Kanaras, Antonios G.
   "Multiplexed mRNA sensing and combinatorial-targeted drug delivery using DNA-Gold nanoparticle dimers", *ACS Nano,* **2018** doi: 10.1021/acsnano.7b08620

2. Kyriazi, Maria-Eleni; Kanaras, Antonios G.
   "Investigating the correlation between DNA loading on spherical nucleic acids and susceptibility to enzymatic degradation by cellular nucleases"
   SPIE 2018 - doi: 10.1117/12.2285833

3. Kyriazi, Maria-Eleni; Muskens, Otto L.; Kanaras, Antonios G.
   "Functionalized nanoparticles and applications"
   SPIE 2017 - doi: 10.1117/12.2245441

4. Kyriazi, Maria-Eleni; Heuer Jungemann, Amelie; Kanaras, Antonios G.
   "How can nano-delivery systems selectively kill cancerous cells"
   Future Science 2017 – doi: 10.4155/tde-2016-0086

Abstracts, posters and presentations:

1. Nanax 7 (May 2016, Marburg, Germany)
2. NanoBio&Med (November 2016, Barcelona, Spain)
3. Euromat 2017 (September 2017, Thessaloniki, Greece)

4. SPIE Photonic West 2018 (January 2018, San Francisco, USA)

Awards:

1. NanoBio&Med 2016 (Barcelona, Spain) travel grant for conference participation
2. Young Investigator Award Gold Medal 2018 (SPIE Photonics West)
3. Participated in the 2018 STEM for Britain competition

Signed: .....

Date: .....

Acknowledgements

First and foremost I would like to thank my two supervisors Dr. Antonios Kanaras and Professor Otto Muskens for giving me the opportunity to complete a 3 and a half-year PhD project in such a great scientific field and whose support and advice has been invaluable over these past few years. Apart from developing a great tool kit of skills such as the preparation of academic journals and grant applications my supervisors have also given me the opportunity to develop my presentation skills by allowing me to attend several international conferences over the past few years. Thank you also to Dr. Peter Lackie who has allowed me to use his cell culture laboratory as well as providing me with the cell lines I have needed for my research. Furthermore, I am grateful to the entire Biomedical Imaging Unit who have helped me with the imaging aspect of the project and who have always been so helpful with providing scientific advice and support. I would also like to thank Professor Tom Brown and Dr. Afaf El-Sagheer who have synthesised all the oligonucleotides used as well as provided scientific advice in the process of oligonucleotide design. Without them this project would not have been feasible.

A big thank you to my research group including Dr. Amelie Heuer-Jungemann who helped me out so much when I first started my PhD as well as the future Dr. Johanna Midelet for always being so supportive. I would also like to thank my friends from Greece Ioli, Paola Anastasia, Malvina, Zoi and Rallou who kept me sane when writing my thesis!

The biggest thank you goes to my family. Thank you to my brothers Alexi, Philip and Andrea who are my best friends and always know how to make me laugh. Thank you to my mum for always being so caring and selfless and has always been there for me and finally thank you to my amazing dad for working so hard all these years so I could have the best education possible and always finding time to gossip with me. They have both been invaluable and I am so lucky to call them my parents.

Definitions and Abbreviations

2D – two dimensional

3D – three dimensional

A – Adenine

ALF – artificial lysosomal fluid

AuNP – AuNPs

AuNR – gold nanorod

BBB – blood brain barrier

BLAST – Basic Local Alignment Search Tool

BSPP – Bis(p-sulfonatophenyl)phenylphosphine

C – Cytosine

cDNA – complementary deoxyribonucleic acid

CSC – circulating stem cells

CTAB – cetyltrimethylammonium bromide

DAPI – 4',6-diamidino-2-phenylindole

DDA – discrete dipole approximation

DLS – dynamic light scattering

DMF – dimethylformamide

DNA – deoxyribonucleic acid

DNAse – deoxyribonuclease

DOX – doxorubicin

dsDNA – double stranded deoxyribonucleic acid

DTT – dithiothreitol

DVLO – Derjaguin-Landau-Verwey-Overbeek

EDC – 1-(3-(dimethylamino)propyl)-3-ethyl-carbodiimidemethiodide

FDTD – finite difference time domain

FRET – fluorescence resonance energy transfer

fs – femtosecond

G – guanine

GBM – gleoblastoma multiforme

gmRNA – general messenger ribonucleic acid

h – hour

HBSS – hank's balanced salt solution

HIV – human immunodeficiency virus

HPLC – high-performance liquid chromatography

ICP-MS – inductively coupled plasma mass spectrometry

iPS – induced pluripotent stem cells

kV – kilo volt

LSPR – local surface plasmon resonance

M - molar

MEM – minimum essential medium

mg – milli gram

MGMT – O-6methylguanine methyltransferase

MHz – mega hertz

min – minutes

mL – millilitres

μL – microliters

μM – micromolar

mM – millimolar

mRNA – messenger ribonucleic acid

MXT – mitoxantrone

NASH – non-alcoholic fatty liver disease

nm – nanometres

O.D. – optical density

PAGE – polyacrylamide gel

PBS – phosphate buffer saline

PFA – paraformaldehyde

pH – potential hydrohen

PIPES – piperazine-N, N'-bis

RNA – ribonucleic acid

RNAi – ribonucleic acid interference

rpm – rounds per minute

RPMI – roswell part memorial institute

RT-qPCR – real time quantitative polymerase chain reaction

Rxn – reaction

s – second

siRNA – silencing ribonucleic acid

SNA – spherical nucleic acid

snRNA – small nuclear ribonucleic acid

SR-A – scavenger receptor A

ssDNA – single strand deoxyribonucleic acid

T – thymine

TBE – tris borate edta

TEAB – triethylammonium bicarbonate

TEM – transmission electron micrsoscopy

Tm – melting temperature

TMZ – tomozolomide

TPPL – two photon photoluminescence

UV-Vis – ultra violet – visible

Wt – weight

°C – degrees Celsius

Chapter 1 – Introduction

In recent years, nanoscale particles that possess properties suitable for a range of biological and biomedical applications have been developed.[1-4] Compared with other types of nanoparticles, gold nanoparticles (AuNPs) have been extensively used due to the vast range of methods to tailor their size, and shape, resulting in tuneable optical and thermal properties.[5, 6]

Spherical AuNPs are broadly employed due to their fast and facile synthesis, low cytotoxicity and ease of bioconjugation.[7] Furthermore, the surface of AuNPs can be readily modified with ligands containing functional groups such as thiols, phosphines and amines, which exhibit a great affinity for gold surfaces and can impart even greater functionality to AuNPs.[2, 8]

One of the most promising surface modification ligands for AuNPs are oligonucleotides.[9-11] An important property of oligonucleotide functionalized AuNPs is their ability to bind complementary nucleic acids with a high affinity through Watson-Crick base pairing.[1, 2] Furthermore, the realization of such systems has led to exciting opportunities where the unique properties of oligonucleotides as well as the properties of AuNP can be combined into one structure.

The research presented in this thesis has focused on the synthesis and functionalization of AuNPs with oligonucleotides for intracellular applications.

Chapter 4 discusses the synthesis of AuNPs including those with spherical and anisotropic shape as well as the functionalization of spherical AuNPs with oligonucleotides.

In **Chapter 5** we firstly show how single DNA-coated AuNPs can be assembled into nanoparticle dimers. By chemically modifying the oligonucleotides that link the two separate nanoparticles together with azide or alkyne groups, AuNP dimers could be ligated using copper-free click chemistry. Ligated AuNP dimers were then used for the simultaneous detection of up to two mRNA targets in live cells using fluorophore tagged oligonucleotides. Moreover, the synergistic capabilities of the AuNP dimers are demonstrated as they were subsequently developed into a drug delivery vehicle. Doxorubicin (DOX) and mitoxantrone (MTX), two chemotherapeutic drugs, were intercalated within the nanoparticle dimer and released only to cells expressing specific mRNA targets thereby significantly affecting the cell viability.

Finally in **Chapter 6** we probe the intracellular fate of DNA-coated AuNPs after cellular uptake. The location of the gold core was investigated as well as the time and location of cell specific mRNA detection. Furthermore, we show the development of a home-built microscopy setup capable of imaging both the gold core and the process of mRNA detection within the same endocellular environment.

Chapter 2 – Theoretical Background

The research presented in this thesis focuses on the development of DNA-coated spherical AuNP assemblies for live cell mRNA detection and simultaneous delivery of up to two anti-cancer drugs to the same endocellular microenvironment. Furthermore, the intracellular fate of DNA-coated AuNPs after uptake was studied to determine the location of AuNPs as well as the time point and location of mRNA detection.

This chapter will introduce relevant theoretical background on each aspect of the project. The basic principles of AuNP preparation as well as their unique optical properties will be discussed in **section 2.1 and 2.2**. This will be followed by a general overview on the properties of oligonucleotides and the modification of spherical AuNPs with oligonucleotides as well as further modifications with silica. **Section 2.5** will then discuss how AuNPs can be used within live cells for mRNA detection as well as dug delivery and imaging.

Finally, with a view of creating DNA-coated AuNP assemblies that can perform synergistic tasks within live cells, the readers' attention will be drawn to recent developments focusing on the design and synthesis of AuNP assemblies (**section 2.6**) and their interaction with cells.

2.1 Synthesis of AuNPs

Wet chemistry methods were employed for the synthesis of AuNPs of various shapes and sizes including spherical, rod-shaped and branched AuNPs. Synthetic routes including detailed reaction mechanisms involved in nanoparticle synthesis will be presented in the following sub sections.

2.1.1 Synthesis of spherical AuNPs

Colloidal AuNPs are one of the oldest known nanomaterials with a rich history in chemistry dating back to the Roman times when they were frequently used as decorative pigments for glass staining.[12, 13] The "Lycurgus Cup", dating back to the 4th century, is one of the most famous examples where gold particles were used for glass colouring.[14] However, it wasn't until the 19th century when Faraday reported a systematic study on the synthesis and optical properties of colloidal nanoparticles.[15] Since then spherical AuNPs have been widely used for applications in different fields of science.

Following the Faraday study in 1951, Turkevich developed a new method to synthesise AuNPs based on the reduction of gold salt with citrate, which was then refined by Frens in 1970.[16-18] This method, which allows for the synthesis of monodisperse spherical AuNPs (between 10 and 20 nm) involves the use of two aqueous starting materials: sodium tetrachloroaurate and trisodium citrate dissolved in Milli-Q water. By mixing both solutions at a high temperature (100 °C) and at different molar ratios the size of the resulting nanoparticles can be tuned.[19] Even though adjustments to this protocol have been published the mechanism of nanoparticle formation in each case relies on the use of trisodium citrate as both the reducing agent and the capping ligand, providing an increase in stability to the formed nanoparticles.[20, 21] A detailed mechanism leading to nanoparticle formation has been investigated over the past few years with Kumar and co-workers proposing a simultaneous 3-step reaction mechanism as seen below in Scheme 2.1.[22]

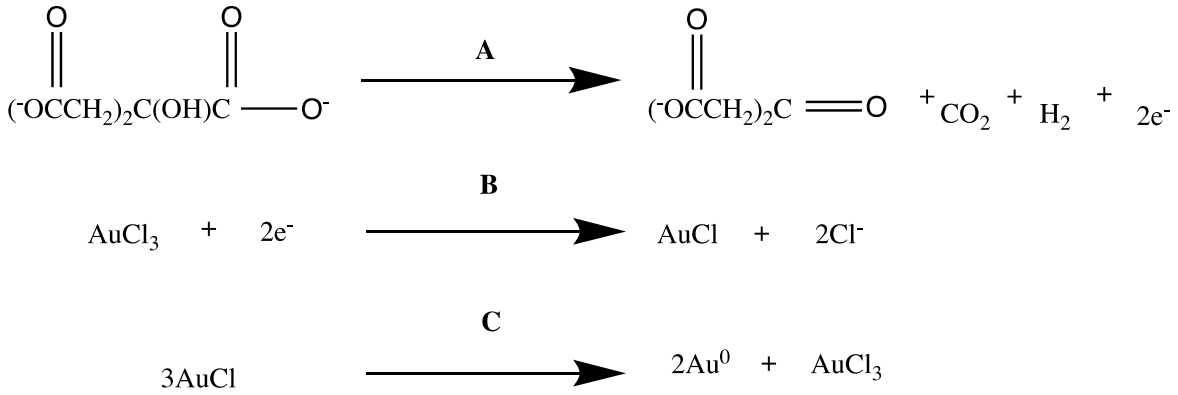

Scheme 2.1 Reaction mechanism leading to the formation of AuNPs involving citrate oxidation (A), reduction of the gold salt (B) and disproportionation of gold chloride (C). Scheme taken from [22].

The initial step of this process involves the oxidation of citrate yielding dicarboxy acetone (Scheme 2.1 **A**). This is followed by the reduction of the gold precursor (Au^{3+}) to an aurous salt (Au^{+}) (Scheme 2.1 **B**). The Au^{+} cations are able to form complexes with dicarboxy acetone, which according to Turkevich plays the role of organizer through the formation of a complex.[16] An illustration of the formed complex is presented in Scheme 2.2. According to findings by Kumar's group at least three Au^{+} can be tethered to by a minimum of two dicarboxy acetone molecules. Finally disproportionation of aurous species to gold atoms (Au^{0}) takes place (Scheme 2.1 **C**). Gold atoms are able to further absorb Au^{+} and by complexation with dicarboxy acetone, can form large aggregates. Further disproportionation leads to larger gold atoms, which eventually form a nucleus once a critical size is reached. The nucleus is able to absorb further gold atoms produced by disproportionation leading to nanoparticle growth.

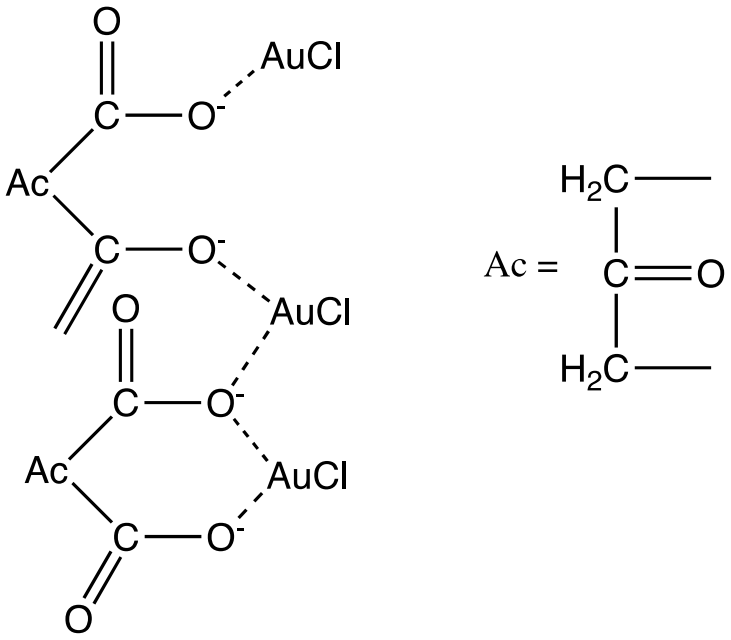

Scheme 2.2 Illustration of the complex formed between the aurous salt (Au^{+}) and dicarboxy acetone

It has been shown that nanoparticle monodispersity is dependent upon the formation of gold atoms following disproportionation of aurous species. Thus rapid formation of dicarboxy acetone will promote rapid disproportionation leading to more uniform and monodisperse particles.[23, 24] However, as discussed by Xia *et al.* dicarboxy acetone can also decompose into acetone, which is able to also reduce the gold precursor (Au^{3+}). This process can result in further nucleation events at different time points leading to particles with a wide size distribution.[23] However, Kumar *et al.* discussed that this side reaction only affect the growth process when low citrate concentrations are used because the reduction of the gold salt by acetone compared to citrate is slower. [22]

Apart from acting as a reducing agent and a nanoparticle stabilizer by electrostatically binding to the surface, trisodium citrate, as demonstrated

by Peng *et al.*, can also act as a pH modulator influencing the reaction kinetics.[19] Depending on the pH the reaction can follow one of two possible pathways. At low pH (3.7 – 6.5) a fast nucleation takes place (10 s), which is followed by fast random attachment of gold atoms leading to elongated structures. The final step involves intra-particle ripening leading to the formation of spherical nanoparticles. At higher pH (6.5 – 7.7) the nucleation process takes longer (60 s) however the slow growth that follows leads to uniform spherical nanoparticles.

The differences in the reaction kinetics were attributed to the reactive species of gold and citrate, which are found in the reaction mixture at different pH values. At the low pH conditions the gold precursor is found as $(AuCl_3)OH))^-$, which is very reactive and initiates rapid nucleation. On the other hand at higher pH it is found as $(AuCl_2(OH))_2^-$ and $(AuCl(OH))_3^-$, which are both less reactive thus leading to slower nucleation and growth.

pH 3.7 – 6.5 $[AuCl_3(OH)]^- + H_2Ct^- / HCt^{2-}$

pH 6.5 – 7.7 $[AuCl_2(OH)]_2^- / [AuCl(OH)]_3^- + HCt^{2-} / Ct^{3-}$

Scheme 2.3 Gold and citrate species found at low and high pH taken from [19].

One drawback of the Turkevich method is the ability to produce nanoparticles with a narrow size distribution in the range of 10 to 20 nm. Even though larger particles can be synthesized by varying the reaction conditions (solution pH, citrate to gold salt molar ratio), the quality of the

resulting particles (size and distribution) is poor and the shapes obtained are non-uniform and irregular, such as triangles and ellipsoids.[25] Therefore for the synthesis of larger monodisperse spheres a seeding mediated synthesis strategy based on separating nucleation and growth has been developed.[26-28] This method relies on the growth of pre-formed Au seeds *via* the reduction of injected Au(III) to Au(I) using a mild reducing agent. The reaction conditions need to be carefully controlled to prevent the formation of new nuclei that can lead to the formation of uneven sized particles. This synthesis was pioneered by Natan and co-workers who *via* the use of weak reducing agents, such as ascorbic acid and hydroxylamine, were able to obtain larger nanoparticles. However, their synthetic route also resulted in the synthesis of rod-shaped particles.[27, 29, 30] Further improvements to this synthesis were made by Murphy and Liz-Marzan who reported the synthesis of uniform spherical nanoparticles, up to 180 nm in size, using ascorbic acid and cetyl-trimmethyl ammonium bromide (CTAB) as a cationic surfactant.[31, 32] Even though the use of CTAB allows for the precise control of nanoparticle morphology, strong binding to the surface limits the possibility of further functionalizing/replacing the CTAB with thiol-terminated ligands. This is therefore considered as a drawback, as the ability to render biological functionality to AuNPs *via* their functionalization with oligonucleotides is essential to this study. To address this issue Puntes *et al.* developed a synthetic route leading to the kinetically controlled synthesis of up to 200 nm sized particles *via* the use of citrate as a mild reducing agent.[26] They found that by carefully tuning the ratio between gold seeds and added gold precursor as well as the concentration of citrate added they were able to prevent new nucleation events or irregular growth due to Ostwald ripening. They also stated that lowering the temperature to 90 °C and controlling the amount of gold precursor added by successive injections lead to a narrower size of citrate stabilized spherical nanoparticles.

2.1.2 Synthesis of gold nanorods

As opposed to nanoparticles of a spherical shape, gold nanorods (AuNRs) have an anisotropic shape. They are one of the most studied colloidal plasmonic nanostructures due to their broadly tuneable aspect-ratio-dependant longitudinal surface plasmon resonance (LSPR), which can range from the visible to the near-infrared.[33]

A seed mediated AuNR synthesis controlled by surfactant molecules has emerged as the most popular synthetic route due to the fact that the particle aspect ratio can be tuned and it leads to high product uniformity (see **section 3.1.2** for experimental details).[34-36] The mechanism through which AuNRs are obtained is still debated, however, depending on the presence of Ag^+ ions it can be categorized into two mechanisms.[37, 38] In the absence of Ag^+ ions growth is caused by preferential binding of CTAB to the specific crystal facets of the Au seed. CTAB preferentially binds to the (100) surface therefore newly reduced Au(0) atoms deposit on the available (111) facet resulting in structure elongation along the (100) direction. On the other hand, in the presence of Ag^+ ions preferential reduction to Ag atoms occurs on the AuNR side due to underpotential deposition.[36] This blocks the deposition of Au atoms as a strong interaction is formed between the deposited Ag atoms and the Br^- ions of CTAB. As a result the Au seeds will elongate along the longitudinal direction.

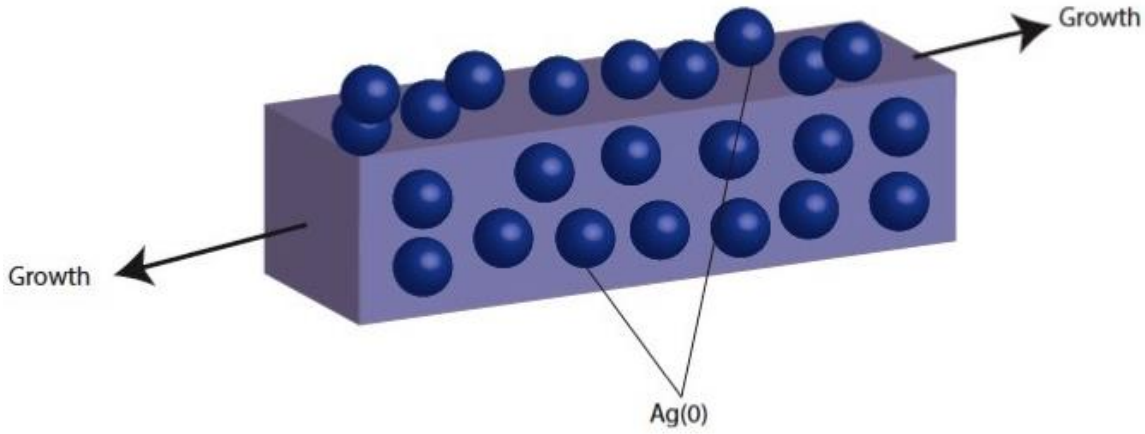

Figure 2.1 Illustration of nanorod growth along the longitudinal axis promoted by under potential deposition of silver (Ag^0).

The seed mediated route to the synthesis of AuNRs was first developed by Murphy *et al.* who followed a two-step procedure.[34] Citrate stabilised AuNPs (2 – 3 nm) were firstly synthesised according to a modified Turkevich method and were used as seeds. Reduction of the gold salt was achieved by using a strong reducing agent ($NaBH_4$) in the presence of citrate (see Scheme 2.4). Growth was then carried out by adding the citrate stabilized seeds into the growth solution containing CTAB, ascorbic acid, gold salt and silver nitrate). However, nanorods prepared using this method also contained a large portion of spherical nanoparticles. This synthesis was further improved by El-Sayed *et al.* who replaced the citrate with CTAB during seed synthesis.[39] They also demonstrated that the nanorod aspect ratio could be controlled by adjusting the Ag^+ ion concentration in the growth solution. Following these developments Orendorff and co-workers proposed a detailed mechanism leading to nanorod formation. In this mechanism, $AuCl^{4-}$ bound to CTAB micelles, forms $AuCl^{2-}$ by the reduction of Au^{3+} to Au^+ through the addition of ascorbic acid. Subsequent collisions of the CTAB micelle – $AuCl^{2-}$complexes

with CTAB-protected seed particles lead to the formation of growing gold particles bearing Au (110) and (100) facets. The frequency of collisions determines the rate of nanorod growth. Fast silver deposition on the (110) facet followed by strong CTAB binding inhibits gold growth on the side of rods and leads to preferential growth at the ends. [38]

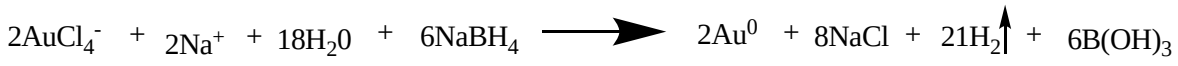

Scheme 2.4 Reduction of the gold precursor with sodium borohydride.

2.1.3 Synthesis of branched nanoparticles

Similar to AuNRs branched AuNPs are also anisotropic in structure and characterised by tunable optical properties.[40-43] However, as opposed to AuNRs, the growth mechanism is far more challenging and complex as anisotropic growth must be initiated at multiple sites of a seed and then maintained in order to generate branched arms with controlled lengths. Even though the mechanism of formation is yet to be fully elucidated it is thought that two mechanism are involved in the formation of these nanostructures.[44] The first involves site selective deposition of Au^0 atoms on a gold seed followed by attachment of many seed particles promoting growth. During this synthesis the reaction temperature is thought to be crucial and should be kept relatively low as higher temperatures can lead to more thermodynamically favoured shapes such as Wulff polyhedral.[45]

The seed mediated approach for the synthesis of branched AuNPs is the most commonly used as it provides better control over the morphology and size distribution. Carrol *et al.* were the first to report a seed mediated approach in which Ag nanoplates were used as seeds to generate single

crystal Au multipods.[43] Murphy *et al.* also demonstrated that by modifying the seeded growth method previously used for AuNRs, gold nanostructures with branched arms could be synthesised with dimensions in the range of 70 to 300 nm.[46] It was shown that by changing the surfactant and additive concentrations deposition rates of Au^0 on to different facets could be altered. CTAB and $AgNO_3$ were used as the surfactant and additive to promote anisotropic growth where specifically the Br^- ions from CTAB have been shown to be crucial to the growth of branches. Day *et al.* demonstrated that an increase in the concentration of the reducing agent resulted in AuNPs with a higher degree of branching whereas increasing the concentration of silver nitrate lead to AuNPs that were spherical in shape. They suggested that the gold seeds used presented (100) and (111) facets. Due to preferential deposition of silver atoms on the (100) facet followed by strong CTAB binding, gold deposition was promoted on the (111) facet causing anisotropic growth and a branched morphology. In the presence of a higher silver nitrate concentration Day *et al.* suggested that although deposition of silver atoms would occur on the (100) facet it would occur on the (111) facet as well. As a result, all facets would be coated with CTAB before excessive gold deposition could take place leading to larger spherical AuNPs. On the other hand, they suggested that an increased ascorbic acid concentration would promote a faster reduction process thus increasing the rate at which gold ions became available. In turn, the presence of more reactive species would lead to the generation of particles with more branches.[47]

Apart from CTAB other surfactants have also been shown to induce the formation of branched structures. Replacing CTAB with dodecyl sulphate (SDS) leads to small branched structures (40 nm) whereas polyvinylpyrrolidone (PVP) can lead to an overall branched AuNP size ranging from 45 to 60 nm.[48-50] In addition the reducing agent can also

affect the final structure because of its direct impact on the reaction kinetics. For example thin horns were obtained when NH_2OH was used as the reducing agent in the presence of $AgNO_3$ and citrate stabilised seeds.[51] Similarly hydroxylamine sulfate with sulphuric acid can also generate nanoparticles with branched arms.[52] Liz-Marzan *et al.* reported the synthesis of branched AuNPs using dimethylformamide (DMF) as the reductant. They also stated that by varying the concentration of seeds nanostructures with branched arms could be tuned from 45 to 160 nm in size whilst maintaining structure uniformity.[49, 50]

Although a number of protocols exist, the mechanism for the synthesis of branched AuNPs is complex and dependant on numerous parameters including temperature, reducing agent as well as seed concentration. As a result it remains challenging to finely control the yield as well as the uniformity of the resulting product.

2.2 Optical properties of AuNPs

Gold is considered to be a precious metal with a characteristic bright golden yellow colour. However, AuNPs exhibit significantly different properties compared to their bulk. When processed into sub nm structures AuNP solutions can vary in colour ranging from ruby red to blue depending on the nanoparticle shape and size.[53] Faraday was the first to discover that “fine” particles could be formed by treating an aqueous $HAuCl_4$ solution with phosphorus dissolved in CS_2 in a two-phase system producing a red coloured solution.[15] Although he suspected that “a mere variation in the size of its particles gives rise to a variety of colours” Gustav Mie was the first to establish, by solving Maxwell’s equation, that the colour of the AuNP solution could be attributed to the absorption and scattering of light by the AuNPs in solution.[54]

When light interacts with AuNPs the free conduction band electrons on the surface will sense the electromagnetic field of the incident light causing a collective oscillation of the surface electrons. This phenomenon is known as local surface plasmon resonance (LSPR) and is determined by a number of parameters including size, shape, morphology and the environment surrounding the surface of the nanoparticle.[54-56] Scheme 2.5 shows a schematic illustration of this phenomenon for spherical AuNPs.

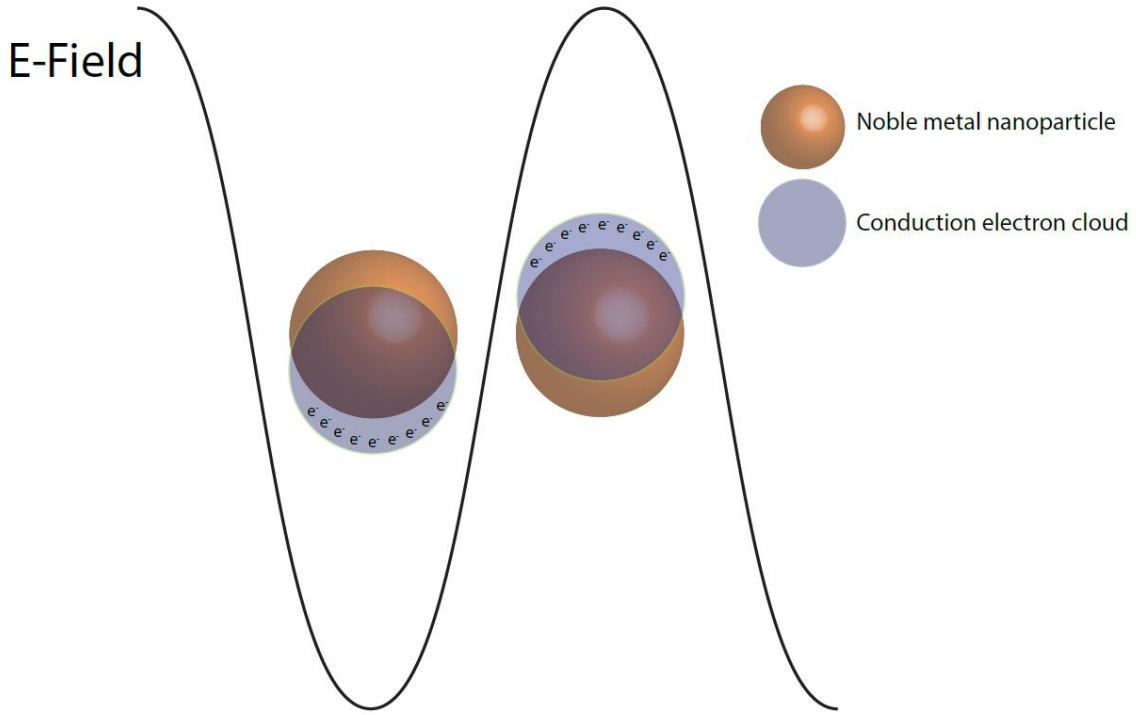

Scheme 2.5 Localised surface plasmon resonance (LSPR) of AuNPs resulting from the interactions between metal nanoparticles and the electromagnetic radiation o incident light. Adapted from ref [57].

In 1908 Mie proposed the first quantitative description of the LSPR for small particles of a spherical shape where the extinction cross-section (C_{ext}) is expressed as the sum of both the absorption (C_{abs}) and scattering (C_{sca})

cross-section as seen in Equation 2.1. The surrounding medium is characterised by a dielectric constant ε_m and the dielectric constant of the nanoparticle is presented as a complex number with a real part ε_r and an imaginary part ε_i. The real part of the dielectric constant determines the position of the peak because the extinction cross-section reaches a maximum at $\varepsilon_r = -2\varepsilon_m$ whereas the imaginary part determines the width of the peak.[57]

$$\boldsymbol{Cext} = \frac{\boldsymbol{24\,\pi^2 r^3 m_2^3}}{\boldsymbol{\lambda}} \frac{\boldsymbol{\varepsilon i}}{(\boldsymbol{\varepsilon r} + \boldsymbol{2\varepsilon m})^2 + \boldsymbol{\varepsilon i^2}}$$

Equation 2.1 Calculation of the total extinction cross section where r = radius of the nanoparticle, λ = wavelength, ε_m = dielectric constant of the medium, ε_r and ε_i = used to express the dielectric constant of the metal.

Mie theory however, only holds true under a number of assumptions. Firstly the dielectric constants of both the nanoparticle and the surrounding medium are homogenous and can be described as their bulk dielectric functions, secondly the size of the nanoparticle is much smaller relative to the wavelength of incident light so only dipolar oscillations need to be considered and finally the local electric field of light in the nanoparticle is uniform and constant so as to ignore the retardation effect. These assumptions only hold true for particles smaller than 25 nm.[58, 59] For larger gold spheres the retardation effect can not be neglected as it gives rise to oscillation modes in higher orders and at lower frequencies leading to a red-shift (longer wavelengths) of the overall LSPR peaks.[57]

For more complex geometries such as AuNRs or branched AuNPs more advanced methods should be employed in order to correctly describe their

optical properties. These include discrete dipole approximations (DDA) and the finite-difference-time-domain method (FDTD).[57] When a nanosphere is elongated along one axis to produce a nanorod, free electrons can oscillate in two different directions, parallel to the short axis and the long axis respectively. As a result the LSPR peak splits into two modes: the transverse mode that remains in the same positions associated with the nanospheres and the longitudinal mode, which can be tuned according to the aspect ratio. Gan theory has been used to describe the LSPR of a nanorod where depolarisation factors for the nanorod axis have been included whilst El-Sayed *et al.* observed a linear relationship between the longitudinal LSPR peak and the aspect ratio.[60, 61] On the other hand, branched AuNPs are not as monodisperse as other nanoparticle shapes, which is reflected in their LSPR spectrum.[57] Work by Wang *et al.* suggested that their LSPR spectral features are highly dependant upon the number and orientation of the protruding spikes with broad spectra being observed when obtaining an average particle spectrum. For single particle spectra clear peaks can be observed, which can be attributed to a specific spike in the structure.[62] However, further enlargement of branched AuNPs leads to broadening of the peaks and a weakened absorption due to an increase in the Rayleigh scattering.[52] Hafner *et al.* also observed an increase of the extinction cross section at the spike tips, which may be responsible for their very effective scattering properties.[63]

Metal nanoparticles are also capable of photoluminescence, which has been shown to correlate strongly with their well-defined plasmon resonances. [57] Mohamed *et al*. observed that the quantum efficiency of a single luminescence from gold nanorods is enhanced by a factor of one million under plasmon resonant conditions.[64] Single photon luminescence was first reported from bulk copper and gold by Mooradian in 1969 followed by Boyd *et al.* who found that a much larger single

photon induced luminescence was observed on roughened metal surfaces whilst they also found that two photon photoluminescence (TPPL), that depends quadratically on excitation intensity, could also be observed. Since then TPPL has been identified as a serial process involving sequential absorption of two photons leading to excitation of electrons from the d to the sp band and emission from the recombination of electrons in the sp band and holes in the d band.[65, 66] It is a powerful bio-imaging technique that allows for non-invasive imaging of AuNPs within cells with a higher penetration depth.

Many previous studies have shown that TPPL properties of nanoparticles are strongly dependent on nanoparticle shape due to shape sensitive LSPR as a large TPPL efficiency is found when incident light wavelength coincides with the longitudinal surface plasmon mode. The strong localised electric field can interact with incoming light and consequently affect the photoluminescence.[67] A systematic study of shape-dependent TPPL showed that branched AuNPs followed by AuNRs display the strongest TPPL and thus they have been systematically used for imaging in *in vitro* applications.[67-70]

2.3 Structure and properties of DNA

Deoxyriboneucleic acid (DNA) is a biological polymeric macromolecule that carries the genetic instructions used in the growth, development and functioning of all living organisms.[71] It is made up of two important components: the phosphate backbone and the nucleobases. Each backbone carries one negative charge per phosphate group, which is maintained over the whole pH range due to its low pKa value of 2. DNA is also made up of four different nucleobases: the purines Guanine (G) and Adenine (A) and the pyrimidines Cytosine (C) and Thymine (T).

Nucleobases linked together *via* their phosphate backbone make up a DNA single strand as shown in Figure 2.2.[72]

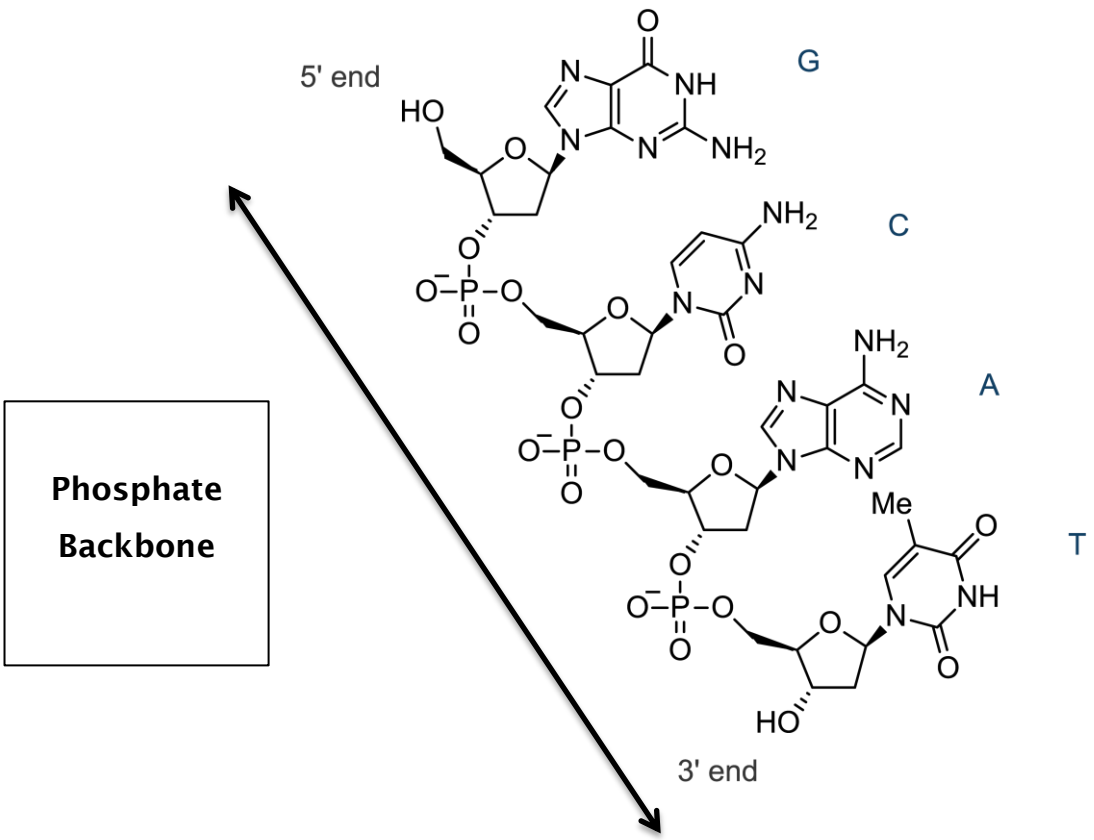

Figure 2.2 Chemical structures of the oligonucleotide dGCAT.[73]

In the 1950s Watson and Crick established that a double stranded helical structure is adopted between complementary single strands with A and T always forming a base pair whilst C always forms a base pair with G. Bonding is also directional i.e. two single strands need to be in reverse order to interact. Therefore a 5' GCAT 3' sequence will form a double strand with a 3' CGTA 5' complementary strand. Furthermore, the forces that hold the double stranded helix together are two fold: a) attractive hydrogen bonding and π stacking between the nucleobases and b) repulsive forces between the negatively charged phosphate backbone.[74]

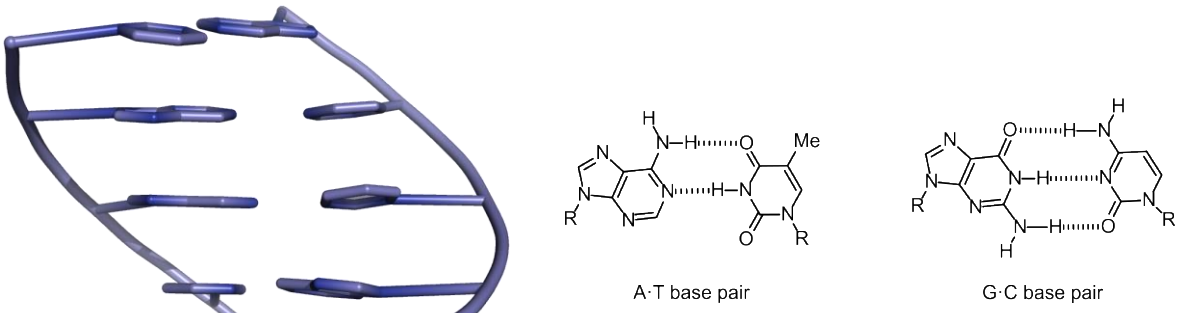

Figure 2.3 Representation of base stacking in a double helix as well as hydrogen bonding between AT and GC base pairs.[73]

Due to the presence of the repulsive forces between the negatively charged phosphate backbone (see Figure 2.2) DNA hybridization is sensitive to the conditions in the surrounding environment such as the pH, ionic strength and temperature of the solution.[75]. Controlling the temperature is crucial for maintaining the intermolecular forces holding the double stranded helix together. An increase in temperature can lead to breaking of the bonds and the dissociation of the double strand to its respective single strands. Controlling the pH of the solution is also important as acidic (pH < 5) or basic (pH > 10) pH values may negatively affect the structure due to protonation or deprotonation of the bases respectively. In general successful hybridization is assisted by the presence of cations, which shield the negative charge of the phosphate backbone thus overcoming the electrostatic repulsion barrier

Another important measurement, which is essential to consider when designing DNA strands for *in vitro* applications is the melting temperature (*Tm*) of DNA. This is the temperature at which 50 % of the double stranded DNA has dehybridised into single strands.[76] One way to experimentally

determine this value is by performing a so-called melting curve where the temperature is gradually increased whilst monitoring changes in the UV absorption of DNA. This technique relies on the hyperchromic effect of DNA. Purine and pyrimidine rings absorb UV light with a max at 260 nm, however, in a double stranded conformation stacking interactions reduce the resonance of the rings and thus their corresponding absorbance.[77] An expected melting curve, which shows the characteristic sigmoidal curve, is depicted in Figure 2.4 where the *Tm* corresponds to the mid-point of a smooth transition. The *Tm* can also be calculated theoretically using various models such as the nearest neighbour method. This method takes into account the enthalpy of formation of a double strand as well as the stacking of the nearest neighbours producing a good approximation that is similar to the experimentally calculated values.[78]

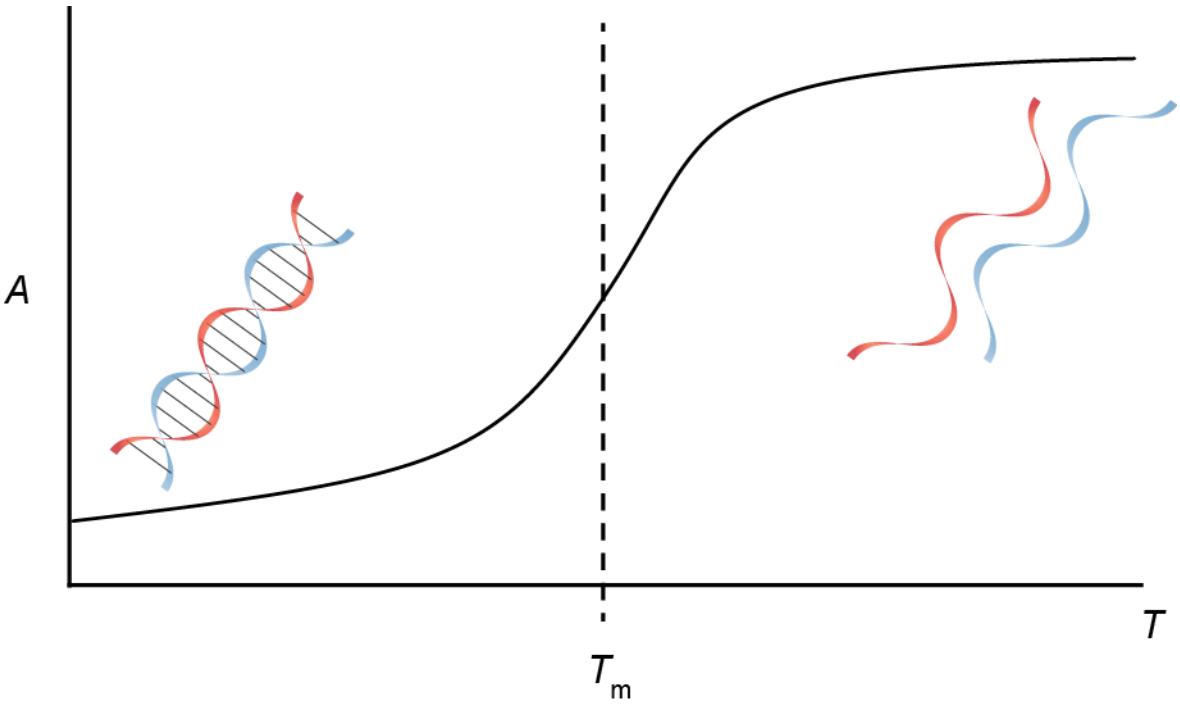

Figure 2.4 A typical melting curve of UV absorbance vs temperature. The melting temperature (*Tm*) is determined at the point of inflection of the curve and corresponds to the temperature at which 50 % of the double stranded DNA is dehybridised.[73]

Finally, one more reason, which makes DNA so appealing for their use in a number of different applications, is the ease of synthesis. Synthetic DNA strands, termed oligonucleotides, can be produced by automated solid phase phosphoramidite synthesis, which allows for the synthesis of strands of any sequence required.[73, 79-81] Moreover, they can be functionalised with a range of functional groups including fluorescent dyes or molecules that can allow for further chemical reactions such as clicking groups.[82, 83] Due to the afformentioned properties including their inherent accurate addressability, oligonucleotides have recently been employed for a number of biomedical applications including mRNA sensing (see **section 2.5.1**) and drug delivery (see **section 2.5.2**) as well as

a scaffold for the programmed self-assembly of nanoparticles into larger structures such as dimers and trimers.[84-88]

2.3.1 DNA/RNA interaction

As previously mentioned, two complementary DNA strands are held together by strong attractive interactions including hydrogen bonding and base stacking. The two strands are able to coil around each other into a right handed double helix where the hydrophobic base pairs are arranged in the centre and the sugar moieties as well as the negatively charged phosphates form the hydrophilic backbone. However, depending on the conditions present the DNA double helix can adopt a number of different structural conformations.

The principle form that helical DNA adopts is known as B-DNA (see Figure 2.5) and is believed to predominate in cells. It consists of a wide major groove and narrow minor groove along the entire length of the molecule. On the other hand, A-DNA, another biologically active helical structure, is shorter and more compact with the base pairs no longer being perpendicular to the helical axis. Nevertheless, this structure is also right-handed and has been found to form under dehydrating conditions (see Figure 2.5). Finally the Z-DNA (see Figure 2.5), an alternative structure determined from an X-ray crystal structure of a chemically synthesised DNA strand, has been found to spontaneously form in aqueous buffer. Compared to A-DNA and B-DNA, it is a left-handed helix and appears to be "zig-zag" in shape. Although its biological relevance has not been determined, it appears to form with when alternating an alternating sequence of GC bases in used.

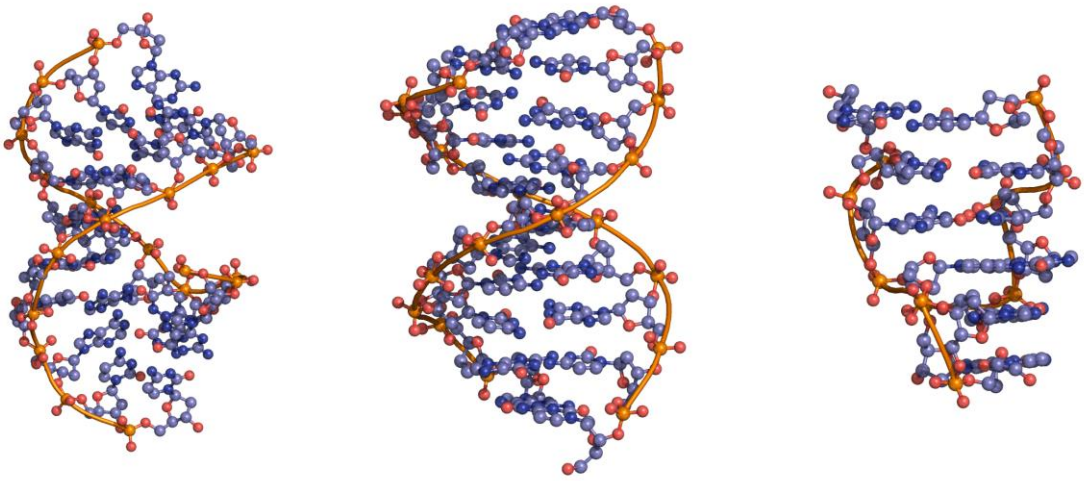

Figure 2.5 Figure showing the three different helical structures that DNA can adopt

For in vitro applications involving the use of DNA within a cellular environment for the detection of RNA molecules as discussed in section 2.5.1 it is also important to consider the stability of an RNA/DNA hybrid duplex.

RNA is commonly used by some organisms, such as retroviruses as storage for genetic information. Although chemically very similar to DNA, RNA displays two very important differences as shown in Figure 2.6. Firstly a hydroxyl group is attached to the 2' position of the sugar moiety and secondly the pyrimidine uracil replaces thymine.

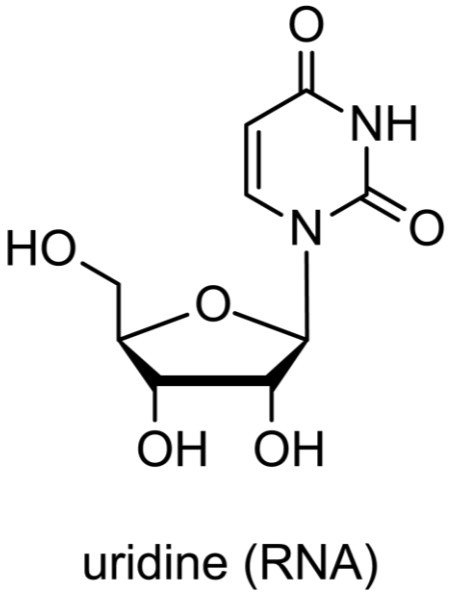

Figure 2.6 Structure of a uridine nucleoside

Although RNA most commonly exists as a single strand, it can also form a right-handed duplex according to the same base pair rules where a G base will hydrogen bond with a C base whereas a U base will hydrogen bond with an A base. However, unlike DNA, a RNA duplex is most commonly found in the A-form where the major groove is deep and the minor groove is shallow. This structural difference could pose some stability risks when a DNA/RNA hybrid duplex in formed in the case of mRNA or μRNA detection as discussed in section 2.5. As DNA predominantly exists in the B-form, hybridization to a complementary RNA strand that structurally prefers the A-form will result in a less stable duplex that could be increasingly prone to de hybridization. Nevertheless DNA strands are preferentially used throughout the work presented in this thesis due to the increased susceptibility of RNA strands to degradation. The additional OH group on the sugar moiety renders the strand increasingly prone to degradation by RNase enzymes compared to a DNA strand. Research however, has focused on tackling this issue by modifying the synthesis of

synthetic RNA strands to include protecting groups at the 2'-position of the sugar moiety. Most commonly used modifications include 2'-OMe, locked nucleic acids (LNA) or phosphorothioates. These modifications endow the RNA strand with increased stability towards digestion by nucleases whilst also maintaining the RNA structure.

2.4 Surface functionalization of spherical AuNPs with oligonucleotides

Spherical AuNPs have been used in many applications ranging from labels for *in vitro* detection to gene regulation materials. This is due to their intrinsic optical properties as well as their rich surface chemistry. They can act as a scaffold for attaching and orienting a variety of surface ligands that endow the system with new functional properties.[84]

Ligands that can be conjugated to a nanoparticle surface include amongst others peptides as well as antibodies.[87] Peptide coated nanoparticles have been shown to alter intracellular localization and increase the efficacy of conjugated biomolecules.[89] For example peptide sequences derived from the HIV Tat protein have been extensively used with a view of increasing the delivery of synthetic materials to the cell nucleus.[90, 91] On the other hand, antibody-labelled nanoparticles specific for the targeting of cancer cells have recently been used in imaging as well as photothermal therapy.[92]

Mirkin and co-workers were the first to show that a 13 nm spherical AuNP core can be densely functionalised with a shell of synthetic oligonucleotides coordinated *via* sulphur groups to the gold as shown in Figure 2.7.[10] These structures, termed spherical nucleic acids (SNAs),

were found to exhibit cooperative properties such as higher binding constants of up to two magnitudes compared to free strands of the same sequence, sharp melting transitions, an increased resistance to degradation by nucleases as well as the capability of being taken up by a plethora of cell lines without the need of physical or chemical transfection methods.[93-95] Although SNAs are composed of a gold inorganic core, the aforementioned properties mainly result from the density and orientation of the oligonucleotides on the surface, which create a 3D structure.[84]

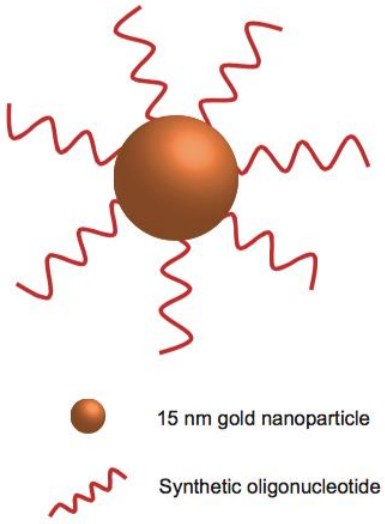

Figure 2.7 Representative figure of a spherical nucleic acid that consists of a gold nanoparticle core functionalized with multiple synthetic oligonucleotides.

A synthetic method leading to the synthesis of a robust SNA was first introduced by Mirkin and co-workers. The so-called salt-ageing protocol allows for the conjugation of multiple oligonucleotides by screening the negative charge of the phosphate backbone of neighbouring strands. This

is successfully achieved by gradually increasing the NaCl concentration in solution over an 8 h period to > 0.15 M (up to 2 M in the presence of surfactants) as shown in Scheme 2.6.[84, 96]

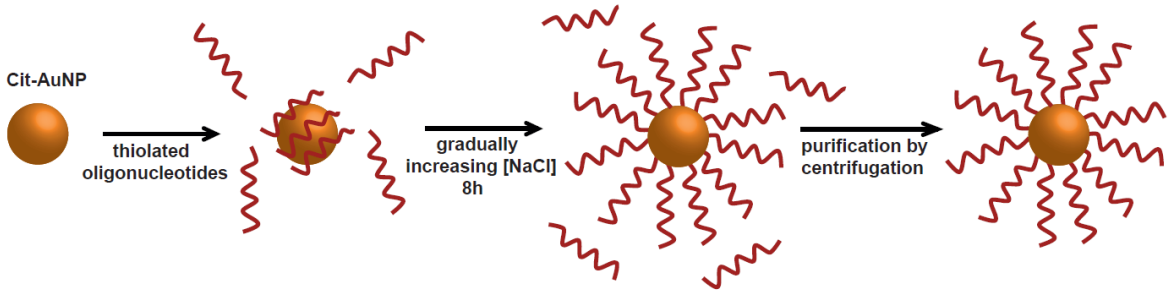

Scheme 2.6 Schematic illustration of oligonucleotide attachment to an AuNP surface *via* the salt-ageing method.

Higher salt concentrations generally lead to higher oligonucleotide densities until steric constraints prohibit further adsorption onto the surface with the resulting monolayer being especially stable due to the strong Au-S bond (40 kcal/mol).[84, 97] The strength of this covalent bond is similar to that of a Au-Au bond and thus using thiol terminated ligands is one of the most common methods to achieve conjugation onto a AuNP surface.[98]

The maximum number of oligonucleotides bound to a AuNP surface is size dependent. In general nanoparticles of a smaller size can support a larger density due to a higher radius curvature. Research by Hill *et al.* showed that a higher curvature results in a natural deflection angle between neighbouring strands creating additional space, which minimises electrostatic and steric repulsion constraints. As the size increases and the

radius curvature decreases this effect is minimised and conjugation become less effective.[99]

Another important variable is the type of nucleobases closer to the AuNP surface. Hurst *et al.* found that a spacer sequence of approximately 8 – 10 bases (~ 3 nm) can extend the active oligonucleotide sequence away from the surface, which increases flexibility in binding and minimises steric barriers in terms of complement hybridisation with research by the same group suggesting that T and A spacers can provide increased rigidity in comparison to G and C bases.[100, 101] Nevertheless, Mirkin and co-workers have reported that for 15 nm spherical AuNPs a loading range spanning from 50 to 200 oligonucleotides per AuNP can be achieved depending on the experimental conditions and oligonucleotide sequences used.[84]

Apart from the well-known salt-ageing method other techniques have also been reported for the functionalization of AuNPs. Kanaras *et al.* showed that careful vacuum centrifugation of a nanoparticle solution with 0.1 M NaCl ensured a gradual and steady increase in ionic strength and oligonucleotide concentration as the volume of the solution decreased resulting in stable DNA-coated AuNPs with a calculated density of approximately 230 oligonucleotides per AuNP surface.[102] On the other hand Zhand *et al.* reported a pH-assisted method that allows for quantitative oligonucleotide adsorption using a low pH buffer (pH ~ 3) of a designated number of oligonucleotides.[103]

Mirkin and co-workers were the first to report on the dense functionalization of AuNPs with oligonucleotides, however, it was Alivisatos and co-workers who first demonstrated the ability to functionalise gold surfaces with a distinct (1,2) number of oligonucleotides

per AuNP.[9] In order to control the stoichiometry the ratio of oligonucleotides to AuNPs has to be precisely regulated. However, even with a ratio of 1:1 a population of di- and tri- conjugates is also observed as well as particles that have not been functionalised as illustrated in Scheme 2.7.[104-106] Therefore purification is an important step in achieving discrete DNA-AuNP conjugates.

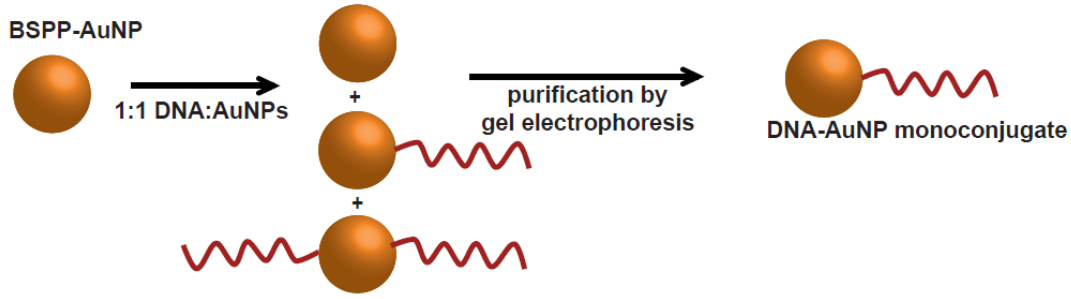

Scheme 2.7 Synthesis of AuNPs functionalised with one oligonucleotide strand (ssDNA - AuNP monoconjugates). Even when a ratio of 1:1 (oligonucleotide: AuNP) is used a variety in the number of oligonucleotides per nanoparticle is achieved. Resulting products are separated and isolated *via* agarose gel electrophoresis.

Although anion exchange high performance liquid chromatography can be used as a purification technique of AuNPs functionalised with a varied number of oligonucleotides, gel electrophoresis represents an alternative as well as less costly method.[107] Zanchet *et al.* showed that by controlling the density of the agarose gel, AuNPs with a discrete number of oligonucleotides could be clearly separated by applying a voltage. However, they also reported that for sufficient separation a AuNP size to oligonucleotide length of at least 1:10 is suggested. Nonetheless, they stated that by hybridising longer complements to short oligonucleotides on the surface of the AuNP isolation can be improved with Busson *et al.*

even purifying larger AuNPs (30 nm) conjugated to short strands.[108, 109]

This work represents an important landmark in the functionalization of AuNPs and has led to the use of AuNPs as building blocks for the programmed assembly of larger structures such as dimers as well as the development of systems to be used within live cells with great further potential as seen in **Chapter 5.**

2.5 Interaction of DNA-coated AuNPs with mammalian cells

Ever since the development of DNA-coated AuNPs, their use within cells for *in vitro* applications has been increasingly growing especially for the detection of RNA.[93, 110-112]

Important biological processes such as cancer progression rely not only on bulk mRNA expression, but are highly dependent on cell-to-cell variations in mRNA levels.[112-114] Previously reported methods for the detection of mRNA include real time polymerase chain reaction (RT-PCR) and microarray analysis. However, these techniques can only give an indication of average mRNA expression from cell lysates and are incapable of detecting cell-to-cell variation.[112, 113] Alternative approaches that could be used within live cells include synthetic fluorophore labelled oligonucleotides such as FRET probes or molecular beacons, which translate target binding into a fluorescence signal. However, these techniques are hindered by their instability in biological environments as well as the requirement of transfection agents to assist with cellular internalisation, which can be toxic or can alter cellular processes.[87, 115-117]

One approach to overcoming these drawbacks related to live cell mRNA detection uses a probe based on the development of SNAs termed nanoflares. In this system SNAs are designed with a thiol modified sense strand that is conjugated to the AuNP surface. To this, a shorter fluorophore modified oligonucleotide is attached termed flare strand. The sense sequence can be designed to detect a specific mRNA target thus when the target mRNA binds, the flare strand will be released due to competitive hybridization and a fluorescence signal will be detected. In the absence of the target the flare will remain bound and the fluorescence signal corresponding to the dye will be quenched by the gold core.[110, 111] A representative illustration is shown in Scheme 2.8.

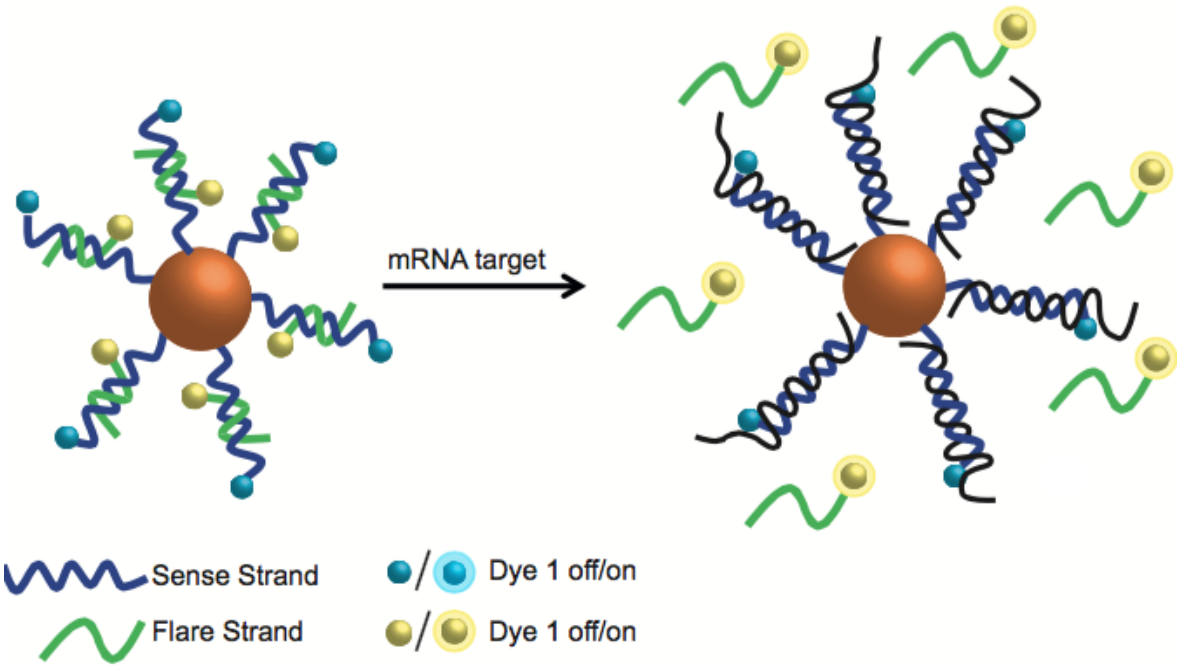

Scheme 2.8 Schematic illustration of nanoflares used for live cell mRNA detection. Fluorophore tagged oligonucleotides are used which due to the close proximity to the gold core are quenched. When

the target mRNA binds to the sense strand the release of the flare can be detected as an increase in its fluorescence signature.

As with SNAs, one of the most important properties of nanoflares is their ability to enter a wide variety of cells without the need of transfection agents.[1, 84, 87] This surprising property, which was first noticed for SNAs, has been a topic of on going investigation.

The facile uptake was not predicted due to the negative charge of the system however, Giljohann *et al.* showed that SNAs can be added to cell media and internalised by various cell lines including primary cells and neurons. Inductively coupled plasma mass spectrometry (ICP-MS) measurements performed to quantify internalization showed that uptake is dependent on cell type, concentration and incubation time with DNA density being the most important factor as bare citrate stabilised particles passivated with BSA showed orders of magnitude lower cellular uptake.[101] Chithrani *et al.* demonstrated the importance of the polyvalent arrangement around the AuNP core as they found that HeLa cells were able to internalize over a million SNAs compared to only a few thousand citrate-coated AuNPs.[118]

Given the surprising ability to enter cells, the mechanism of uptake has consequently been extensively investigated and is thought to be dependent on the adsorption of proteins from cell culture media.[101] Exposure has been found to result in a greater positive charge that could aid with internalization across the negatively charged membrane. Giljohann *et al.* demonstrated that a decrease in oligonucleotide loading caused a decrease in protein adsorption, which in turn affected cellular uptake.[101] Chinen *et al.* also investigated how differences in oligonucleotide sequences can impact the protein corona. They concluded

that G rich sequences increased protein binding both in number and type, which in turn led to higher cellular uptake rates in macrophages.[119] A general mechanism for SNA endocytosis was proposed by Choi *et al.* who suggested that SNAs bind strongly to scavenger receptors A (SR-A), which mediate cellular uptake. Upon binding to SR-A, SNAs are subsequently internalized via a caveolae-mediated pathway due to the close proximity of SR-A and lipid raft domains.[120]

Finally, the ability of SNAs and subsequently nanoflares to resist enzymatic degradation is one of the most important fundamental properties of this system, which is thought to be due to the high local ion concentration.[1, 84, 87, 121] Simulations by both Zwanikken and Lee have demonstrated an enhanced local ion concentration near the nanoparticle surface where specifically the concentration of sodium ions was found to be 20 % higher than in the bulk solution.[122, 123] It has been found that changes in oligonucleotide density renders the nanoflare structure more susceptible to degradation by enzymes such as DNase I.[124] The dense packing of oligonucleotides resulting in steric inhibition of enzyme binding was suggested as a possible explanation.[87] However, the Lineweaver-Burk analysis suggested that enzyme binding is not reduced but in fact enhanced thus an increase in resistance as a function of density was most likely due to other effects rather than steric inhibition.[125] Seferos *et al.* suggested that the high local ion concentration, which increases with oligonucleotide density, was in fact the most likely reason.[125] Indeed it has been suggested that monovalent cations such as Na^{+} can displace Ca^{2+} and Mg^{2+} that are bound to the enzyme and are required for their activity.[126] To further elucidate this hypothesis, a nuclease engineered to be able to tolerate high ion concentrations (Turbo DNase) was tested and consistent with the proposed hypothesis a high rate of degradation was observed.[125]

2.5.1 DNA-coated AuNPs for live cell RNA detection

Since their initial development nanoflares have been used extensively for the detection of mRNA targets by monitoring the fluorescence output of the flare strand as shown in Scheme 2.8. The first example of the use of nanoflares for mRNA detection was demonstrated by Seferos *et al.* where the survivin mRNA transcript was targeted.[110] The SURVIVIN protein functions to inhibit apoptosis of the cell whilst also regulating cell proliferation and is expressed in high numbers in many human cancers.[127] SKBR3 (human breast cancer) and HeLa (human cervical cancer) cells were treated with nanoparticle probes for the detection of survivin mRNA and a 2.5-fold higher fluorescence signal was detected compared to treatment with non-targeting nanoprobes.[111, 128] Nanoflares have also been employed in cancer stem cells (CSC), a distinct subpopulation within a tumor, which is thought to drive tumor progression. Owen *et al.* designed a probe specific for the detection and isolation of viable CSC using flow cytometry *via* the specific detection of nanog mRNA, a marker that is highly expressed in CSC and that correlates with patient survival.[129] On the other hand, Hendrix *et al.* monitored the expression of nodal mRNA in melanoma, which has been shown to underlie unregulated cell growth, metastasis and the CSC phenotype.[130] Li and co-workers adapted SNAs in order to monitor the expression of runx2 and sox9 mRNA, two targets that can be used to assess the osteogenic differentiation of human bone marrow derived mesenchymal stromal cells (hBMSCs).[131] Krane *et al.* demonstrated the expression of NANOG and GDF3 in embryonic stem cells and induced pluripotents stem (iPS) cells of murine, human and porcine origin. Furthermore, they also monitored the expression of *Gapdh*, a common house-keeping gene, in somatic cells.[132]

In another category of studies, the nanoflare design was altered to include hairpin-forming oligonucleotides containing a terminal dye, which were then attached to an AuNP quencher to act as fluorescent molecular beacons upon the detection of a specific mRNA. For example, Sun and co-workers designed a hairpin nanoparticle probe targeting exon8 of brca1 mRNA, a human tumour suppressor gene that plays an important role in repairing damaged DNA, whilst Gu and co-workers focused on the detection of stat5b mRNA, which provides insight into tumour progression, in MCF 7 cells (human breast cancer).[133, 134]

Another class of nanoflares termed fluorescence resonance energy transfer (FRET) nanoflares have also been developed that compared to single dye systems avoid false positive signal due to possible intracellular degradation. In this system the flare strand is fluorescently labelled with both a donor and an acceptor at the 5' and 3' ends respectively and is designed to form a hairpin structure when not bound to the sense strand. In the absence of the specific target only the fluorescence from the donor will be detected, however, when the target is present the flare is released and is able to adopt the hairpin structure. This will allow for high FRET efficiency between the donor and the acceptor and the ratio of Fa/Fd can be used as a signal.[117, 135, 136] Chen and co-workers demonstrated how this system could successfully be used to evaluate the presence of telomerase, a relative specific cancer marker, in a number of different cell lines such as HeLa and MCF-7 cells.[136] Furthermore, Yang *et al.* also used this system to detect tk1 mRNA, which is associated with cell division in HepG2 and MCF-7 cells as well as L02 cells, which were selected as a negative control.[135]

Simultaneous detection of more than one mRNA target has also been in prime focus, as imaging of multiple intracellular biomarkers holds great

promise for the early detection of cancer. As a first example of a multiplexed nanoprobe, Prigodich *et al.* designed a nanoflare probe capable of detecting, simultaneously, two different mRNA targets related to survivin and actin, by monitoring two separate fluorescent outputs.[137] Tang and co-workers adapted this approach and developed nanoparticle probes for the simultaneous detection of three and four intracellular mRNA biomarkers (c-myc, tk1, ga1nac-t and survivin mRNA) all related to the process of tumor progression.[138, 139] However, the ratio among the sense oligonucleotide strands on the nanoparticle was not controlled, a limitation that can influence significantly the efficiency of nanoparticles to detect all the relevant mRNA targets.

Apart from the detection of mRNA Briley *et al.* reported a novel SNA construct, termed stickyflares that allow for the spatiotemporal analysis of RNA transport and localization. This was made possible with a simple design change of the nanoflare system where the flare sequence is made longer and complimentary to the target RNA transcript. Using this construct they were able to track and analyze the spatial distribution of β-actin mRNA and U1 small nuclear RNA (snRNA) in MEF and HeLa cells.[140]

Apart from mRNA, microRNA, a small group of non-coding RNAs, have also been used as targets for detection. As opposed to mRNA, aberrant expression of microRNA is commonly observed in cancer initiation, oncogenesis and tumor response to treatment thus representing an interesting target for detection.[141] Tu *et al.* used a molecular beacon type nanoflare for the detection of miR-122 in Huh7 cells. This target constitutes 70 % of the microRNA in the liver and reduction can be associated with hepatocellular carcinoma.[141] Furthermore, Huang *et al.* made use of the already developed multiplexed nanoflare system for the

simultaneous detection of two microRNA targets, miR-21 and miR-141 in live cancer cells including HeLa cells and LOVE-1 cells.[142]

2.5.2 DNA-coated AuNPs as therapeutic agents

Apart from RNA sensing and tracking SNAs have also been evaluated as potential therapeutic agents for the treatment of diseases including cancer with the aim of overcoming common drawbacks in current treatments.[84]

One important example is their use for targeted gene silencing by using conjugates functionalized with RNA-capping ligands capable of interfering with the RNA interface (RNAi) pathway.[87] Recent developments including the use of small molecule inhibitors and antibodies that target the signaling pathway have revolutionized the treatment of diseases, however these protein based therapeutics are not only costly but can also lead to systemic toxicity.[143] One alternative strategy was the use of silencing RNA (siRNA) SNAs for the blocking and or degradation of mRNA prior to protein translation. This leads to targeted protein down-regulation and function inhibition. These structures are almost 6 times more stable than molecular RNA and due to the facile uptake they have a more persistent ability to silence genes.[144] Furthermore, research by Barnaby *et al.* has found that the stability of siRNA SNAs could be further increased *via* the incorporation of 2-O-methyl RNA nucleotides at sites that are more susceptible to hydrolysis.[145]

Jensen *et al.* successfully designed a siRNA SNA conjugate as an RNAi based therapy for gleoblastoma multiform (GBM), a neurologically debilitating disease that culminates in death 14 to 16 months after initial diagnosis. Their study focused on targeting and knocking down bcl2l12 mRNA and subsequently protein levels, which is overexpressed in GBM

relative to a normal brain. They demonstrated that siRNA SNAs could be systematically delivered by crossing the blood brain barrier (BBB), leading to reduced BCL2L12 protein expression in intracerebral GBM, increased intratumoral apoptosis and reduced tumor burden without side effects.[146] Following this study Sita *et al.* used siRNA SNAs designed to target O6-methylguanine-DNA-methyltransferase (MGMT) repair protein with the aim of improving the chemotherapeutic treatment targeting GBM. Temozolomide (TMZ) is the most common chemotherapeutic agent to treat GBM, however treatment is hindered by MGMT that removes the cytostasis and apoptosis inducing methyl adducts added by TMZ. Their analysis reveals that not only were the conjugates able to pass the BBB as expected but they were also effective in silencing MGMT thus significantly enhancing the effectiveness of TMZ at reducing tumor size of mice bearing intracranial xenografts.[147]

Apart from their use in cancer treatment siRNA SNAs have also proven to be effective in other research areas including diabetic wound healing. Randeria *et al.* proposed that by targeting ganglioside-monosialic acid 3 (GM3) synthase, a mediator in impaired would healing in type 2 diabetic mice, wound healing could be accelerated.[148] Zheng *et al.* also suggested that topical skin application is possible for suppressing genes in the skin whilst Nemati *et al.* further reaffirmed this result by using siRNA SNAs for the treatment of psoriasis.[143, 144]

Another class of therapeutic SNAs has recently been reported by Moreno *et al.* termed immunomodulatory SNAs. Modulating immunity in a targeted approach has shown promising early results particularly for treating infectious diseases, cancer, allergy and autoimmune diseases. Several techniques have been developed capable of stimulating or repressing immunity however the use of nucleic acids has proven to be the most

successful. They are able to stimulate immunity by binding endosomal toll-like receptors or antagonizing them with the aim of treating diseases such as autoimmune disorders. Nevertheless a key challenge that still remains is increasing activity in humans. Moreno *et al.* demonstrated that by specifically functionalizing AuNPs with oligonucleotide pharmacophores, immunomodulatory SNAs could be used to stimulate or regulate immune responses. Moreover, they demonstrated that due to the ease of uptake and endosomal compartmentalization activity was significantly improved compared to free oligonucleotide counterparts. Treatment of mice with cancer using immunostimulatory SNAs and mice with non-alcoholic steatohepatitis (NASH), an extreme liver disease, with immunoregulatory SNAs showed exceptional outcomes compared to their unstructured counterparts.[149]

Finally apart from regulating gene expression or modulating immunity, SNAs have also been presented as efficient vehicles for the targeted delivery of chemical agents such as chemotherapeutic drugs. Recent work by our group has shown that the sense/flare duplex of the nanoflare system presented in Scheme 2.8 can be used for the delivery of DOX only to cells expressing the mRNA target, which the nanoflare was designed to detect. Being a natural DNA intercalator, DOX was loaded in the sense/flare DNA duplex and only released in the presence of the specific mRNA target whilst in the absence of the target the drug payload was retained within the duplex. Heuer-Jungemann *et al.* were able to monitor drug release *via* confocal microscopy due to the drugs inherent fluorescent properties and observed that drug release resulted in significant cell death. In the absence of the mRNA target cell viability remained unaffected.[150] Lee *et al.* also demonstrated that DOX intercalation into a duplex attached to the AuNP core represents an important development to overcoming the poor cellular translocation of DOX and its low efficacy. Similar to results

presented by Heuer-Jungemann *et al.* they found that DOX was stable within the oligonucleotide duplex and was easily uptaken by SW480 cells, a colorectal cancer cell line, causing significant toxicity even at low concentrations. Furthermore, *in vivo* studies demonstrated how this system could significantly suppress cancer growth in mouse xengraft compared to free DOX.[151] On the other hand Dhar *et al.* illustrated how metal complexes such as platinum (IV) prodrugs can be covalently linked to SNA AuNPs for the delivery of cisplatin. Once internalized the platinum (IV) complexes were reduced to the cytotoxic Pt (II) analogue and released to the cytoplasm through reductive elimination of their axial ligands. They found that when introduced into the cell *via* a SNA-AuNP system a more significant effect was observed than when introducing cisplatin alone due to insufficient cellular uptake.[152] Additionally Zhang *et al.* demonstrated how drugs that are non soluble thus rendering them hard to administer such as placlitaxel can be conjugated to a SNA shell. They not only noticed and increase in solubility by over 50 times but they also found that the drug exhibited lower IC_{50} values compared to the free drug.[153]

2.5.3 TPPL imaging of AuNPs in cells

In previous sections the vast capabilities of SNAs were presented including their use as RNA sensors and as therapeutic agents for the targeted treatment of diseases including skin conditions. However, as mentioned in **section 2.2** AuNPs also demonstrate interesting optical properties that can be used for their direct imaging within cells.

AuNPs that display strong TPPL are attractive as contrast agents for bioimaging as it allows for non-invasive imaging of living tissue with high penetration depths, 3D mapping capabilities and reduced photobleaching.[67] Furthermore, TPPL strongly increases the signal to

noise ratio and is appealing due to the absence of a background signal, which is important when imaging in scattering media. In the past, small organic or biological fluorophores have been used for live cell imaging however, their use was limited due to short observation times as a result of photobleaching as well as their low signal compared to background autofluorescence. For prolonged live cell tracking, quantum dots were presented as a feasible alternative due to their enhanced stability relative to organic dyes. However, the most well-studied quantum dots are composed of heavy metals that are cytotoxic making them unsuitable for *in vivo* clinical applications.[66, 67, 154] AuNPs on the other hand, are biocompatible and have a large two-photon action cross-section making them ideal alternative candidates.[67]

Research by Gao *et al.* suggested that TPPL is shape dependent with branched AuNPs and AuNRs displaying the strongest TPPL.[67] However, AuNRs are more commonly used. AuNRs as small as 8 × 40 nm can be easily detected with a high signal to noise ratio. Furthermore, they are easily functionalized, are non-cytotoxic and their longitudinal plasmon resonance can be tuned to the near infrared wavelengths where biological tissue exhibits relatively small extinction coefficients.[154] One study involved the use of folate nanorods for the targeted delivery to KB cells (a tumor cell line derived from oral epithelium), which is known to overexpress folate receptors. *Via* TPPL imaging it was noticed that 6 h after incubation a high density was present on the outer membrane with complete internalization occurring after 17 h. Furthermore, when incubated with a cell line lacking these receptors little to no uptake was observed.[155] However, TPPL imaging has also proven useful for imaging in 3D using cancer cells supported in a collagen matrix to mimic tissue. Durr *et al.* also showed that by conjugating anti-EGFR antibodies to AuNRs of 14 and 48 nm in width and length, EGFR overexpressing A431 skin

cancer cells could be imaged by TPPL with characteristic bright rings being observed as well as bright spots in the cytoplasm, which they suggest was indicative of endosomal uptake.[66] The strong TPPL signal of AuNRs was also taken advantage of by Wang *et al.* who successfully demonstrated how they could be used as *in vivo* imaging agents. By monitoring the TPPL signal the flow of AuNRs through mouse ear blood vessels could be tracked. TPPL signal was found to be 3 times higher than the background and interestingly no signal could be detected after 30 minutes indicating successful clearance from circulation.[65]

On the other hand Liu *et al.* demonstrated how branched nanoparticles could also be imaged *in vivo*. As mentioned in **section 2.2,** branched AuNPs have a high TPPL signal mainly due to their sharp spikes that result in larger TPPL action cross-section. Their study highlighted the ability of successfully imaging branched nanoparticles of two different sizes (30 and 60 nm) after intravenous injection into mice with xengraft sarcomas. However, when testing 12 nm AuNPs no TPPL signal could be detected.[156] In contrary to this result, Rane *et al.* found that TPPL imaging of AuNPs ranging from 10 to 70 nm coated with an oligonucleotide shell could be successfully imaged in 2D and 3D models of the HCT116 cell line, a colorectal carcinoma cell line.[157]

2.6 Nanoparticle assemblies

In recent years, advances in experimental protocols to functionalize AuNPs with thiol-modified oligonucleotides have enabled the design of sophisticated nanoparticles as well as the formation of precisely organized nanostructures.[9-11] Oligonucleotides are superior ligands because of their biological relevance, high specificity, selectivity and versatility in conjunction with the ease of their chemical manipulation.[2] Several

groups have used oligonucleotide functionalized AuNPs to create nanoparticle dimers, trimers and tetramers with tunable nanoparticle distances as well as mesoscale structures containing millions of nanoparticles in precise arrangements (*e.g.* body-centered cubic and face-centered cubic).[88, 158-161]

2.6.1 Click chemistry

Following the discovery that DNA can be used as a tool for the precise organization of nanoparticles into larger assemblies, methods to develop more stable DNA nanoparticle assemblies have been explored. Forming a covalent bond rather than relying on the event of hybridization would endow the assembly with higher stability towards changes in temperature as well as ionic strength.[162]

Since its discovery by Kolb, Fin and Sharpless, copper (I) catalyzed click chemistry has provided an alternative method for the precise linking of molecules.[163] However, the need for a Cu (I) complex catalyst represents a major drawback especially when used within aqueous solutions as Cu (I) can easily be converted to Cu (II), which is inactive. To overcome this challenge our group recently combined advances in the synthesis of DNA-coated AuNPs and click chemistry to form DNA AuNP assemblies stable under DNA denaturing conditions or biologically complex environments.[162, 164] In one of these methods, a copper-free click chemistry strategy was utilized to permanently ligate DNA-AuNP conjugates. Synthetic oligonucleotides modified by an alkyne or azide group were brought into close proximity *via* a templating splint strand. Partial complementarity to both modified oligonucleotides resulted in successful oligonucleotide hybridization bringing in close proximity the alkyne and azide groups, catalyzing a ligation reaction. This approach to

manipulating AuNP assemblies allowed the formation of AuNP dimers and trimers in high yield, which were stable even under DNA denaturing conditions.[162] The reaction relies on a Cu free Huisgen cycloaddition involving a strained alkyne and an azide as shown in Scheme 2.9. This leads to a highly stable triazole moiety that can resist extreme conditions such as high temperatures.[83]

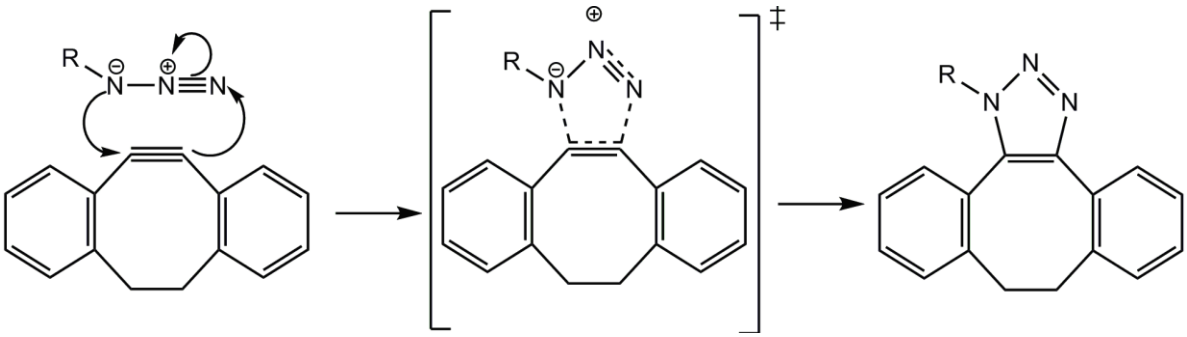

Scheme 2.9 Mechanism of ring-strain promoted, copper free cycloaddition.

Results presented in **Chapter 5** show how Cu free click chemistry can be successfully utilized for the programmed ligation of two DNA-coated AuNPs for biomedical applications.

2.6.2 Interaction of nanoparticle assemblies and cells

Even though the interaction of DNA-coated AuNPs with cells for a plethora of applications has been well investigated as described in **section 2.5**, the use of assemblies within cells has not been as thoroughly studied.

Kotov and co-workers showed that nanoparticle assemblies composed of a gold nanorod core surrounded by gold spheres *via* DNA mediated assembly could be imaged in live cells using Raman spectroscopy.[165] On the other hand Chou *et al.* demonstrated the synthesis of an assembly for

biological applications composed of spherical nanoparticles. However, when taken up by macrophages dissociation of the assembly was observed.[166] Moreover Ohta *et al.* designed an assembly composed of a AuNP core surrounded by smaller satellites capable of changing conformations. By transforming the structure in response to DNA they demonstrated how cellular targeting and subsequent uptake could be precisely controlled.[167] Finally Chan and co-workers recently showed how assemblies following a core satellite design, which involves the use of a nanorod as the core and spherical nanoparticles as satelites could be used as a drug delivery vehicle. By loading the structure with DOX via duplex intercalation, they showed not only significant cellular uptake of the assembly but also tuned drug release leading to significant cell death of up to 80 % in HeLa cells.[168]

Chapter 3 – Experimental procedures

This chapter includes procedures for the synthesis and surface modification of gold nanomaterials presented in **sections 3.1 and 3.2**. All characterisation techniques and cell culture studies are shown in **sections 3.4 and 3.5**.

3.1 Synthesis of AuNPs

AuNPs of different shapes and sizes were synthesised in aqueous solutions using well-established bottom-up approaches. Protocols for their synthesis and characterisation of the resulting products can be found in **sections 3.1 and 3.4** respectively.

3.1.1 Synthesis of spherical AuNPs

Spherical AuNPs of two different sizes (15 ± 1 nm and 43 ± 4 nm) were synthesised via the reduction of sodium tetrachloroaurate (III) dihydrate by citrate.

3.1.1.1 15 ± 1 nm spherical AuNPs

15 ± 1 nm spherical AuNPs were synthesised by the reduction of sodium tetrachloroaurate by citrate, a method pioneered by J. Turkevich [16, 17] and refined by G. Frens [18]. This synthesis produces monodisperse particles that can be suspended in water.

In detail, a sodium tetrachloroaurate solution in water (100 mL, 1 mM) was brought to the boil whilst stirring (700 rpm). To this a trisodium citrate

solution (5 mL, 2 % wt) was added and colour change from yellow to colourless to purple was observed with a final solution colour of wine red, indicating the successful formation of nanoparticles. The solution was left to stir for an additional 15 min under boiling and subsequently cooled to room temperature under slow stirring (200 rpm). Once cooled, citrate ligands on the surface of the nanoparticles were exchanged with bis(p-sulfonatophenyl)phenyl phosphine dehydrate dipotassium salt (BSPP) by adding 20 mg to the solution. After stirring overnight, a concentrated solution of NaCl (~ 1.5 mL) was added until a colour change to purple/blue was observed indicating particle aggregation *via* charge screening. Particles were then purified by 2 sets of centrifugation (5,000 rpm, 15 min) and re-dispersed in Milli-Q water. Remaining large aggregates were subsequently purified by filtration (0.2 μm, VWR) and particles were stored at 4 °C prior to further functionalization (see **section 3.2.1**).

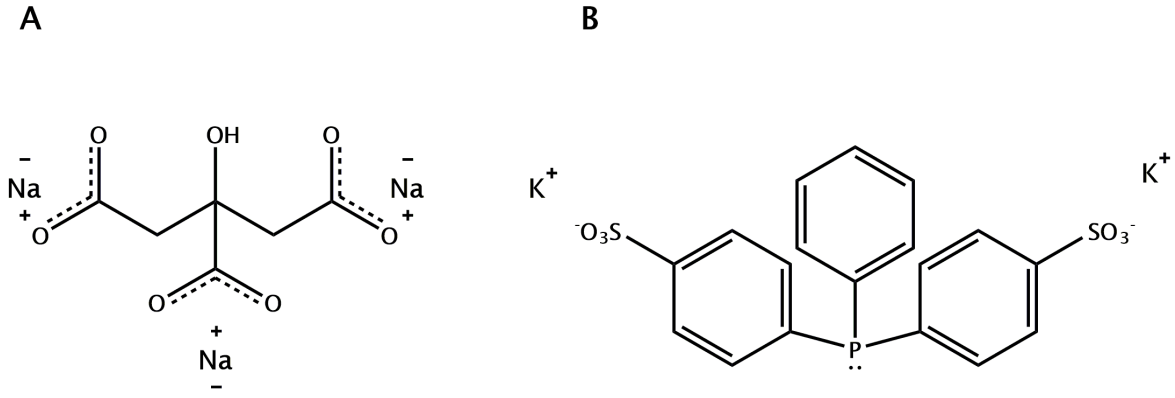

Figure 3.1 Chemical structures of citrate (A) and BSPP (B)

3.1.1.2 43 ± 4 nm spherical AuNPs

For the synthesis of larger particles (> 20 nm) a kinetically controlled seeded growth strategy was followed developed by Puntes et al.[26] This

method allows for the synthesis of monodisperse citrate-stabilised AuNPs with a quasi-spherical shape and a narrow size distribution.

In detail, the Au seed solution was firstly prepared by heating a solution of sodium citrate in Milli-Q water to boiling conditions (150 mL, 2.2 mM) with a heating mantle under vigorous stirring. A three-necked round-bottomed flask (250 mL) was used, which was fitted with a condenser to avoid solvent evaporation. Once boiling had commenced, a solution of $NaAuCl_4$ (25 mM, 1 mL) was quickly injected. After boiling for a further 10 min the colour of the solution had changed from yellow to bluish grey to light pink. Immediately after the temperature of the solution was cooled to 90 °C and a $NaAuCl_4$ solution (1 mL, 25 mM) was injected. After 30 min one more addition of a gold solution (1 mL, 25 mM) was performed to form the initial generation of particles (g0). After that, the sample was diluted by extracting 55 mL of sample and adding 53 mL of Milli-Q water and sodium citrate solution (2 mL, 60 mM). This solution was then used as a seed solution, which was injected with three consecutive gold solution additions every 30 min at 90 °C to generate the next generation of particles (g1).

After synthesis was complete, citrate-capped gold nanospheres were purified by two rounds of centrifugation (6,000 rpm, 20 min), decantation and re-dispersion in Milli-Q water. Larger aggregates were then removed by filtration (0.2 μm, VWR). Sample was stored at 4 °C prior to further functionalization (see **section 3.2.1.3**).

3.1.2 Synthesis of AuNRs

Anisotropic AuNRs of varying aspect ratios were synthesised following a modified seed mediated approach where additive ions such as Ag^+ assist in the growth of rod-shaped AuNPs.[33, 38, 39, 169]

In detail, the seed solution was firstly prepared by heating a solution of cetyltrimethylammonium bromide (CTAB, 1 mL, 0.2 M) to 40 °C. To this, an aqueous solution of sodium tetrachloroaurate (1 mL, 5 mM) was added. Under vigorous stirring, an ice-cold solution of sodium borohydride (0.5 mL, 0.01M) was pipetted dropwise into the reaction mixture and a colour change from yellow to light brown was observed indicating the successful formation of small particles (~ 2 nm). After two minutes of vigorous stirring the solution was left to stand at 40 °C until the growth solution was prepared.

The growth solution was prepared by heating a solution of CTAB (14.24 mL, 0.2 M) to 40 °C. To this, an aqueous solution of sodium tetrachloroaurate (2 mL, 5 mM) was added followed by a solution of silver nitrate (150 – 400 μL, 5 mM). By varying the volume of silver nitrate added to the reaction mixture the AuNR aspect ratio could be accordingly tuned. Under gentle stirring a freshly prepared L-ascorbic acid solution (160 μL, 78.8 mM) was added and a colour change to colourless was observed. After 30 s of slow stirring the solution (16 μL) was pipetted into the reaction mixture. The stirring was immediately stopped and the AuNRs were left to grow overnight. Depending on the aspect ratio of AuNRs synthesised the colour of the solution changed accordingly. AuNRs were purified by two rounds of centrifugation (6,000 rpm, 15 min), decantation and re-dispersion in Milli-Q water. For purification using an ultracentrifuge, sucrose gradients (20, 40, 60 and 80 %) were prepared and layered carefully on top of each other. The AuNR solution was carefully pipetted on to the top surface and centrifuged (10,000 g, 45 min). The required layer was removed using a syringe and purified once more by normal centrifugation (16, 400 rpm, 15 min) and re-dispersed in Milli-Q water. The final solution was stored at 4 °C prior to further surface modification (see **section 3.2.2**).

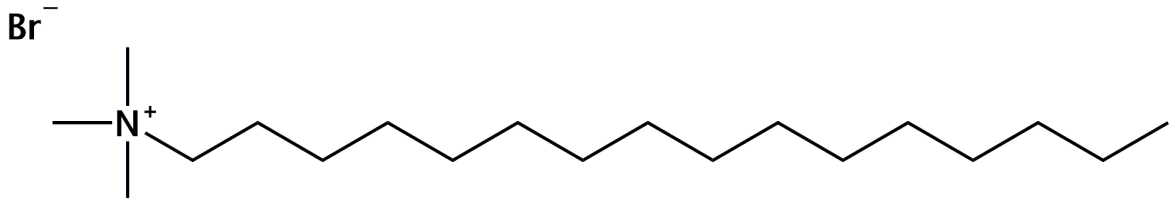

Figure 3.2 Chemical structure of CTAB

3.1.3 Synthesis of branched AuNPs

Branched AuNPs were synthesised by a modified surfactant-guided, seed-mediated growth method.[170] A growth solution was prepared by mixing an aqueous solution of CTAB (14.24 mL, 0.2 M), sodium tetrachloroaurate (III) dihydrate (2 mL, 5 mM) and silver nitrate (410 μL, 5 mM). BSPP coated coated 15 nm AuNPs (16 μL, 5mM, see **section 3.1.1.1**) were injected into the solution followed by a freshly prepared aqueous solution of L-ascorbic acid (160 μL, 157.6 mM). The reaction mixture was left to slowly stir at 40 °C for 1 h 30 min. The formation of anisotropic AuNPs was indicated by a colour change from colourless to scattering blue after the addition of L-ascorbic acid.

Excess CTAB was removed from the solution mixture by two rounds of centrifugation (8,000 rpm, 10 min), decantation and redispersion in Milli Q water (3 mL). Sample was stored at 4 °C prior to further use.

3.2 Surface modification of AuNPs

The surface of gold nanomaterials of different morphologies were modified for either optical or biomedical purposes.

3.2.1 Surface modification of spherical AuNPs with oligonucleotides

For conjugation of oligonucleotides with AuNPs, thiol-terminated oligonucleotides were utilized. Modified oligonucleotides were synthesised by Dr Afaf El-Sagheer from Prof. Tom Brown's group (University of Oxford) (see **section 3.3.2** for protocol).

3.2.1.1 Oligonucleotide attachment to 15 ± 1 nm spherical AuNPs

15 nm spherical AuNPs were modified with either one oligonucleotide strand (monoconjugates) or with a complete shell of oligonucleotides, termed spherical nucleic acids (SNAs).

3.2.1.1.1 Synthesis of spherical AuNP monoconjugates

BSPP coated 15 ± 1 nm spherical AuNPs (1 mL, 50 nM)(see **section 3.1.1.1**) in attachement buffer (20 mM phosphate, 6 mM NaCl) were incubated with thiol modified oligonucleotides bearing an alkyne or azide moiety at a 1:1 ratio. BSPP (10 μL, 1 mg/20 μL) was added to the reaction mixture, which was left to shake gently for 1 h. Functionalised spherical AuNPs were purified by gel electrophoresis (2% agarose gel, 100 V, 1 h) (see **section 3.4.1**) and the respective bands in the gel were extracted, cut into small pieces and stored in 0.5 × Tris/Borate/EDTA (TBE) buffer overnight whilst shaking gently.[108] Once monoconjugates had fully diffused out of the gel they were purified by three rounds of centrifugation (16,400 rpm, 30 min, 4 °C), decantation and redispersion in hybridisation buffer (5 mM PBS, 80 mM NaCl). Monoconjugates were stored at 4 °C prior to further use (see **section 3.3.3**).

3.2.1.1.2 Synthesis of 15 ± 1 nm spherical nucleic acids

15 ± 1 nm spherical AuNPs were modified with a shell of oligonucleotides according to a well-established literature procedure.[93] This involves a slow salt-ageing procedure where the negative charge of the oligonucleotide phosphate backbone and the AuNP surface is screened by the gradual addition of a NaCl solution as illustrated in Scheme 2.6. [99]

In detail BSPP coated 15 nm spherical AuNPs (1 mL, 10 nM) (see **section 3.1.1.1**) in Milli-Q water were incubated with thiol modified oligonucleotides (1 mL, 3 μM) overnight to allow the mixture to equilibrate. BSPP (10 μL, 1 mg/ 20 μL), phosphate buffer (0.1 M, pH 7.4) and sodium dodecyl sulphate (SDS) (10 %) were added the spherical AuNP/oligonucleotide solution to achieve a final concentration of 0.01 M phosphate and 1 % SDS respectively. The NaCl concentration was brought up to 0.3 M over an 8 h period in a stepwise manner by the gradual addition of NaCl. The solution was sonicated (5 min) after every addition to keep the particles well-dispersed during the salting procedure. Following the NaCl additions, the solution was shaken for an additional 16-20 h to yield fully functionalised AuNPs. In order to remove any unbound oligonucleotides, the sample was purified by three rounds of centrifugation (16,400 rpm, 20 min) including supernatant removal and resuspension in phosphate buffer saline (PBS) and were stored at 4 °C.

3.2.1.2 Modifying the oligonucleotide loading on 15 ± 1 nm AuNPs

In order to coat our gold nanoparticles with a defined number of oligonucleotides a salt-ageing method was employed. Briefly, BSPP coated 15 nm gold DNA monoconjugates (1 mL, 10 nM) in water were incubated with thiol modified DNA strands at different ratios to achieve different

loading denisties (3 μM, 1.5 μM, 0.5 μM and 0.2 μM and 0.1 μm in 1 mL) and the reaction mixture was left to shake for 24 h. BSPP (10 μL, 1 mg/20 μL), phosphate buffer (0.1 M, pH 7.4) and sodium dodecyl sulfate (10 %) were then added to the nanoparticles' solution to achieve final concentrations of 0.01 M phosphate and 1 % SDS respectively. A final salt concentration of 0.30 M was achieved by 6 additions of a NaCl (2 M) solution over a period of 8 h. When incubated with a decreased concentration of oligonucleotides (0.5 μM, 0.2 μM and 0.1 μm) the final salt concentration achieved was 100 mM over 6 consecutive additions in 8 h. The resulting DNA-coated gold nanoparticles were purified by three steps of centrifugation (16,400 rpm, 20 min) and were stored at 4 °C in a hybridisation buffer (5 mM phosphate buffer, 80 mM NaCl).

3.2.1.3 Oligonucleotide attachment to 43 ± 4 nm spherical AuNPs

Oligonucleotide attachment to larger spherical AuNPs was successfully achieved using a pH-assisted protocol. This method allows for the instantaneous DNA adsorption onto the gold surface via the use of a pH 3 citrate buffer.[103]

Briefly citrate capped 43 ± 4 nm spherical AuNPs (1.35 mL, 10 pmol) were mixed with a 300 x excess of thiol terminated oligonucleotides (20.88 μL, 3 nmol) and vigorously stirred for 1 min. This was followed by the addition of a pH 3 citrate buffer (30 μL, 500 mM). After 3 min the Na^+ ion concentration was increased via the addition of a NaCl solution (225 μL, 2 M) to reach a final concentration of 0.3 M within the final solution. The solution was left to stir for 1 min before three rounds of centrifugation (12,000 rpm, 15 min), decantation and redispersion in PBS. The purified solution was stored at 4 °C prior to their use in further applications.

3.2.2 Surface modification of AuNRs with silica

CTAB-stabilized AuNRs were coated with a uniform SiO_2 shell via modified published protocols.[171, 172]

Whilst stirring on a hotplate at 40 °C, CTAB (275 μL, 40 mM) was added to an AuNR solution (10 mL, 1.25 pmol) to make the final concentration of CTAB in the solution up to 1.1 mM. An aqueous solution of NaOH (100 μL, 0.1 M) was pipetted into the AuNR solution followed by a solution of dissolved tetraethyl orthosilicate (TEOS) in methanol (20 % v/v). Three aliquots of the TEOS solution (30 μL, 20% v/v) were pipetted into the AuNR solution at 30 min intervals. This was then left to slowly stir for 18 h at 40 °C. Purification was then achieved by two rounds of centrifugation (5,000 rpm, 15 minutes). Silanised particles were re-dissolved in 5 mL of ethanol and stored at 4 °C prior to further use.

3.3 DNA – coated AuNP dimers

DNA – coated AuNP dimer assemblies have been used throughout this project for live cell detection of up to two mRNA targets[1, 2, 111, 128, 133, 137-139] as well as the simultaneous delivery of up to two anticancer drugs, DOX and MTX [150]. The design and synthesis of modified oligonucleotides is outlined in **section 3.3.1 and 3.3.2,** which are specific for the detection of vimentin and keratin 8 mRNA whereas the assembly synthesis and drug incorporation is outlined in **section 3.3.3**. Characterisation techniques are outlined in **section 3.4 and 3.5.6**.

3.3.1 Design of specific oligonucleotide sequences

Oligonucleotide sequences were designed in order to assemble single AuNPs into dimers as well as for the detection of specific mRNA targets. Important factor such as sequence length, melting temperatures and chemical modifications have been taken into account to ensure the successful assembly of the most stable and target specific AuNP dimer.

3.3.1.1 Design of oligonucleotide linker strands

Two complementary oligonucleotide strands were designed to assemble two AuNPs into dimers. In order to separate AuNPs with one strand attached (monoconjugates, see **section 3.2.1.1.1**) from AuNPs that have no or more than one oligonucleotide strands attached, the oligonucleotide strand had to consist of 50 bases or more. Shorter oligonucleotide strands would result in unresolved bands when purifying *via* gel electrophoresis.[173] Both oligonucleotide strands were therefore designed to have a total length of 86 bases each with a 26 base pair complementarity between them that would result in a melting temperature of ~ 76 ºC (see **Table 3.1** for relevant sequences). Sequences were also modified with clicking groups (see **Figure 3.3** for chemical structures) to ligate the oligonucleotide strands when in close proximity to each other due to hybridization[162].

Table 3.1 Sequence of oligonucleotide strands designed to ligate AuNPs into dimers. X: thiol modifiier 6 S-S (CPG resin from Glen Reserach), M1: alkyne derivative, M2: azide derivative

Name	Oligonucleotide sequences (5' to 3') with modifications
Linker Strand 1	X-TTTGGCCGAGGACTCCTGCTCCGCTGCGGTTTGGCGAACTGGACCGTCTACTTA CCGTT **TCCGACGAGCCACA-M1-CCGGAACAGCCC**
Linker Strand 2	X - TTTCGCGCACCTGAGACCTTCTAATAGGGTTTGCGACAGTCGACGACTAGAATGC CCTTT**GGGCTGTTCCGGA-M2-GTGGCTCGTCGG**

3.3.1.2 Design of oligonucleotide sense/flare strands

mRNA sequences for vimentin and keratin 8 mRNA as well as "scrambled" sequences that do not detect any cellular mRNA were designed using the NCBI database (http://www.ncbi.nlm.nih.gov/nucleotide/). **B**asic **L**ocal **A**lignment **S**earch **T**ool (BLAST) was used to determine an appropriate sense and flare strand sequence that would be specific for the target mRNA. The nucleotide-specific blast (blastn) was used with the following settings: Database: RefSeq RNA, Entrez Query: all (filter) NOT predicted

(title), Species: Homo Sapiens, Expected Threshold: 10 Match/Mismatch scores: 2/-3. A sense sequence was designed with the following criteria: length: 21-23 bases, GC content < 50 %, E value < 0.05, E value of nearest match > 1. A flare strand was designed, complementary to the sense sequence with a length of 10-12 bases and a melting temperature of > 40 ºC (see Table 3.2 for relevant sequences). All strands were also modified with fluorescent dyes for their use in biomedical applications.

Table 3.2 Sense and flare oligonucleotide sequences. X: thiol modifier 6 S-S (CPG resin from Glen Research)

Name	Oligonucleotide sequences (5' to 3') and modifications
Keratin 8 (sense strand 1)	**FAM** – GGTGGTCTTCGTATGAATACAAAAAAAA – **X**
Keratin 8 (flare strand 1)	**Cy3** – GTATTCATACGAAG
Vimentin (sense strand 2)	**FAM** – CTTTGCTCGAATGTGCGGACTTAAAAAAAA – **X**
Vimentin (flare strand 2)	**Cy5** – AAGTCCGCACA
Scramble sense 1	**FAM** – ATGGTATACCGAAAGACTGTTAAAAA – **X**
Scramble flare 1	**Cy3** – AACAGTCTTTCG
Scramble sense 2	**FAM** – TATGCCGTATAGCGGTAACACTAAAAAAAA– **X**
Scramble flare 2	**Cy3** – AGTGTTACCGCTAT
gmRNA (sense strand)	**X**-AAA CGG GCT TTT TTT TTT TTT TTT TTT TTT TTT TTT T-**FAM**
gmRNA (flare strand)	AAA AAA AAA AAA GCC C-**Cy5**

3.3.2 Synthesis of oligonucleotides

Modified oligonucleotides were synthesized by Dr Afaf El Sagheer (Prof Tom Brown's research group) at the University of Oxford using the following protocol.

In detail, standard DNA phosphoramidites, solid supports, and additional reagents were purchased from Link Technologies Ltd, Glen Research and Applied Biosystems Ltd. All oligonucleotides were synthesized on an Applied Biosystems 394 automated DNA/ RNA synthesizer using a standard 0.2 or 1.0 μmole phosphoramidite cycle of acid-catalyzed detritylation, coupling, capping, and iodine oxidation. Stepwise coupling efficiencies and overall yields were determined by the automated trityl cation conductivity monitoring facility and in all cases were >98.0 %. All β-cyanoethyl phosphoramidite monomers were dissolved in anhydrous acetonitrile to a concentration of 0.1 M immediately prior to use. The coupling time for normal A, G, C, and T monomers was 60 s, and the coupling time for the Amino-Modifier C6 dT, 5'-FAM, 5'-Cy3, 5'-Cy5 and 5'-thiol C6-S-S phosphoramidite monomers (From Link Technologies Ltd) was extended to 600 s. for the amino modifier C6 dT, the resin in the column was washed with 20 % diethylamine in acetonitrile before cleaving and deprotection. For oligonucleotides modified with 3'-thiol, 3'-modifier C6 S-S CPG resin from Glen research was used. Unless stated elsewhere, cleavage of the oligonucleotides from the solid support and deprotection was achieved by exposure to concentrated aqueous ammonia solution for 60 min at room temperature followed by heating in a sealed tube for 5 h at 55 °C. Purification of oligonucleotides was carried out by reversed-phase HPLC on a Gilson system using a Brownlee Aquapore column (C8, 8 mm x 250 mm, 300 Å pore) with a gradient of acetonitrile in triethylammonium bicarbonate (TEAB) increasing from 0 % to 50 % buffer B over 30 min with a

flow rate of 4 mL/min (buffer A: 0.1 M triethylammonium bicarbonate, pH 7.0, buffer B: 0.1 M triethylammonium bicarbonate, pH 7.0 with 50 % acetonitrile). Elution of oligonucleotides was monitored by ultraviolet absorption at 295 or 300 nm. After HPLC purification, oligonucleotides were freeze-dried then dissolved in water without the need for desalting. For long oligonucleotides, polyacrylamide gel electrophoresis was used for purification. Oligonucleotide bands were then visualized using a UV lamp and the desired bands excised, crushed and soaked in water overnight at 37 °C. After evaporation, samples were desalted using NAP-25 followed by NAP-10 columns (G.E. Healthcare Life Sciences).

For azide labelled oligonucleotide, the oligonucleotide was synthesized with an Amino-Modifier C6 dT for post-synthetic labelling. The freeze-dried oligonucleotide was dissolved in Na_2CO_3/$NaHCO_3$ buffer (80 µL, 0.5 M, pH 8.75). 6-azidohexanoic acid NHS ester (1 mg) was dissolved in DMSO (80 µL) and added to the oligonucleotide. After 4 h, the now fully labelled oligonucleotide was desalted using a NAP-10 column (GE Healthcare) and purified by RP-HPLC. For alkyne labelling, the oligonucleotide was synthesised with a Amino-Modifier C6 dT for post-synthetic labelling. After freeze-drying, it was dissolved in Na_2CO_3/$NaHCO_3$ buffer (160 µL, 0.5 M, pH 8.75). DIBO active ester (1.8 mg) was dissolved in DMF (160 µL), added to the oligonucleotide and the mixture incubated at 55 °C for 4 h. The labelled oligonucleotide was then desalted using a NAP-10 column, followed by purification by RP-HPLC.

All Purified oligonucleotides were characterised by electrospray mass spectrometry. Mass spectra of oligonucleotides were recorded either using a Bruker micrOTOFTM II focus ESI-TOF MS instrument in ES- mode or a XEVO G2-QTOF MS instrument in ES- mode. Data were processed using MaxEnt and in all cases confirmed the integrity of the sequences.

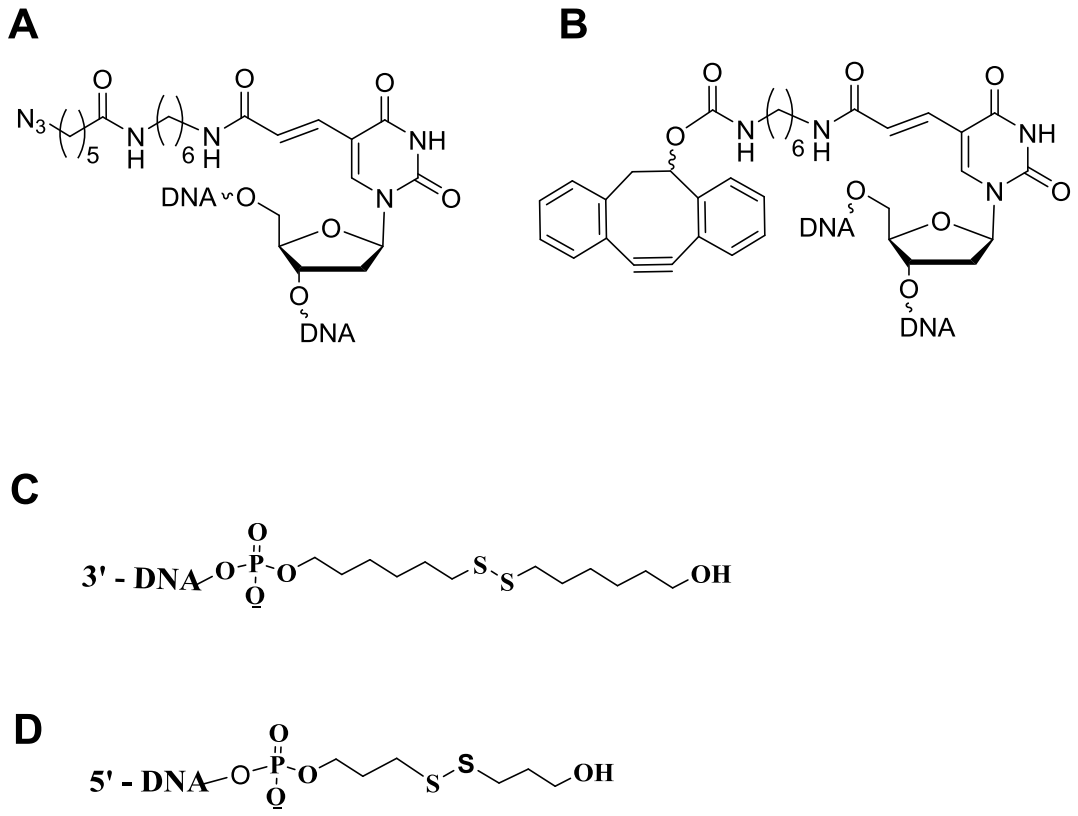

Figure 3.3 Chemical modifications of oligonucleotides. A) DNA with internal amino C6 dT labelled post-synthetically with azido hexanoic acid NHS ester, B) DNA with internal amino C6 dT labelled post-synthetically with DIBO NHS carbonate, C) DNA with 5'-Thiol modifier C6 S-S, D) DNA with 3'-Thiol modifier C3 S-S

3.3.3 Synthesis of AuNP dimers for live cell applications

BSPP coated 15 ± 1 nm spherical AuNPs were firstly modified with a single oligonucleotide strand (monoconjugate, see **section 3.2.1.1.1**) bearing either an alkyne or an azide moiety (chemical structures shown in Figure 3.3). The salt-ageing method (see **section 3.2.1.1.2**) was then

employed to achieve a shell of sense oligonucleotide strands (targeting either vimentin or keratin 8 mRNA) around each batch of AuNP monoconjugates.

Nanoparticle dimers were formed by combining the oligonucleotide-coated AuNP batches at a molar ratio of 1:1 and by heating at 80 °C for 5 min and then cooling to room temperature. The close proximity between the azide and alkyne moieties after hybridisation resulted in the chemical ligation of the linker strands between the two nanoparticles. The resulting product was subjected to denaturing conditions *via* incubation with formamide (50 % v/v).[174] The solution was heated to 80 °C for 15 min followed by immediate purification by gel electrophoresis (1.75 % agarose gel, 10 V/cm, 30 min) and stored in PBS.

For flare hybridisation, nanoparticle dimers (200 μL, 3.75 nM) were mixed with an excess of the complementary flare strands (200 μL, 75 nM). The solution was heated up to 55 °C for 5 min followed by slow cooling to room temperature to allow hybridisation to occur. Samples were purified by two rounds of centrifugation (16,400 rpm, 15 min) or until no background fluorescence was observed from flare strands within the solution and re-dispersed in PBS.

For drug incorporation (see Figure 3.4 for chemical structures), nanoparticle dimers in PBS (200 μL, 3.75 nM) were firstly incubated with an excess of DOX (1mg/ 4mL) and keratin 8 flare strands (200 μL, 75 nM). The solution was heated up to 60 ºC for 5 min and left to cool down to room temperature. The solution was purified by three rounds of centrifugation (16,400 rpm, 4 ºC, 30 min) or until no fluorescence from DOX was detectable in the supernatant. Dimer AuNPs were dispersed in a buffer (200 μL, Tris 10mM, $MgCl_2$ 7.5 mM and NaCl 300 mM) and incubated

with an excess of MXT (1 mg/ 4 mL) and vimentin flare strands (200 μL, 75 nM). For cell viability experiments, AuNP dimers were loaded with more DOX and MXT by increasing the number of flare strands attached per nanoparticle for both keratin 8 (200 μL, 225 nM) and vimentin (200 μL, 225 nM). $MgCl_2$ (200 μL, 7.5 mM) and an increased salt concentration (200 μL, 300 mM) was used when hybridising the vimentin flare to assist with hybridization. The solution was sonicated for 5 min and then left to shake overnight. After 3 rounds of purification by centrifugation (16,400 rpm, 4 ºC, 30 min) and ensuring that there is no MXT fluorescence in the supernatant, the AuNP dimers were dispersed in PBS and used in further cellular experiments.

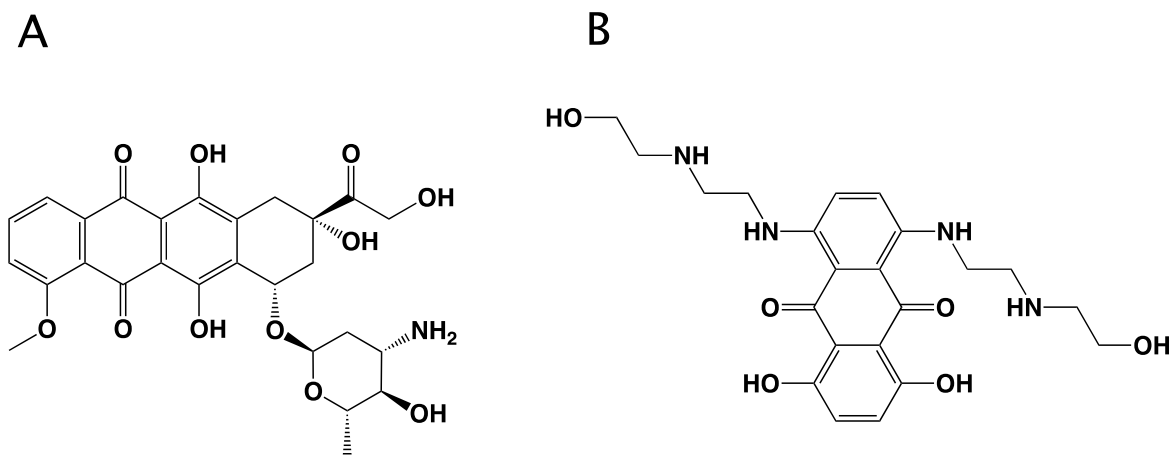

Figure 3.4 Chemical structure of doxorubicin (A) and mitoxantrone (B)

3.4 Characterisation techniques

Oligonucleotides and nanomaterials, including DNA-AuNPs, were characterised by employing a number of different techniques outlined in the following sections ranging from gel electrophoresis (see **section 3.4.1**) to confocal microscopy (see **section 3.4.3.2**).

3.4.1 Gel electrophoresis

Gel electrophoresis has become an important tool for the analysis and purification of DNA sequences and nanoparticles and describes the movement of particles or molecules in a gel matrix under an electric filed. Separation of the objects relies on the size and charge of the particles or molecules being analysed. Gel matrices of different pore sizes and density are used to separate between different populations within the same sample as they significantly alter their electrophoretic mobility. Typically two different types of gel matrices are used, agarose (see **section 3.4.1.1**) and polyacrylamide (see **section 3.4.1.2**) gels.

3.4.1.1 Agarose gel electrophoresis

Agarose gel electrophoresis was employed for sample analysis and purification of nanoparticles due to the larger pore size within the matrix, which starts off from several hundred nanometres for a 1 % gel.[175, 176]

Gels were prepared by dissolving agarose (1.75 or 2 %) in 0.5 × TBE. This was heated in a microwave for 5 min ensuring that the agarose has completely dissolved. The solution was subsequently poured into a gel cast and combs were inserted to create wells. After allowing to stand for 2 h, the gel was placed in an electrophoretic chamber containing 0.5 × TBE. Prior to inserting within the wells, samples were mixed with a solution of Ficoll (15 % in 3 × TBE) in order to increase the density of the sample. The loaded samples were then run at 10 V/cm for approximately 50 min or until a clear separation between bands was visible. If used for the purification of samples, bands of interest were extracted from the gel, cut into small pieces and left overnight shaking in 0.5 × TBE buffer to allow the sample to dissolve out of the gel. The recovered sample was then filtered

(0.2 μm, VWR) and centrifuged three times (16,400 rpm, 15 min). Final sample was re-dispersed in Milli-Q water or PBS.

3.4.1.2 Polyacrylamide gel electrophoresis (PAGE)

Polyacrylamide gels have pore sizes that range from few tens of nanometres to several hundred nanometres depending on the concentration of polyacrylamide making it suitable for the separation of small molecules such as oligonucleotides.[177]

A 6 % PAGE gel was prepared in a 70 mL volume. A solution containing a 40 % acrylamide: bis-acrylamide (19:1) solution (10.5 mL) and 5 × TBE (14 mL) was made up to 70 mL using Milli Q water. The polymerization was initiated by the addition of an intiator (560 μL, amine persulfate) and a crosslinker (56 μL, N,N,N',N'-tetramethylethylenediamine, TEMED) (see Figure 3.5). The solution was then immediately syringed into the glass construct and a comb was inserted to create the appropriate wells to hold the samples. Denaturing polyacrylamide gels were prepared in the same way except for the additional dissolution of urea to a final concentration of 7 M. After allowing to polymerise for 1 h at room temperature, the gel was placed into the electrophoresis chamber in a 1 × TBE buffer. The combs were then removed, the electrodes were connected to a power supply and the gel was run at 10 W for 1h to fill the matrix pores with the buffer. The oligonucleotide samples (50 μL) were mixed with a Ficoll solution (15 % in 3 × TBE) and subsequently loaded into the wells of the gel. If necessary oligonucleotides were also subjected to denaturing conditions prior to loading within the gel. This involved heating up the oligonucleotide sample (90 °C, 15 min) containing formamide (50 % v/v).[174] Samples were then mixed with Ficoll (15 % in 3 × TBE) and loaded within the gel. The loaded gel was run at 10 W for 1.5 h. It was removed from the glass cast and

stained in a SYBR Safe solution for 10 minutes prior to imaging on a blue tray in a Bio-Rad Gel Doc EZ System.

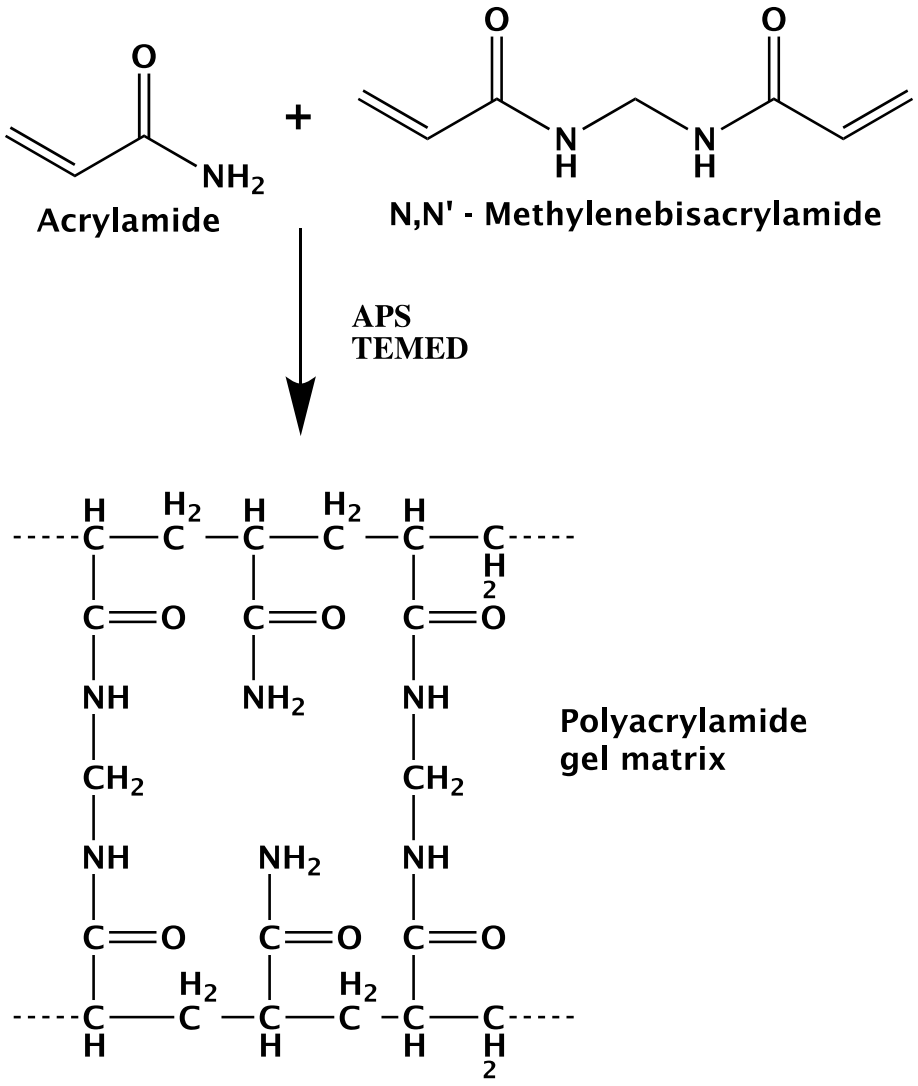

Figure 3.5 Formation of the polyacrylamide gel matrix from its precursors

3.4.2 Spectroscopy

3.4.2.1 Ultraviolet-visible spectroscopy

This technique is widely used in research for the analysis of absorbing materials where a sample is scanned over the ultraviolet and visible range of light and possible changes in intensity are monitored. The concentration of gold colloid and oligonucleotide solutions was determined this way by monitoring the absorption maximum over a wavelength range of 200 to 800 nm.[178] Spectra were gathered using a black Low Volume Quartz Cuvette using a Cary 100 UV-vis spectrophotometer. For dilute samples and negligible scattering the concentration of the analysed solution was determined by using the Beer-Lambert equation.

$$c = \frac{A \ D}{\varepsilon \ l}$$

Equation 3.1 Rearranged Beer-Lambert equation used to determine the concentration of colloidal gold and oligonucleotide solutions. A = absorbance at the peak maximum (a.u.), D = dilution factor, ε= extinction coefficient (L mol^{-1} cm^{-1}), l = path length of light (cm)

The extinction coefficient value is dependent on the type and size of the AuNPs[179] being analysed whereas for oligonucleotides it is sequence dependent and can be calculated using the nearest neighbour or base composition model.[177] Extinction coefficients for all oligonucleotide strands used throughout this project have been determined by Dr Afaf El-Sagheer.

3.4.2.1.1 UV melting analysis of oligonucleotide strands

Melting temperature of linker oligonucleotide strands (see Table 3.1 for sequences) used to assemble two AuNPs into dimers was determined by UV absorption at 260 nm. Two oligonucleotide strands were combined in equimolar amounts (1 mL, 40 nM) in hybridization buffer (300 mM NaCl) in a Suprasil Quartz Absorption cuvette. The solution was heated gradually from 25 ºC to 90 ºC at a rate of 1 ºC/min and then cooled to room temperature at the same rate. This heating and cooling cycle was repeated three times. Absorption readings were taken at a rate of 1 ºC/min at a wavelength of 260 nm on a Carry 300 Bio UV-vis spectrophotometer.

3.4.2.1.2 Oligonucleotide strand loading on spherical AuNPs

The number of oligonucleotide attached to the spherical AuNP surface after salt-ageing (see **section 3.2.1.1.2**) was determined *via* dissolution of the gold core. A solution of KI/I_2 (ratio of I_2 to KI was 1:6) was slowly added (1 µL per addition) to the oligonucleotide-coated AuNP solution (8.33 nM, 120 µL). Successful gold core dissolution was determined by a change in color from wine red to yellow.[180]

The solution was then made up to 1 mL using Milli Q water and loaded onto a NAP 10 desalting column. After the solution had entered the column it was eluted using Milli Q water (1.5 mL). The oligonucleotide O.D. was measured at 260 nm on a DeNovix DS – 11 spectrophotometer. This

value together with the initial O.D. of the oligonucleotide solution synthesised by Dr. Afaf El-Sagheer allowed for determination of the concentration and hence the number of moles of oligonucleotides in solution. Using this information we were then able to determine the number of oligonucleotide "sense" strands attached to the surface of each AuNP.

3.4.2.2 Fluorescence spectroscopy

Fluorescence spectroscopy is a sensitive method for the analysis of light emitting specimens and relies on the radiative relaxation of a molecule from an excited to a lower state. Samples are excited at a specific wavelength and the emitted light is monitored at higher wavelengths.

Fluorescence melting analysis of all samples were performed on a Carry Eclipse Fluorescence spectrophotometer using a low volume quartz florescence cuvette.

3.4.2.2.1 Nuclease assays

The stability of our DNA AuNP dimers was assessed in the presence of cytosolic DNase I and lysosomal DNase II. By monitoring the fluorescence output from the dye on the sense strand and by normalising against 100 % release from the gold surface *via* gold dissolution (see **section 3.4.2.1.2**), the percentage of oligonucleotides remaining bound to the surface of the AuNP dimers could be determined.

In detail, DNA-coated AuNP dimers (150 µL, 2.5 nM) in a solution containing Tris-HCl (10 mM), $MgCl_2$ (2.5 mM) and $CaCl_2$ (0.5 mM) at pH 7.4 were incubated with DNase I (from bovine pancreas, Sigma Aldrich, 2 U/L).

For DNase II nuclease assays, nanoparticle dimers (150 µL, 2.5 nM) in artificial lysosomal fluid (ALF) were incubated with DNase II (from porcine spleen, Sigma Aldrich, 5 U/rxn).[181] Samples were incubated overnight at 37 ºC and fluorescence measurements of the sense strand (FAM) were then taken during a 24 h period to determine the degree of degradation to the sense strands (excitation: 495 nm, emission range: 505 - 800 nm). All experiments were performed in triplicates.

3.4.2.2.2 Fluorescence melting analysis of sense/flare oligonucleotides

Melting analysis was performed on the sense/flare duplex by monitoring the increase in fluorescence intensity of the fluorophore modified flare strand as the temperature gradually increased.[182]

DNA-coated AuNP dimers (150 µL, 2.5 nM) in hybridisation buffer were slowly heated (0.1 ºC/min) from 25 ºC to 70 ºC. The solution was then cooled to room temperature at the same rate. Readings of the fluorescence from each respective flare were taken at a rate of 0.1 ºC/min (excitation wavelengths: 544 nm (Cy3) or 635 nm (Cy5), emission wavelengths: 562 nm (Cy3) or 662 nm (Cy5)).

3.4.2.2.3 Determination of the number of sense/flare duplexes per spherical AuNP

In order to assess the number of duplexes per spherical AuNP a DNA-coated AuNP solution (1 nM, 200 µL) was incubated with the fully complementary target leading to flare dehybridization due to an increased complementarity. The sample was subsequently centrifuged (16,400 rpm, 20 min) and the fluorescence in the supernatant was recorded (keratin 8 – Cy3 excitation: 544 nm, emission: 554 – 800 nm, vimentin – Cy5

excitation: 635 nm, emission: 645 – 800 nm). The number of duplexes formed were determined by using a calibration curve for each flare strand.

3.4.2.2.4 Efficiency of flare hybridisation at room temperature

The efficiency of vimentin flare hybridisation at room temperature was tested in 3 separate buffers with a higher ionic strength compared to PBS.

Table 3.3 Composition of hybridisation buffers

	Tris Concentration (mM)	$MgCl_2$ Concentration (mM)	NaCl Concentration (mM)
Hybridisation Buffer 1	10	1.5	300
Hybridisation buffer 2	10	7.5	300
Hybridisation buffer 3	10	15	300

DNA-coated AuNP dimers (150 µL, 2.5 nM) were re-dispersed in hybridisation buffer 1, 2 and 3 with the complementary flare strand. After sonication for 5 min at room temperature samples were left to shake overnight. They were then purified by three round of centrifugation

(16,400 rpm, 30 min) or until no fluorescence was detected in the supernatant.

To test the efficiency of flare hybridisation, DNA-coated AuNP dimers were treated with the fully complementary target and centrifuged (16,400 rpm, 15 min). The fluorescence signal in the supernatant was recorded to evaluate the efficiency of flare hybridisation and compared to a control sample (flare hybridised in PBS *via* heating).

3.4.2.2.5 Target specificity of AuNP dimers

DNA-coated AuNP dimers in PBS (150 µL, 2.5 nM) were incubated with the target sequences (perfect target, 1 base mismatch, 2 base mismatches and non-complementary targets) at 37 ºC and fluorescence readings were recorded after 2 min until a plateau was reached. Fluorescence spectra were recorded, exciting at 545 nm (Cy3) and 635 nm (Cy5) and scanning the emission over a range of 505-800 nm (FAM), 550-800 nm (Cy3) and 640-800 nm (Cy5).

3.4.2.2.6 Efficiency of drug intercalation

DNA-coated AuNP dimers (8.33 nM, 120 µL) loaded with both DOX and MXT, within their corresponding sense/flare strands, in PBS were heated to 80 °C for 10 min and were subsequently centrifuged (16,400 rpm, 10 min). The fluorescence of the supernatant was then recorded (DOX excitation: 480 nm, emission: 500 – 800 nm, MXT excitation: 610 nm, emission: 640 – 800 nm). Using a calibration curve of each drug and by monitoring the fluorescence intensity of the drug in the supernatant the average loading of DOX and MXT could be determined.

3.4.2.3 Dynamic light scattering (DLS)

The size of colloidal AuNPs suspended in a liquid medium were estimated using dynamic light scattering, which relies both on the Brownian motion and Rayleigh scattering.[183] During this process the sample is illuminated using a monochromatic light source such as a laser, which causes the molecules to scatter light in all directions. This scattered light creates an interference pattern, which due to the constant movement of particles within the liquid medium constantly fluctuates. Finally the hydrodynamic diameter is calculated with the Stokes-Einstein relation by analysing the fluctuations within the sample and correlating them to the diffusion coefficient of the sample.

All samples were made up to 1 mL and placed in disposable cuvettes. All measurements were performed on a Malvern Zetasizer Nano ZS with a He-Ne light source (633 nm wavelength). Each measurement was performed with a 173° backscattering arrangement, consisted of 10 sub-runs of 15 s and was repeated three times.

3.4.3 Microscopy

3.4.3.1 Transmission electron microscopy (TEM)

Light microscopes are limited in their use for the imaging of nanoparticulate structures as the wavelength of light that illuminates the specimen limits the resolution, which is in the range of a few hundred of nanometres. TEM operates under the same basic principles however, electrons are used instead of light. Due to their much lower wavelength (de Broglie wavelength of about 1 nm) the resolution can be improved by a factor of 100 making it possible to image smaller objects

AuNPs were visualised on a Hitachi H7000 transmission electron microscope (operating at an accelerating voltage of 75 kV). For sample preparation, a small amount (~ 10 μL) of the solution to be analyzed was deposited on a 400 mesh formvar coated copper grid and left to air dry overnight.

3.4.3.2 Confocal microscopy

Confocal microscopy is an optical imaging technique used for the analysis of fluorescent specimens. Compared to fluorescence microscopy where the entire sample is flooded evenly in light from a light source, confocal microscopy uses point illumination and a pinhole in front of the detector to eliminate out-of-focus signal. It provides the capacity for direct non-invasive imaging of thick specimens such as cells *via* the use of fluorescent dyes or probes.

For the purposes of this project, nanoparticles bearing fluorescent oligonucleotides and intercalated drugs were incubated with cells (see **section 3.5.6**) and fluorescence was monitored and imaged on a Leica TCS SP8 confocal platform using a × 63 oil immersion objective. Types of lasers used included a Diode 505, Argon, DPSS 561 and HeNe 633. The optimum settings for each dye and fluorescent drug are found in Table 3.4.

Table 3.4 Confocal imaging settings used to monitor the fluorescence signature of each dye and intercalated drug

Fluorescent dyes	**Excitation laser line**
DAPI	405 nm UV
FAM	488 nm Vis
Cy3	561 nm Vis
Cy5	633 nm Vis
Fluorescent drugs	
Doxorubicin	488 nm Vis
Mitoxantrone	633 nm Vis

3.5 Cell cultures

In order to investigate the interaction of nanoparticles with live cells three model cell lines were chosen. Human bronchial epithelial cells (16 HBE), human fetal lung fibroblasts (MRC 5) and adenocarcinomic human alveolar basal epithelial cells (A 549) were cultured and used to study the intracellular fate of AuNPs including mRNA detection and targeted drug delivery only to cells of interest.

3.5.1 Subculturing of cells

16 HBE (in Minimum Essential Medium (MEM)), MRC 5 (in MEM) and A 549 (in Roswell Park Memorial Institute medium (RPMI)) cell lines were cultured in Corning cell culture flasks using the appropriate medium, which was supplemented with 100 U penicillin 100 mg streptomycin (Gibco), 0.29 mg/mL of L-glutamine (Gibco), 1 mL nystatin (Gibco) and 10 % foetal bovine serum (FBS, Sigma Aldrich). The cells were kept at 37 ºC in a 5 % CO_2 atmosphere in a Sanyo CO_2 incubator. Cells were left to grow up to 90 % confluency after which they were passaged.

For passaging, the media was first removed and replaced with Hank's Balanced Salt Solution (HBSS, 10 mL, 5 min) after which cells were displaced using trypsin (5 mL, 0.25 % trypsin, 0.01 % EDTA solution). After 3 minutes the trypsin was inactivated by the addition of full growth media with serum (13 mL). The cell suspension was pelleted by centrifugation (1000 rpm, 5 min) and re-suspended in the appropriate medium (400 – 600 µL). A small amount of this (100 µl) was seeded in a new cell culture flask already containing medium (13 mL, MEM or RPMI depending on the cell culture). The remainder of the cells were used for further experiments.

3.5.2 Cell fixation

For cell fixation the following protocol was used. Cells were grown on coverslips until 90 % confluent. Media was then removed from confluent cells, which were washed with PBS (3 ×, 5 min). After washing, cells were rinsed with 4 % paraformaldehyde (PFA) in piperazine-N,N'-bis(2-ethanesulfonic acid) (PIPES) and left for 1 h at 37 °C. Cells were then washed with PBS (3 ×, 5 min) followed by an incubation step with 4',6-diamidino-2-phenylindole (DAPI) (1/500) in PBS for 15 min. Coverslips were then mounted with Mowiol Glycerol onto glass slides.

3.5.3 Reverse transcription quantitative polymerase chain reaction (RT-qPCR)

3.5.3.1 RNA isolation from cell cultures

Cells at a confluency of 90 % were gently displaced by using trypsin (5 mL, 0.25 % trypsin, 0.01 % EDTA solution). The total RNA corresponding to each cell line was isolated using the Trizol kit (Promega, UK) and the purity of the isolated RNA from each cell line was assessed through UV-vis measurements (A260/A280 ratios between 1.8-2.2), by placing 2 µl of each sample onto a Denovix spectrophotometer (Denovix, UK). Extracted RNA was kept in sterile RNAse free water at -20 °C for a short period of time or stored at -80 °C for longer period to minimize the risk of any RNAse activity and subsequent degradation.

3.5.3.2 Design of specific primers for RT-qPCR

Forward and Reverse oligonucleotide sequences complementary to sections of mRNA coding for vimentin and keratin8 associated proteins in

MRC 5, 16 HBE and A 549 cells were identified in the NCBI database (https://www.ncbi.nlm.nih.gov/) under the Genebank accession number NM_003380.4 (vimentin), NG_008402.2 (keratin8) and AY340484.1 (*Gapdh*). Sequences were then analysed for alignments with other sequences (i.e. similarities) using the NCBI's Basic Local Alignment Search Tool (BLAST) (https://blast.ncbi.nlm.nih.gov/Blast.cgi). Appropriate sequence were chosen with the following criteria: length of sense strand: 20-22 bases, melting temperature ~50 °C, GC content ≤ 50 %, E value ≤ 0.05, E value of nearest match > 1. The used sequences for the specific Forward (F) and Reverse (R) primers were reported in the following table:

Table 3.5 Forward and Reverse sequences for keratin 8, vimentin and GAPDH

Name	Oligonucleotide primer sequences (5' to 3')
Keratin 8 (F)	AAGGTAGAGCTGGAGTCTCGC
Keratin 8 (R)	GTTGGCATCCTTAATGGCC
Vimentin (F)	TGTCCAAATCGATGTGGATGTTTC
Vimentin (R)	TTGTACCATTCTTCTGCCTCCTG
GAPDH (F)	CCCCGGTTTCTATAAATTGAGC
GAPDH (R)	CACCTTCCCCATGGTGTCT

3.5.3.3 cDNA synthesis and RT-qPCR analysis

First-strand cDNA synthesis using 1 μg of total RNA was carried out using the ImProm-IITM reverse transcriptase kit (Promega, USA) with an oligo (dT) primer according to manufacturer's instructions. Samples were first denatured for 5 min at 72 °C before adding the master mix solution as described by the provider. Samples were run through a cycle that included heating at 25 °C for 5 min, followed by 42 °C for 60 min and finally 70 °C for 15 min. The obtained cDNA were kept on ice until further use on the RT-PCR or stored. PCR reactions were performed using a peqSTAR 96 Universal PCR machine (Peqlab, Germany) and Real-time qPCR was

performed on a Step-One Plus instrument (ThermoFisher Scientific, UK) in a RT-PCR 96 well plate. The process included an initial denaturation step at 95 °C for 10 min, followed by 40 cycles of denaturation at 95 °C for 15 s. This was followed by annealing/extension at 60 °C for 60 s, with a final melting curve increment of 0.1 °C/s in the range between 60 and 95 °C. Direct measurements of the raw data were gathered on the Opticon software provided by the instrument provider. Relative quantification gene analysis was performed accordingly to the method previously described by Pfaffl *et al.* taking into account the efficiency of specific forward and reverse primers. Briefly gene expression levels for vimentin and keratin8 were standardised by normalizing them to the house-keeping gene (*Gapdh*).[184] The quantification data collected were representative of a pool of biological triplicates for each cell line, and two technical repeats.

3.5.4 Immunofluorescent labelling

Cell lines were analysed for the expression of specific proteins to determine their suitability for the relevant experiments. Secondary immunofluorescence was used to assess the expression of the keratin 8 and vimentin protein. This process involves the use of two antibodies; the unlabelled primary antibody that specifically binds to the target molecule, and the secondary antibody, which carries the fluorophore. The secondary antibody recognises the primary antibody and binds to it, which is detected as a fluorescence signal when imaged *via* confocal microscopy.

In detail, the desired cell line was seeded on cover slips in a 24-well plate. At 70 % confluency the medium was removed and replaced with ice-cold methanol (15 min) to fix the cells. The methanol was removed and the cells were washed with PBS (5 min x 3). Cells were subsequently blocked

using 1 % BSA in PBS (15 min) and stained with the primary antibody (30 µL) at the appropriate dilution (45 min). After washing with 0.1 % BSA in PBS (5 min x 3) the cells were stained with the secondary antibody (labelled with Alexa Fluor 488) at the appropriate dilution (45 min). Cells were then washed using 0.1% BSA in PBS (5 min x 3) and PBS (1 min). The cell nuclei were counter stained using DAPI at a 1:1000 dilution (10 min) and washed using PBS (5 min x 2). Excess buffer was absorbed from the cover slip with a tissue before mounting on a glass slide using Mowiol containing Citifluor. Cover slips were stored at 4 ºC. Imaging was carried out on a Leica SP8 microscope using a x 63 oil immersion objective.

3.5.5 Incubation of cells with CellLight® markers

CellLight® reagents are fluorescent protein-signal peptide fusions that provide accurate and specific targeting to cellular structures for live-cell imaging applications. Cellular labelling utilizes BacMam technology, which uses an insect cell virus (baculovirus) coupled with a mammalian promoter. Transgenes under the mammalian promoter are expressed, while baculoviral genes and their promoters are not recognized.

16 HBE and MRC 5 cells were seeded in an open µ-slide with 8 wells and a glass bottom at a density which would allow for cells to be 70 % confluent within 3 days. The desired CellLight® marker for the labelling of early endosomes (RFP), late endosomes (GFP) or mitochondria (RFP) was pipetted into each well (4 µL/ 10,000 cells) and incubated for 16 h before imaging.

3.5.6 Interaction of AuNPs with cells

The interaction of AuNPs with live and fixed cells was studied by incubating AuNPs with 16 HBE, MRC 5 and A549 cells and assessing the

specificity of mRNA detection, targeted drug release, cellular viability as well as intracellular location.

3.5.6.1 Incubation of AuNP probes with cells

Cells were seeded in an open µ-slide with 8 wells and a glass bottom at a density which would allow for cells to be 90 % confluent within 3 days. Once 90 % confluent the media was exchanged with fresh media containing single nanoparticle probes (0.8 nM, 200 µL) or nanoparticle dimers (1.9 nM, 200 µL) for 18 h. Prior to imaging cells were also incubated for with Hoechst 33342 (2 µL, 10 min) to stain the nuclei. All imaging was carried out on a Leica SP8 confocal microscope at 37 °C with a constant flow of CO_2 to ensure that the cells are maintained in a healthy environment (see **section 3.4.3.2** for imaging conditions). Sequential imaging was performed when necessary.

3.5.6.2 Ultra-thin sectioning of cells for transmission electron microscopy

In order to investigate the intracellular fate and location of both single nanoparticle probes and nanoparticle dimers after cellular uptake, cells were fixed and embedded in resin. Ultra-thin sections were cut and visualized by TEM.

For fixation and embedding cells were seeded on cellulose transwell inserts in 12 well plates at a cell concentration of 1×10^5 cells/mL for 16 HBEs and 0.5×10^5 cells/mL for MRC 5 and A 549 cells. At a confluency of 90 % all cell lines were incubated with general mRNA coated nanoparticle dimers for 18 h after which they were fixed for 1 h in 4 % formaldehyde/ 3 % glutaraldehyde in piperazine-N,N′-bis(2-ethanesulfonic acid) (PIPES, 0.1 M, pH 7.2). Three washing steps followed (10 min) with PIPES. Cells were

then treated with a post fixative for 1 h consisting of 1 % osmium tetroxide in PIPES buffer. After two steps of buffer rinsing (10 min each) and briefly rinsing with deionized water (30 s), cells were stained with a solution of 2 % (aq) uranyl acetate for 20 min. Samples were then dehydrated by incubating in increasing percentages of ethanol solutions (30, 50, 70, 95 %) for 10 min each. After incubation in 50 % ethanol, transwell inserts were cut from the plastic holders to avoid plastic dissolution in high alcohol concentrations. Transwell membranes were placed in glass vials and completely dehydrated by two consecutive washes (20 min) in complete ethanol. To prepare for resin embedding, samples were treated with acetonitrile for 10 min followed by 1:1 acetonitrile:SPURR resin overnight. The sample was then completely embedded in pure SPURR resin and left for 6 h. After 6 h transwell were cut in half, embedded in fresh SPURR resin in small embedding capsules and polymerized at 60 °C for 24 h.

Resin blocks were cut using a Leica RM 2255 ultramicrotome to produce ultrathin section of cells (<100 nm) that were placed on TEM grids (200 mesh). Sections were visualized *via* TEM (see **section 3.4.3.1**)

3.5.6.3 Viability assay

The effect of DNA-coated AuNP dimers intercalated with DOX and MXT on the percentage viability of 16 HBEs, MRC 5s and A549s was evaluated *via* a trypan blue viability assay.[185]

Cells were seeded in 24 well plates up to 90 % confluency. Then they were incubated with the fully assembled nanoparticle dimers (500 µL, 32 nM) for 18 h. Nanoparticle dimers were loaded with an excess of keratin 8 and vimentin flare as well as an excess of DOX and MXT according to

previously stated method. Then cells were washed with Hank's salt (HBSS) followed by incubation with trypsin (250 µL, 0.25 % trypsin 0.01 % EDTA solution) to detach cells from the surface. After 5 min incubation at 37 ºC the trypsin was inhibited with cell culture medium. This was combined with the previously removed medium and the cells were pelleted by centrifugation (5,000 rpm, 5 min). Pelleted cells were dispersed in fresh medium (10 µL) along with an equal amount of trypan blue (10 µL). Cells were counted using a Neubauer hemocytometer where cell viability was assessed by counting both live (clear cytoplasm) and dead (blue colored cytoplasm) cells. Cell viability was calculated based on triplicates of experiments.

Chapter 4 – Results and discussion on the synthesis and functionalization of AuNPs

The synthesis of highly monodisperse particles and their surface chemistry is of utmost importance for the architectural design of functional nanomaterials.

The following chapters will look into the synthesis and surface functionalization of AuNPs for their further use in biological applications (see **Chapter 5 and Chapter 6**). Biocompatible AuNPs have been synthesised that displayed excellent water solubility as well as stability against aggregation in high ionic strength media. To achieve this, modified synthetic protocols were developed not only for the synthesis of AuNPs but also for their further functionalization with stabilizing ligands such as charged molecules and synthetic oligonucleotides.

The following chapter will discuss the synthesis of AuNPs of different shapes and sizes such as spherical AuNPs (see **section 4.1.1**) and AuNRs (see **section 4.1.3**) as well as their precise surface modification for their use in further applications.

4.1 Gold nanoparticles

4.1.1 Spherical AuNPs

Spherical AuNPs of two distinct size populations were synthesised according to well-established literature procedures. Both protocols resulted in highly monodisperse and stable nanoparticles.

4.1.1.1 15 ± 1 nm spherical AuNPs

15 nm spherical AuNPs were synthesised according to a well-defined synthetic route first established by J. Turkevich and further optimised by F. Frens.[16-18] This involves the reduction of a Au (III) salt by citrate (full synthetic protocol can be found in **section 3.1.1.1)** which produced monodisperse spherical AuNPs. Figure 4.1 shows a representative TEM image along with the size distribution of 15 ± 1 spherical AuNPs, which show that nanoparticles are colloidally stable. Furthermore, the size distribution (determined by counting ~500 spherical AuNPs using the Image J software) is fairly narrow with an exact mean of 14.7 nm and a standard deviation of 1.2 nm.

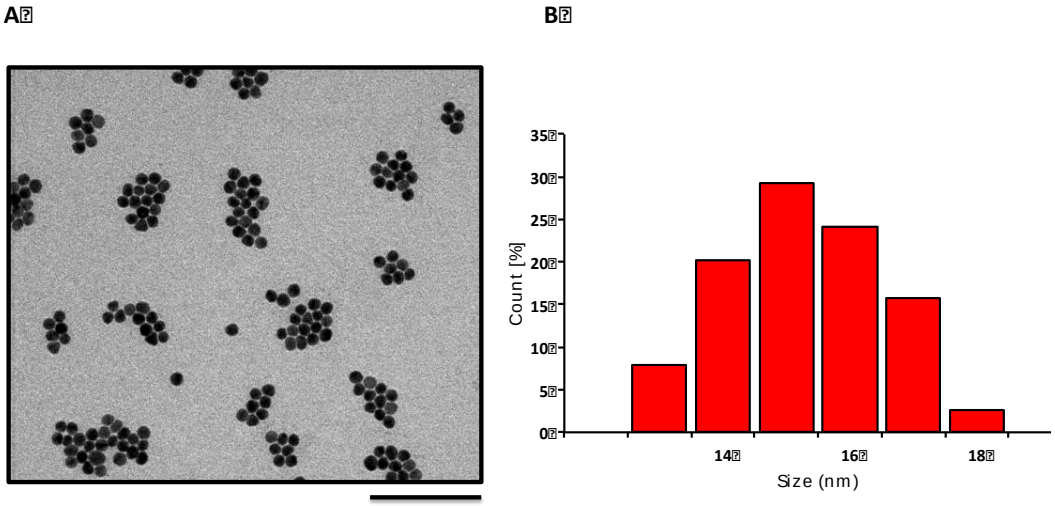

Figure 4.1 (A) TEM image of 15 ± 1 nm spherical AuNPs synthesised according to the citrate reduction method. (B) Histogram showing the size distribution of spherical AuNPs. Scale bar is 100 nm.

In this synthesis citrate not only acts as the reducing agent but it is also absorbed onto the surface of the nanoparticle acting as a stabilising ligand. Due to its three pKa values (3.13, 4.76 and 6.40) citrate is partially deprotonated around pH 7. Thus the particles have a net negative charge, which leads to their electrostatic repulsion according to the Derjaguin, Verway, Landau and Overbeek (DVLO) theory.[186] However, AuNPs are still susceptible to irreversible aggregation in conditions of higher salt concentration (>30 mM) or in the presence of divalent cations due to the weak electrostatic interactions between the AuNP surface and citrate.[187] Colloidal stability is therefore improved *via* a ligand exchange reaction where citrate molecules are replaced with BSPP (see Scheme 4.1).[188, 189]

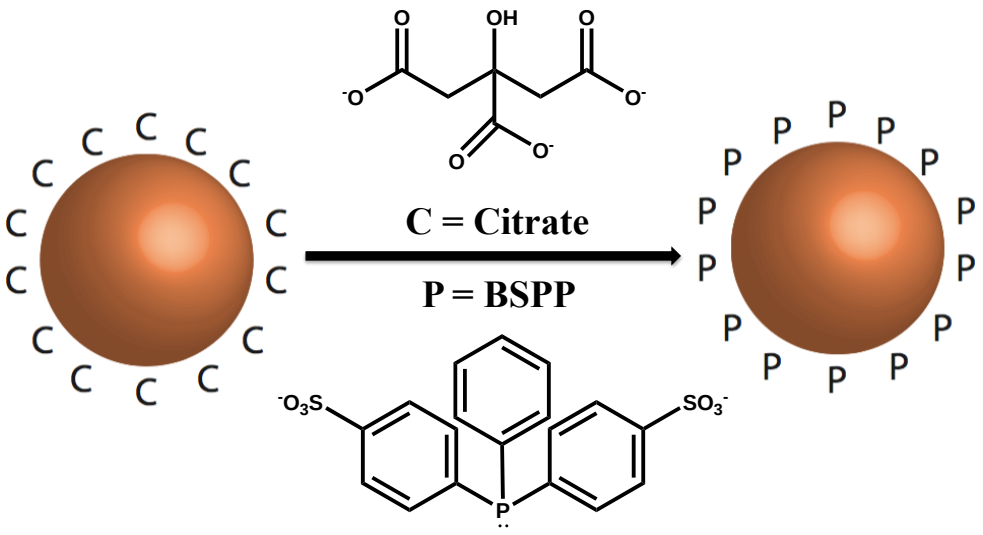

Scheme 4.1 Ligand exchange between citrate and BSPP

The phosphine group readily replaces citrate due to its higher affinity for the AuNP surface. An increase in stability arises from the larger size of the BSPP molecule as well as the negative charges from the sulfonate groups ($R\text{-}SO_3^-$), which prevents particle aggregation due to an increase in steric hindrance. Functionalization with BSPP also allows for the reversible

aggregation of particles in the presence of a high salt concentration and therefore their subsequent successful purification by centrifugation.

UV-Vis spectroscopy (see **section 3.4.2.1**) was used to determine the optical signature of the colloid solution, which stems from the LSPR (described in **section 2.2**). The extinction peak reached a maximum at around 520 nm for citrate coated spherical AuNPs with a slight red shift (~ 1.5 nm) for BSPP coated spherical AuNPs. The single and sharp peak shown in Figure 4.2 suggested a monodisperse colloid solution.

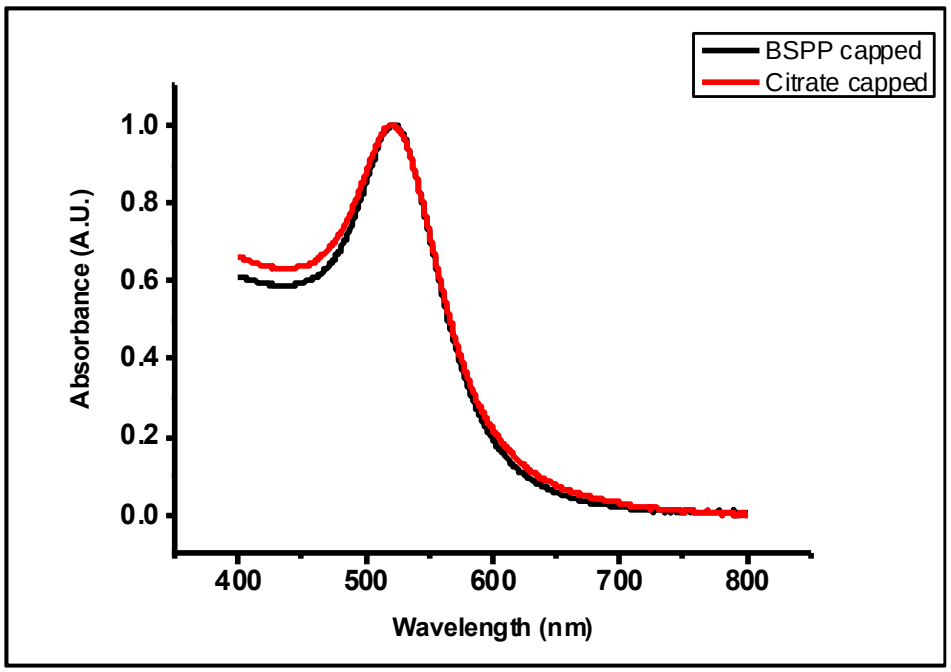

Figure 4.2 UV-Vis spectra of citrate and BSPP stabilised 15 ± 1 nm spherical AuNPs. After ligand exchange with BSPP a slight red shift of 1.5 nm is observed due to an increase in the refractive index.

A polydisperse colloid solution would display a broad peak whereas aggregation would be evident from a secondary peak in the range of 700

nm. The absence of both characteristics demonstrates that the sample is of suitable quality for use in further applications.

4.1.1.2 43 ± 4 nm spherical AuNPs

For the synthesis of larger spherical AuNPs the molar ratio between the gold precursor and the citrate reductant could be adjusted. However, this experimental route results in polydisperse larger AuNPs.[190] In order to accommodate both size and dispersity requirements, larger AuNPs were synthesised according to a protocol developed by the Puntes group (see **section 3.1.1.2** for synthetic protocol).[26] This synthesis involves the use of spherical AuNPs as seeds, which are gradually grown by further additions of both the gold precursor and citrate. After every three additions half the sample was extracted (termed generation *n*) for further analysis whereas the other half was further grown into larger size AuNPs. In this case AuNPs of generation 1 (G1) were synthesised (~ 40 nm in size), analysed and used in further applications (see **section 4.2.1.2.2**). Once again citrate ligands were replaced with BSPP to increase AuNP stability and allow for concentration *via* centrifugation. A representative TEM image and size distribution analysis is presented in Figure 4.3.

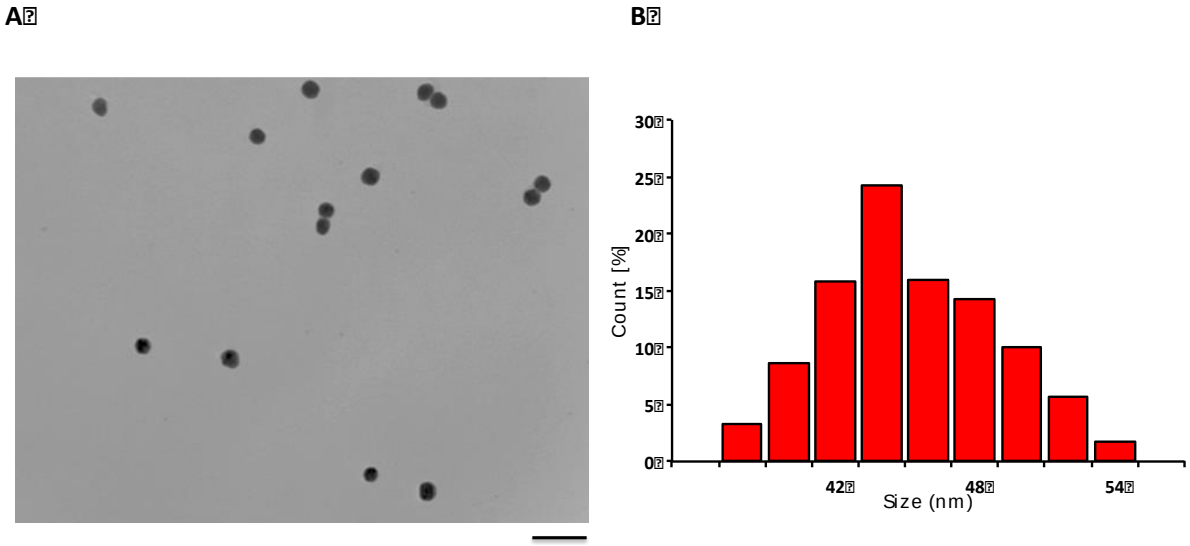

Figure 4.3 (A) TEM image of 43 ± 4 nm spherical AuNPs synthesised according to the Puntes method. (B) Histogram showing the size distribution of spherical AuNPs. Scale bar is 100 nm.

Particles were found to have a narrow size distribution. The mean size was determined to be 43.5 nm with a standard deviation of 4.3 nm (counting ~ 500 NPs using Image J software). The increase in NP size was also assessed by UV-Vis spectroscopy as seen in Figure 4.4.

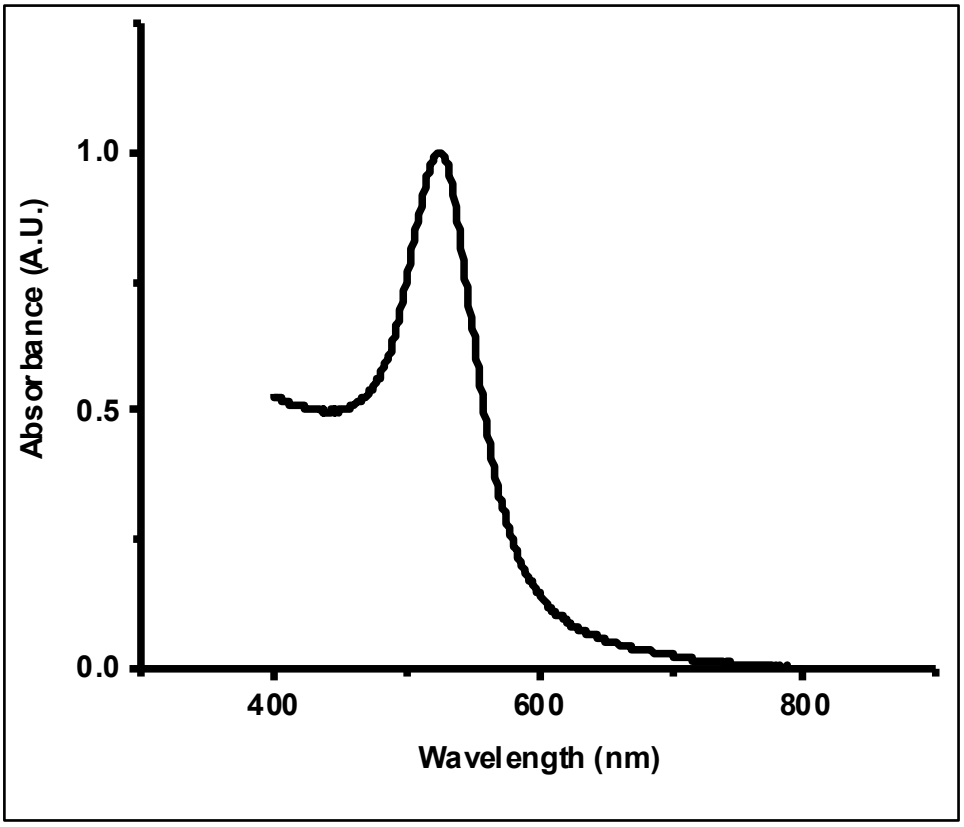

Figure 4.4 UV-Vis spectra of BSPP coated 43 ± 4 nm spherical AuNPs.

Increasing AuNP size is known to cause a red shift in the LSPR band of AuNPs. In this case the plasmon resonance shifted from 521.5 nm for 15 ± 1 nm BSPP coated spherical AuNPs to 528 nm for 43 ± 4 nm BSPP coated AuNPs. This shift, which is in good agreement with previously published results, is attributed to the effect of electromagnetic retardation in larger nanoparticls as well as to contributions from multipolar terms where higher order oscillations start to take important roles.[191-194] However, an increase in AuNP size also causes an increase in the absorption intensity. This can be explained by an increase in the sphere volume as well as an increase in the relative contribution of scattering to the total extinction (C_{sca}/C_{abs}) whereas for smaller size spheres (< 20 nm) the total extinction is nearly all contributed by absorption. These trends therefore

suggest that larger NPs (> 40 nm) could be suited for imaging applications (see **Chapter 6**).[191]

4.1.2 Branched AuNPs

For the synthesis of anisotropic branched AuNPs a modified seeded growth method was followed.[195] This protocol follows a two-step growth procedure, which involved the growth of seeds using a reducing agent followed by the initiation of nanocrystal growth using a surfactant guided process in the presence of a weak reducing agent.

In this instance, CTAB is used as the capping reagent, which in the presence of Ag^{+} ions kinetically controls the growth rate of various facets of the Au seeds to create branched nanoparticulate structures.[196] Further research into the detailed growth mechanism has suggested that this is due to the under potential of silver as discussed in **section 2.1.3**.[197]

Branched AuNPs were analysed by TEM as well as UV-Vis spectroscopy and were found to be between 75 and 125 nm in size, depending on the degree of branching, with a strong SPR peak (see Figure 4.5).

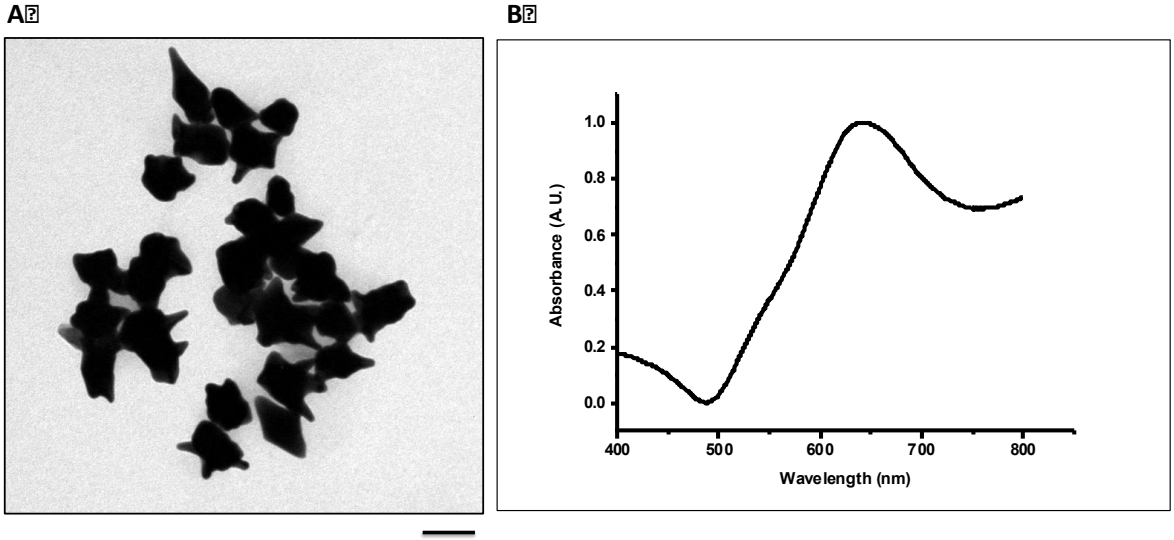

Figure 4.5 (A) Representative TEM image of anisotropic branched AuNPs (B) UV-Vis spectrum showing a strong SPR maximum peak at 640 nm. Scale bar is 100 nm

When comparing the absorption band of branched AuNPs to spherical AuNPs peaks for branched NPs were found to be more red shifted and broader. The shift has been suggested to be associated with the branches around the AuNPs whereas the broadening of the peak is thought to be a result of the Rayleigh scattering as well as the variable sizes of the branches.[52]

4.1.3 Gold nanorods

AuNRs coated with CTAB were synthesised in solution following a seed-mediated modified published procedure (see **section 3.1.2** for experimental procedure).[35, 39, 198] During this method, which included the addition of Ag^{+} ions, $AuCl^{4-}$ bound to CTAB micelles, forms $AuCl^{2-}$ by the reduction of Au^{3+} to Au^{+} through the addition of ascorbic acid. Subsequent collisions of the CTAB micelle – $AuCl^{2-}$complexes with CTAB-

protected seed particles (diameter of 2-4 nm) lead to the formation of growing gold particles. Ag^+ ions which undergo preferential under-potential deposition on the sides of the AuNRs followed by strong CTAB binding inhibits gold growth on the side of rods and leads to preferential growth at the ends.[36, 38] By varying the silver content, rods with varying aspect ratios can be produced, as will be demonstrated in this section.[199] An increase in silver nitrate concentration resulted in the formation of nanorods with a length-to-width aspect ratio extended from 2.3 to 3.2 (see Figure 4.6).

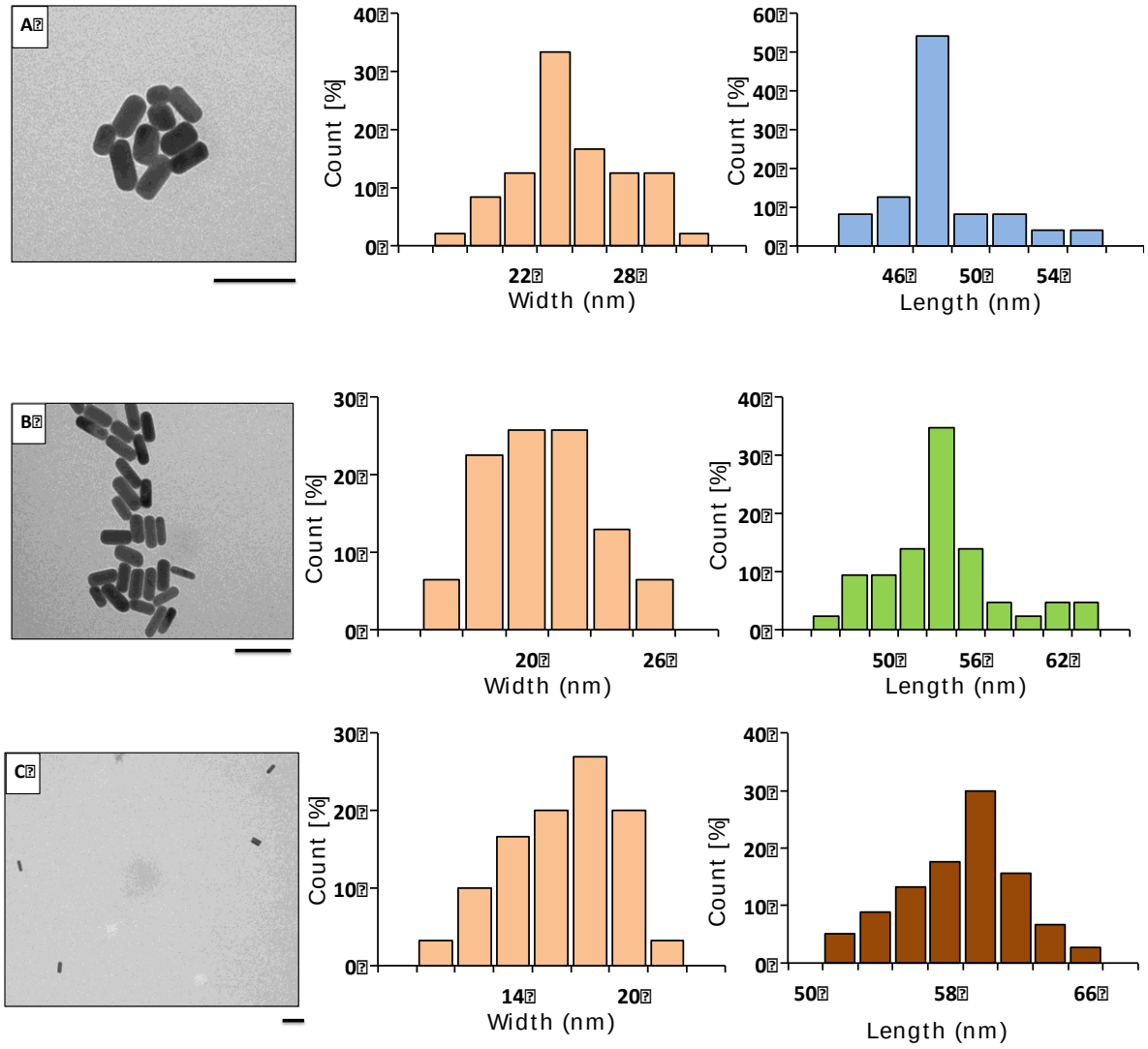

Figure 4.6 TEM images and representative size distribution histograms of gold nanorods prepared with 0.15 mL (A), 0.21 mL (B) and 0.4 mL of silver nitrate. Aspect ratios increase from approximately 2.3 (A), to 2.8 (B) to 3.2 (C). Scale bars are 100 nm.

The reaction yielded a good percentage of rod-like structures with only a few spheres and cubes left in solution (Figure 4.6 **(A)**). It was also noticeable that as the concentration of silver nitrate increased, nanorods

became longer in length overall increasing the aspect ratio of the structure.

The change in aspect ratio can also be directly determined by UV-Vis spectroscopy. AuNR absorption spectra exhibit two plasmon bands, which correspond to LSPR along their length (longitudinal resonance) and diameter (transverse resonance).[13, 191, 200, 201] As the aspect ratio increases, the longitudinal peak red shifts, giving rise to colloidal AuNR solutions of different colours as seen in Figure 4.7 **A**.

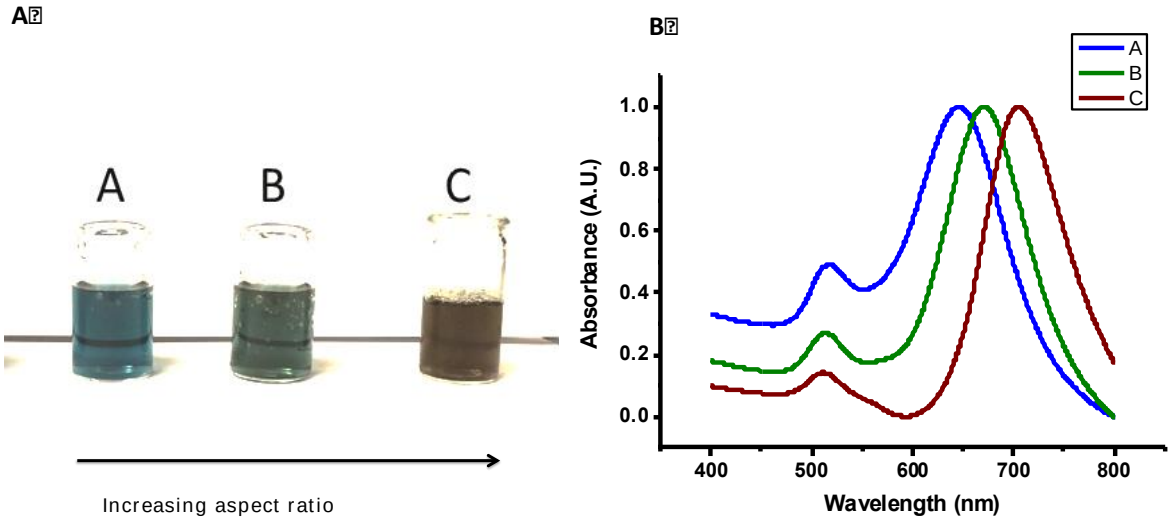

Figure 4.7 Digital image (A) and UV-Vis spectrum (B) of gold nanorods prepared with 0.15 mL (blue), 0.21 mL (green) and 0.4 mL (brown) of silver nitrate.

However, as previously mentioned one downfall of the seed mediated method is the polydispersity of the obtained AuNRs, as can be seen in Figure 4.8.

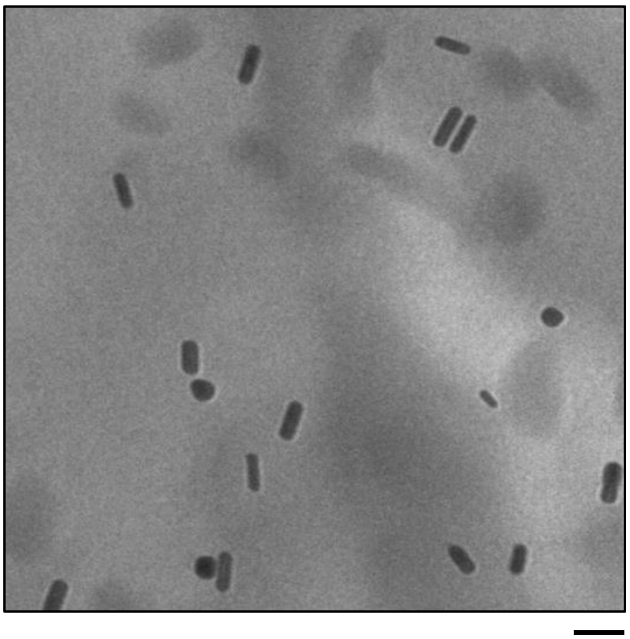

Figure 4.8 Example of a TEM image illustrating the potential for polydispersity of the seed-mediated synthetic approach. Scale bar is 100 nm.

Although the synthesis produces a high yield of rod shaped NPs (nanoparticles), spherical and cubed shaped structures are also produced. When used in further applications it is crucial to have a sample that is monodisperse in size but also shape. To achieve this, samples were purified using a sucrose gradient and centrifuged using an ultracentrifuge. This allowed for the separation of particles according to their density as can be seen from Figure 4.9.

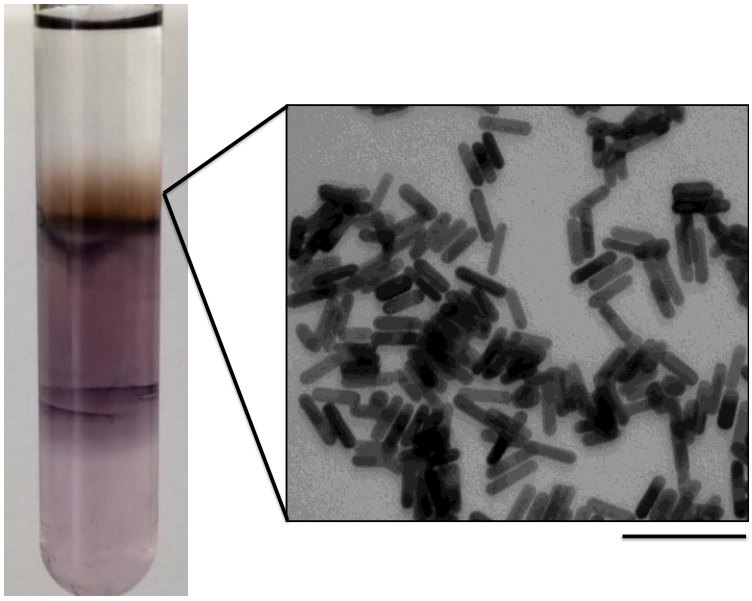

Figure 4.9 Image of sample after ultracentrifugation with the corresponding TEM image of the top layer. Scale bar is 100 nm.

As can be seen from Figure 4.9 by removing the top layer (brown), a sample of AuNRs with an increase in uniformity was obtained indicating that density gradient centrifugation was successfully applied to achieve efficient separation. Monodisperse samples were then used for further surface functionalization (see **section 4.2.2**) and applications (see **section 6.3.1.2**)

4.2 Surface modification of AuNPs

AuNPs including spherical and rod-shaped structures were further modified with surface ligands to endow the nanoparticles with unique properties for their successful use in bio imaging.

4.2.1 Modification of spherical AuNPs with oligonucleotides

Attaching oligonucleotides on AuNPs has been extremely important in nanotechnology and especially bionanotechnology as DNA-coated AuNPs combine the programmability and molecular recognition properties of the DNA with the optical and thermal properties of the gold core making them ideal candidates for their use in a wide range of applications.[202] Oligonucleotides are conjugated to AuNP surfaces by using a thiol linker chemically modified to either the 5' or 3' end. Thiols have a very strong affinity for gold where a S-Au bond is thought to be chemically and energetically equivalent to a Au-Au bond.[8, 98, 203] By taking advantage of this property spherical AuNPs modified with a discrete number or a shell of oligonucleotides were prepared.[9, 10, 204, 205]

4.2.1.1 Modification of spherical AuNPs with a discrete number of oligonucleotides

For many applications it is desirable to obtain AuNPs functionalised with a discrete number of oligonucleotides (mono-1, di-2, tri-3 conjugates). For example mixing a batch of AuNPs functionalised with single stranded DNA (ssDNA), which is complementary to another ssDNA-AuNP batch will result in the formation of AuNP dimers.[107]

Alivisatos and co-workers were the first to show that a limited number of DNA strands could be attached to a AuNP.[9, 206] The remaining surface was passivated with a monolayer of anionic phosphine molecules, which renders the particles stable to up to 50 mM salt, which is necessary for oligonucleotide conjugation. However, isolating AuNPs with different oligonucleotide surface loadings within the same sample has proven difficult.

Agarose gel electrophoresis has been successfully used as a purification technique of spherical AuNPs modified with a discrete number of oliconucleotides. Molecules are separated according to their size and charge and give rise to discrete bands.[107, 108, 207, 208] Apart from depending on the size to length ratio of AuNPs to oligonucleotides as discussed in **section 2.4** band separation is also dependant on the quality of the AuNP sample, which has to be homogenous in size to avoid band smearing.

In this study 15 ± 1 nm spherical AuNPs were functionalised with 86 mer thiolated oligonucleotides bearing either an alkyne or an azide modification (see Table 3.1 for oligonucleotide sequences). As can be seen in Figure 4.10 monoconjugates structures were successfully purified and were further used in biological applications (see **Chapter 5**).

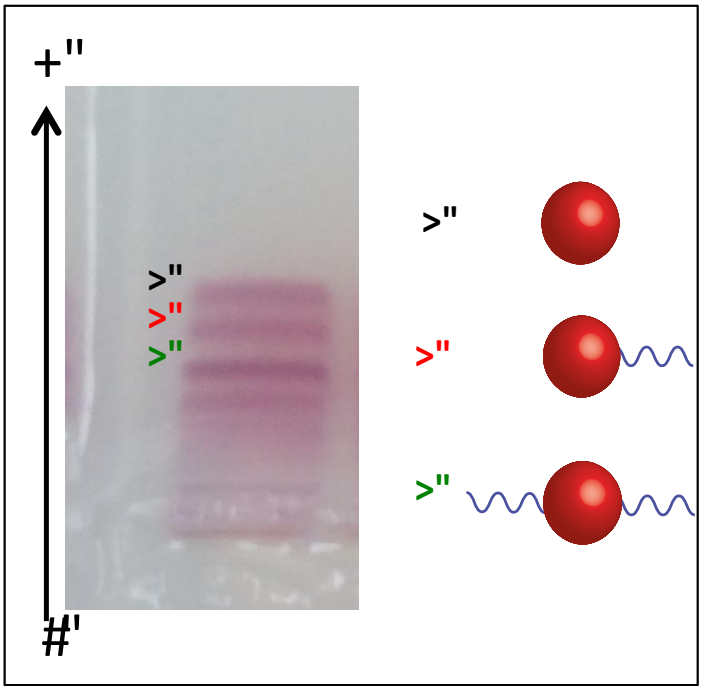

Figure 4.10 Agarose gel electrophoresis employed for the separation of mono- and diconjugate DNA-AuNPs.

4.2.1.2 Modification of spherical AuNPs with a shell of oligonucleotides

Mirkin and co-workers showed that a spherical AuNP surface could be coated with a dense oligonucleotide shell consisting of multiple oligonucleotide strands, creating a three-dimensional (3D) oligonucleotide structure.[2, 10, 11, 204, 209] These structures are quite sophisticated in nature and exhibit cooperative properties that result from their polyvalent surfaces. These include higher binding constants for their complements than free strands of the same sequence, resistance to nuclease degradation and the capability of transfecting multiple cell lines without the need for ancillary physical or chemical transfection.[11] Although these structures consist of a gold inorganic core, important properties emerge from the density and configuration of the oligonucleotides on the AuNP

surface.[11] These properties make the structures ideal candidates for their use in intracellular biomedical applications such as live cell mRNA detection and drug delivery (see **Chapter 5**).[1, 2]

For this study 15 ± 1 nm and 43 ± 4 nm (see **section 4.1.1.1 and 4.1.1.2)** spherical AuNPs were coated with a shell of oligonucleotides using two different methods.

4.2.1.2.1 Surface coating of 15 ± 1 nm spherical AuNPs

15 ± 1 nm spherical AuNPs were coated with a shell of oligonucleotides using a salt-ageing approach (see **section 3.2.1.1.2** for experimental details).[93, 204] This method can be applied for any oligonucleotide sequence and allows for high-density packing of thiol-terminated oligonucleotides on the AuNP surface.[99] Over a period of 8 h the salt concentration is gradually increased to 0.3 M, which screens the repulsive interactions between neighbouring strands, thereby promoting efficient packing of oligonucleotides on the AuNP surface.[204] The resulting structure is stable due to the overall negative charge that prevents aggregation.[210] DNA-coated AuNPs show an increased stability in solutions over a wide range of pH and ionic strength conditions.[11]

UV-visible spectroscopy and gel electrophoresis were employed to qualitatively assess the success of DNA conjugation to the AuNP surface to form a 3D shell as can be seen in Figure 4.11.

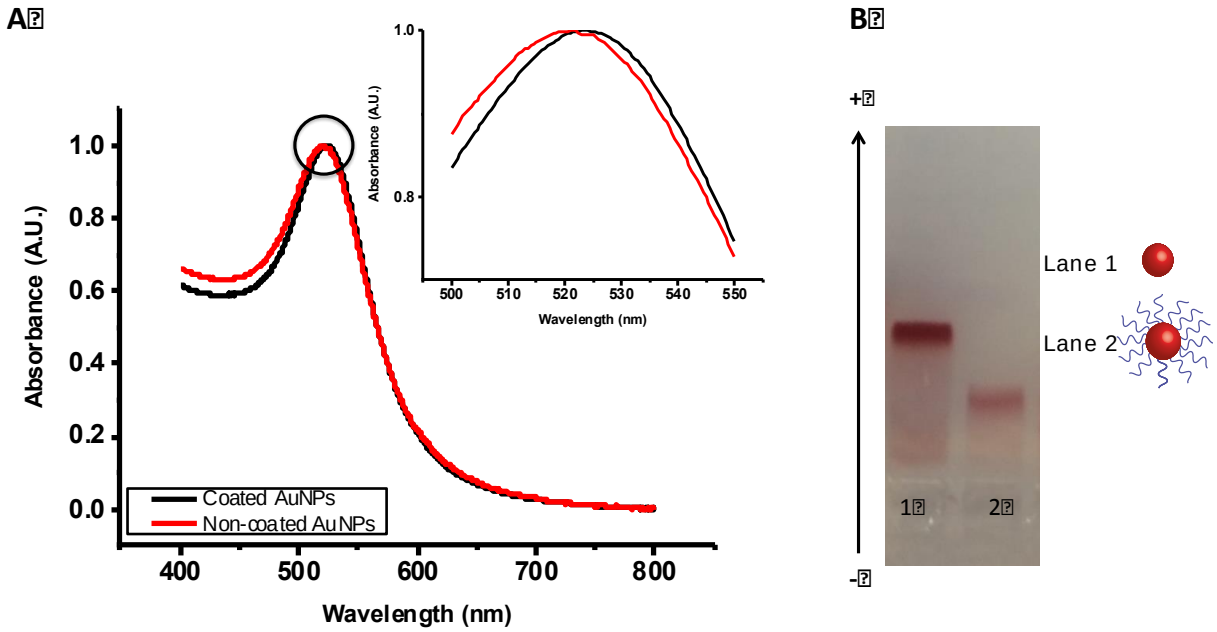

Figure 4.11 (A) UV-vis spectra comparing the SPR peak maximum of both DNA-coated and non-coated (BSPP stabilised) 15 ± 1 nm spherical AuNPs and (B) agarose gel electrophoresis comparing 15 ± 1 nm BSPP coated AuNPs (lane 1) and 15 ± 1 nm AuNPs coated with a shell of oligonucleotides (lane 2).

UV-Vis spectroscopy (see Figure 4.11 **(A)**) of oligonucleotide coated 15 ± 1 nm spherical AuNPs revealed a sharp peak with a SPR maximum at 525 nm. Compared to BSPP coated AuNPs, there is no broadening of the peak suggesting a monodisperse sample with a narrow size distribution range. However, a small red shift was observed (~4 nm) which is thought to be associated with an increase in the refractive index of the sample due to the oligonucleotide attached to the AuNP surface.[211]

Agarose gel electrophoresis was also employed as an alternative method to qualitatively assess oligonucleotide conjugation.[106, 176] Figure 4.11 **(B)** shows a representative agarose gel where a sample of 15 ± 1 nm

spherical AuNPs coated with a shell of oligonucleotides was run against a spherical AuNP sample stabilised only by BSPP ligands. A decrease in the electrophoretic mobility (Figure 4.11 **(B)** (lane 2)) confirms successful oligonucleotide attachment. An increase in size due to the oligonucleotide shell causes a significant delay in the band when compared to unmodified AuNPs.

For many biomedical applications it is necessary to also quantitatively determine the exact number of oligonucleotide strands attached per AuNP. A number of different methods have been used to assess the degree of oligonucleotide loading, which involve the use of fluorophore modified synthetic oligonucleotides. It has been shown that DNA can be chemically displaced from the AuNP surface using dithiothreitol (DTT).[8, 93, 209] The concentration of released oligonucleotides was determined by monitoring the fluorescence signal in solution. When attached to the AuNP surface the fluorescence of the dye is quenched by the AuNP core. However, when no longer in close proximity the fluorescence signal is recovered and can be monitored via fluorescence spectroscopy.[138, 139, 212] Other methods include the dissolution of the gold core by oxidatively dissolving the AuNP. Dissolution can be achieved either by using KCN or a solution of KI/I_2.[180, 213] In both cases the fluorescence signal of the fluorophore-modified oligonucleotides could once again be measured in solution. For non-fluorophore labelled DNA, a DNA staining dye such as Oligreen or SYBR Green I can be used.[145] Alternatively the oligonucleotide concentration in solution can be assessed by measuring the DNA absorbance at 260 nm using UV-Vis spectroscopy.[214]

In this study, we dissolved the AuNP core using a solution of KI/I_2 (see **section 3.4.2.1.2** for experimental protocol) and after purification we determined the number of oligonucleotides attached per AuNP by

monitoring the absorbance of oligonucleotides liberated from the AuNP core. The RedOx reaction that leads to the etching of the gold core is outlined below.

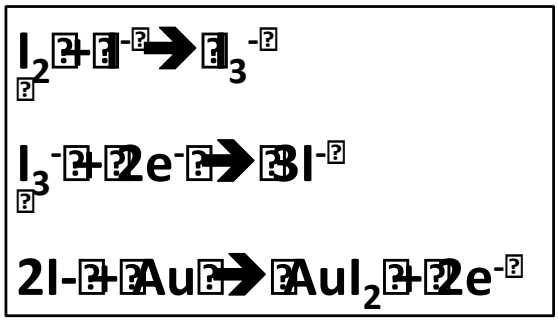

Scheme 4.2 RedOx reaction resulting in dissolution of the gold core

Using this method it was found that the oligonucleotide loading on a 15 ± 1 nm AuNP surface was approximately 128 oligonucleotide strands per AuNP.

4.2.1.2.2 Surface coating of 43 ± 4 nm spherical AuNPs

For the functionalization of larger spherical AuNPs (> 40 nm) salt-ageing protocols have been reported, which however involve a decrease in the salt concentration.[204, 209] Nevertheless, it has been found that the oligonucleotide density decreases as the AuNP size increases. This is thought to be due to the surface curvature of spherical AuNPs, which significantly affects the loading of oligonucleotides. Oligonucleotide strands are found closer together thus intensifying interstrand repulsion as discussed in **section 2.4**.[99, 209] The salt-ageing procedure has therefore been stated to not work as efficiently for larger spherical AuNPs.[103, 204]

In order to overcome the limitations associated with the salt-ageing process, a low pH assisted method can be employed for the functionalization of larger spherical AuNPs (see **section 3.2.1.3** for experimental procedure). This involves the use of a pH 3 citrate buffer which can lead to efficient DNA adsorption even at low salt concentrations. The role of the citrate buffer is to overcome the kinetic barrier of DNA attachment, which is more pronounced for larger AuNPs. This occurs *via* the protonation of bases namely adenine and cytosine, which are protonated at pH 3. These protonated bases reduce the repulsion between the oligonucleotides and AuNPs but most importantly between oligonucleotide strands on a AuNPs surface.[103, 204]

In this study we employed the pH method for the surface functionalization of 43 nm spherical AuNPs (see **section 3.2.1.3** for experimental procedure) and UV-Vis spectroscopy was employed to qualitatively assess the oligonucleotide attachment to the NP surface.

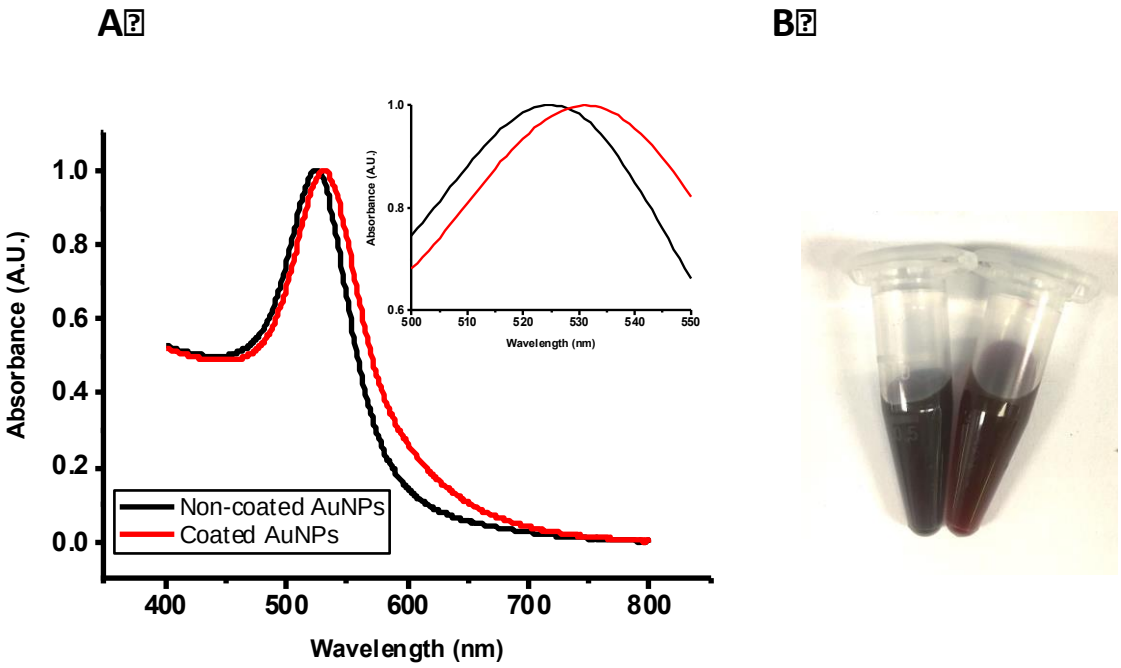

Figure 4.12 (A) UV-Vis spectra of coated and non-coated 43 ± 4 nm spherical AuNPs. (B) Digital image of non-coated (left epperdorf) and coated (right eppendorf) AuNPs in PBS.

By examining the UV-Vis spectra of both coated and citrate stabilised AuNPs, a red shift of 4 nm in the SPR peak was observed (see Figure 4.12). The absence of a second peak at a longer wavelength also indicates that no aggregation took place during the attachment procedure.[215] Successful oligonucleotide coating was also assessed by dispersing particles in PBS and comparing it against citrate stabilised spherical AuNPs (see Figure 4.12). Whereas the citrate stabilised nanoparticle solution immediately changed colour to dark blue indicating AuNP aggregation due to weak citrate stabilization, the oligonucleotide modified spherical AuNPs retained their dark red colour.

Samples were also analysed by gel electrophoresis where a difference in sample mobility was expected to be observed.[106, 176]

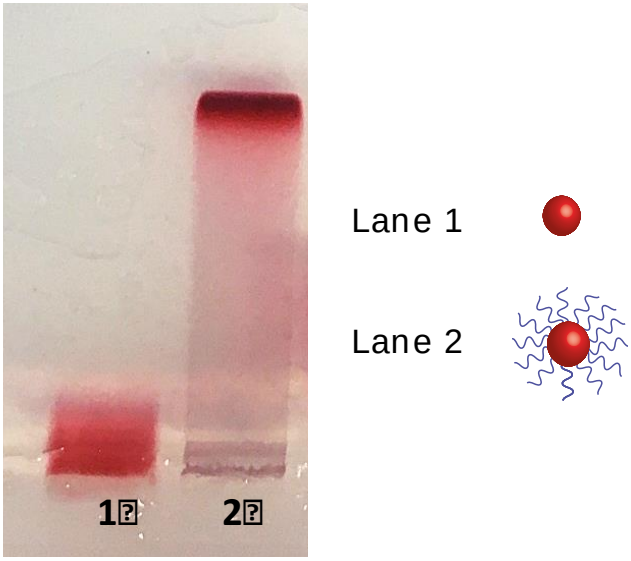

Figure 4.13 Agarose gel electrophoresis comparing citrate (Lane 1) and oligonucleotide (Lane 2) stabilised 43 ± 4 nm spherical AuNPs.

When comparing both citrate and oligonucleotide stabilized spherical AuNPs a significant difference in band mobility was observed as shown in Figure 4.13. Citrate stabilized spherical AuNPs (lane 1) did not run through the gel and appeared to be stuck within the sample well. This was attributed to the applied voltage, which caused a temperature increase, which in turn is thought to have led to the dissociation of the weakly attached citrate ligands. On the other hand, oligonucleotide stabilized AuNPs were successfully run with a clear band being observed (lane 2).

Oligonucleotide loading was also quantitatively analysed by etching of the gold core using a KI/I_2 solution (see Scheme 4.2 and **section 3.4.2.1.2** for experimental procedure).[180] A surface coverage of 421 ± 9 oligonucleotide strands per spherical AuNP surface was calculated from

three independent measurements, which correlates well with previous published reports on the functionalization of similar size AuNPs.[99]

4.2.2 Modification of AuNRs with silica

As mentioned in **section 4.1.3** AuNRs have distinctive shape-dependant optical properties that make them suitable for their use in further applications such as imaging.[201] AuNRs are synthesised *via* a surfactant-mediated approach where the final shape and size strongly rely on the use of cationic surfactant CTAB as the shape-inducing agent.[35, 36, 38, 39] A large excess of CTAB is required, above its critical micelle concentration (0.9 mM), to ensure adequate micelle rod shape formation in solution.[171] However, this limits their potential success in their use in a number of applications as removal of excess CTAB may lead to uncontrollable AuNR aggregation.[172] Therefore, efforts have been made to increase AuNR stabilization. Takahashi *et al.* showed that CTAB could be successfully displaced by phosphatidycholine (PC) in the chloroform phase whereas Sonnichsen and co-workers showed that AuNR suspensions could be stabilised with mono- and bifunctional polyethylene glycol (PEG).[216, 217] Another method to stabilise AuNRs is their encapsulation in SiO_2 shells. This enhances their colloidal stability by preserving their rod shape and longitudinal surface plasmon resonance.[171, 172, 218, 219]

AuNPs have a very low affinity for silica, because unlike other metals it does not form a passivating oxide film in solution. Therefore it can not be directly attached onto the gold surface.[220] Various methods such as modifying the surface with polymer templates have been suggested. Recently the Stober method, widely used for the synthesis of spherical SiO_2 particles has been adapted for the functionalization of AuNPs using CTAB as a template.[221-223] Gorelikov and Matsuura first reported a single

step procedure for coating AuNRs using CTAB as a template and tetraethoxysilane (TEOS) yielding porous silica shells under basic conditions.[218, 224] Tracy *et al.* further investigated the effect of TEOS and showed that the shell thickness can be tuned by varying the volume of TEOS added to the solution.[171]

In this study CTAB coated AuNRs were functionalized with a SiO_2 shell using TEOS and NaOH. Final samples were analysed by TEM and UV-Vis spectroscopy to determine successful coating (see Figure 4.14).

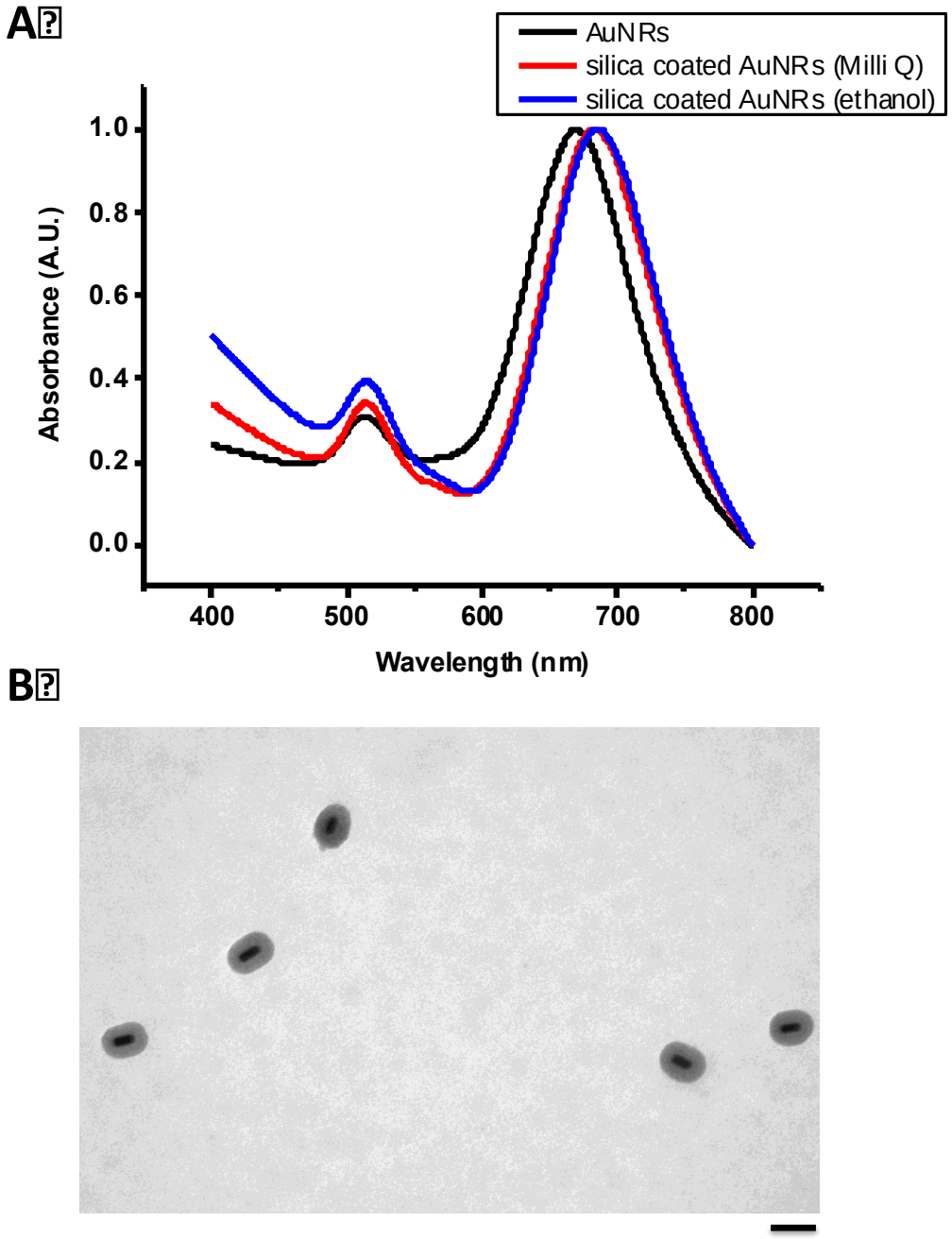

Figure 4.14 (A) UV-Vis spectra of non-coated and silica coated AuNRs as well as (B) a representative TEM image showing successful AuNR silanization. Scale bar is 100 nm.

Figure 4.14 **(A)** shows the absorbance spectra of CTAB stabilized and silica coated AuNRs in Milli Q water and in ethanol. Spectra were acquired after purification and a LSPR redshift was observed after successful silanization for the longitudinal peak. This effect, also observed by others, was attributed to the sensitivity of the SPR to the dielectric constant of the metal and surrounding dielectric. The observed redshift was therefore due to the increased refractive index of SiO_2, which scales with its density.[171, 220, 222, 225] On the other hand, no shift was observed for the transverse peak, which is in accordance to previous published reports.[171, 226] Moreover, the width of the LSPR band did not significantly change after SiO_2 deposition signifying that AuNRs are well dispersed in solution with no large aggregates present. Unlike CTAB coated AuNRs, which are stable only in water, SiO_2 coated AuNRs were also found to be stable in ethanol with no significant difference being observed when comparing the LSPR peaks.

Successful coating was also assessed *via* TEM. Figure 4.14 **(B)** shows that AuNRs are well separated and coated with a uniform SiO_2 shell (~ 100 nm in thickness from side to side). The absence of SiO_2 nanoparticles that do not encapsulate AuNRs is a strong indication of the absence of excess CTAB micelles. It has been stated that poor AuNR purification from free CTAB can lead to empty CTAB micelles in solution, which in turn can allow for undesired growth of hollow SiO_2 nanoparticles.[171]

Chapter 5 – Results and discussion on the design and synthesis of nanoparticle dimers for mRNA sensing and drug delivery

The design of nanoparticulate systems, which can perform multiple synergistic functions in cells with high specificity and selectivity, is of great importance in applications including disease diagnosis such as cancer and its targeted treatment. In this chapter we combine recent advances in DNA-AuNP self-assembly, nanoparticle functionalization and sensing to develop for the first time DNA-coated AuNP dimers that are able to perform multiplex synergistic functions within a cellular environment.

For this aim, 15 ± 1 nm DNA-coated spherical AuNPs (see **section 4.2.1.2.1** for discussion on functionalization) were assembled into permanent dimers by taking advantage of the well-established copper free click chemistry (see **section 3.3.3** for experimental procedure). We show that synthesised AuNP dimers are able to efficiently enter cells and can coordinate the delivery of two chemotherapeutic drugs only to cells expressing specific mRNA targets.

The efficiency of DNA-coated AuNP dimers for live cell mRNA detection is first addressed (see **section 5.4**) followed by their development into potential vehicles for targeted drug delivery of one or two intercalating drugs (see **section 5.5**).

5.1 Synthesis and characterization of AuNP dimers

AuNP dimers were formed *via* the covalent linking of single 15 ± 1 nm AuNPs using copper-free click chemistry. Two batches of oligonucleotide (modified with eiher an azide or an alkyne group)-AuNPs were prepared and purified through agarose gel electrophoresis in order to isolate AuNPs bound to only one oligonucleotide (monoconjugates) (see **section 3.2.1.1.1** for experimental procedure). Each batch of monoconjugates was chemically modified with either an azide group (Linker strand 1) or an alkyne group (Linker strand 2) (see Figure 3.3 for chemical structures) and was further functionalised with a shell of oligonucleotide sense strands (Sense strands 1 and 2, see **section 3.2.1.1.2** for experimental procedure), designed to capture a specific mRNA target (see Table 3.1 and Table 3.2 for oligonucleotide sequences) as shown in Scheme 5.1.

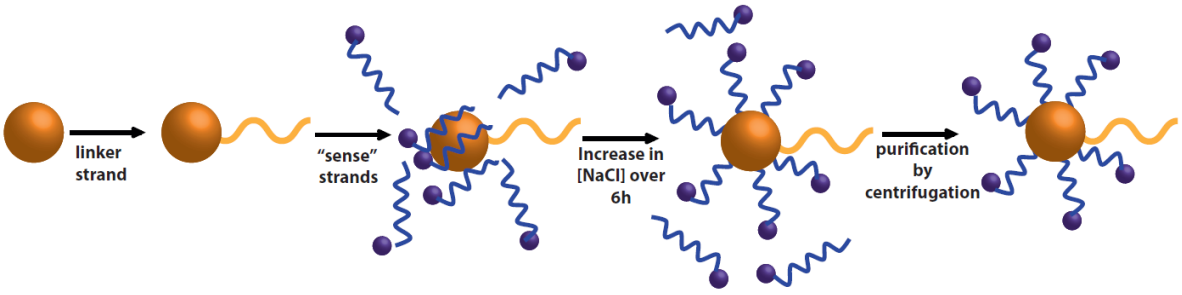

Scheme 5.1 Schematic illustration of oligonucleotide conjugation to a AuNP surface. A single linker strand is first attached followed by the salt-ageing procedure resulting in a shell of sense strand.

DNA-ligated nanoparticle dimers were then hybridised as seen in Scheme 5.2 because of the complementarity between linker strand 1 and linker strand 2 and purified by gel electrophoresis under DNA denaturing

conditions in order to disregard particles that did not form dimers or that were not chemically ligated (see **section 3.3.3**).

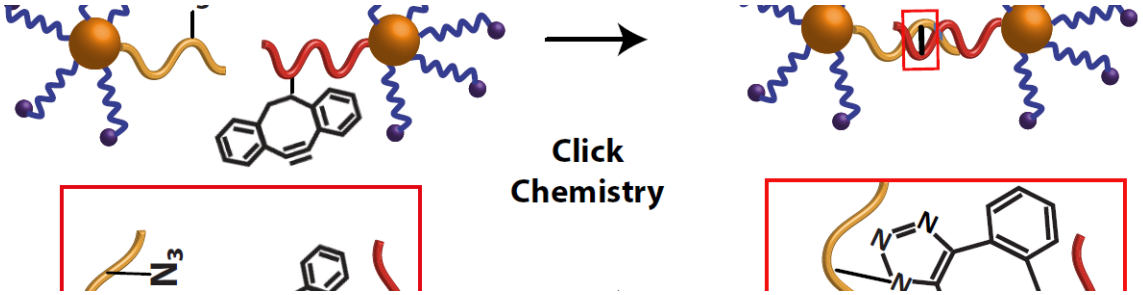

Scheme 5.2 Schematic illustration of the AuNP dimer formation. Spherical AuNPs are able to assemble into dimers due to partial complementarity between linker strands. Once hybridised, clicking groups are able to react and form a covalent bond.

For mRNA detection, short fluorophore-modified oligonucleotides (flare strands 1 and 2) were added to the sample and hybridized to their complementary sense strands (see Table 3.2 for oligonucleotide sequences) as seen in Scheme 5.3.

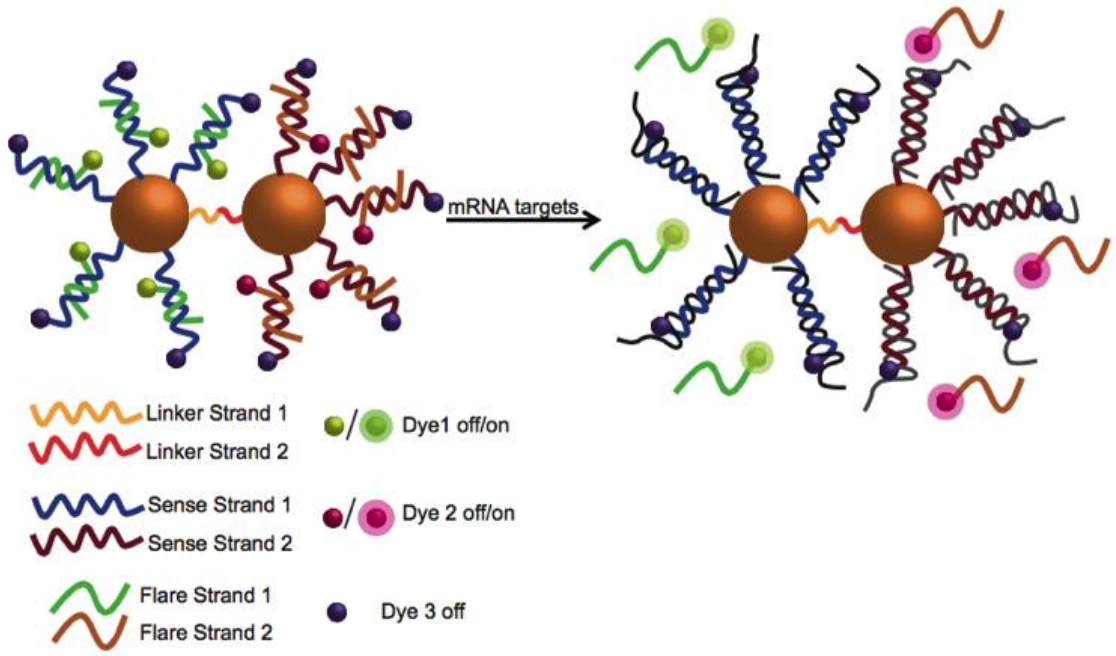

Scheme 5.3 Schematic illustration of multiplexed AuNP dimers and the process of mRNA detection.

Scheme 5.3 shows the design of the fully assembled DNA-coated AuNP dimers and illustrates the process of mRNA detection. The nanoparticle dimer design includes sense strands (attached to the AuNP surface), bearing a 5' fluorophore modification, which are partially hybridised to shorter oligonucleotide complements, termed flare strands, chemically modified at the 3' end with another dye. Once hybridised, the fluorescence of all fluorophores is quenched, due to the close proximity to the AuNP surface.[227, 228] However, once the target mRNA binds to the corresponding sense sequence *via* competitive hybridization, the concomitant displacement of the flare can be detected as an increase in fluorescence at the specific wavelength of the fluorophore. [1, 111, 128, 137, 229]. The fluorophore on the sense strand in this design acts as a

reporter that ensures the integrity and specificity of the system. A corresponding signal from the sense strand should not be detectable unless degradation due to the presence of nucleases has taken place. In this study oligonucleotide sequences on the surface of the AuNP dimers were designed to detect two specific mRNA targets, keratin 8 and vimentin.

5.1.1 Efficiency of linker strand ligation for the formation of AuNP dimers

Recently ligation methods to covalently bind DNA-coated AuNP assemblies, enhancing their stability under DNA denaturing conditions or biologically complex environments have been developed.[162, 164] In one of these methods, a copper-free click chemistry strategy was utilized to permanently ligate oligonucleotide-coated AuNPs. Synthetic oligonucleotides modified with an alkyne or azide group were brought into close proximity *via* a templating splint strand. Partial complementarity to both modified oligonucleotides resulted in successful oligonucleotide hybridization bringing in close proximity the alkyne and azide groups, catalyzing a ligation reaction. This approach to manipulating AuNP assemblies allowed the formation of AuNP dimers and trimers in high yield, which were stable even under DNA denaturing conditions.[162]

In this study, a similar approach was adopted where linker strands 1 and 2 (see Table 3.1 for oligonucleotide sequences) were modified with clicking groups (either an azide or an alkyne). DNA complementarity brought both clicking groups into close proximity resulting in successful clicking and the formation of a permanent covalent bond. A schematic illustration of the DNA ligation between two AuNPs is shown in Scheme 5.4.

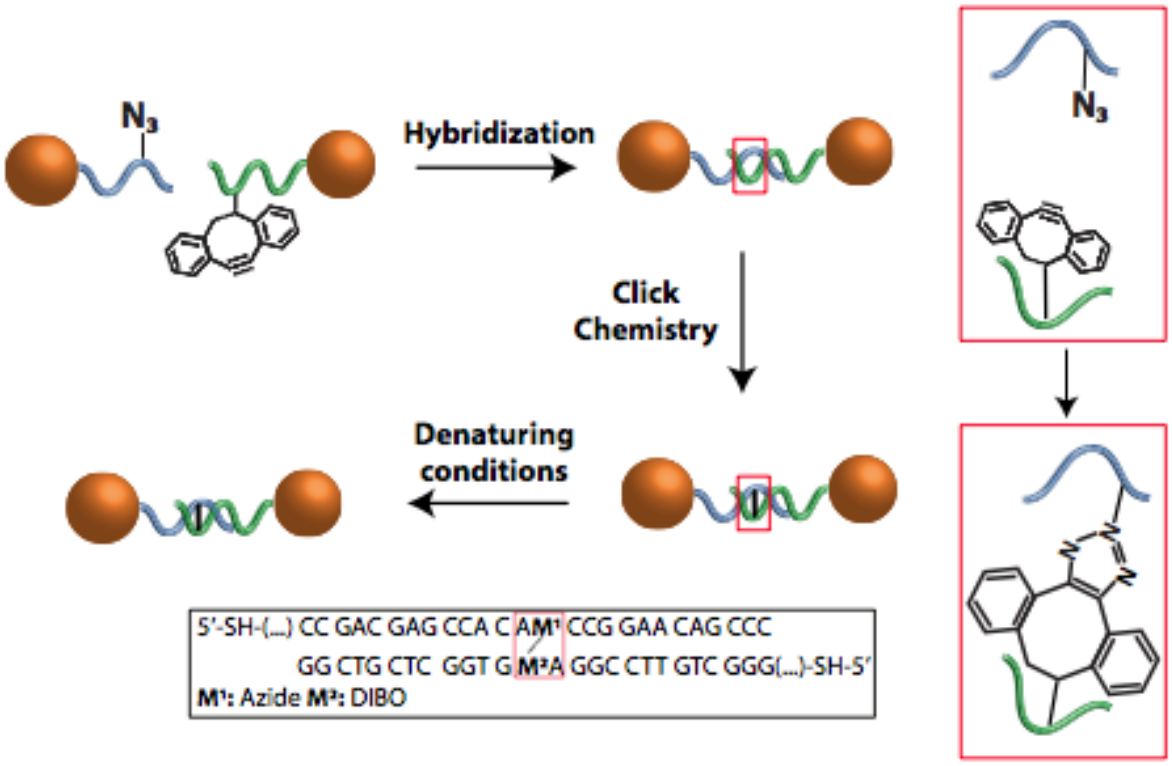

Scheme 5.4 AuNP dimer formation using copper free click chemistry.

5.1.1.1 Efficiency of hybridization between linker strands

The efficiency of hybridization between linker strands 1 and 2 (see Table 3.1 for detailed sequences) was first assessed by conducting a melting analysis where the absorbance was measured at 260 nm. Oligonucleotide strands were mixed in equimolar amounts in PBS (containing 300 mM NaCl) and three consecutive heating and cooling cycles were followed from 25 to 90 °C (see **section 3.4.2.1.1** for experimental details). The melting curve is plotted in Figure 5.1, which shows the typical hyperchromic effect as the temperature is increased and the hybridised double stranded DNA (dsDNA) is denatured.[77]

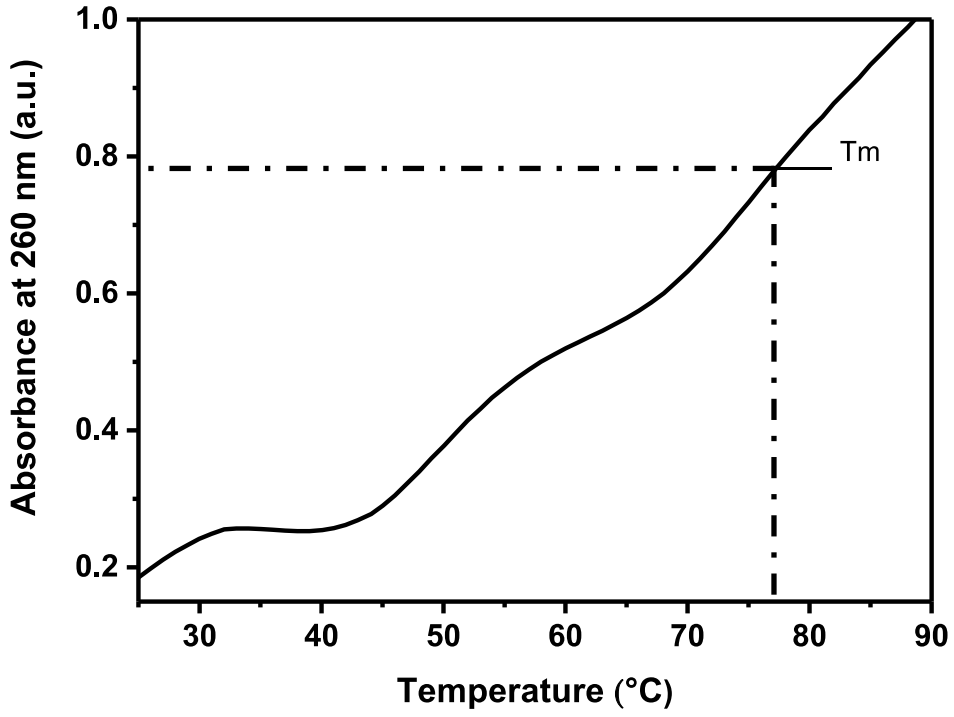

Figure 5.1 Melting curve of Linker 1 and 2. The curve was determined from an average of three cycles.

As can be seen in Figure 5.1 an increase in absorbance is observed as the temperature is gradually increased, which is an indication of successful hybridization. However, due to the long length of both linker strands there was a small self-complementarity in each strand (up to 6 bases) as well as partial complementarity (up to 5 bases) between the linker strands other than the full complementarity. The curve therefore, does not demonstrate the expected sigmoidal shape. As the temperature is increased these loosely bound duplexes dehybridize at much lower temperatures than the fully complementary 26 bases thus leading to a steady increase in absorption.

OligoCalc was used to calculate the theoretical melting temperature of the duplex using the nearest-neighbour approach.[78] For the fully complementary 26 base pairs at a salt concentration of 300 mM a theoretical melting temperature of 76.5 °C was calculated, which is in a good agreement with the experimental melting temperature calculated.

5.1.1.2 Efficiency of click chemistry after hybridization

Following hybridization the efficiency of clicking between azide and alkyne groups on complementary linker strands was investigated when free in solution as well as when bound to AuNPs by heating under DNA denaturing conditions (see **section 3.3.3**). Formamide lowers the melting temperature of DNA by destabilising the DNA duplex, therefore oligonucleotides that are not permanently ligated will dehybridise.[174] Successful clicking was determined by PAGE and/or agarose gel electrophoresis (Figure 5.2)

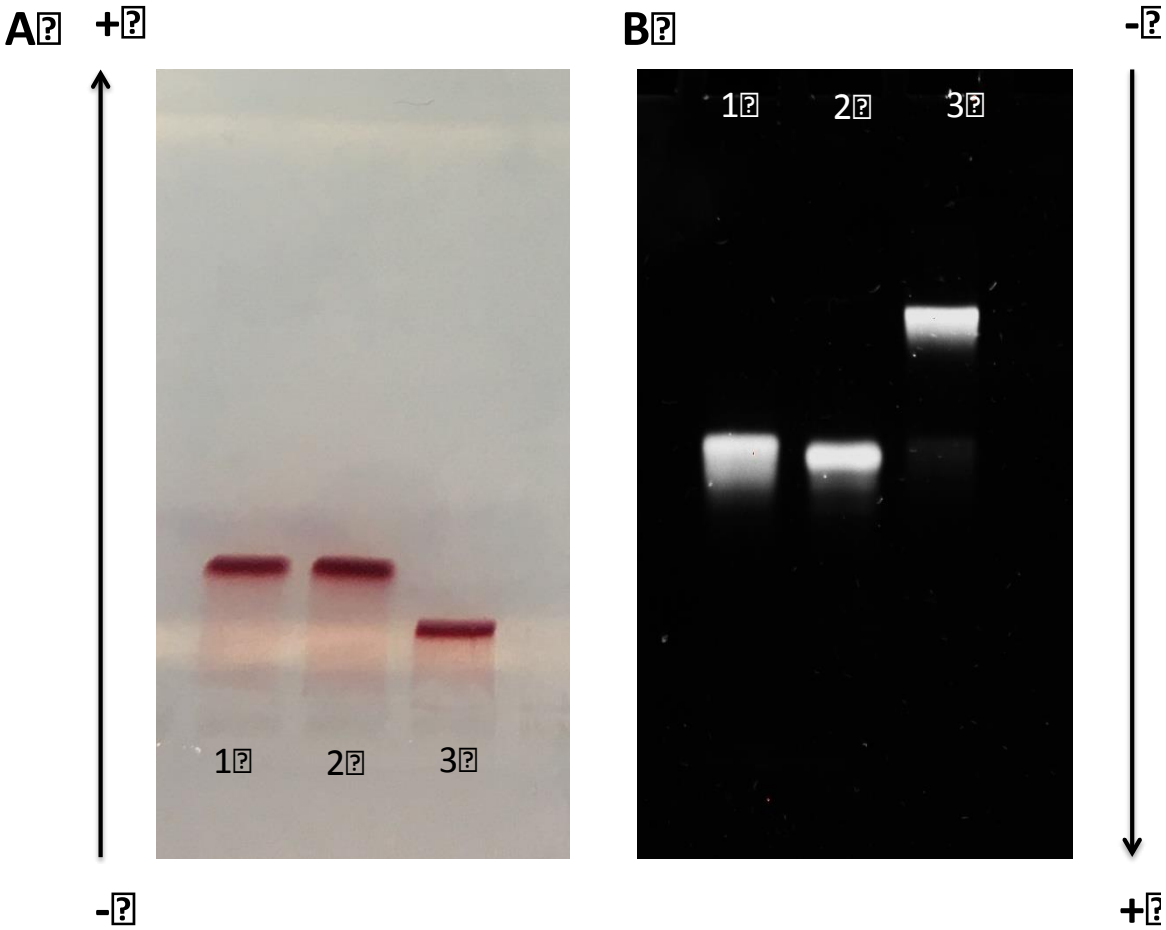

Figure 5.2 (A) agarose gel and (B) PAGE gel electrophoresis used to determine the efficiency of clicking and permanent ligation between linker strands 1 and 2. Agarose gel electrophoresis was used to assess the efficiency of clicking following hybridization when linker strands were conjugated to an AuNP surface whereas PAGE gel was employed to investigate the efficiency of clicking of free modified linker strands hybridized in solution

Figure 5.2 demonstrates the efficiency of clicking between linker strands 1 and 2 when modified onto an AuNP surface (Figure 5.2 **A**) and when free in solution (Figure 5.2 **B**). Lane 1 shows AuNP oligonucleotide

monoconjugates (A) and a single linker strand (B), Lane 2 represents non-ligated DNA-coated AuNP dimers (A) and non-ligated dsDNA (B) incubated with formamide whereas lane 3 shows ligated DNA-coated AuNP dimers (A) and ligated dsDNA (B) incubated with formamide. In both cases it is evident that in the absence of a clicking reaction between linker strands 1 and 2, there is dehybridization under denaturing conditions. On the other hand, when linker strands were ligated the dimer structure was not compromised even under denaturing thus confirming the efficiency of click chemistry.

5.1.2 Melting analysis of sense/flare duplex

Having successfully demonstrated that DNA-coated AuNPs can be permanently ligated into a dimer structure the hybridization between the sense/flare duplexes was assessed and thus their suitability for future live cell experiments (**section 5.4**).

Hybridization of the flare strand was determined *via* fluorescence melting rather than UV. Samples were gradually heated from 25 to 70 °C whilst monitoring fluorescence output from the flare strand (see **section 3.4.2.2.2** for experimental details). As previously mentioned, when hybridised to the sense strand, the dye on the flare strand is quenched by the Au core (see Scheme 5.3 for AuNP dimer structure).[227] Upon melting of the DNA duplex due to an increase in temperature, the flare diffuses away from the AuNP core leading to a concomitant increase in its fluorescence signature.[1] The flare corresponding to vimentin consisted of a Cy5 dye modification whereas the flare displaced due to the detection of keratin 8 mRNA was modified with a Cy3 dye (see **section 3.4.2.2.2** for excitation and emission wavelengths).

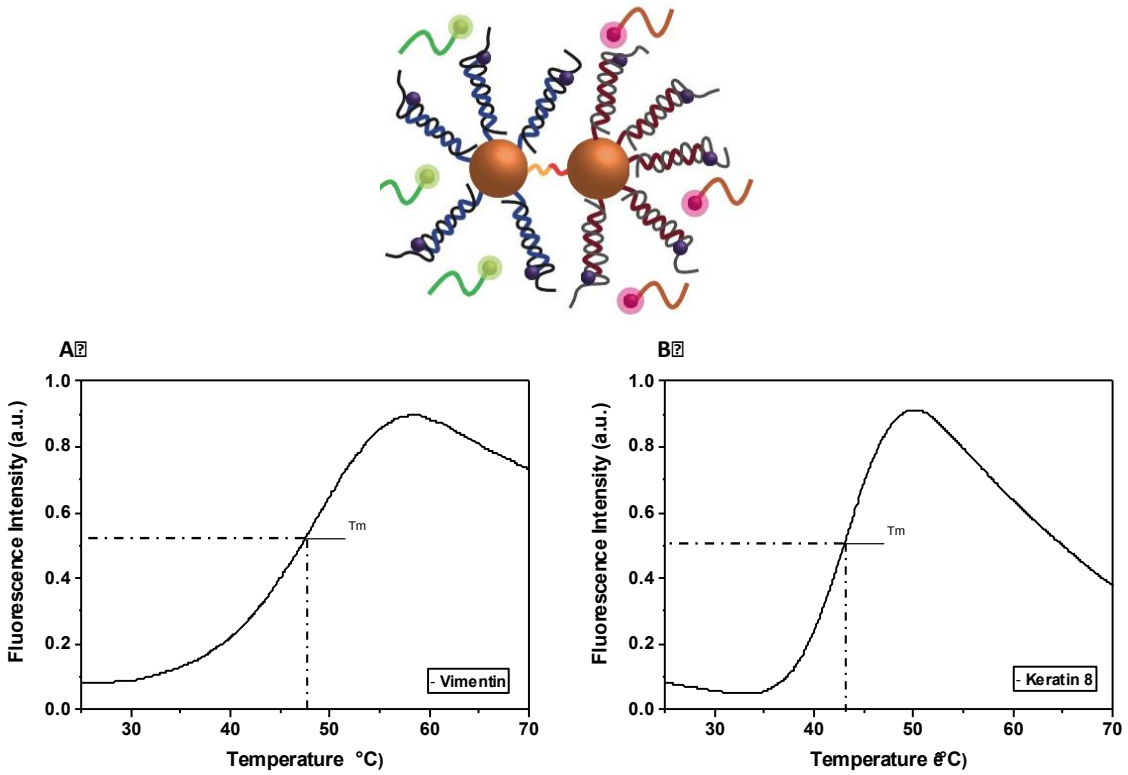

Figure 5.3 Fluorescence melting curve of (A) vimentin and (B) keratin 8 flares.

As can be seen in Figure 5.3 a characteristic sigmoidal curve was observed with melting temperatures of approximately 47 and 44 °C for vimentin and keratin 8 respectively suggesting successful flare hybridization. A higher melting temperature was observed for vimentin compared to keratin 8, which was attributed to a higher number of GC bases in the vimentin sense/flare duplex (55 %) as opposed to the keratin 8 duplex (36 %).[230] The observed melting temperatures indicated that our DNA-coated AuNP dimers could be used for *in vitro* cell experiments. A melting temperature below 37 °C would lead to non-specific flare release and a false positive fluorescence signal.

5.1.3 Efficiency of oligonucleotide loading on the AuNP dimer

The use of DNA-coated AuNP dimers as potential candidates for diagnostic and therapeutic applications also relies on the ability to maximize and tailor the amount of oligonucleotides on the AuNP surface. Studies by Mirkin and co-workers have shown that the degree of loading is sequence specific and could in turn affect the degree of cellular uptake as discussed in **section 2.4**.[119, 231] It was therefore imperative to quantify the degree of loading for the sequence specific vimentin and keratin 8 sense strands respectively (see Table 3.2 for sequences) followed by the exact number of duplexes formed.

The degree of oligonucleotide loading was quantified *via* dissolution of the Au core followed by determination of the oligonucleotide concentration in solution (see **section 3.4.2.1.2 and 4.2.1.2.1**). This allowed for the direct calculation of the number of oligonucleotides per AuNP for both vimentin and keratin 8 sense strands as seen in Table 5.1.

Table 5.1Degree of sense strand loading for both vimentin and keratin 8

Oligonucleotide sense strand	Oligonucleotides/AuNP	Error
Vimentin	126	4
Keratin 8	128	2

No significant variation was found in the degree of oligonucleotide loading between sequences specific for the detection of vimentin and keratin 8 indicating that both 15 ± 1 nm nanoparticles of an AuNP dimer were uniformly coated.

For the use of DNA-coated AuNP dimers as drug delivery vehicles (see **section 5.5**) the number of sense/flare strand duplexes per AuNP also had to be quantitatively determined. This was achieved by taking advantage of the fluorescent properties of the dye modified flare strands (see **section 3.4.2.2.3** for experimental details).

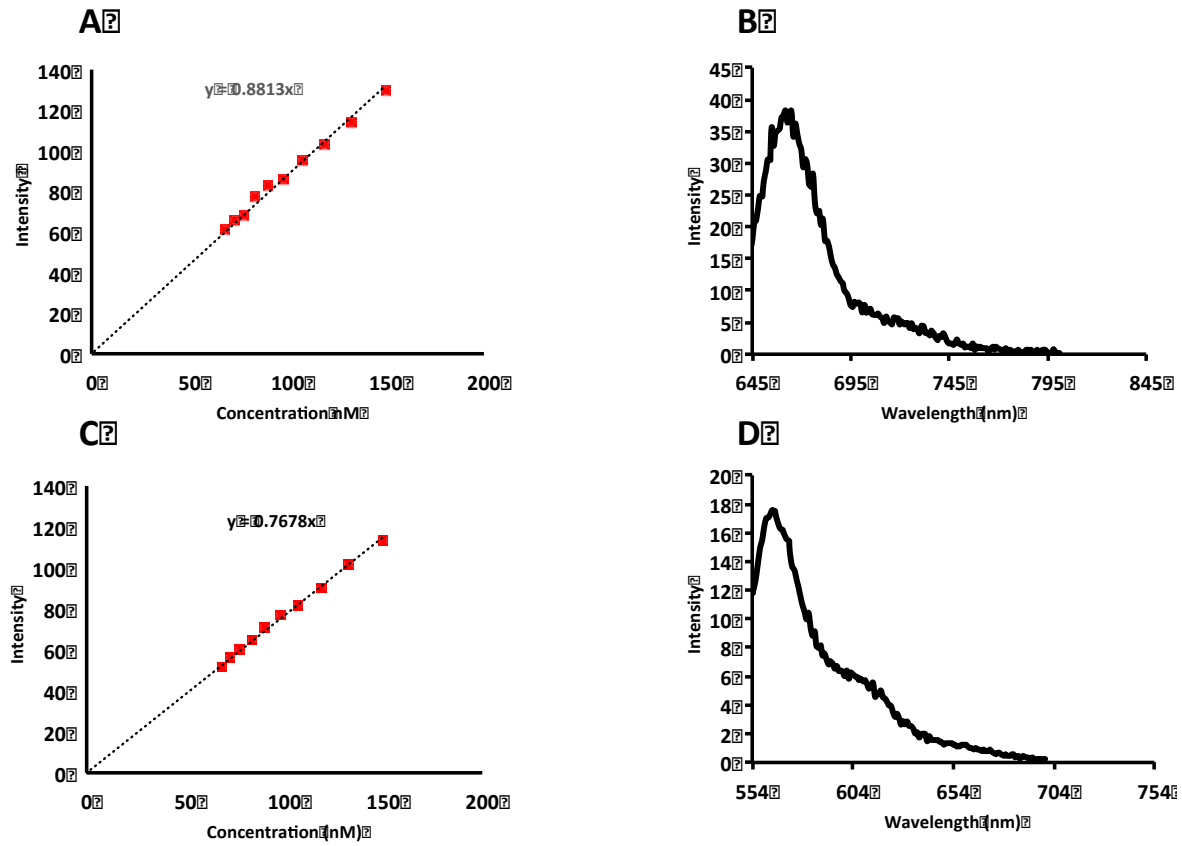

Figure 5.4 Fluorescence calibration curves for vimentin (A) and keratin 8 (C) flares along with spectra showing the fluorescence signatures of Cy5 (A) and Cy3 (D)

The amount of duplexes formed per AuNP were determined by using the respective fluorescence calibration curve for each flare strand as seen in Figure 5.4 and by monitoring the fluorescence signature of the dye in solution. The number of duplexes were therefore estimated and shown in Table 5.2 (see **Appendix B.1.2** for calculation examples).

Table 5.2 Estimated number of duplexes per AuNP for vimentin and keratin 8

Oligonucleotide flare strand	Duplexes per AuNP	
	40 ×	**120** ×
Vimentin	35	116
Error	6	2
Keratin 8	38	118
Error	4	4

5.2 Stability of AuNP dimers against nucleases

Research that involves the use of nucleic acids in biological environments is often hindered by the process of enzymatic hydrolysis, which leads to

their degradation and renders them inactive due to the cells inherent defence mechanism.[232] Thus one inherent complication with using oligonucleotide based nanoparticle systems for intracellular applications is their susceptibility to degradation by enzymes. Specifically, DNase I is an endonuclease, which is present within the cytoplasm and nonspecifically cleaves DNA by catalyzing the hydrolytic cleavage of the phosphodiester bonds in the DNA backbone. Several studies, have suggested that DNA-coated AuNPs have shown an increased resistance to nucleases such as DNase I.[2, 150, 213, 229] This increased resistance is thought to be due to the close packing of oligonucleotides on the AuNP surface, leading to a high concentration of cations around the surface, which hinders enzyme activity as discussed in **section 2.5**.[93, 124] On the other hand, molecular DNA, treated to the same incubation conditions, shows no stability towards degradation.

Initially, a free duplex of DNA was incubated with DNase I (see **section 3.4.2.2.1** for experimental details) and visualized using PAGE in order to assess the efficiency of DNase I to degrade free dsDNA.

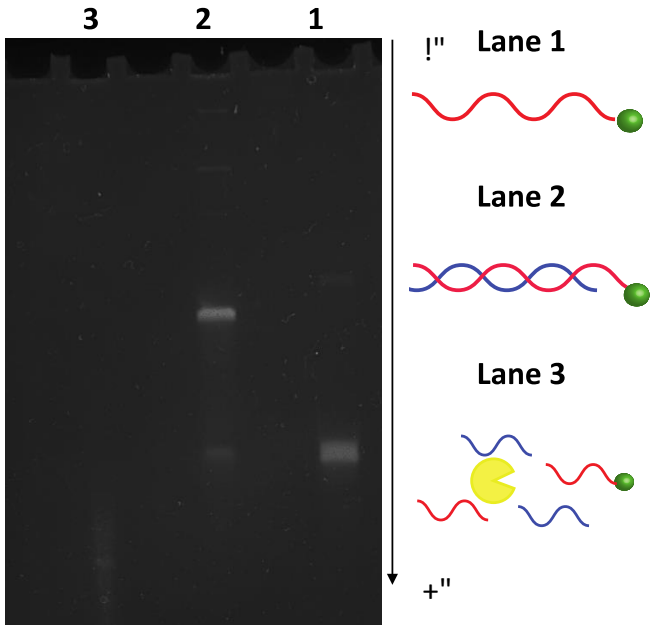

Figure 5.5 PAGE gel displaying a single stranded DNA (Lane 1), ds DNA (Lane 2) and the degradation of a free DNA duplex (Lane 3).

Lane 1 shows the band of a single DNA strand, lane 2 shows the band of a DNA duplex and lane 3 shows the same DNA duplex as lane 2 degraded by DNAse I into smaller fragments that can barely be visualised.

To test if the hypothesis that DNA-coated AuNPs are able to resist degradation by nucleases holds true for our system as well, DNA-coated AuNP dimers were incubated with DNase I at 37 °C (see **section 3.4.2.2.1** for experimental details). When oligonucleotides are bound to the gold nanoparticle core the fluorescence from the dye is quenched. However, if the oligonucleotides are digested due to enzymatic degradation, the dyes would be released in solution and quenching would no longer occur. The fluorescence signal of the dye at the 5' end of the sense strands was therefore monitored over the 24 h incubation period

(see **Appendix B.2.4** for corresponding fluorescence measurements over 24 h)

By monitoring the fluorescence signal of the dye-modified sense strand, the percentage of oligonucleotide strands that remained bound to the AuNP surface was determined. Gel electrophoresis was also employed in order to assess the integrity of the AuNP dimer structure.

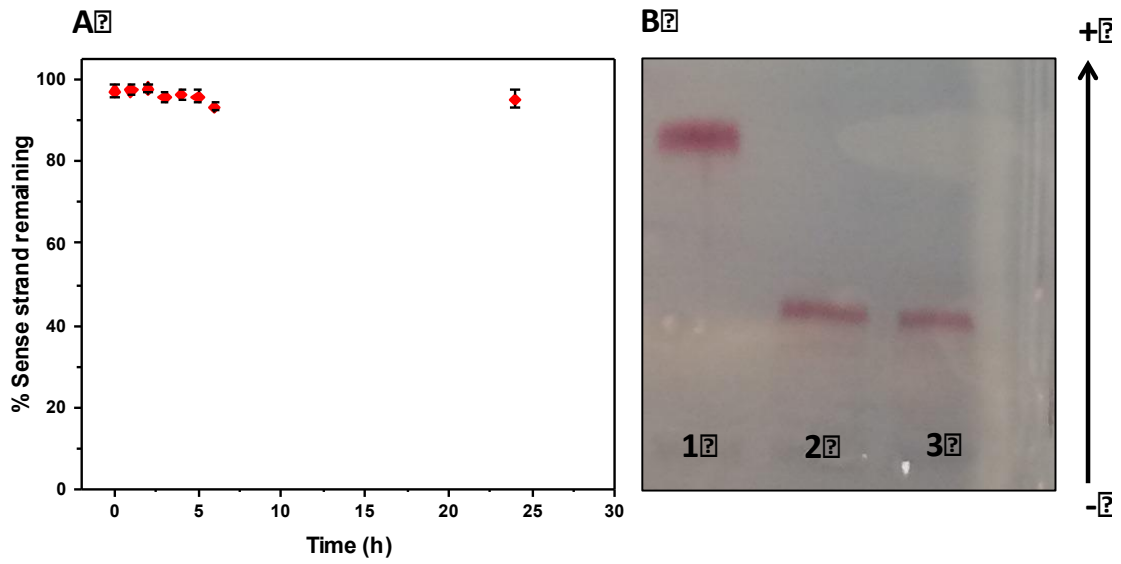

Figure 5.6 Susceptibility of AuNP dimers towards degradation by DNase I. The stability of the sense strand was monitored *via* fluorescence microscopy (A) whilst the stability of the nanoparticle dimers was ascertained via gel electrophoresis (B) (Lane 1: 13 nm AuNPs, Lane 2: nanoparticle dimers in PBS, Lane 3: nanoparticle dimers incubated with DNase I). Data are shown as mean ± SEM (n = 3).

From Figure 5.6 **(A)** it is evident that after a 24 h incubation period with DNase I no significant loss to the oligonucleotide shell occurred as our AuNP dimers retained more than 95 % of their initial surface coverage.

Furthermore, analysis *via* gel electrophoresis (B) confirmed that the structure of our DNA-coated AuNP dimers remained intact and was not degraded into the single AuNP counterparts.

DNA degradation catalysed by enzymes has been modelled as a 2-step reaction. The first step involves enzyme association with the substrate whereas the second involves the hydrolysis of the nucleic acid.[233] DNA-coated AuNPs could therefore show an increased resistance due to the decreased rate of one or both of these steps. Research into the physical characteristics of DNA-coated AuNPs that lead to this unique property has suggested that DNA density is one important parameter that endows the system with increased stability.[2, 93] Indeed it has been found that AuNPs with less oligonucleotides bound to their surface display shorter half-lives.[234] In order to investigate this further single AuNPs were modified with a varied number of oligonucleotides and their susceptibility to degradation by DNase I was investigated.

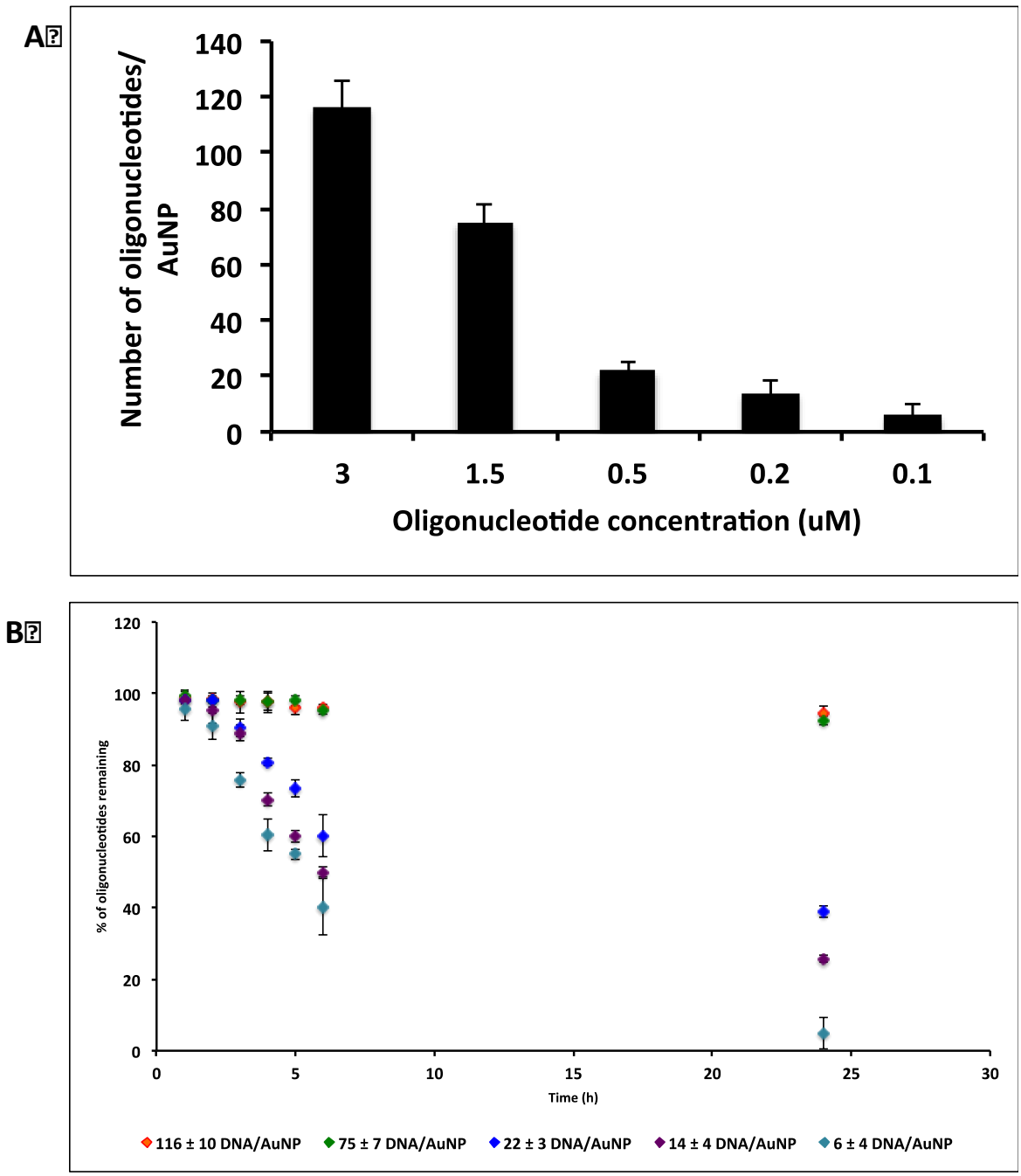

Figure 5.7 (A) Number of oligonucleotides attached per AuNP with varying oligonucleotide per reaction. (B) Graph showing the percentage of oligonucleotides remaining attached to the AuNP surface after a 24 h incubation period with DNase I for the different loading densities achieved

As is evident from Figure 5.7 a general trend is observed where a decrease in the oligonucleotide loading on the AuNP surface leads to a concomitant decrease in the percentage of oligonucleotides that remain bound to the surface after 24 h. However, when comparing the two highest loading densities the level of degradation is not considered to be significant and both have a similar percentage of oligonucleotides that remain bound to the surface. We could therefore consider the possibility that DNA-coated AuNPs display resistance to nuclease degradation over a range of oligonucleotide loading. Below this range the density of oligonucleotides are not sufficient to protect DNAs against digestion. Even though for a decreased number of oligonucleotides digestion is not complete within 24 h, the continuous decreasing trend observed is an indication that for longer incubation times complete digestion would possibly be observed. It is therefore evident that nuclease resistance is highly dependent on the number of oligonucleotide strands that coat the AuNP surface.

As previously mentioned, a suggested factor for the increased resistance displayed by DNA-coated AuNPs is the high local salt concentration at the nanoparticle surface.[2, 121, 123, 234] Previous work by Mirkin *et al.* has demonstrated that monovalent cations, including Na^+, inhibit DNase I as well as related nucleases. This inhibition is caused by the displacement of Ca_2^+ and Mg_2^+ by Na^+ ions that are bound to the enzyme and are required for efficient activity. An increased concentration of Na^+ ions has furthermore been associated with an increase in the oligonucleotide surface density that requires more charge balancing counterions.[234] Pellegrino *et al*. have also shown that DNA attached to a AuNP surface can undergo slight conformation changes.[106] These changes can therefore prevent binding of DNase I, which is known to be a minor groove binder.[235] Nevertheless, it can be concluded that the demonstrated increased resistance is in part due to the dense packing of the

oligonucleotides and the resulting high cation concentration that prevents efficient enzyme activity. This is an important property that renders these structures extremely promising for their use within cellular environments.

The stability of DNA-coated AuNP dimers was also investigated in the presence od DNase II. As opposed to DNase I, DNaseI II is found within intracellular compartments, most noticeably lysosomes and functions optimally at acidic pH in he absence of divalent cations by catalyzing the hydrolysis of the phosphodiester backbone.[236-238] Its location within lysosomes suggests that its responsible for the degradation of exogenous DNA encountered by phagocytosis. It has also been suggested that it is important in DNA fragmentation and degradation during cell death.[238] We therefore tested the stability of our AuNP dimers in the presence of DNase II as well.

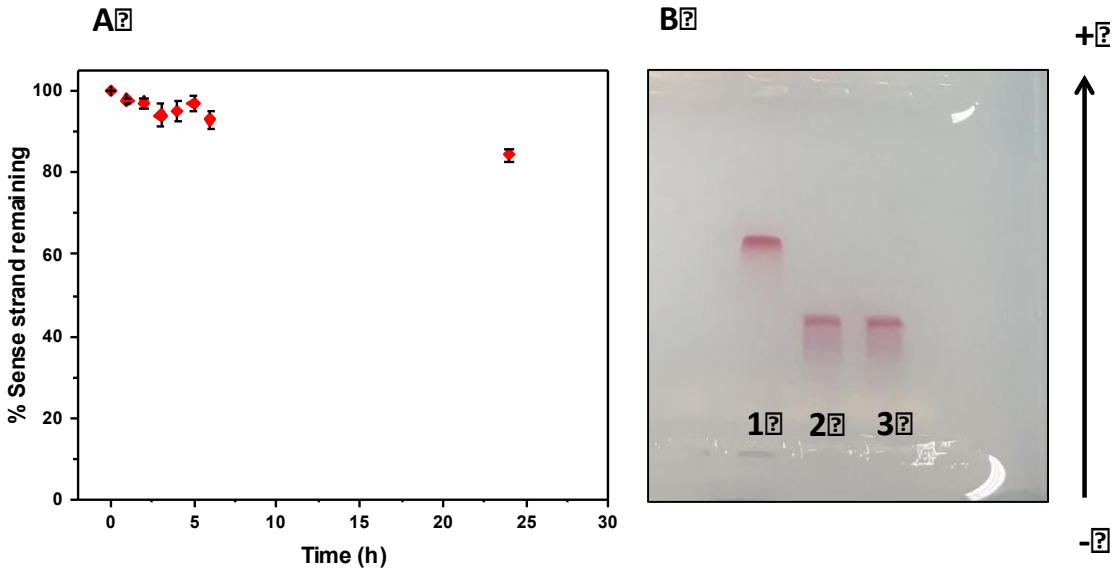

Figure 5.8 Susceptibility of AuNP dimers towards degradation by DNase II. The stability of the sense strand was monitored *via* fluorescence microscopy (A) whilst the stability of the nanoparticle dimers was ascertained via gel electrophoresis (B) (Lane 1: 13 nm AuNPs, Lane 2: nanoparticle dimers in PBS, Lane 3: nanoparticle dimers incubated with DNase II). Data are shown as mean ± SEM (n = 3).

Once again by monitoring the fluorescence intensity from the FAM modified sense strands (see **Appendix B.2.5** for fluorescence measurements) the % of sense strand degradation could be determined. As can be seen from Figure 5.8 **(A)** our DNA-coated AuNP dimers retained more than 80 % of their initial oligonucleotide surface coating as well as the dimeric structure as can be seen from Figure 5.8 **(B)**. This suggested that even in the presence of DNase II our AuNP dimers displayed unique stability making them suitable for their use within live cells (see **section 5.4.2**).

5.3 Specificity of AuNP dimers

In order to detect target mRNA within living cells it is imperative for the AuNP dimers to respond to their target rapidly and efficiently. Binding studies were therefore conducted *in vitro* and within a testube using perfectly matched synthetic oligonucleotide targets for vimentin and keratin 8 mRNA respectively.

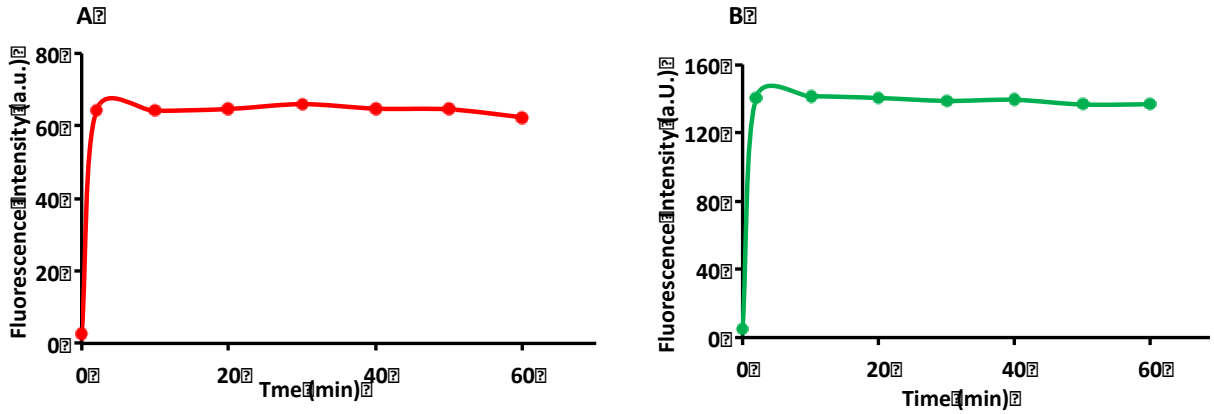

Figure 5.9 Time course of fluorescence associated with flare release when AuNP dimers are incubated with synthetic target oligonucleotide strands leading to the displacement of vimentin (A) and keratin 8 (B) flares.

Testing our DNA-coated AuNP dimers with synthetic fully complementary oligonucleotide targets as shown in Figure 5.9 demonstrated that the system responded with an increase in the fluorescence signal upon recognition and binding within the first 2 min. This result indicated that our AuNP dimers were efficient at signalling the presence of a specific target in buffered conditions.

Having established that DNA-coated AuNP dimers respond rapidly to their complementary target we next investigated their specificity. AuNP dimers were challenged with a series of targets containing 1 or 2 base pair mismatches as well as with a target showing no complementarity. Following incubation, the fluorescence signal was monitored to evaluate binding and subsequent flare release.

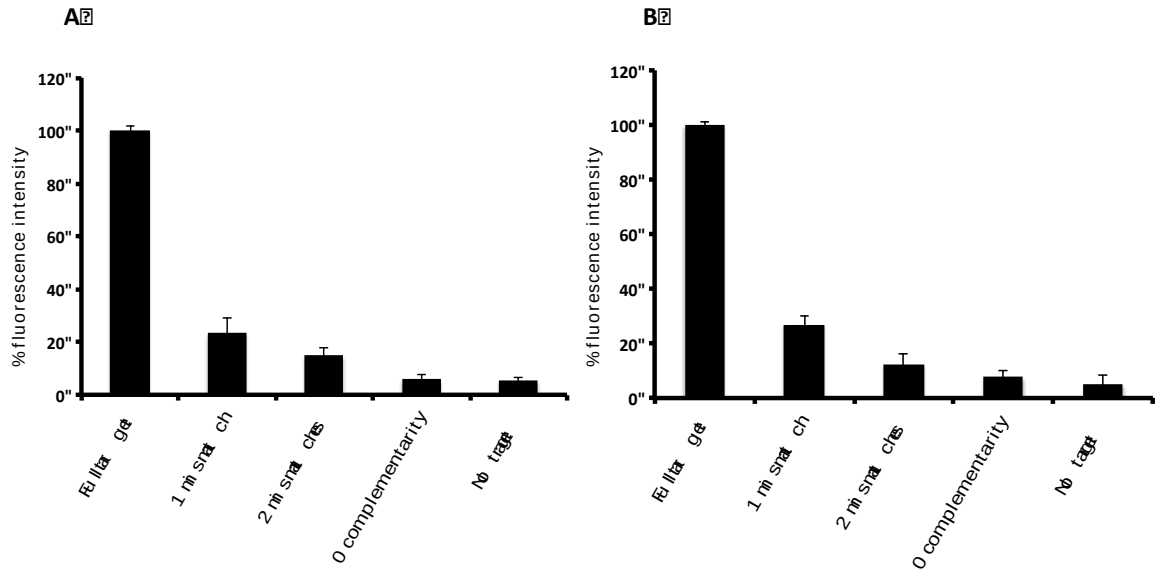

Figure 5.10 Target specificity of AuNP dimers in the presence of a fully complementary target, mismatched targets and no target for the detection of vimentin (A) and keratin 8 (B) mRNA

As can be seen from Figure 5.10 a target containing 2 base pair mismatches and a target with no base pair complementarity showed a fluorescence signal of comparable magnitude to the background fluorescence (no target). On the other hand, incubation with a target incorporating a one base pair mismatch showed a slightly higher response to flare release. However, the signal was easily distinguished from that of the fully complementary target because it was more than 70 % less intense.

These results demonstrated that our DNA-coated AuNP dimers were capable of responding to their complementary target quickly, independently and in a sequence specific manner, which is in accordance with previously published reports.[111, 128, 133, 134, 137-139]

5.4 Interaction of AuNP dimers with cell cultures

Having confirmed that our AuNP dimers show increased stability, specificity and selectivity in an extracellular environment, their ability to independently detect up to two mRNA targets was then studied in living cells.

As previously mentioned the oligonucleotide sequences on the surface of the AuNP dimers were designed to detect keratin 8 and vimentin mRNAs. The 16 HBE cell line was therefore initially chosen as a model for epithelial cells that strongly express keratin 8 while not expressing vimentin. On the other hand, whilst keratin 8 is expressed in epithelial cells, vimentin is expressed in mesenchymal cells (MRC 5), which were used as model cells to demonstrate the specific detection of vimentin mRNA. Furthermore, in order to demonstrate the ability of the AuNP dimer to sense more than one target mRNA simultaneously, we employed the adenocarcinoma-derived human alveolar cell line A 549. This cell line expresses both keratin 8 and vimentin and was used to demonstrate the ability of this system for simultaneous detection of both targets.

5.4.1 A549 expression of vimentin and keratin 8

Vimentin, a type III intermediate filament, is found in mesenchymal cells of various types of tissue during their developmental stage and it maintains cell and tissue integrity. It therefore represents a common cell marker for

MRC 5 cells.[150, 239, 240] Similarly, cytokeratin proteins are expressed in epithelial cells (such as 16 HBEs) and are found in the intracytoplasmic cytoskeleton of epithelial tissue where they help resist mechanical stress.[150, 241, 242] Whereas the expression of vimentin in MRC 5s and the expression of keratin 8 in 16 HBE cells has been well studied, protein expression of A 549 cells is more ambiguous. As they are known to be adenocarcenomic epithelial cells, keratin 8 expression was expected to be observed.[243] However, studies have also shown that in various epithelial cancers including lung cancer, vimentin can be overexpressed and is correlated with tumour growth and progression, thus serving as an attractive target.[239, 244, 245] In order to ascertain whether this cell line could be used for this study, the expression of both vimentin and keratin 8 proteins was investigated.

5.4.1.1 Immunofluorescent labelling of A 549 cells

In this study, immunofluorescent labelling was initially used to test for expression of keratin 8 and vimentin proteins in A 459 cells. Cells were fixed and labelled with the appropriate antibody for each protein and subsequently with the fluorophore-labelled (AlexaFluor 488, Invitrogen) secondary antibody for visualization by confocal microscopy (see **section 3.5.4** for experimental details). Corresponding images are depicted in Figure 5.11.

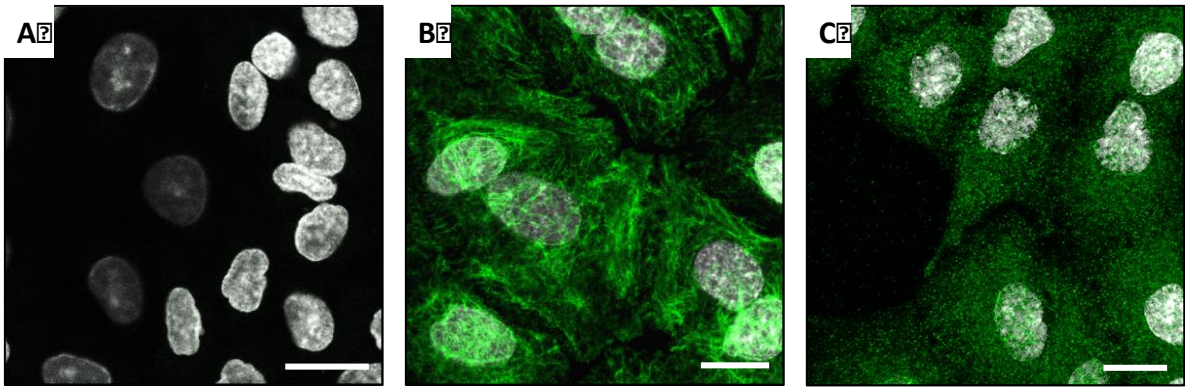

Figure 5.11 Immunofluorescent labelling of A549 cells to study the expression of keratin 8 (B) and vimentin (C). Cells only stained with the secondary antibody (A) were used as a control. Nuclei are stained with DAPI (white). Scale bar is 15 μm.

Confocal images show that A549 cells express both keratin 8 (Figure 5.11 **B**) and vimentin (Figure 5.11 **C**). The fact that no signal was detected when cells were labelled with the secondary antibody in the absence of the primary antibody (Figure 5.11 **A**) is a strong indication that the fluorescence signal detected in both cases was due to specific binding and protein expression. These results suggested that the A 549 cell line could be used as an appropriate model to demonstrate the capability of multiplexed detection by our AuNP dimers.

5.4.1.2 RT-qPCR on 16 HBE, MRC 5 and A 549 cells

Although the expression of both vimentin and keratin 8 was verified *via* immunostaining, RT-qPCR was employed in order to quantitatively assess the relative expression of keratin 8 and vimentin mRNA in 16 HBE, MRC 5 and A 549 cells against a known housekeeping gene (*Gapdh*) (see **section 3.5.3** for experimental details) as seen in Figure 5.12.

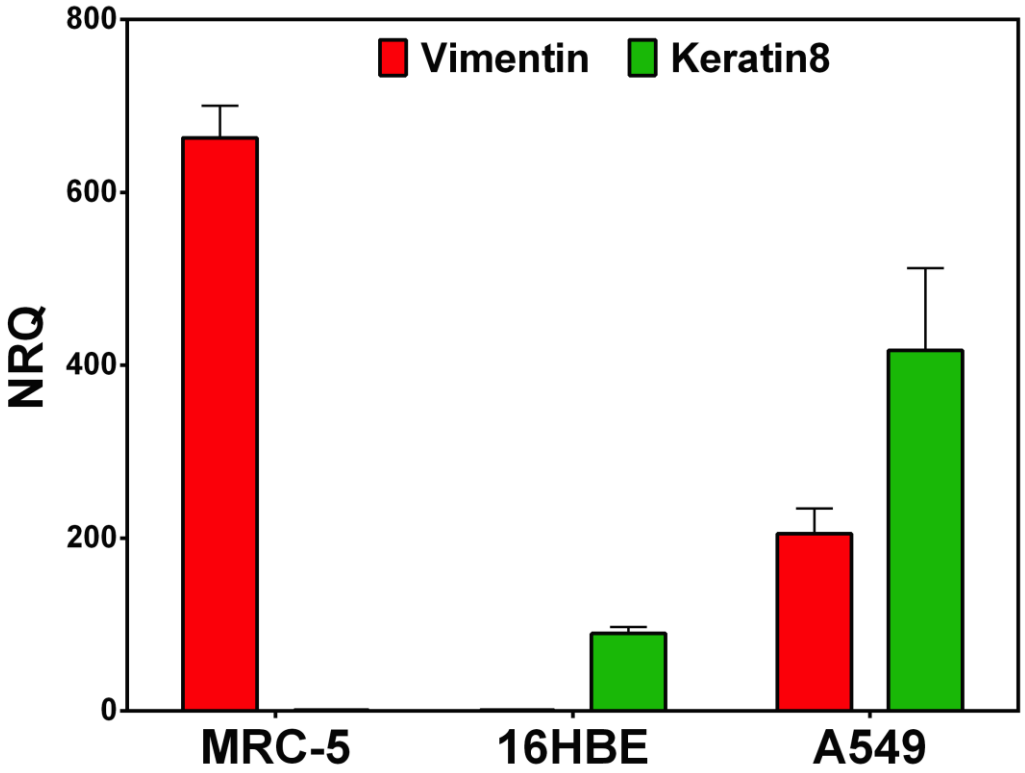

Figure 5.12 RT-qPCR analysis on cells as indicated in figure showing the differential expression of vimentin (red) and keratin 8 (green) within different cells lines NRQ (Normalized Relative Quantification), Fold difference in gene expression for vimentin and keratin 8 were normalized to the house keeping gene (*Gapdh*) values of fold changes.

As expected the MRC 5 cell line showed high level of vimentin expression and no expression of keratin 8. On the contrary 16 HBE cells exhibited a consistent expression of keratin 8 and no expression of vimentin mRNA. A 549 cells showed the expression of both vimentin and keratin 8 mRNA with lower expression of vimentin as expected. These results indicate that the chosen cell lines are suitable to study the efficiency of our DNA-coated AuNP dimers to detect specific mRNA targets.

5.4.2 Live cell mRNA detection using DNA-coated AuNP dimers

In recent years the need to detect intracellular mRNA has been increasingly growing. Research has shown that changes in the mRNA expression of cells can be a strong indication of cancer progression.[137, 139]

In this study we show that covalently linked DNA-coated AuNP dimers (see Scheme 5.3), which have demonstrated high levels of stability and specificity can be used to efficiently detect up to two mRNA targets (vimentin and keratin 8). Superiority in this design comes from the ability to precisely control the number of oligonucleotides on the surface of each AuNP therefore ensuring equal efficiency of detection on a single cell level. In our experiments 16 HBE, MRC 5 and A 549 cells were incubated with AuNP dimers and visualized *via* confocal microscopy.

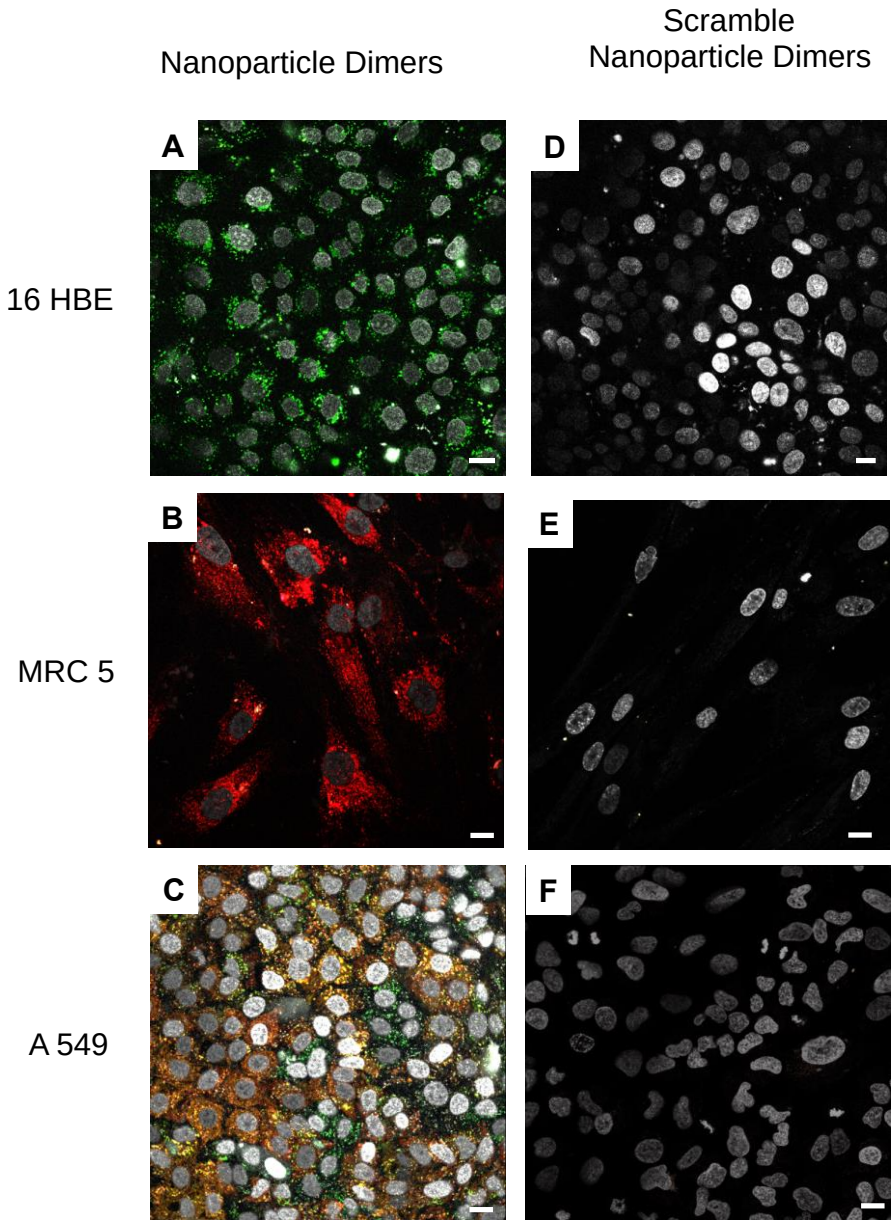

Figure 5.13 Confocal microscopy of cells incubated with AuNP dimers (A, B and C) and scramble AuNP dimers (D, E and F). Color guide: keratin 8 flare strand – green, vimentin flare strand – red, vimentin and keratin 8 sense strand – blue, scrambled flare strand – green, scrambled sense strand – blue, nuclear counterstain – white. Scale bars are 15 μm.

Figure 5.13 shows a confocal microscopy image of live cells that were incubated with the AuNP dimers. The 16 HBE cells displayed a single fluorescence signal (green) corresponding to the specific detection of keratin 8 mRNA. The absence of a fluorescence signal from the sense strands (blue) or the flare oligonucleotide strand corresponding to vimentin mRNA (red) confirmed the specific function of the nanoparticle dimers. Whilst keratin 8 is expressed in epithelial cells, as previously mentioned, vimentin is expressed in mesenchymal cells (MRC 5). Figure 5.13 **B** shows that when mesenchymal cells (MRC 5) were incubated with the same AuNP dimers, a red fluorescence signal corresponding to the detection of vimentin mRNA was observed but no blue or green signals as in the case of 16 HBE cells, confirming the presence of only vimentin mRNA in MRC 5 cells.

In order to demonstrate the ability of the AuNP dimer to sense more than one target mRNA simultaneously AuNP dimers were also incubated with A 549 cells. This cell line expresses both keratin 8 and vimentin as observed from immunostaining experiments (see **section 5.4.1**). Therefore both of these mRNAs were expected to be detected in live A549 cells. Figure 5.13 **C** shows that after incubation of the nanoparticle dimers with A 549 cells, two fluorescence signals (red and green) corresponding to the detection of both keratin 8 and vimentin mRNAs were observed. To further confirm the specificity of the particles, all three cell lines were also incubated with scrambled AuNP dimers (see Table 3.2 for sequences). The sense strands were designed to not target any cellular mRNA and therefore no fluorescence signal should be observed corresponding to flare release. Figure 5.13 **D, E and F** shows that in all three cases, no significant fluorescence signal was detected from either the flare strand or the anchored sense strand.

5.4.3 Intracellular location of AuNP dimers

After demonstrating the capability of our DNA-coated AuNP dimers to efficiently detect up to two mRNA targets, studies focused on investigating their intracellular fate. In order to identify the location of the AuNP dimers within a cell; we analyzed several ultra-thin sections of cells incubated with the AuNP dimers and imaged *via* TEM.

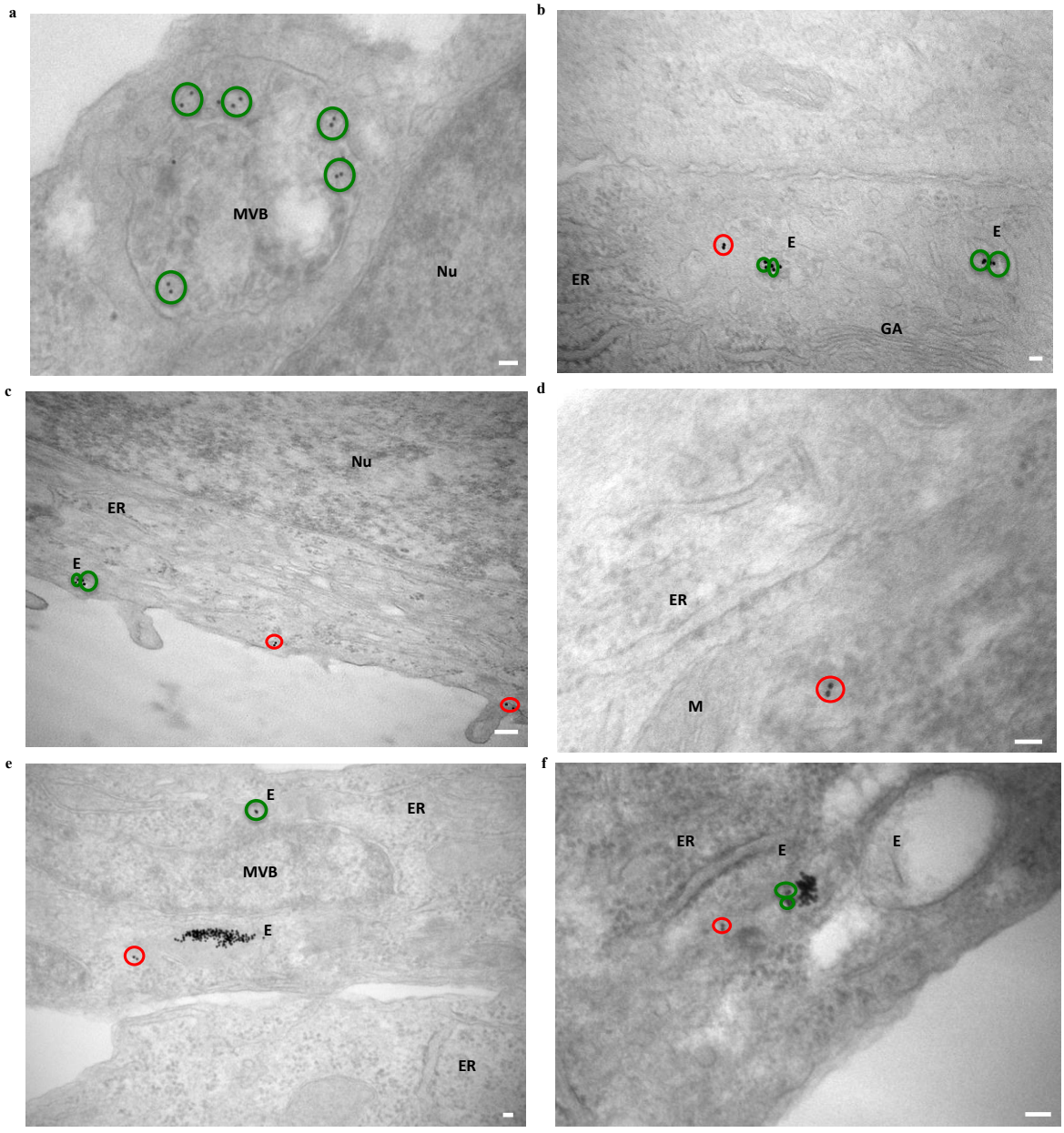

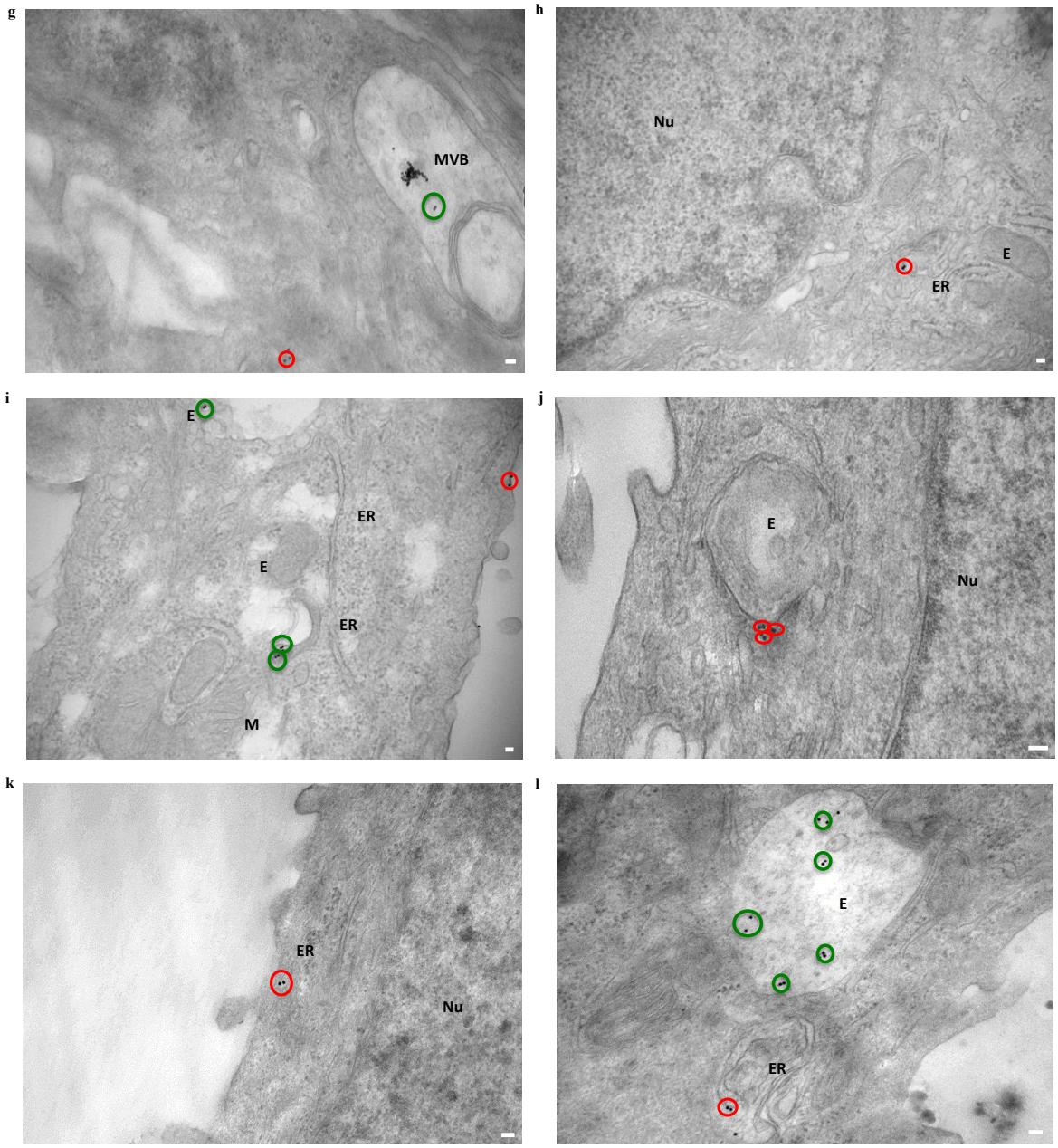

Figure 5.14 TEM images of cells incubated with the nanoparticle dimers for 18 h. (a – d) show sections of 16 HBE cells, A549 cells are shown in images (e – h) whereas images (i – l) show sections of MRC 5 cells. ER: Endoplasmic Reticulum, E: Endosomes, M: Mitochondria, GA: Golgi Apparatus, Nu: Nucleus, MVB: Multi

Vesicular Body. Green circles indicate AuNP dimers within endosomes or multivesicular bodies whereas red circles indicate nanoparticle dimers with a cytoplasmic location. Distance between each particle within a dimer could be up to 50 nm. Scale bar is 50 μm.

Our TEM analysis showed that 2.21 %, 2.99 % and 2.04 % of our AuNP dimers were found outside endosomes in 16 HBE, MRC 5 and A 549 cells respectively as shown in Figure 5.14**,** concluding that these ones are responsible for the highly specific signals we obtained.

5.5 DNA-coated AuNP dimers as drug delivery vehicles

Apart from their use for gene silencing and mRNA detection, AuNPs have also emerged as promising agents for cancer therapy as discussed in **section 2.5.2**. To date the most commonly used anti-cancer drugs are hindered by severe side effects associated with poor uptake and inadequate accumulation at diseased sites.[7, 246, 247] There is therefore intense interest in modifying existing drugs in order to reduce potential side effects, enabling higher dose delivery to target tissue.[248]

Current research is now focusing on the use of AuNPs as drug delivery vehicles to tackle the aforementioned issues and improve the treatment of cancer. An important demonstration was the use of 5 nm AuNPs covalently bound to cetuximab, an active targeting agent, and gemcitabine as a therapeutic payload for the treatment of pancreatic cancer.[249] Other examples include the use of cytotoxic platinum anti-cancer compounds conjugated to AuNPs as well as the use of AuNP spheres and rods to deliver anthracycline drugs such as doxorubicin.[250-255] Recently research by our group reported how DNA-coated AuNPs could be designed

and finely tuned to achieve localized and specific endocellular drug delivery upon the detection of a specific mRNA target.[150] Using DNA-coated AuNPs we were able to selectively kill only mesenchymal cells without affecting epithelial cells demonstrating that they can deliver their cargo only in cells having a specific mRNA signature.[256] However, the need to deliver a precise payload of more than one drug to the same endocellular environment is increasingly growing.

In this work the development of our DNA-coated AuNP dimers into drug delivery vehicles is shown, which can coordinate the delivery of two different DNA intercalating drugs into the local cellular microenvironment with high selectivity and specificity. After successfully testing the ability of the AuNP dimers to sense two mRNA signatures independently or simultaneously (see **section 5.4.2**), we assessed their ability to act as a drug delivery vehicle of more than one drug. DOX and MTX were chosen as widely recognized anti-cancer drugs. Both bind within a DNA duplex by intercalation of the tetracyclic region (DOX) and anthraquinone ring (MXT) into the DNA base pairs.[257, 258]

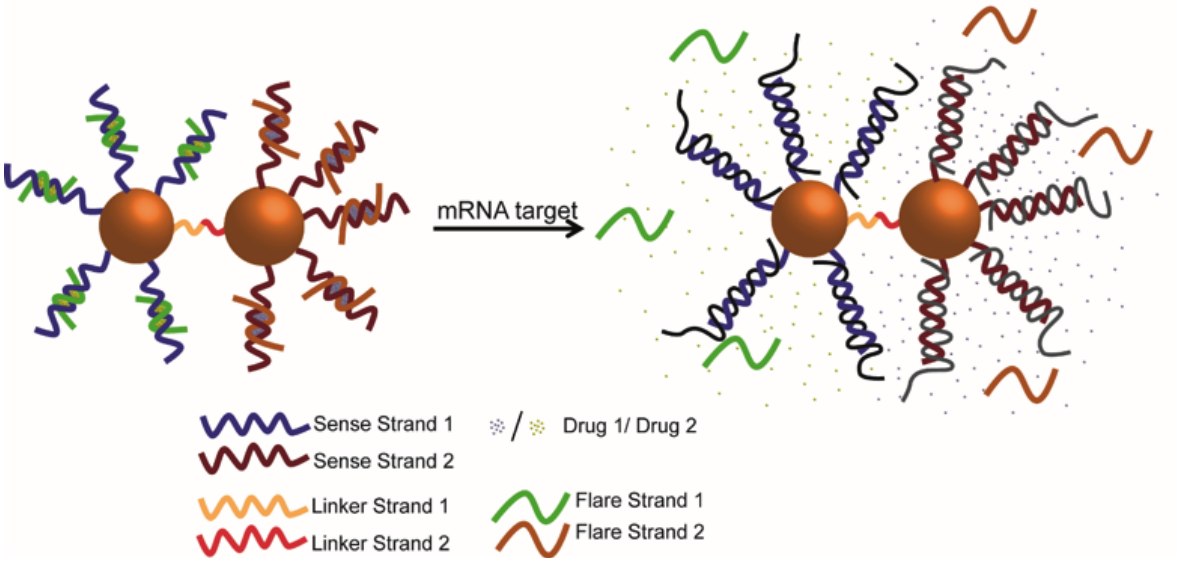

Figure 5.15 Schematic illustration of nanoparticle dimer used in drug release experiments. (Left) Dimer loaded with DOX (Drug 1) and MTX (Drug 2). When the target mRNA binds to the sense strand the intercalated drugs are released (right) causing an increase in the fluorescence signal.

Figure 5.15 shows the design of the nanoparticle dimers as drug delivery vehicles for DOX and MTX. DOX was intercalated in the DNA duplex that detects the keratin 8 mRNA whereas MXT was intercalated in the DNA duplex that detects vimentin mRNA (see **section 3.3.3** for experimental details). No additional fluorophore labels were used in this experiment apart from DOX and MTX, which by themselves have specific fluorescent signatures. When intercalated in the DNA duplex, close to the AuNP surface, their fluorescence is quenched, however, when a target mRNA binds to the correspondent sense sequence the flare is displaced leading to the release of the intercalated drug, which is detected as a corresponding increase in the fluorescence signal of the drug *via* confocal microscopy.

The following section will discuss the physicochemical characterization of our drug loaded AuNP dimers as well as their interaction with live-cell cultures and their capability to induce targeted cell death.

5.5.1 Characterization of drug loaded AuNP dimers

5.5.1.1 Hybridization of flare strand at room temperature

Incorporation of both DNA intercalators within the AuNP dimers, which is explained in detail in **section 3.3.3**, involves a two-step process. First, DOX was mixed together with the keratin 8 flare strand as well as the AuNP dimers and a heat-cool step was performed to smoothly intercalate the DOX between the sense and flare strand keratin 8 duplex. The sample was purified from excess of free drug, after which the same AuNP dimers were mixed together with MXT and the vimentin flare strand. However, in order to avoid the release of DOX from the AuNP dimers, while at the same time achieving the hybridization of the vimentin sense and flare strands and therefore the intercalation of MTX, hybridization had to be performed at room temperature rather than adopting a heat-cool approach.

The efficiency of vimentin flare hybridization was therefore tested in three different buffers (see Table 3.3 for buffer compositions) with a higher ionic strength compared to PBS (see **section 3.4.2.2.4**) and the efficiency of hybridization was compared against a control sample where flare hybridization was achieved *via* a heat-cool approach as seen in Figure 5.16**.**

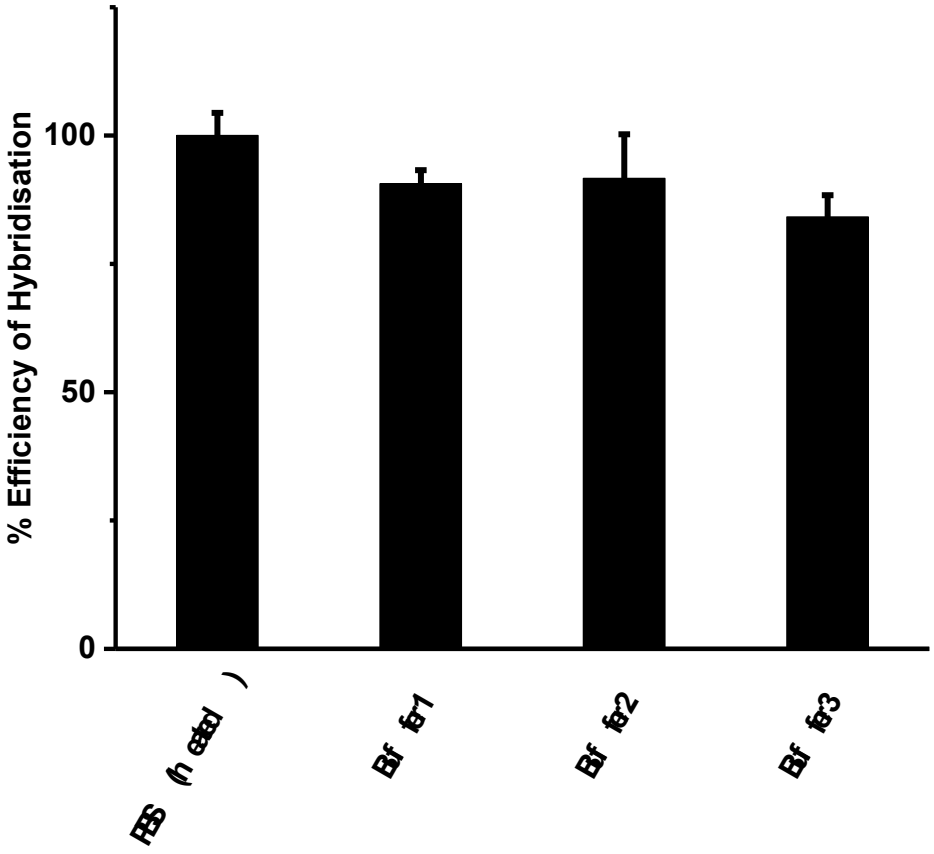

Figure 5.16 Efficiency of flare hybridisation under room temperature conditions using three buffers of varying composition. Flare hybridisation was compared to the efficiency of hybridisation under heating conditions (70 ºC) in PBS.

As can be seen from Figure 5.16 a higher efficiency of hybridization at room temperature is achieved when using Buffer 2 as opposed to buffer 1 or 3. A lower efficiency when using buffer 1 could be due to the lower ionic strength of the solution as it contains the lowest concentration of $MgCl_2$. On the other hand, although buffer 3 has the highest $MgCl_2$ concentration and the highest hybridization efficiency was expected to be observed, the higher ionic strength of the solution may be resulting in particle aggregation therefore decreasing the efficiency of flare

hybridization. Buffer 2 was therefore chosen as the suitable buffer to achieve flare hybridization and drug intercalation at room temperature. Scheme 5.5 shows the overall process of drug intercalation.

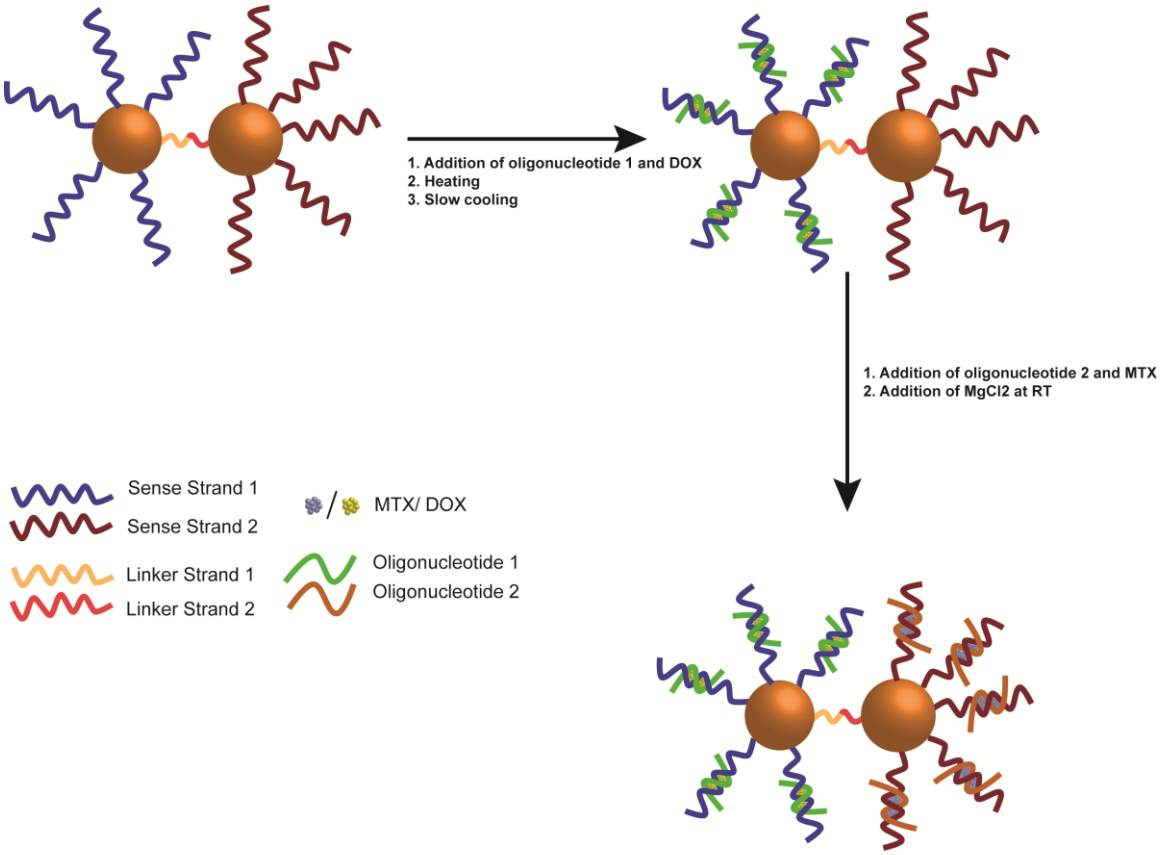

Scheme 5.5 Schematic illustration of drug incorporation. DOX is first loaded into the duplex responsible for the detection of keratin 8 *via* a heat cool step. On the other hand, MTX is incorporated into the duplex responsible for the detection of vimentin at room temperature by using buffer 2 that consisted of 7.5 mM $MgCl_2$

5.5.1.2 Efficiency of drug intercalation

DOX and MTX are two of the most widely used anti-cancer chemotherapeutic drugs that have been intensively investigated over the past decade. One of their most attractive properties is their ability to efficiently intercalate within a DNA duplex, a property that has been taken advantage of in our group to achieve specific drug delivery only to cells of interest.[150]

DOX (see Figure 3.4 **A** for chemical structure) belongs to a class of compounds with similar structures called anthracyclines. These are planar molecules that preferentially intercalate between neighbouring DNA base pairs. Studies focusing on the mechanism of DNA/DOX interaction have suggested that DOX is anchored on one side *via* the daunomicine sugar unit, which sits in the DNA minor groove whist the planar rings interact with the aromatic DNA bases *via* Van der Waals interactions. As a DNA intercalator DOX prefers intercalation sites containing adjacent GC base pairs most likely due to the formation of H bonding between DOX and guanine.[257, 259-261]

On the other hand, MTX (see Figure 3.4 **B**) is an aminoanthraquinone that belongs to a chemical class of agents known as anthracenediones. Similar to DOX it has a planar anthraquinone ring that intercalates between DNA base pairs whereas the nitrogen containing side chain electrostatically binds the negatively charged phosphate backbone of DNA. As with DOX a GC base pair specificity has been reported.[258, 262, 263]

In both cases, drug intercalation has been found to cause structural changes to the DNA conformation as well as changes to the fluorescence behaviour of both drugs. Both DOX and MTX have specific fluorescent

signatures when free in solution, however reports have suggested that upon binding to DNA the fluorescence of both drugs is quenched.[257, 259, 262] Therefore fluorescence of both DOX and MTX loaded onto our AuNP dimers was quenched not only by the close proximity to the AuNP core but also by DNA binding. Making use of this inherent fluorescent property the precise number of DOX and MTX molecules loaded into our AuNP dimers was evaluated. Figure 5.17 shows concentration dependant fluorescence calibration curves for both drugs as well as representative fluorescence spectra of DOX and MTX after liberation from the AuNP dimer.

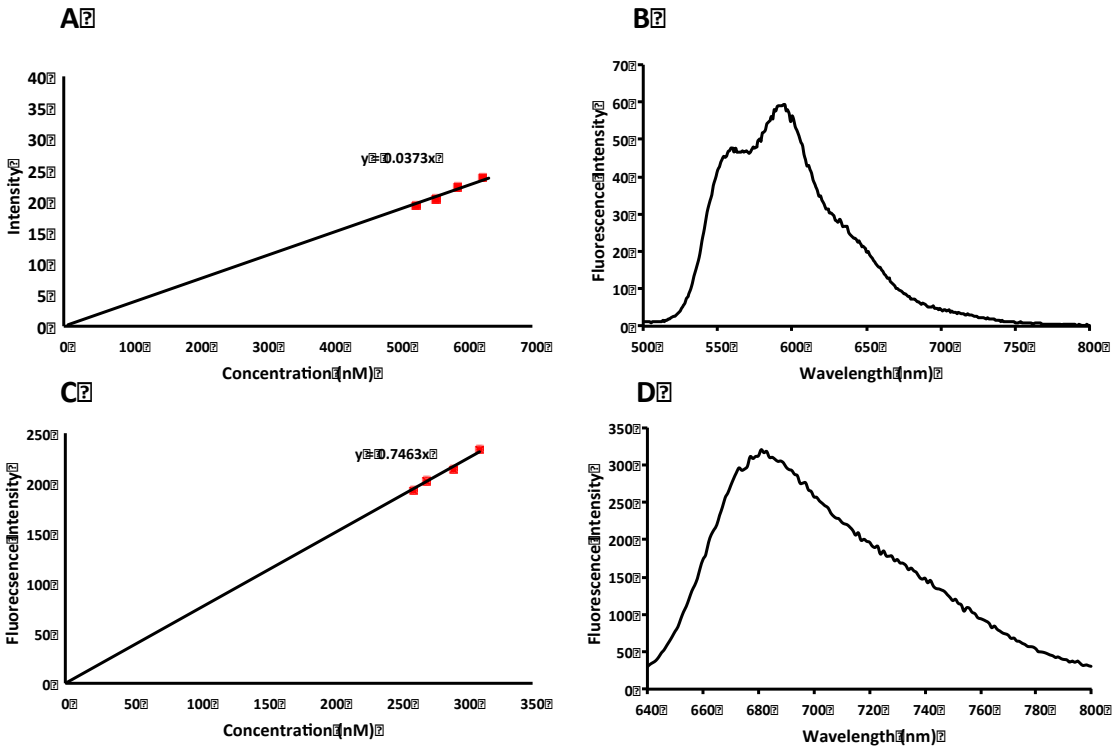

Figure 5.17 Fluorescence calibration curves for concentration-dependent DOX (A) and MTX (C) fluorescence as well as representative fluorescence spectra of free DOX (B) and MTX (D) in solution.

By relying on the fluorescence behaviour of both DOX and MTX we found that drug loading was strongly dependant on the number of duplexes that were formed. For "40×" duplexes 35 ± 2 DOX molecules and 30 ± 1 MTX molecules were interacalated within keratin 8 and vimentin respectively. When the number of duplexes were increased to "120×", we found that 117 ± 2 and 113 ± 3 DOX and MTX molecules were intercalated within their respective duplexes (see **Appendix B.1.3** for calculations).

Having established successful drug intercalation the ability of drug loaded AuNP dimers to retain their payload in the absence of external stimuli was evaluated over 24 h at 37 °C. The fluorescence output (see **Appendix B.2.5** for fluorescence measurements over 24 h) was monitored and used to calculate the percentage of DOX and MTX leaking over 24 h as shown in Figure 5.18.

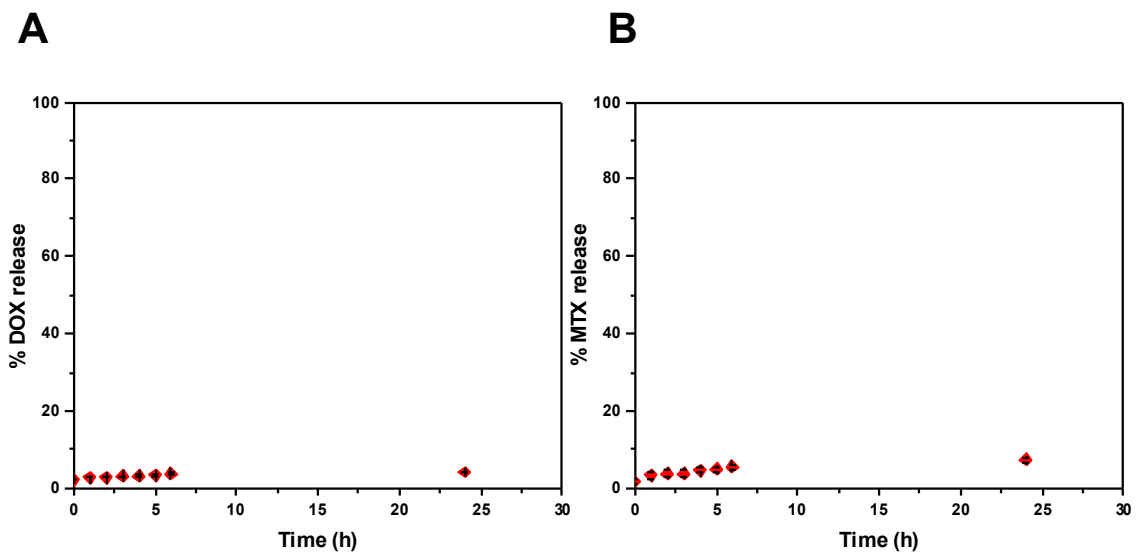

Figure 5.18 Percentage of DOX (A) and MTX (B) molecules that is released from our AuNP dimer after a 24 h period whilst maintaining a constant temperature of 37 °C in the absence of a complemetray target.

As can be seen from Figure 5.18 our AuNP dimers were able to retain more than 97 % of their loaded payload at a temperature commonly used to maintain healthy cell cultures. Thus they were deemed suitable for their further use in cellular application (see **section 5.5.2**).

5.5.2 Interaction of drug loaded AuNP dimers with cell cultures

Having observed that the DNA-coated AuNP dimers are highly specific to mRNA detection (see Figure 5.13), and can be efficiently uploaded with two drugs simultaneously without observing any significant drug leakage (see Figure 5.18), we used them for drug delivery in live cells. Model epithelial (16 HBE), mesenchymal (MRC 5), and cancerous (A 549) cell lines were treated with the AuNP dimers loaded with both DOX and MXT. By relying

on the fluorescence properties of both drugs, the release of DOX and MXT was monitored *via* confocal microscopy. Figure 5.19 shows confocal images where DOX and MXT were only released in the presence of the corresponding target mRNA. When the AuNP dimers were incubated with 16 HBE epithelial cells, only a fluorescence signal corresponding to the release of DOX was observed (Figure 5.19 **A**). In MRC 5 cells only the MXT was released due to the detection of the vimentin mRNA whilst the nanoparticle responsible for the detection of keratin 8 mRNA retained its payload (Figure 5.19 **B**). On the other hand, when the nanoparticle dimers incubated with A 549 cells, which express both vimentin and keratin 8, a fluorescence signal corresponding to the release of both drugs was observed (Figure 5.19 **C**). The specificity of the delivery of both DOX and MXT was further confirmed by using drug loaded scrambled AuNP dimers (see Table 3.2 for sequences). The scrambled sequences on the nanoparticles do not have a recognition site for the mRNAs in these cells and therefore the drugs were not released. From the absence of fluorescence in the confocal images (Figure 5.19 **D**-**I**) it is evident that the scrambled AuNP dimers were able to retain their drug payload in the absence of the appropriate mRNA target over an 18 h incubation period.

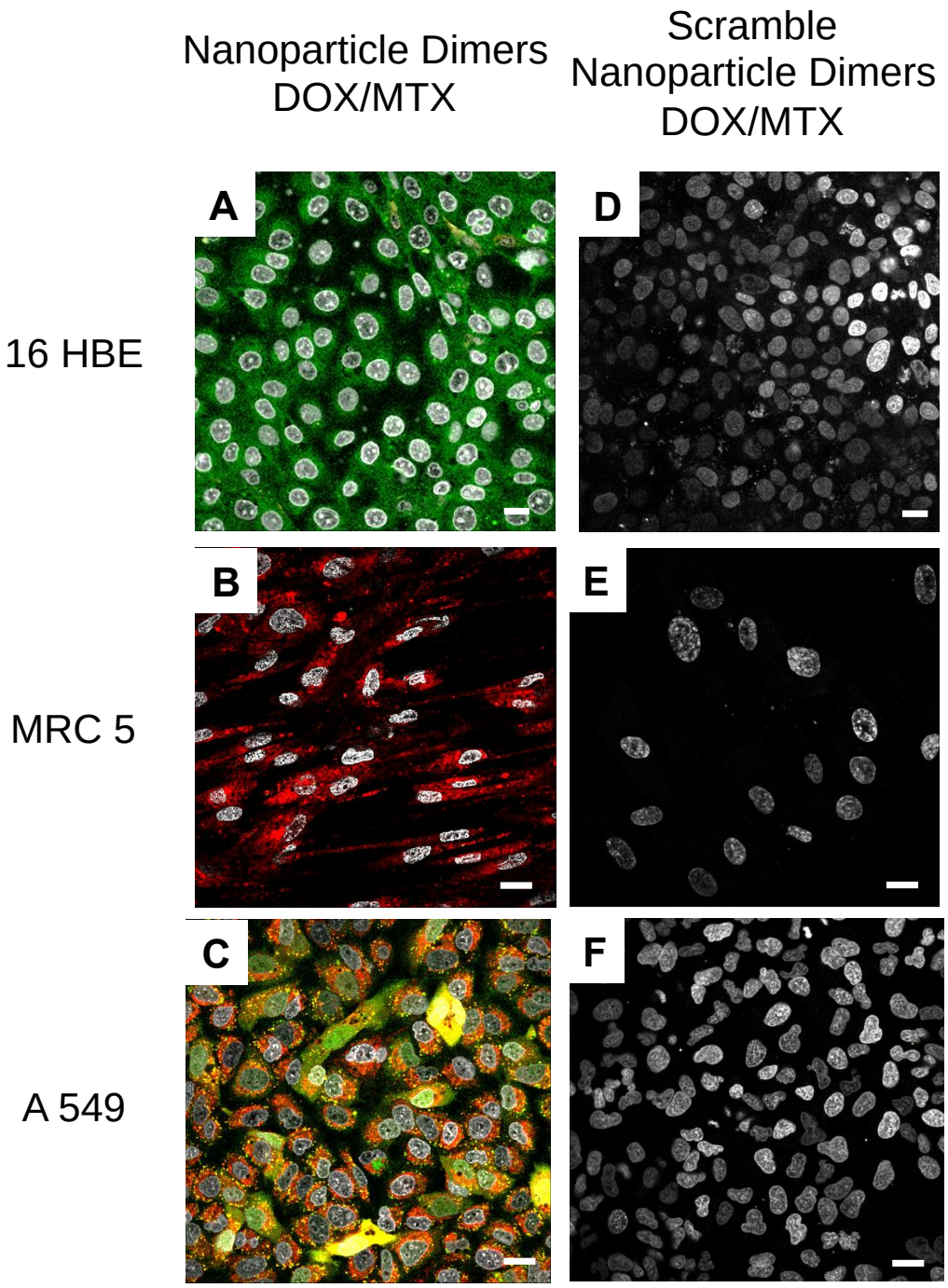

Figure 5.19 Confocal microscopy images of live cells incubated with AuNP dimers. The AuNP dimers were loaded with DOX and MXT (A, B and C). The 16 HBE cells showed release of only DOX, corresponding to the presence of keratin 8 mRNA. In MRC 5 cells

MTX was released, corresponding to the presence of vimentin mRNA whereas in A 549 cells both keratin 8 and vimentin mRNA were detected, therefore both drugs MTX and DOX were released. Scrambled AuNP dimers (D, E and F) did not display any fluorescence signal indicating that they retained their drug payload over 18 hours. Color guide: DOX release – green, MXT release – red, nuclear counterstain – white. Scale bar is 15 μm.

5.5.2.1 Cell viability of cells incubated with drug loaded AuNP dimers

Cell viability assays were conducted to determine the effect of drug specific delivery to the cells. The cell viability of all three cell-lines after an 18 h incubation period was evaluated using trypan blue as shown in Figure 5.20. A range of conditions was tested, including AuNP dimers with and without drugs, scrambled AuNP dimers loaded with drugs and free DOX and MXT in cell culture media.

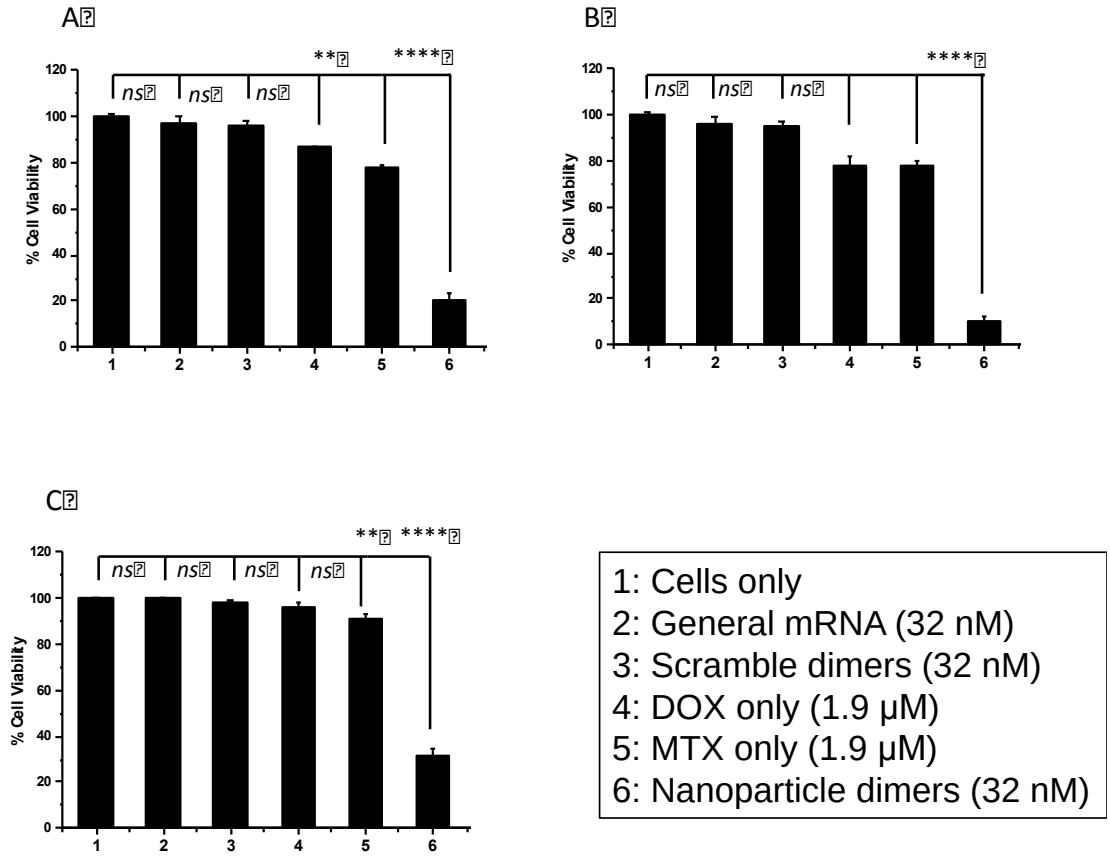

Figure 5.20 Trypan blue cell viability assay of (A) 16 HBE (B) MRC 5 and (C) A 549 cells incubated with the AuNP dimers. Cells were also incubated with nanoparticles sensing all mRNAs (gmRNA) to establish whether the nanoparticle concentration was toxic to cells. They were also incubated with scrambled 'non-targeting' sequences loaded with DOX or MXT. Cell viability was also assessed after the incubation of cells with free DOX and MXT. Data are shown as mean ± SEM (n=3). P-values were determined by a one-way ANOVA. *$p < 0.05$, ****$p<0.0001$

While the AuNP dimers without drugs did not exhibit any toxicity, once loaded with the drugs a dramatic reduction in viable cells was observed for probes bearing specific mRNA sense strands. 16 HBE cell lines showed a

decrease in viability of over 80 % when incubated with the nanoparticle dimers while the viability of the MRC 5 cells' was reduced by up to 92 % (Figure 5.20 **A and B)**. On the other hand, in A 549 cancerous cells the decrease in cell viability was at 70 %. Although one would expect that A 549 cells would be less viable because of the release of two drugs in cells at the same time, this was not observed in our experiments. This observation may be supported by recent literature which states that lung cancer cells, such as A 549 cells, overexpress cytoprotective transcription factors thus exhibiting an increased resistance to anticancer drugs.[264]

Moreover, in order to prove the specificity of the AuNP dimers, all three cell-lines were also incubated with scramble AuNP dimers loaded with either DOX and MXT. In each case, no significant decrease in cell viability was observed. When using high concentrations of free DOX or MXT that had not been loaded onto a nanoparticle carrier, a reduction of viability of around 20 % was observed, much less than when administering these drugs within the AuNP dimers. These observations emphasize the specific and efficient delivery of DOX and MTX when using the AuNP dimer platform.

The mechanism responsible for the cytotoxic effects observed following specific drug release has been the subject of considerable research. Multiple mechanisms of action have been proposed for DOX with one of the earliest studies describing inhibition of DNA biosynthesis as one possible mode of action.[265] Kim *et al.* demonstrated inhibition of both DNA and RNA syntheses in Hela cells at concentrations as low as 0.2 μM.[266] The potential involvement of free radical formation in the observed cytotoxicity has also been mentioned where the quinone structure permits DOX to act as an electron acceptor in reactions mediated by oxoreductive enzymes such as NADH. The electron addition converts

quinones to semiquinone free radicals, which may induce free radical injury to DNA.[267, 268] However, one of the most prominent mechanism of action is thought to be related to the inhibition of topoisomerism II (top2).[269] Top2 is important for ensuring genomic integrity and plays a critical role in DNA replication, transcription and chromosome segregation. DOX is thought to lead in increases in the levels of top2/DNA covalent complexes, leading to DNA strand breaks.[270]

MTX, on the other hand, has a similar mechanism of action to DOX. The drug inhibits cellular RNA and DNA synthesis and causes chromosomal aberrations due to its ability to bind single and double stranded RNA and DNA. Furthermore, as with DOX, MTX has been firmly established as a DNA top2 poison and has been demonstrated to cause DNA/protein cross-links which are highly toxic DNA lesions.[271, 272]

Chapter 6 – Results and discussion on the intracellular fate of DNA-coated AuNPs

DNA-coated AuNPs represent and emerging tool that have been used on an array of biomedical applications including intracellular diagnostic assays, drug delivery and gene knockdown.[93, 111, 143] The remarkable success they have shown in the aforementioned applications is due to the fact that despite their polyanionic nature they are capable of traversing the negatively charged membrane, without the need for a transfection agent, leading to successful intracellular accumulation in a plethora of cell lines. Moreover, the 3D arrangement of oligonucleotides on the AuNP surface is thought to protect this system from degradation by nucleases thus making them appealing candidates for live cell applications.

In **Chapter 5** we demonstrated that with careful design, DNA-coated AuNP assemblies could be synthesised capable of performing multiple synergistic functions including specific mRNA detection as well as targeted drug delivery. However, little is known about the intracellular fate of DNA-coated AuNPs following cellular uptake. By understanding the interactions between these systems and living cells particle design could be further developed leading to optimised processes such as AuNP uptake or endosomal escape, which could have unprecedented benefits for arising diagnostic and therapeutic applications.

This chapter will therefore focus on the intracellular fate of DNA-coated AuNPs following intracellular uptake. Their intracellular location will be addressed as well as the possible location of flare release due to mRNA sensing. Finally, the use of a novel microscopy setup capable of imaging

both the AuNP core as well as the fluorescence from the released flare strand will be described.

6.1 Intracellular location of DNA-coated AuNPs

Recently the intracellular fate of particles and more specifically DNA-coated AuNPs after cellular uptake has been the focus of a vast number of studies. Research by Mirkin *et al.* investigating the intracellular fate of DNA-coated AuNPs suggested that after 1-2 h of incubation with cells nanoparticles are primarily localized in early endosomes. After the 4th h of incubation nanoparticles were found to be located in late endosomes where they were found to largely reside after a 24 h period and did not traffic beyond this point. Furthermore, no appreciable co-localization was observed between DNA-coated AuNPs and lysosomes or the trans-Golgi network. Of these NPs only a small portion was observed to be located within the cytoplasmic region, having escaped the late endosomes, and are thought to be responsible for any effect observed (such as gene silencing or mRNA detection).[213] Similar observation were made by Rotello *et al.* who found that 1-2 % of DNA-coated AuNPs escaped into the cytosol from the late endosomes.[210]

Although it has been shown that several types of functional nanoparticles, mainly coated by peptides or other transfection agents, can escape endosomes following endocytosis *via* various ways, a mechanism for the process of endosomal escape has not been reported yet.[213, 273, 274] Nevertheless, experiments previously reported by our group and others indicated that DNA-coated AuNPs are highly specific for the detection of endocellular mRNAs as well as for the release of DNA-intercalating drugs as also described in **Chapter 5**.[128, 138, 139, 150]

We have previously shown that DNA-coated AuNP dimers after an 18 h incubation period reside in late endosomes and multivesicular bodies with only a small percentage showing a cytoplasmic distribution. In order to probe whether intracellular location is structure dependant, single DNA-coated AuNPs were incubated with 16 HBE and MRC 5 cells for 18 h after which ultra thin section of cells were cut and analysed *via* TEM.

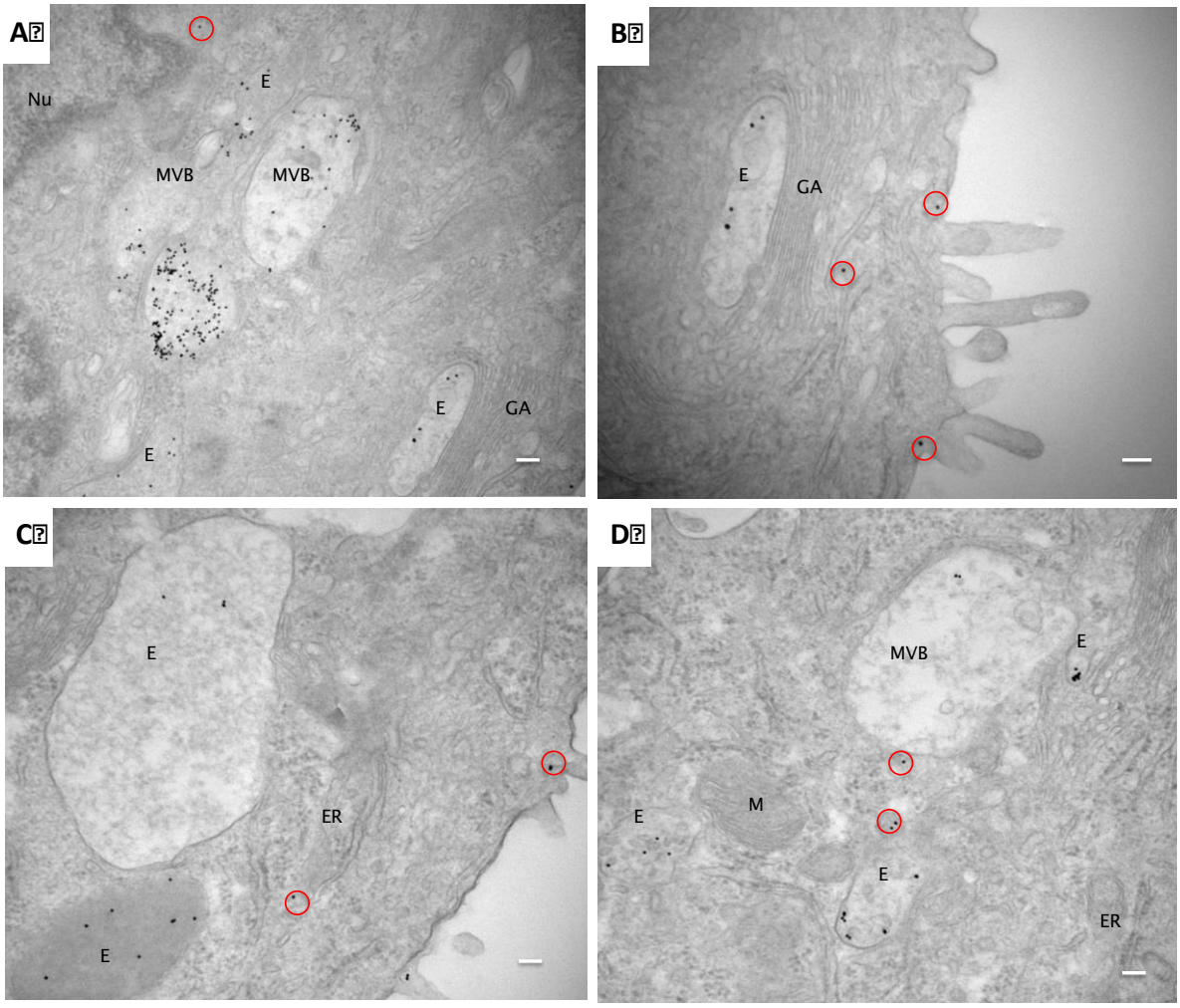
A
Nu
E
MVB
MVB
E
GA
E
B
E
GA
C
E
ER
E
D
MVB
E
M
E
E
ER

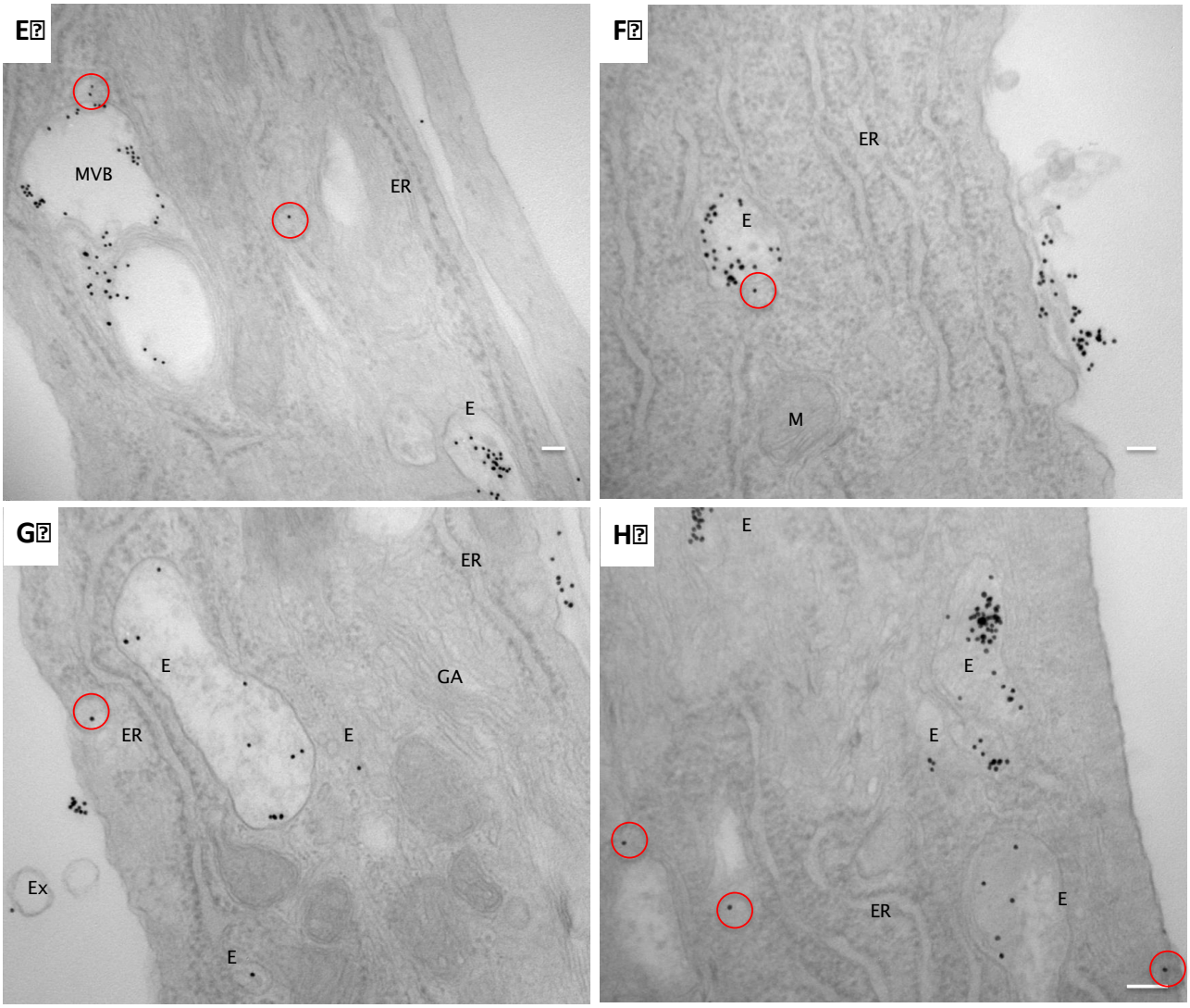

Figure 6.1 TEM images of cells incubated with the single DNA-coated AuNPs for 18 h. (A – D) show sections of 16 HBE cells, whereas images (E – H) show sections of MRC 5 cells. ER: Endoplasmic Reticulum, E: Endosomes, M: Mitochondria, GA: Golgi Apparatus, Nu: Nucleus, MVB: Multi Vesicular Body, Ex: Exosome. Red circles indicate DNA-coated AuNPs with a cytoplasmic location. Scale bar is 100 nm.

By analysing multiple TEM grids for each cell line it was determined that approximately 3.94 % of the total uptaken particles were cytosolic for 16 HBE cells compared to 3.44 % for MRC 5 cells after an 18 h incubation period. The small percentage difference observed not only between cell lines but also between structures (single or dimers see **section 5.4.3**) is a strong indication that the same pathway leading to cytoplasmic localisation is followed in each case regardless of cell line or structure. Nevertheless, despite their low abundance it is thought that the particles located within the cells cytosol are responsible for the highly specific effect observed related to both mRNA detection (see **section 5.4**) and targeted drug delivery (see **section 5.5**). However, the biggest question remaining is how does this small percentage of particles escape vesicular entrapment and localise within the cells cytosol?

6.1.1 Investigating the possibility of an alternate cellular uptake mechanism

Even though intracellular uptake as well as targeted mRNA sensing and drug delivery has been confirmed in **Chapter 5,** the mechanism through which DNA-coated AuNPs localise within the cells cytoplasm rather than in vesicular bodies and endosomes has been questioned with endosomal escape being the most likely explanation. Nevertheless, we proceeded to investigate whether these particles followed a different uptake mechanism, bypassing vesicular entrapment.

Recent research into the uptake of nanoparticles has shown that nanoconjugates can undergo various routes of endocytosis depending upon their physiochemical characteristics such as their charge, size and composition, the cell type tested and the properties of the suspension medium.[231, 275-283] For example it has been found that serum

proteins such as BSA and transferrin, that are found in common cell culture media, can affect cellular internalization of DNA-coated AuNPs. The formation of a protein corona could alter the surface chemistry that is presented to the cell therefore, impacting cellular uptake.

A recent study has shown that G-quadruplexes on the AuNP surface increases the adsorption of proteins over time leading to a higher cellular uptake compared to the corresponding poly T SNAs.[284] Studies have also shown that altering the backbone of oligonucleotides also has an effect on cellular uptake. By changing the chemistry of the oligonucleotide backbone Song *et al.* investigated the effect of backbone chirality, hydrogen bonding and the role of aprotic hydrophilic and small lipophilic groups on the cellular uptake efficiency. Their findings suggested that uptake kinetics vary depending on the chemical structure of the oligonucleotide sugar backbone where DNA-coated AuNPs with increased lipophilicity displayed the highest cellular uptake.

Apart from altering the surface chemistry the effect of size and shape were also investigated. Rod shaped nanoparticles showed a lower cellular uptake than their spherical counterparts, which showed the highest uptake rate with 50 nm DNA-coated AuNPs. Mirkin and co-workers also investigated the mechanism of endocytosis of DNA-coated AuNPs. They reported that NP association with cells occurred within the first 5 minutes and continued to increase at a slower rate over 30 minutes. They determined three key events that define the endocytosis of DNA-coated AuNPs: i) binding to cell membrane, ii) uptake via invaginations and iii) sorting into early endosomes.[285] Data presented by Mirkin and co-workers however, concluded that lipid rafts or more specifically caveolae significantly mediated endocytosis. Their research also suggested that endocytosis was energy dependant leading to speculations that cell

surface receptors present supported binding of DNA-coated AuNPs whose 3D oligonucleotide arrangement contributed to their high binding affinity. DNA-coated AuNPs were found to bind to scavenger receptors (SRs) ten times more strongly than ssDNA with class A SR mediating endocytosis rather than class B.[284, 285]

However, we hypothesised that the small percentage of DNA-coated AuNPs located within the cytoplasm could have been able to bypass active transport and could have been internalised *via* a passive mechanism. This hypothesis was tested by cooling 16 HBE and MRC 5 cells down to 4 °C and maintaining this temperature up until fluorescence imaging. Reports have suggested that at this low temperature cellular uptake decreases as energy dependant uptake is blocked.[286, 287] Therefore if cytoplasmic particles follow an alternate route to active transport a fluorescence signal would still be observed after incubation at 4 °C.

16 HBE and MRC 5 cells were incubated with DNA-coated AuNPs designed to detect all mRNA (gmRNA) at both 4 and 37 °C and imaged *via* confocal microscopy.

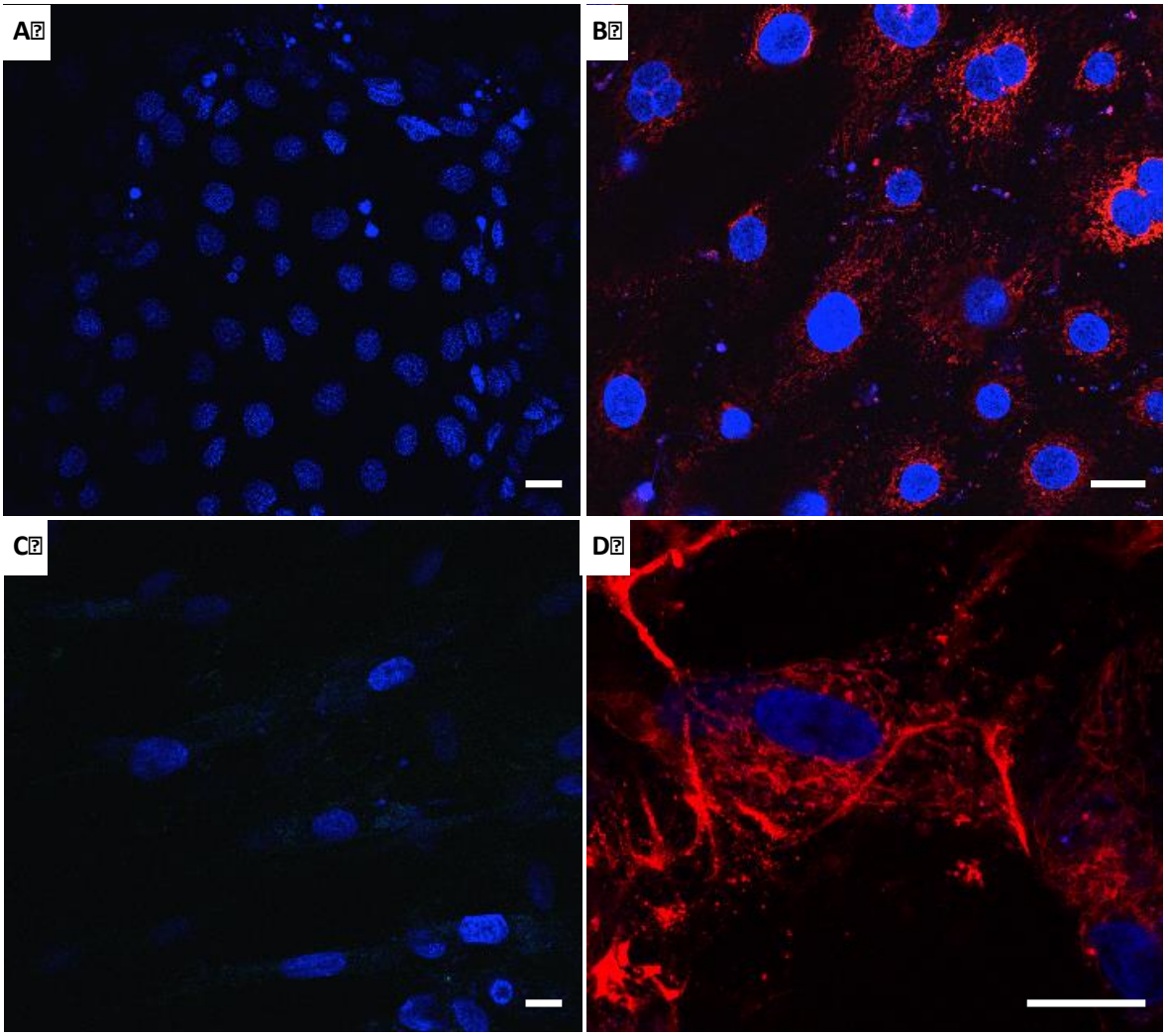

Figure 6.2 Confocal microscopy images of 16 HBE (A and B) and MRC 5 (C and D) cells incubated with gmRNA DNA-coated AuNPs at 4°C (A and C) and at 37 °C (B and D). Colour guide: Nuclear counterstain (Hoechst) – blue, gmRNA flare release – red. Scale bar is 15 μm.

From the images presented in Figure 6.2 it is noticeable that at 4 °C there is no fluorescence signal detected when compared to the cells that were incubated with nanoparticles specific for the detection of gmRNA at 37 °C. This suggests that DNA-coated AuNPs do not enter cells *via* passive

diffusion. Therefore, endosomal escape was concluded to be the most possible mechanism that leads to particles residing in the cytoplasm.

6.2 Investigating the kinetics and location of mRNA detection

Previous studies focusing on the intracellular location of DNA-coated AuNPs (see **section 5.4.3 and 6.1**) have lead to the conclusion that cytosolic DNA-coated AuNPs are most probably responsible for both specific mRNA detection as well as targeted drug delivery observed with endosomal escape being the most likely mechanism through which cytoplasmic accumulation is achieved. Moreover, similarity in results between cell lines suggests that the same pathway of uptake and escape is followed regardless of the type of cell line being investigated. However, important questions such as when does endosomal escape take place and can mRNA detection occur within endosomes still need to be addressed.

6.2.1 Time lapse imaging of live cell mRNA detection

As previously mentioned one important question that has been raised is at what time point after incubation with DNA-coated AuNPs does endosomal escape potentially take place. To determine this, live 16 HBE cells were imaged over a period of 18 h after initial incubation with nanoparticles specific for the detection of gmRNA where flare release corresponding to mRNA detection was evaluated *via* confocal microscopy Resulting images are depicted in Figure 6.3.

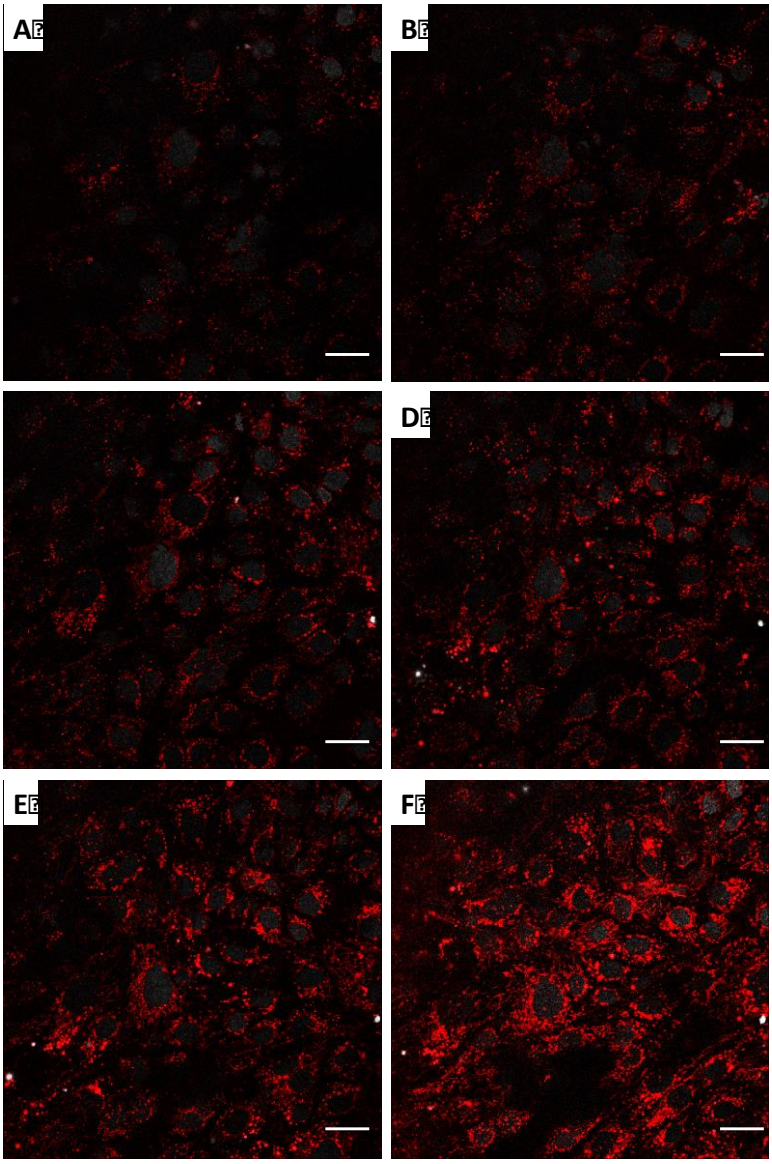

Figure 6.3 Fluorescent time lapse study of live 16 HBE epithelial cells incubated with DNA-coated AuNPs specific for the detection of gmRNA. Confocal microscopy images show flare release after 3 (A), 6 (B), 9 (C), 12 (D), 15 (E) and 18 h (F) post incubation. Colour guide: Red – gmRNA flare release. Scale bar is 15 μm.

From the time lapse images shown in Figure 6.3 one can see that up to 3 h post incubation a faint fluorescence signal is detectable with a slight signal

increase being observed at 6 h. A gradual increase in the fluorescence signal corresponding to flare release is detected after 6 h of incubation with a maximum signal being detected 18 h after incubation with 16 HBEs. The slow increase in fluorescence intensity due to mRNA detection and flare release proves that there is a potential gradual increase of DNA-coated AuNPs present within the cytosol that are able to act as mRNA sensors. This is most likely due to the continuous uptake of nanoparticles by the cell, which are transported into late endosomes prior to endosomal escape.

However, in order to shed more light on the cellular location of mRNA sensing a more in depth study is needed to verify that mRNA detection does not occur in endosomal compartments.

6.2.2 Live cell organelle staining

The flare release study described in **Section 6.2.1** indicates the rough time point of flare release due to mRNA detection. However, to verify that endosomal escape occurs it is necessary to prove that flare fluorescence is not observed within endosomal compartments. In order to test this, endosomes both early and late as well as mitochondria were labelled with a fluorescent dye to allow for co-localisation studies.

To date, previous studies have relied on antibody staining to label and image endosomal compartments in fixed cells.[288] However, this labelling technique cannot be performed in the live cell. For our research endosomes and mitochondria were labelled under live conditions by using a transfection technique known as the BacMam method.

The BacMam technology is based on dsDNA insect viruses known as baculoviruses as vehicles to efficiently deliver and express genes in mammalian cells with no cytotoxic effects. They are easily up taken by a number of mammalian cell types and they are non-replicating in mammalian cells unless a mammalian recognizable promoter is incorporated upstream of a gene of interest. In order to introduce genes of interest into mammalian cells BacMam particles are taken up by endocytosis and subsequently released for transcription and expression after migrating to the nucleus. Using this technology early and late endosomes as well as mitochondria were labelled in the live cell at real time in both 16 HBE and MRC 5 cells as seen in Figure 6.4.

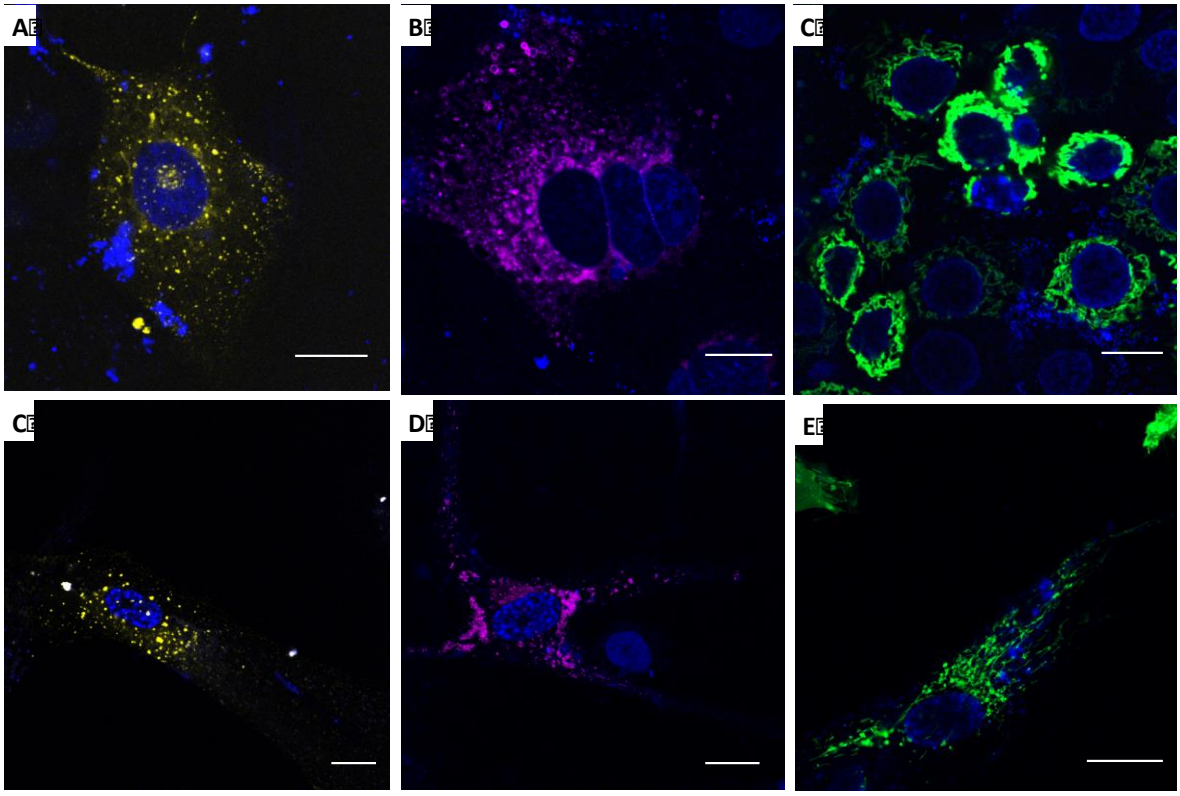

Figure 6.4 Confocal microscopy images of early (A) and late endosomes (B) as well as mitochondria (C) in 16 HBE cells. Images D, E and F show early and late endosomes and mitochondria respectively in MRC 5 cells. All images were taken 24 h post transfection. Colour guide: Nuclear counterstain – blue, early endosomes – yellow, late endosomes – pink, mitochondria – green. Scale bars are 15 μm.

Having established that intracellular organelles can be labelled successfully we proceeded with co-localisation studies where endocellular compartments and mitochondria were imaged along with flare release corresponding to the detection of all cellular mRNA (gmRNA). Co-localisation studies were first performed in MRC 5 cells as seen in Figure 6.5.

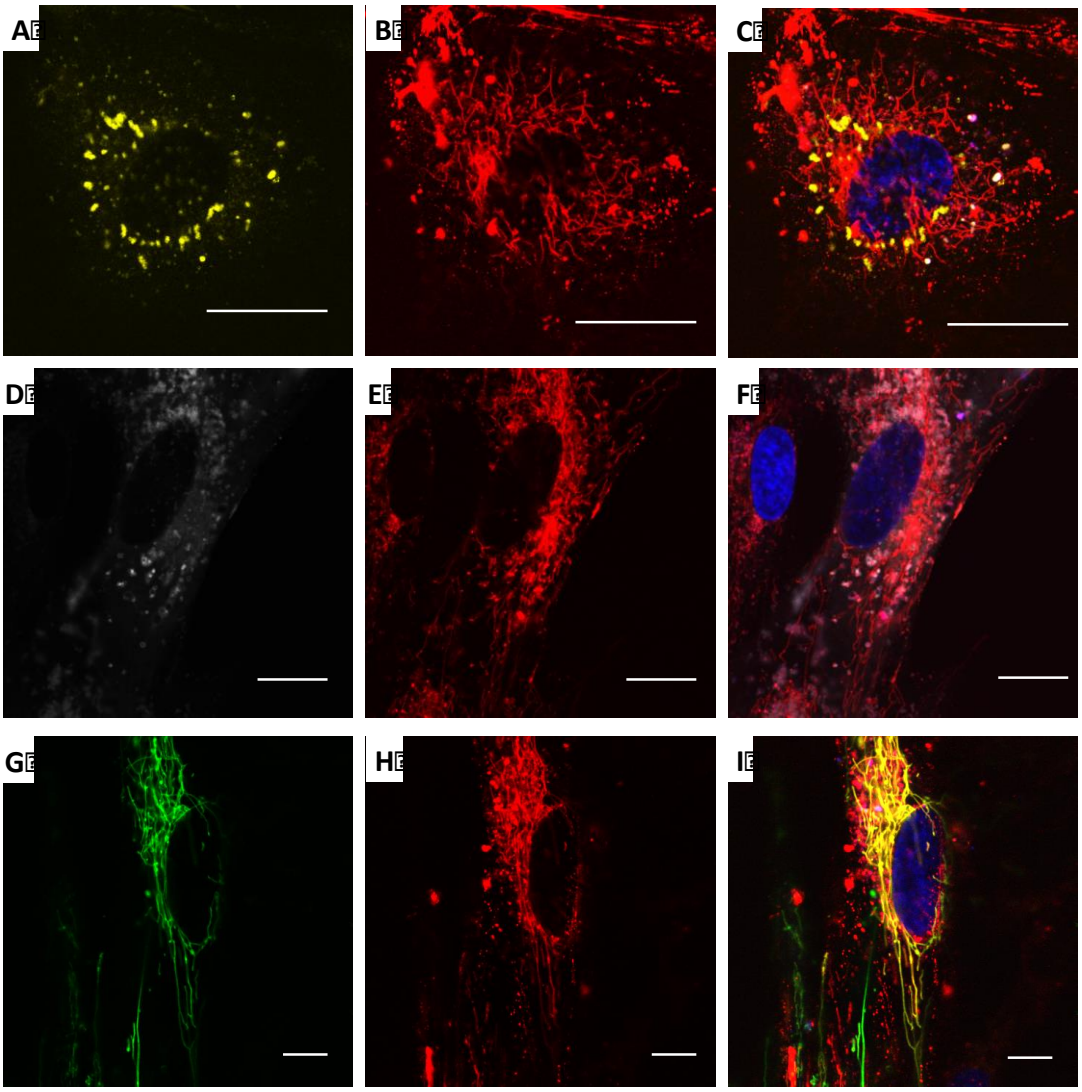

Figure 6.5 Representative confocal microscopy images of live MRC 5 cells transfected with early (A – C) and late endosomal (D – F) stains as well as mitochondrial stains (G – I). Fluorescence corresponding to flare release due to the detection of all cellular mRNA was simultaneously imaged. Channels corresponding to organelle stains (A, D and G) and flare release (B, E and H) have been separated for clarity. Colour guide: Nuclear counterstain – blue, flare release – red, early endosomes – yellow, late endosomes – white and mitochondria – green. Scale bars are 15 μm.

From the images presented in Figure 6.5 as well as further z stack images in **Appendix A B.3.2** no significant co-localisation was observed between flare release and early and late endosomes. However, flare release does appear to be in close proximity to endosomes. This could indicate that mRNA detection occurs immediately after endosomal escape. One important observation made during our studies was the significant co-localisation between the fluorescence corresponding to flare release and mitochondria. In order to determine the significance of these results the same experiment was performed in 16 HBE cells as see in Figure 6.6.

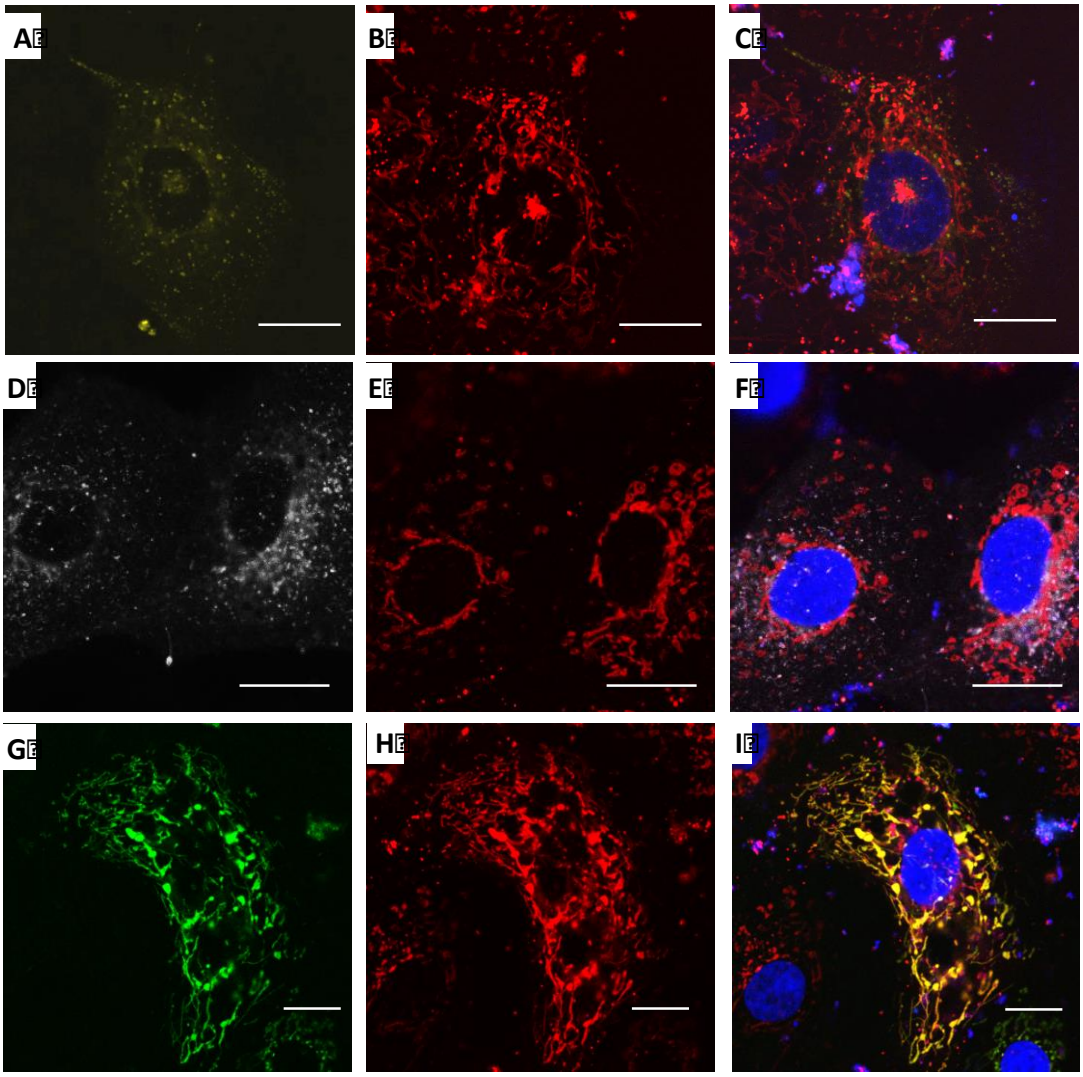

Figure 6.6 Representative confocal microscopy images of live 16 HBE cells transfected with early (A – C) and late endosomal (D – F) stains as well as mitochondrial stains (G – I). Fluorescence corresponding to flare release due to the detection of all cellular mRNA was simultaneously imaged. Channels corresponding to organelle stains (A, D and G) and flare release (B, E and H) have been separated for clarity. Colour guide: Nuclear counterstain – blue, flare release – red, early endosomes – yellow, late endosomes – white and mitochondria – green. Scale bars are 15 μm.

Once again by closely examining confocal microsocopy images as well as z stacks (see **Appendix B B.3.2**) no co-localisation with early and late endosomes was observed with flare release being found on imaging planes either above, below or adjacent to endosomes. However, as with MRC 5s fluorescence corresponding to flare release also shows distinct localisation, corresponding to association with mitochondria. A study by Bao *et al.* showed that 2'-deoxy and 2'-O-methyl oligonucleotides labelled with Cy dyes show co - localisation of fluorescence with mitochondria. Their research suggested that accumulation, which is highly specific to the type of dye, is mediated by the mitochondrial membrane potential.[289] It is therefore, a likely possibility that after mRNA detection flare strands labelled with Cy dyes are trapped within this inner mitochondrial membrane resulting in the filament florescence pattern observed in both confocal images of MRC 5s and 16 HBEs (see Figure 6.5 and Figure 6.6). We therefore concluded that due to the absence of any co-localisation with early or late endosomes, mRNA detection occurs in the cytoplasm following endosomal escape where the released flare localises within the mitochondrial membrane, which explains the significant co-localisation of fluorescence corresponding to the dye modified flare strand and cellular mitochondria. However, in order to completely assess the intracellular fate or DNA-coated AuNPs, imaging of the gold core as well as flare release would be of substantial interest.

6.3 Two photon photoluminescence (TPPL) of AuNPs in vitro

AuNPs and more specifically AuNP spheres have been widely used in a variety of biomedical applications due to the ease of surface modification with a number of different capping ligands including oligonucleotides.[1, 3, 87, 111, 150, 290] As shown in **Chapter 5** 15 ± 1 nm spherical AuNPs

were successfully used as scaffolds for the 3D arrangement of sensing oligonucleotides into an oligonucleotide shell surrounding the AuNP surface.

However, AuNPs also possess unique optical properties, which could be taken advantage of when studying their intracellular fate following incubation and uptake. AuNPs apart from displaying localized surface plasmon resonance (LSPR), which arise from the collective oscillation of conduction band electrons upon interaction with light irradiation have also been observed to display TPPL. As with the LSPR, TPPL properties of noble metal AuNPs including AuNPs have been known to strongly depend on the shape of nanoparticles.[13, 291] It is a powerful bio-imaging technique that allows for the non-invasive imaging of AuNPs in cells or tissue with a high penetration depth and less photodamage.[292, 293] This unique property of nanoparticles was therefore further explored in order to investigate whether the gold core and fluorescence due to flare release could be imaged simultaneously within cells

6.3.1 TPPL of anisotropic AuNPs

Prior to the development of a microscopy setup capable of performing dual imaging, the TPPL properties of particles synthesised within the lab in a cell free environment were investigated. It has been suggested that application relying on the TPPL of metal nanoparticles are limited by their weak TPPL signals. Nevertheless, anisotropic nanoparticles or nanoparticles with sharp tips have been found to display much stronger TPPL signals due to lightening rod effect.[67, 294] We therefore initially tested the TPPL properties of AuNRs (see **section 4.1.3**) and branched AuNPs (see **section 4.1.2**).

6.3.1.1 Microscopy setup

Two photon excitation employs two photon absorption where two photons of comparably lower energy than needed for one photon excitation can excite a AuNP. Each photon carries approximately half the energy required to excite the particle, however, the probability of near simultaneous absorption of two photons is extremely low. A femtosecond (fs) pulsed laser was therefore used which provides a high flux of photons [295].

For the setup built (as seen in Figure 6.7) a Yb:KGW fs-pulsed laser was used. This gave an output of 184 fs pulses at 1030 nm with a 75 MHz repetition rate.

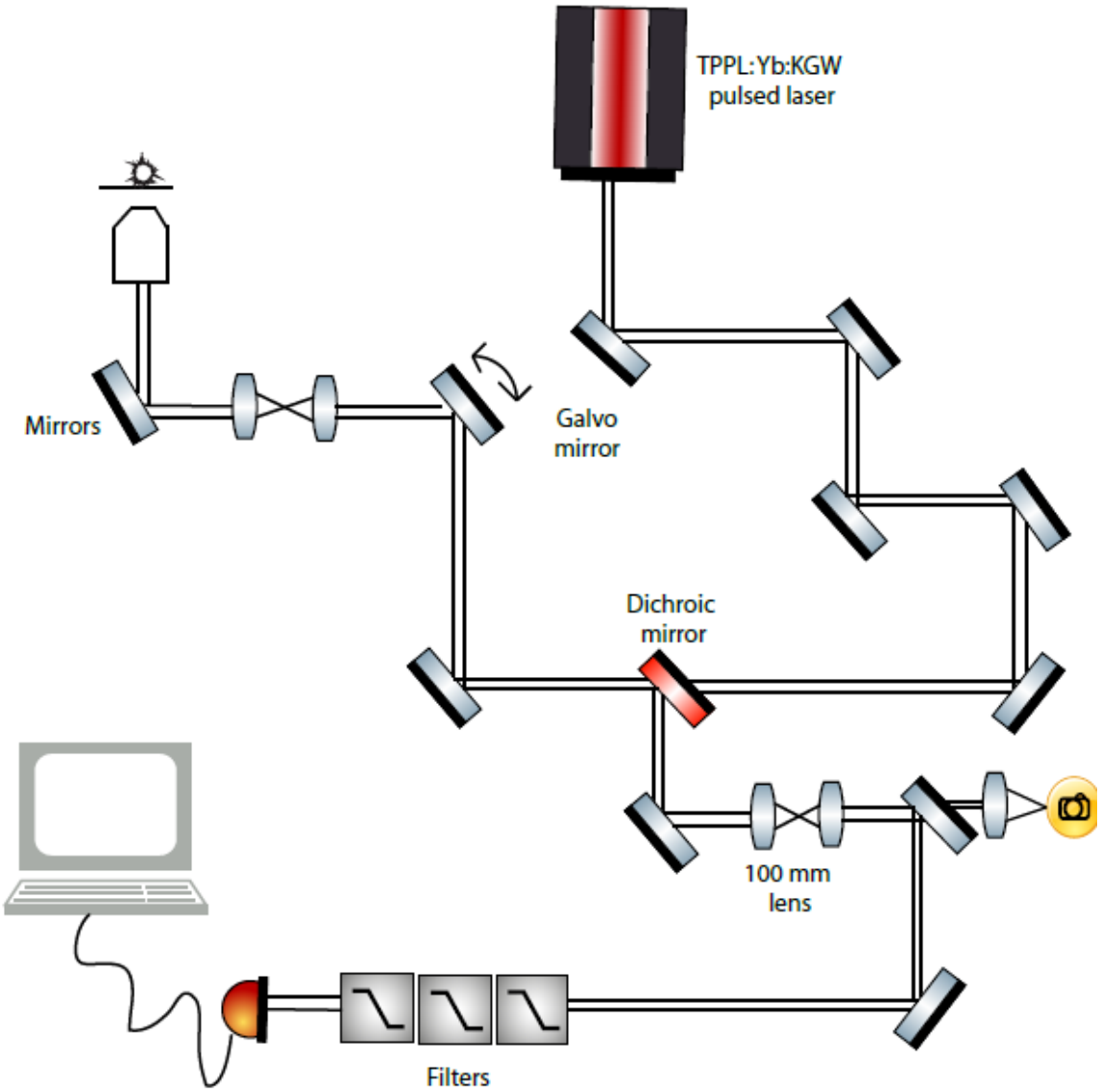

Figure 6.7 Diagram of laser setup built for TPPL. The laser light is directed through a number of mirrors into the objective and up to the sample, which in this case. The scattered light is then directed either to a camera or to a detector giving rise to a TPPL image.

6.3.1.2 TPPL of AuNRs

AuNRs as previously mentioned have recently been found to display strong TPPL. The observed TPPL can be attributed to enhanced local field arising from the longitudinal plasmon resonance of these nanostructures at the wavelength range coincident with the excitation wavelength.[295] The home-built two photon optical microscope presented in Figure 6.7 was used to image gold nanorods that were found to be 60 nm in length with an aspect ratio of 3.2 and a longitudinal peak maximum at 720 nm (see **section 4.1.3**). A representative TPPL image of gold AuNRs dried on a carbon coated TEM grid is presented in Figure 6.8.

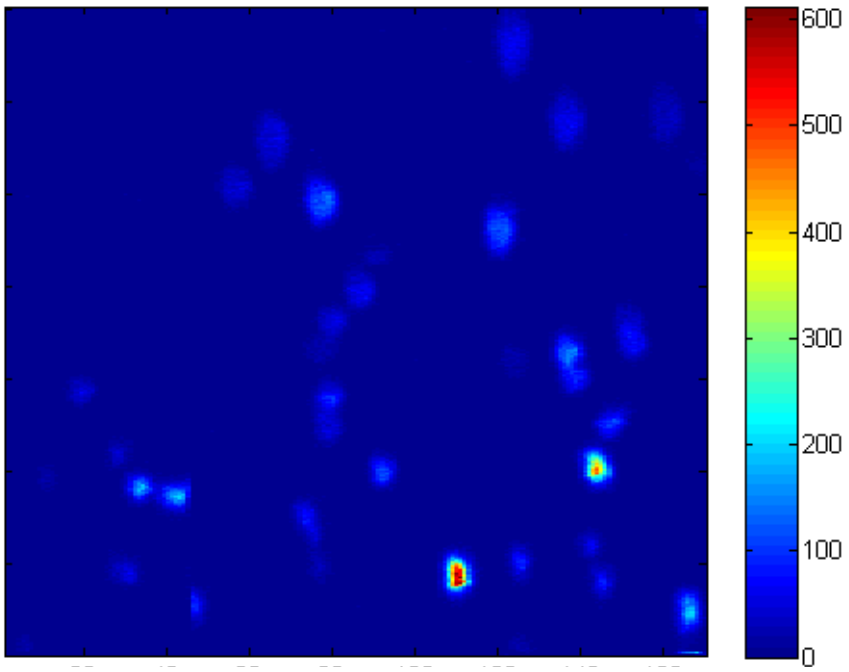

Figure 6.8 TPPL image of a dilute gold nanorod solution deposited onto a carbon coated TEM grid. Each bright spot in the image is thought to represent a small cluster of gold nanorods deposited onto the grid.

Recent research has focused on trying to understand the excitation nature of strong TPPL in gold nanorods with two possible excitation mechanisms being proposed. The first involves a coherent two-photon absorption model, which involves the simultaneous absorption of two photons through a virtual intermediate state. The second proposed model assumes that the excitation process involves two sequential one-photon absorption steps that are mediated by a real intermediate step. The first photon induces an sp ➔ sp intraband transition to create an s electron above the Fermi level. The second photon excites an electron from the d band to the sp band creating a hole in the d band which can then recombine radiatively with the electron in the sp band giving rise to a TPPL signal.[65, 66, 296, 297] Nevertheless as for now, the exact mechanism for TPPL in gold nanorods is till not conclusive.

6.3.1.3 TPPL of branched AuNPs

As with AuNRs, branched AuNPs display strong TPPL with recent research into the shape dependence TPPL suggesting that branched AuNPs display the strongest TPPL out of all nanoparticle shapes.[67] As seen in **section 4.1.2** gold branched nanoparticles display a broader spectrum with overlapping bands, which can be ascribed to multiple plasmon modes arising from the various tips.[41, 298] These sharp tips can be found in different lengths and orientations, which can be different for single particles. Another important property of branched nanoparticles is their tendency to form aggregates when dried on a TEM grid, which has been found to result in enhanced TPPL.[67] We therefore performed a more thorough study of the resulting TPPL of synthesised branched AuNPs (see **section 3.1.3** for experimental details). Branched AuNPs were deposited on a marked TEM grid, which was imaged on our home-built microscope setup as well as on a TEM and a light microscope as seen in Figure 6.9.

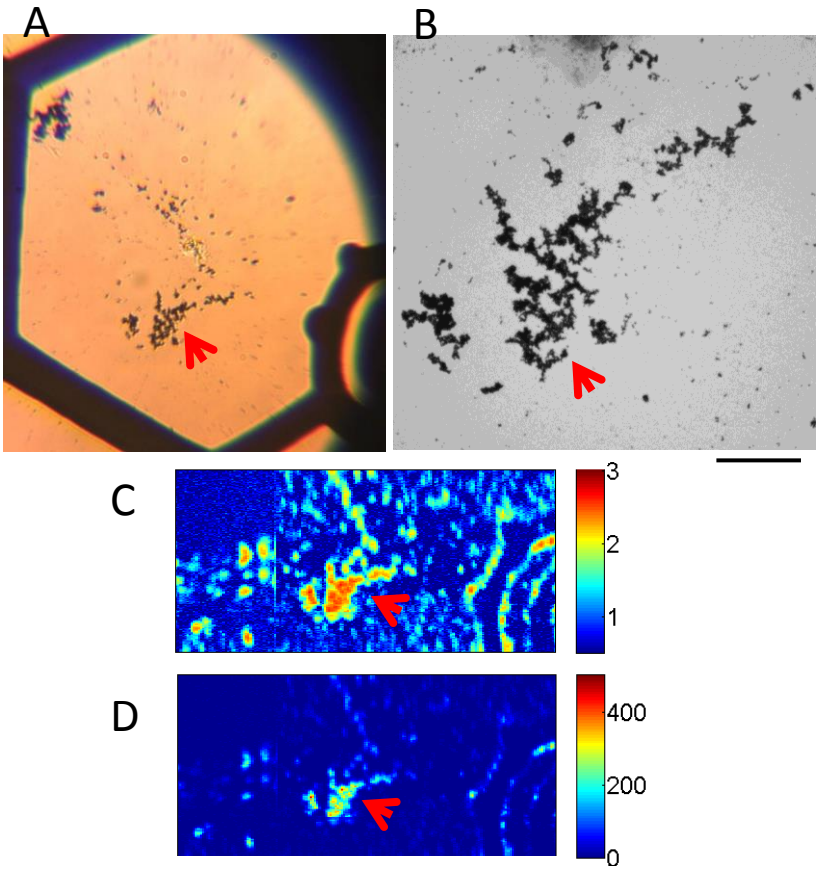

Figure 6.9 Aggregated branched nanoparticles imaged using light micrsoscopy (**A**), TEM (**B**) and the TPPL setup built (**C**: log scale and **D**: linear scale). A distinct curved shape was observed on the grid in each case (indicated by the red arrows). Through TEM it was confirmed that this pattern was indeed made up of aggregated branched nanoparticles indicating that the scattering observed (**C** and **D**) originated from the gold branched nanoparticles. This proved that the setup built could successfully detect nanoparticles.

As seen in Figure 6.9 a strong TPPL signal corresponding to branched AuNPs was imaged. The strong TPPL observed for branched shaped

particles is thought to be due to the sharp edges of the multiple tips. These edges can concentrate charges and subsequently enhance the local electric field strength, owing to the lighting rod effect, resulting in significant enhancement of TPPL efficiency.[41, 62, 64, 299] Xu *et al.* studied in detail the role of these sharp tips by intentionally melting branched nanoparticles whilst monitoring changes in their optical properties. Their study found that *via* constant laser irradiation, particles initially went through gradual rounding and shrinking followed by a sudden collapse to the energetically favoured quasispherical shape. During this process TPPL intensity decreased significantly with a final intensity decreasing to only 0.6 % of the initial TPPL intensity recorded thus proving that the sharp tips play an important role in two-photon excitation efficiency.[67]

6.3.2 Combining TPPL and fluorescence microscopy for imaging within cells

Although results shown in **sections 6.3.1.2 and 6.3.1.3** show promising results regarding the imaging of AuNPs based on their TPPL signal in order to image particles *in vitro* within a cellular environment, important aspects such as the ability of cellular uptake as well as cytotoxicity need to be taken into account. The synthesis of both AuNRs (see **section 3.1.2**) and branched AuNPs (see **section 3.1.3**) involves the use of CTAB, which besides causing nonspecific electrostatic interactions with the cell surfaces, can also be cytotoxic, leading to uncontrolled cell death.[300] Therefore surface modification is required before their use within live cells is feasible. AuNRs can be coated with a silica shell (see **section 3.2.2**), rendering them less cytotoxic however for mRNA sensing a shell of sensing oligonucleotides is required. Although oligonucleotide conjugation onto a silica shell is achievable *via* 1-ethyl-3-(3-

dimethylaminopropyl)carbodiimide (EDC) coupling, the success of conjugation can vary depending on the number of hydroxyl groups present on the surface. On the other hand, although 15 ± 1 nm spherical AuNPs can be easily modified, a TPPL signal would be hard to obtain due to their small size. For this study we therefore employed large DNA-coated 43 ± 4 nm spherical AuNPs (see **section 3.1.1.2 and 3.2.1.3** for synthetic protocols) due to the ease of surface modification without the need of prior surface alteration coupled with stronger TPPL. Furthermore, MRC 5 cells were used rather than 16 HBE cells due to the larger surface area occupied per cell.

6.3.2.1 43 ± 4 nm DNA-coated AuNPs for mRNA detection

43 ± 4 nm AuNPs were coated with a shell of sensing oligonucleotides (see **section 3.2.1.3** for protocol of DNA attachment) designed to detect all mature cellular mRNA *via* their distinct polyA tail (see Table 3.2 for detailed oligonucleotide sequence). DNA-coated AuNPs were further incubated with MRC 5 cells and fixed 18 h post incubation (see **section 3.5.2** for experimental details) in order to preserve and stabilise the cell morphology and allow for continuous imaging over a prolonged period of time without the need of special imaging conditions (temperature of 37 °C and continuous supply of CO_2). Prior to imaging of the sample on our home built microscope setup specific for the imaging of fluorescence and TPPL, the sample was initially imaged *via* confocal microscopy to ensure that a fluorescence signal due to mRNA sensing could be detectable. A representative confocal image is shown below in Figure 6.10.

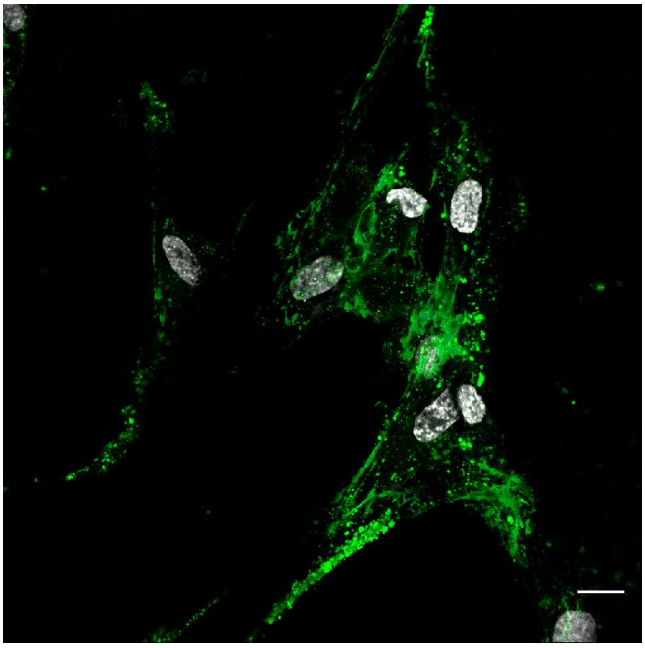

Figure 6.10 Confocal microscopy image of fixed MRC 5 cells incubated with 43 ± 4 nm DNA-coated AuNPs designed to detect all mature cellular mRNA (gmRNA). Colour guide: green – flare release, blue – FAM (dye on sense strand), white – nuclear counterstain. Scale bar is 15 μm.

As can be seen in Figure 6.10 a fluorescence signal corresponding to detection of all cellular mRNA was detected (green colour). The absence of a fluorescence signal from the dye modified sense strand suggested that detection was specific and not due to degradation of surface bound oligonucleotides. After verifying the suitability of the sample it was further imaged on the home-built microscopy setup designed for imaging TPPL and fluorescence.

6.3.2.2 Microscopy setup

TPPL and fluorescence spectra were acquired on an improved home built setup first presented in Figure 6.7. The light source for TPPL was a fianium laser (10 ps, 20 MHz) at a wavelength of 1060 nm whereas for fluorescence measurements a laser source of 532 nm or 405 nm were used for Cy3 (release of flare) and DAPI (nuclear counterstain to image cell nucleus) respectively.

The laser beam was guided through a set of mirrors and lenses to a 60 × objective lens. Emission signal was guided back down through the objective and finally filtered by a 430 nm long pass (LP) and 500 nm short pass (SP) filter (DAPI) or a 550 nm LP filter (Cy3) or a 800 nm SP (TTPL). Depending on the type of measurement the filter was changed accordingly. Images of the setup are presented below in Figure 6.11.

Figure 6.11 Camera images of the home built microscopy setup used for TPPL and fluorescence imaging of MRC 5 cells incubated with 43 ± 4 nm DNA-coated spherical AuNPs designed to detect all mature cellular mRNA.

For clarity a schematic diagram of the setup showing how the laser beam was guided from the laser source, to the sample and back to the detector is shown below in Figure 6.12.

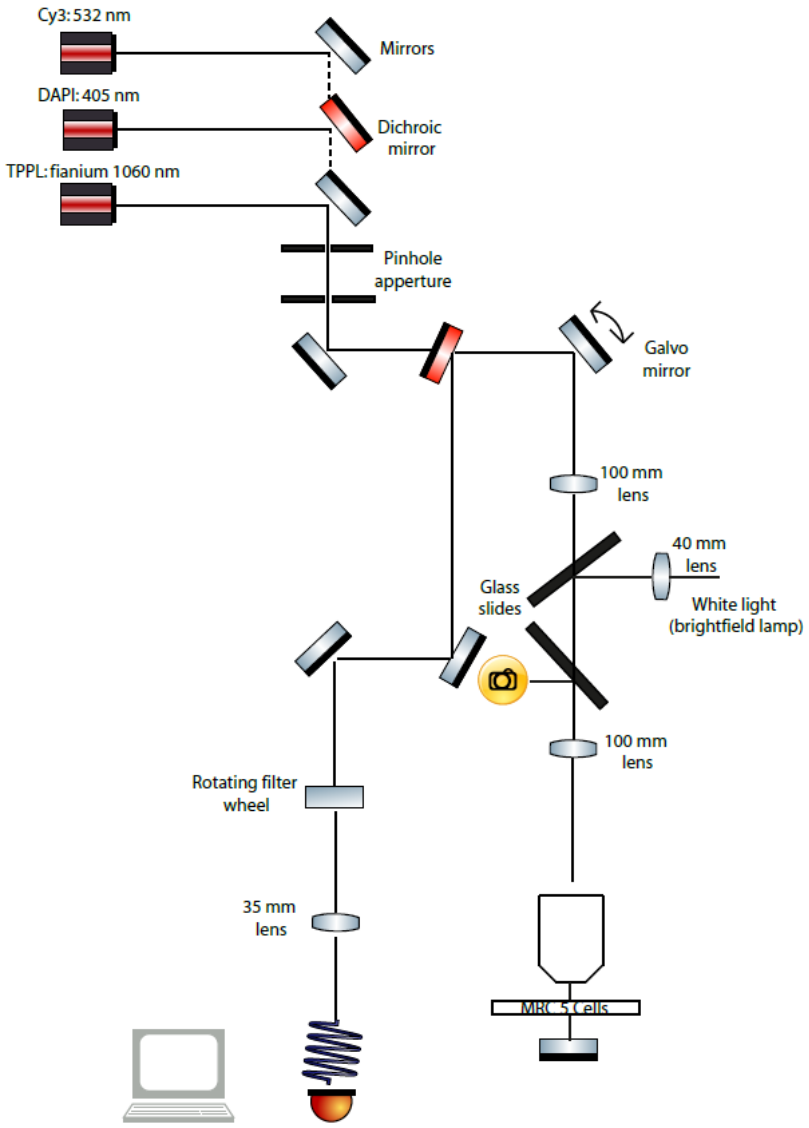

Figure 6.12 Schematic illustration of the microscopy setup used for both TPPL and fluorescence imaging using the MRC 5 cell line.

By using a white light source from a brightfield lamp (annotated in Figure 6.12) a reflection from the surface of the sample could be imaged by guiding the reflected light onto an imaging camera. Figure 6.13 shows the image acquired from the sample surface clearly showing the presence of MRC 5 cells on the surface of the cover slip.

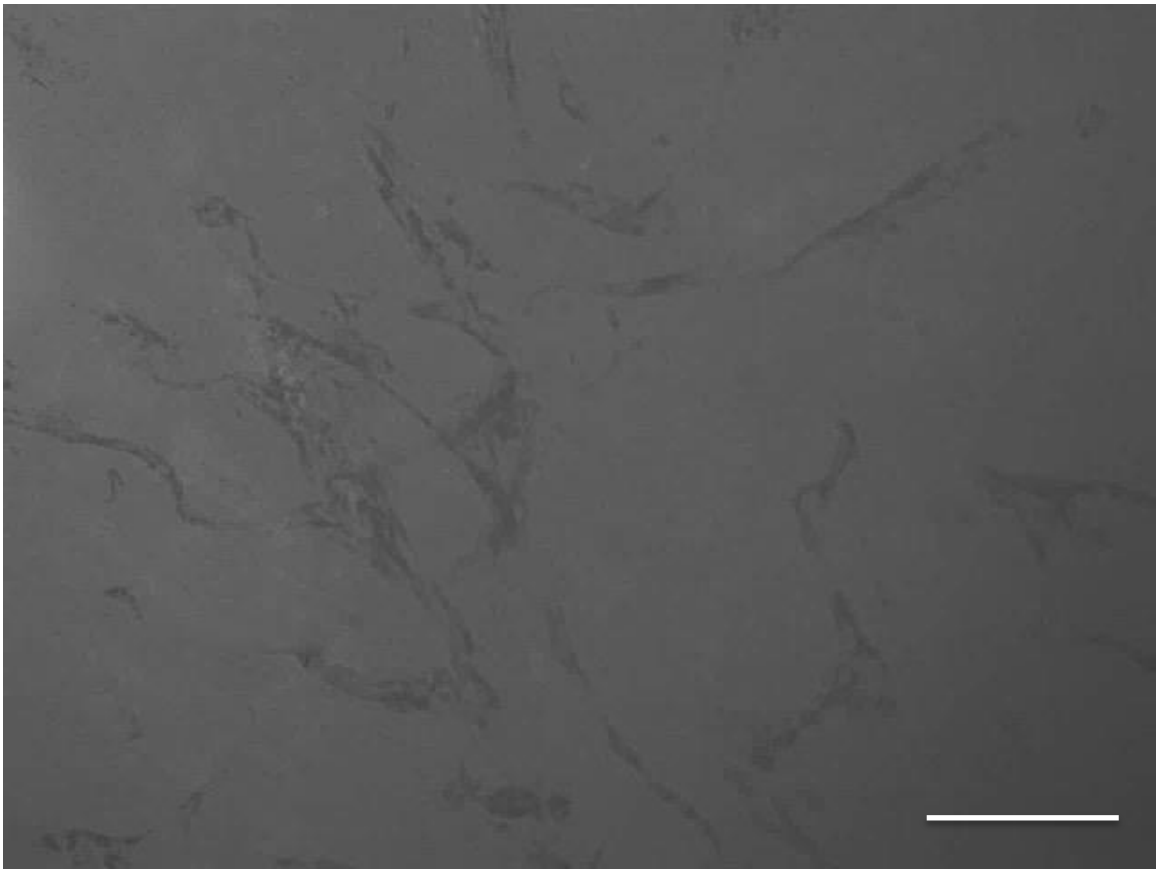

Figure 6.13 Images corresponding to the reflection from the surface of the cover slip clearly showing MRC 5 cells on the surface. Red arrows indicate the presence of individual cells whereas the black arrow points to the presence of AuNPs, which appear to be on the surface of the coverslip and not internalised within a cell. Scale bar is 75 μm.

Once confirming that the setup could successfully be used to image the reflection from the sample surface, the setup was used to further image TPPL and fluorescence corresponding to both Cy3 and DAPI sequentially by using the appropriate laser source and adding the correct filter to the rotating filter wheel as indicated in Figure 6.12**.** Using the correct imaging settings the following spectra were acquired for DAPI, Cy3 and TPPL.

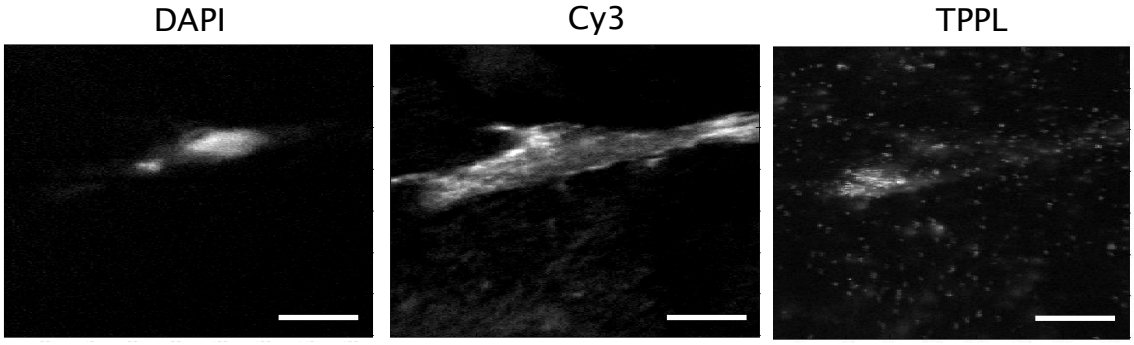

Figure 6.14 Acquired images showing fluorescence from the cell nucleus (DAPI) and from flare release (Cy3) as well as TPPL from the AuNPs. Scale bars are 15 μm.

As can be seen from Figure 6.14 fluorescence from the cell nucleus corresponding to a DAPI signal was clearly imaged. The fluorescence signal showed the characteristic spherical shape of the cell nucleus, which corresponds well with the nuclear shape also imaged on the confocal as can be seen from Figure 6.10**.** This is a strong indication that imaging of the fluorescence signal corresponding to DAPI was successful. Moreover, the Cy3 fluorescence appeared to be located throughout the cell with a stronger intensity being observed at certain sites rather than others. On the other hand a uniform TPPL signal was not imaged throughout the cell with a strong TPPL signal imaged at one position within the cell, which could correlate to clusters of nanoparticles located within multivesicular

bodies or endosomes (either early or late). However, weaker TPPL signals that may correspond to individual nanoparticles were also imaged. These were located both within the cell as well as extracellularly from AuNPs that have been exocytosed or are about to be taken up. As the Cy3 signal was diffuse throughout the cell, co-localisation studies were not possible however single TPPL signals imaged within the cell as well as a Cy3 signal that shows no overlap with AuNP TPPL is a strong indication that some particles are most likely located within the cytoplasm of the cell and not entrapped in a cellular vesicle. Images presented in Figure 6.14 were also overlapped (by taking images from one z plane) for more clarity as shown below in Figure 6.15.

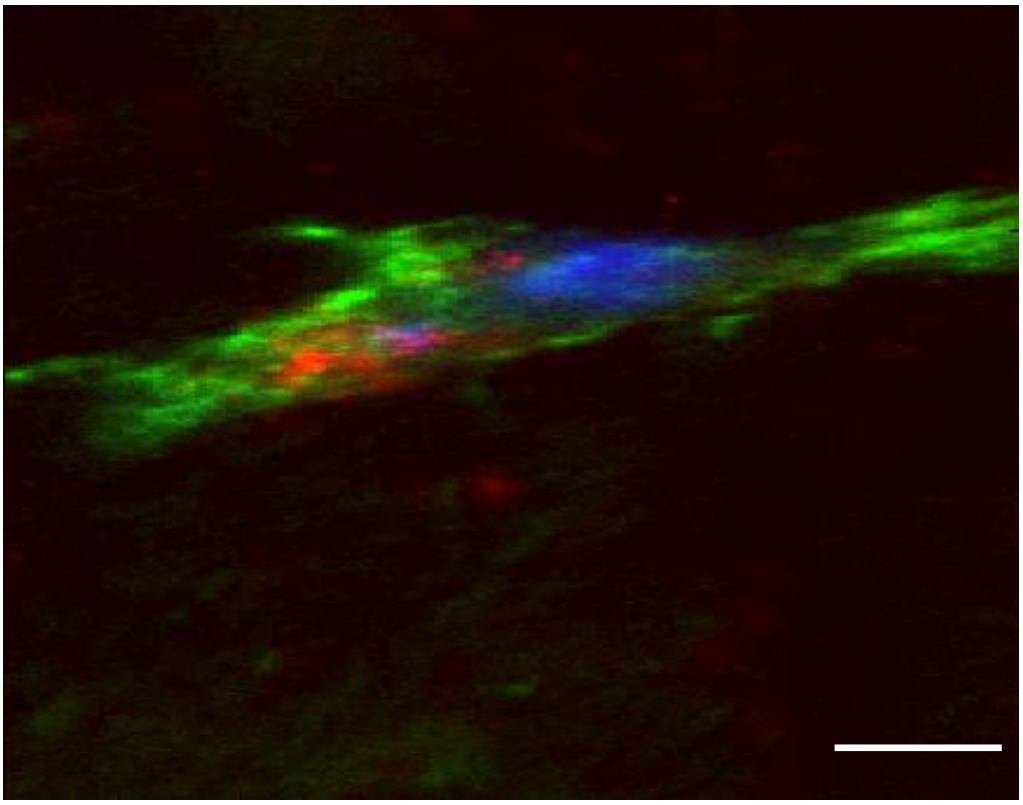

Figure 6.15 Overlayed images DAPI and Cy3 fluorescence as well as TPPL from the AuNP core. A clear diffuse Cy3 signal was imaged throughout the cell, which at points does not co-localise with any TPPL signal and is indicative of cytoplasmic localisation. On the other hand bright TPPL signals were imaged, which could be due to endosomal localisation. Further more, weak TPPL signals were imaged extracellularly which could be due to NP exocytosis as imaging in the perimeter of another cell as Cy3 fluorescence could also be observed at the bottom of the image. Scale bar is 15 μm

Apart from imaging in the x and y direction creating a 2D image, as seen from Figure 6.14, an image at the same position was also acquired in the z

direction creating 3D images of DAPI and Cy3 fluorescence as well as TPPL as seen from the figure below.

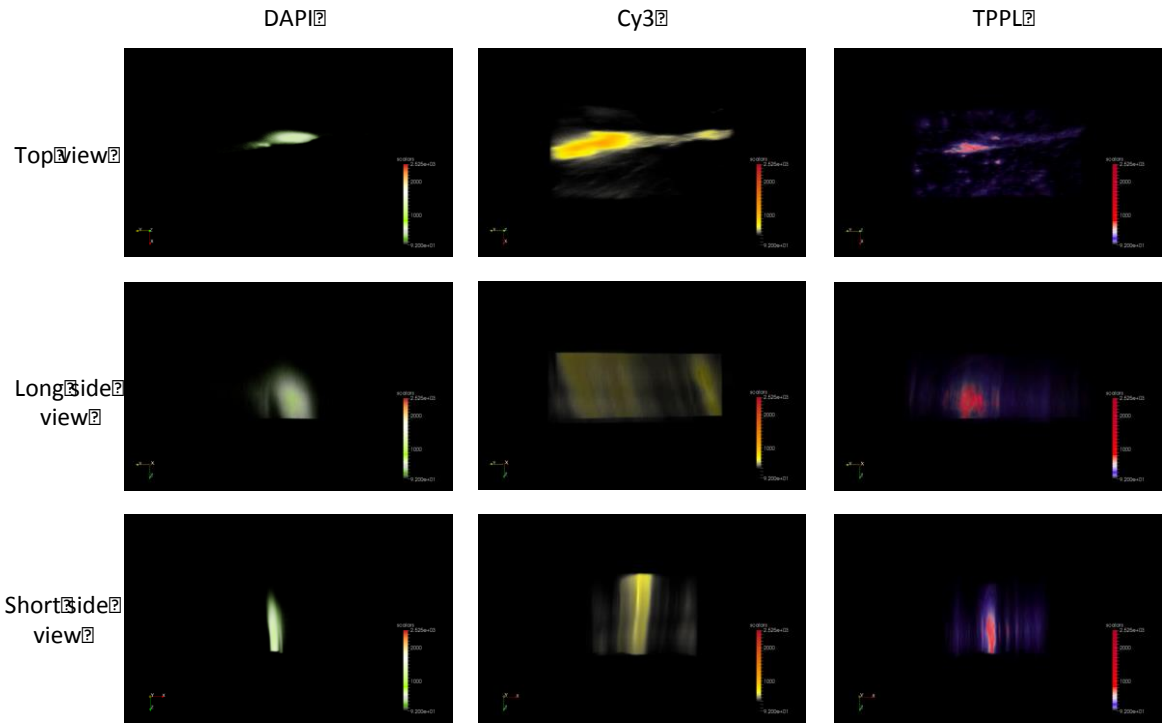

Figure 6.16 3D images created by imaging in the z direction for DAPI and Cy 3 fluorescence as well as TPPL from the AuNP core. Images were analysed and presented as a top view, long side and short side view for each scan.

Once more it can be seen that although the nucleus is well defined, the fluorescence signal corresponding to flare release is diffuse and was imaged throughout the cell. On the other hand, a TPPL signal when analysed in each direction did not appear to be well-dispersed throughout the cell which is a strong indication that flare release is imaged within the cytoplasm leading to an almost uniform fluorescence signal whereas the AuNPs are most likely located within endosomes leading to a very bright aggregated TPPL signal with a weaker signal being imaged in areas which

may correspond to single particles located within the cytoplasm following endosomal escape.

Chapter 7 – Summary and outlook

During the last two decades significant progress has been made in the field of nanoscience that has rendered available a variety of inorganic particles in terms of their chemical composition and morphology and therefore their properties. Moreover, gaining a better understanding of the surface chemistry of nanoparticles has allowed for the development of functional and sophisticated nanoparticulate systems that have been successfully used in a number of different biomedical applications ranging from sensing and gene silencing to drug delivery.

In this thesis the design and development of a DNA-coated AuNP dimer was presented, which was used for live cell imaging and drug delivery applications. Furthermore, the intracellular fate of DNA-coated AuNPs after cellular internalization was investigated. A summary of the results including an outlook to future work is presented below.

7.1 Summary of results

AuNPs of different sizes as well as shapes were synthesised and characterised in order to use them in further applications. In **Chapter 4** we show spherical AuNPs of two different sizes could be produced by varying the synthetic protocol. 15 ± 1 nm spherical AuNPs were firstly synthesised with the standard Turkevich method whereas 43 ± 4 nm spherical AuNPs were synthesised according to a seed mediated growth synthesis. We further showed how surface functionalization with a defined or dense shell

of oligonucleotides could be achieved endowing them with functional properties for their use within biological environments. Furthermore, we demonstrated how anisotropic particles, including AuNRs and branched AuNPs, could be synthesised for their use as imaging agents due to their strong TPPL signal.

In **Chapter 5** DNA-coated 15 ± 1 nm spherical AuNPs were firstly assembled into dimers by taking advantage of the well-established copper-free click chemistry. By using partially complementary linker oligonucleotide strands modified with azide or alkyne groups we were able to show how single AuNPs could be assembled into a dimer structure. Once hybridization had taken place clicking groups within close proximity to each other could chemically react forming a covalent bond. This ensured the stability of the AuNP dimers in stringent conditions such as high temperature or low salt concentrations. Furthermore, we showed that even under denaturing conditions (incubation with formamide) the AuNP dimers were retained. DNA-coated AuNP dimers were then utilised for mRNA sensing and drug delivery.

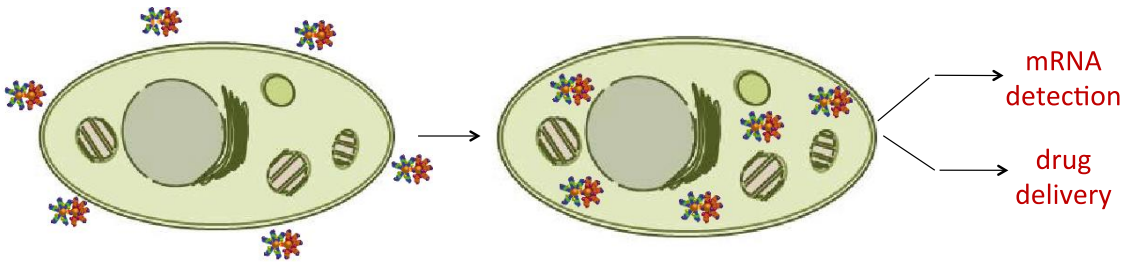

Scheme 7.1 Schematic illustration of the synergistic actions DNA-coated AuNP dimers in cells. Nanoparticle dimers were designed to detect up to two mRNA targets whilst also co-ordinating the release of up to two chemotherapeutic drugs after successful cellular uptake.

Sequence-specific fluorophore modified oligonucleotides conjugated to the AuNP surface were designed to be complementary to two mRNA targets. Oligonucleotide sequences for the detection of vimentin and keratin 8 mRNA were chosen using an extensive BLAST search and were partially hybridised to shorter fluorophore modified oligonucleotides. Three cell lines were chosen that expressed vimentin and keratin 8 in different amounts. 16 HBE epithelial cells expressed only keratin 8 and not vimentin, MRC 5 cells expressed vimentin and not keratin 8 whereas A 549 cells expressed both targets. Incubation of the afformentioned cell lines with DNA-coated AuNP dimers capable of detecting both keratin 8 and vimentin showed that selective mRNA sensing was possible as a fluorescence signal was only observed in the presence of the mRNA target.

As a further development DOX and MTX were intercalated within the sense/flare duplexes attached to the AuNP surface demonstrating the synergistic capabilities of the AuNP dimers. *Via* confocal microscopy we were able to show highly selective release of one or both drugs in conjunction with specific mRNA detection of vimentin and/or keratin 8. Furthermore we found that targeted release could lead to a significant decrease in cell viability in comparison to the use of the free drug in solution thus demonstrating how this system could act as a "Trojan horse". This opens up new possibilities for the successful cellular internalization of other molecules that are not easily taken up by cells.

As discussed above, we have shown that DNA-coated AuNP dimers are taken up by cells and can successfully detect specific mRNA targets whilst also delivering a drug payload. However, the intracellular fate of DNA-coated AuNPs including their intracellular location has been a topic of debate. In **Chapter 6** we explored the possibility of imaging AuNPs in cells. By visualising very thin cell sections *via* transmission electron microscopy

we found that although most of AuNPs accumulate in endosomes and multivesicular bodies a small percentage was found to accumulate within the cytoplasm. The process of endosomal escape was thought to be the most likely mechanism that led to cytoplasmic accumulation as no internalization was observed when the process of active transport was blocked thus ruling out the process of passive diffusion. Furthermore, by monitoring the process of mRNA detection a weak signal could be detected 2 h post incubation, which increased in intensity up to 18 h. By using live organelle stains we found a strong co-localisation between flare release and mitochondria further indicating that mRNA detection most likely takes place within the cytoplasm. Finally by using DNA-coated 43 ± 4 nm AuNPs we demonstrated how a home-built microscopy set-up could be developed capable of imaging both the gold core *via* TPPL and the fluorescence from the release of the flare with the aim of being able to trace both the gold core and mRNA detection in the live cell at real time.

7.2 Outlook and future work

To date, the use of DNA-coated AuNPs has been aimed at understanding the complex interactions of these systems within a cellular environment, including uptake and their subsequent intracellular fate. They represent a starting point and a good “model” system in the fundamental design of a novel drug carrier that can deliver DNA intercalating drugs efficiently and specifically to cells of interest. Having demonstrated a good understanding regarding the design of these materials and a high level of expertise relating to nanoparticle surface chemistry and its manipulation, future work will now focus on developing a biocompatible gold-free drug carrier with a vision of its use in commercial applications.

Future research will focus on the design of a highly stable hollow nanoparticulate drug carrier with a 3D oligonucleotide shell comprised of both ‘sense’ and ‘flare’ sequences intercalated with an anticancer drug.

In order to achieve a dense 3D configuration of oligonucleotides, gold will once more be used as a template. Once the oligonucleotides are organized in a 3D arrangement, as shown in **section 3.2.1.1.2,** we will then experiment with two different strategies to make gold-free nanoparticles. The first strategy will involve the use of programmed copper-free clicked DNA ligation (pioneered by our group). This will involve the design of sense strands, which are further modified close to the 3’ end and the AuNP surface with up to 10 thiol chains modified with clicking groups (either alkyne or azide derrivative) creating a branched structure. Sense strands will be loaded onto the gold surface *via* a well-established protocol, which will lead to the desired 3D arrangement of our design followed by gold core dissolution.

The second synthetic route will involve surface manipulation rather than oligonucleotide modification. The gold core will be modified with a thin and porous shell of silica, which in turn will be modified with a shell of oligonucleotide sense strands. Subsequent dissolution of the gold core will result in a hollow 3D oligonucleotide system, which in turn will be assembled into the same drug delivery carrier as previously mentioned. In both cases we expect our design to exhibit the same cooperative binding behaviour with respect to complementary oligonucleotides compared to the gold-core counterparts as the gold core is primarily used as a template to arrange the oligonucleotides into a densely packed and highly oriented form.

Following successful removal of the gold core our new design will take into account the absence of quenching of the dyes by the gold. This will be tackled by modifying the sense strand with a quenching group in close proximity to the dye of the flare strand. This will allow for the same specificity of detection as previously demonstrated in the presence of the gold core. When the flare is released due to mRNA detection the dye on the flare strand will no longer be quenched and a fluorescence signal corresponding to flare release will be detected.

Given successful synthesis, their stability toward enzymatic degradation will be assessed *in vitro* using a nuclease assays for DNase I and DNase II and their ability to successfully deliver their drug payload only to cells of interest will be determined and compared to their gold-core counterparts *via* confocal microscopy whilst cell viability assays such as trypan or alamar blue will ensure the viability of cells.

Then, we will explore the full capabilities of this novel and most importantly biocompatible nanoparticles for applications within varied areas of cancer research. Collaborative work for *in vivo* experiments will be conducted for the design of probes capable of delivering anticancer drugs including new intercalating agents such as Paclitaxel and Bleomycin to osteosarcoma *via* the design of probes for the detection of related mRNA targets including sclerostin and runx 2.

This work will therefore prove that this new system should be expandable to the biocompatible delivery of any DNA intercalating anticancer drug presenting a new milestone in the field of targeted drug delivery.

Appendix A

A.1 List of suppliers and reagents

Fischer Scientific: Potassium iodide, iodine, acrylamide: bis acrylamide 40 %, boric acid

Agar Scientific: osmium tetroxide, lead nitrate, uranyl acetate, spurr resin, formaldehyde, piperazine-1,4-bis(2-ethanesulfonic acid)

Invitrogen: Antibodies for Vimentin and Keratin 8 (mouse monoclonal AB), Goat anti-mouse IgG (Alexa Fluor 568), minumun essential media (MEM), roswell park memorial institute (RPMI), Pen/Strep, L glutamine, trypsin, nystatin, fetal bovine serum (FBS), HBSS, Hoechst 33342, trypan blue, BacMam organelle stains (early and late endosomes and mitochondria)

Sigma Aldrich: Sodium tetrachloroaurate (III) dihydrate, bis(p-sulfonatophenyl)phenyl phosphine dihydrate dipotassium salt (BSPP), trisodium citrate, DNase I, DNase II, Tris base, (ethylenedinitrilo)tetraacetic acid (EDTA), $MgCl_2$, bovine serum albumin (BSA), sodium dodecyl sulphate (SDS), phosphate buffered saline (PBS) N,N,N',N'-tetramethylethylenediamine (TEMED), ammonium persulfate (APS), doxorubicin hydrochloride, mitoxantrone dihydrochloride, ficoll, urea

Oligonucleotides including their modifications were synthesised by Dr. Afaf El-Sagheer at the University of Oxford.

Cell lines were provided by Dr. Peter Lackie (MRC 5, 16 HBE) at the Biomedical Imaging Unit (Southampton General Hospital). A 549 cells were

provided by Dr. Alastair Watson and Dr. Mirella C. Spaluto based at Southampton General Hospital (WISH Lab).

Appendix B

B.1 Sample calculations

B.1.1 Calculating the concentration of a colloidal gold solution

The concentration of a colloidal gold solution was determined by using the corresponding absorption spectrum as well as the Beer-Lambert Law (see Equation 3.1) using the appropriate molar extinction coefficient depending on the size of the AuNP. For 15 ± 1 nm AuNPs the concentration was calculated as follows.

$$c = \frac{A\ x\ D}{\varepsilon\ x\ l} = \frac{0.5\ x\ 100}{2.27\ x\ 10^{8}\ L\ mol^{-1}\ cm^{-1}\ x\ 1\ cm} = 220.2\ nM$$

Equation A.B 1 Sample calculation showing how the concentration of a AuNP solution can be determined based on the corresponding absorption spectrum

B.1.2 Calculation of sense/flare duplexes per AuNP

From the calibration curves (see Figure 5.4) of concentration dependant fluorescence intensity of the flare strands the number of duplexes could be estimated. Results from three independent measurements are presented in Table A.B 1.

Table A.B 1Determination of sense/flare duplexes per AuNP

		Keratin8				Vimentin		
		"40x" flare				"40x" flare		
Measurement	**Abs. (a.u.)**	**Conc. (nM)**	**No. of moles (pmol)**	**Equiv.**	**Abs. (a.u.)**	**Conc. (nM)**	**No. of moles (pmol)**	**Equiv.**
1	179.23	233.43	46.68	46.68	211.35	239.81	47.96	47.96
2	134.62	175.33	35.07	35.07	132.51	150.36	30.07	30.07
3	125.79	163.83	32.76	32.76	123.53	140.17	28.03	28.03
SEM	16.54	190.87	4.31	4.31	27.90	31.65	6.33	6.33
Average	146.55	15.23	38.17	38.17	155.80	176.78	35.35	35.35
		"120x"				**"120x"**		
Measurement	**Abs. (a.u.)**	**Conc. (nM)**	**No. of moles (pmol)**	**Equiv.**	**Abs. (a.u.)**	**Conc. (nM)**	**No. of moles (pmol)**	**Equiv.**
1	469.12	610.99	122.20	122.20	496.93	563.86	112.77	112.77
2	452.88	589.84	117.97	117.97	529.32	600.61	120.12	120.12
3	440.12	573.22	114.64	114.64	510.09	578.79	115.76	115.76
SEM	8.39	10.93	2.18	2.18	9.40	10.67	2.13	2.13
Average	454.04	591.35	118.27	118.27	512.11	581.10	116.22	116.22

B.1.3 Calculation of drug loading

AuNP dimers were loaded with a varying amount of DOX and MTX depending on the number of sense/flare duplexes per AuNP. By monitoring the fluorescence of DOX and MTX *via* duplex melting the number of drug molecules intercalated could be calculated using a concentration dependant calibration curve of fluorescence intensity (see Figure 5.17) as shown in Table A.B 2 where results from three independent measurements are summarized.

Table A.B 2 Determination of DOX and MTX loading per AuNP

		DOX/Keratin8				MXT/Vimentin		
		"40x" flare				"40x" flare		
Measurement	**Abs. (a.u.)**	**Conc. (nM)**	**No. of moles (pmol)**	**Equiv.**	**Abs. (a.u.)**	**Conc. (nM)**	**No. of moles (pmol)**	**Equiv.**
1	9.52	255.44	30.65	30.65	15.06	248.58	29.83	29.83
2	10.86	291.17	34.94	34.94	16.18	267.25	32.07	32.07
3	11.93	320.00	38.40	38.40	14.32	236.42	28.37	28.37
SEM	0.70	18.67	2.24	2.24	0.54	8.96	1.07	1.07
Average	10.77	288.87	34.66	34.66	15.18	250.75	30.09	30.09
		"120x" flare				**"120x" flare**		
Measurement	**Abs. (a.u.)**	**Conc. (nM)**	**No. of moles (pmol)**	**Equiv.**	**Abs. (a.u.)**	**Conc. (nM)**	**No. of moles (pmol)**	**Equiv.**
1	37.56	83.34	120.85	120.85	58.21	79.55	115.35	115.35
2	35.67	79.13	114.74	114.74	58.22	79.56	115.36	115.36
3	35.90	79.65	115.49	115.49	54.36	74.29	107.72	107.72
SEM	0.60	1.32	1.92	1.92	1.28	1.75	2.54	2.54
Average	36.37	80.71	117.02	117.02	56.93	77.80	112.81	112.81

B.2 Additional data on AuNP dimer characterization

B.2.1 TEM images

Prior to their use within live cells, ligated AuNP dimers were also visualized by TEM as shown in Figure A.B 1. Images were acquired after purification from non-ligated AuNP dimers by gel electrophoresis.

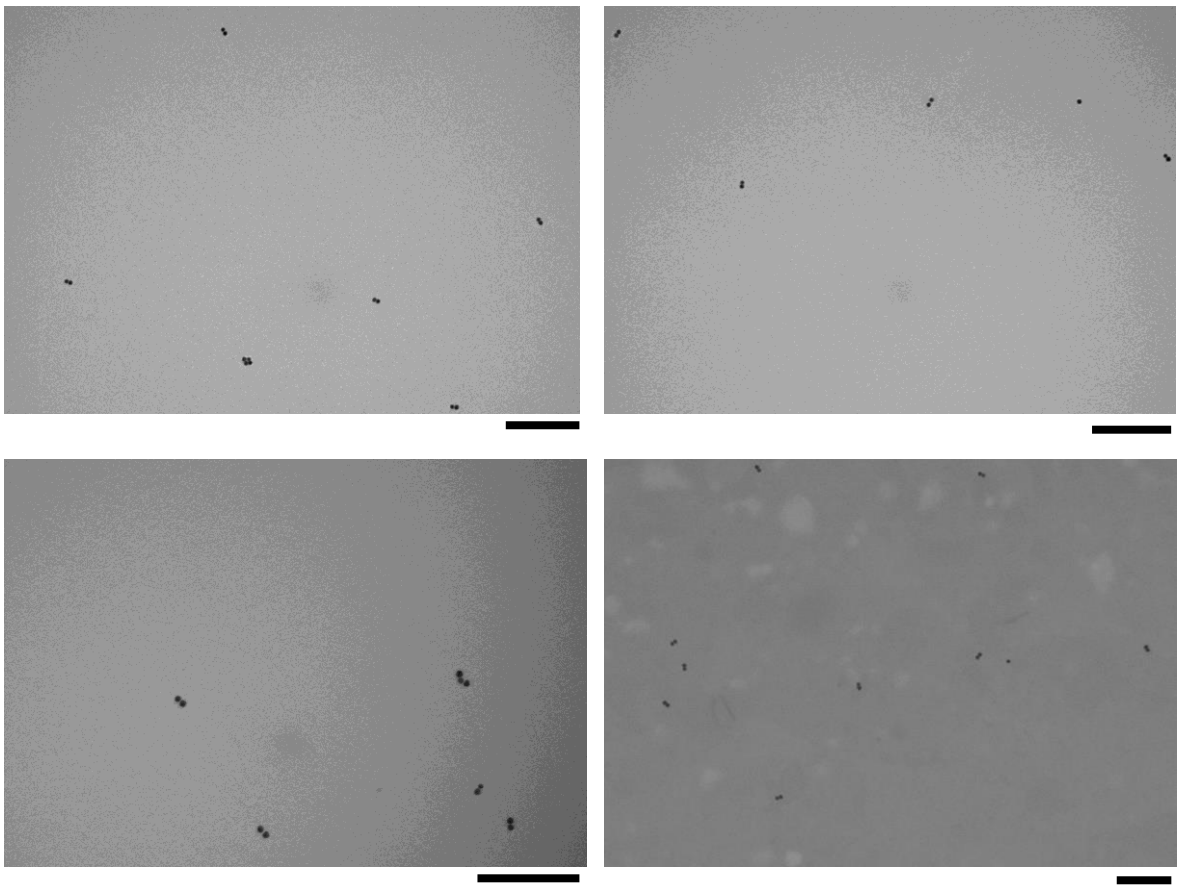

Figure A.B 1 TEM images of ligated AuNP dimers after purification by gel electrophoresis

B.2.2 Dynamic light scattering (DLS)

DLS was used to evaluate the hydrodynamic diameter of the AuNP dimers. BSPP coated AuNPs as well as single DNA-coated AuNPs were also evaluated and used as controls. The obtained results are presented in Figure A.B 2.

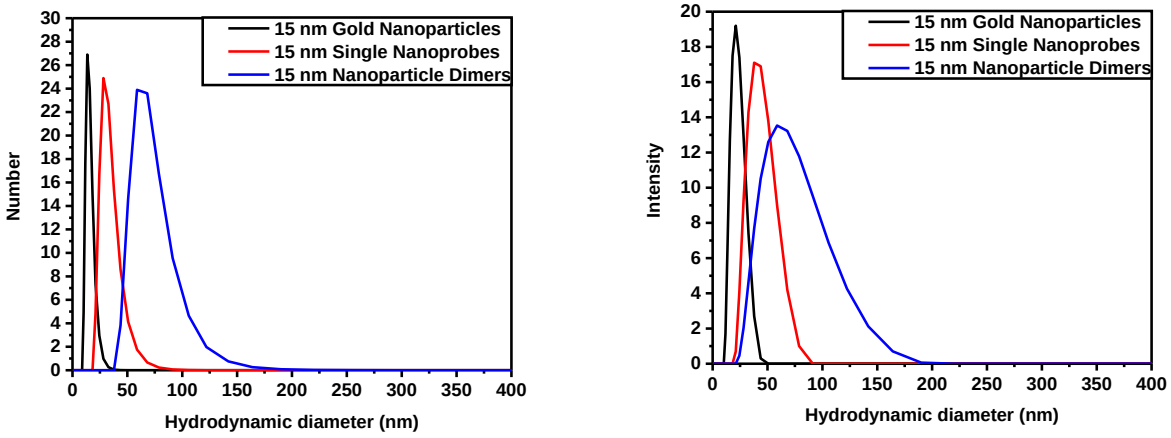

Figure A.B 2 Ligated AuNP dimers were found to have an average hydrodynamic diameter of 78 nm (number: 68 nm, PDI 0.157). As a comparison the hydrodynamic diameters of 15 nm BSPP coated AuNPs (intensity: 21 nm, number: 15 nm, PDI: 0.184) and DNA-coated AuNPs (intensity: 41 nm, number: 28, PDI: 0.178) were also evaluated.

B.2.3 Efficiency of quenching

The ability to detect specific mRNA targets within live cells relies on the ability of the AuNP core to quench the fluorescence of the fluorophores attached to the oligonucleotides. However as quenching is never 100 % successful we evaluated the degree of quenching when attached to the

AuNP surface. Representative fluorescence spectra are presented in Figure A.B 3.

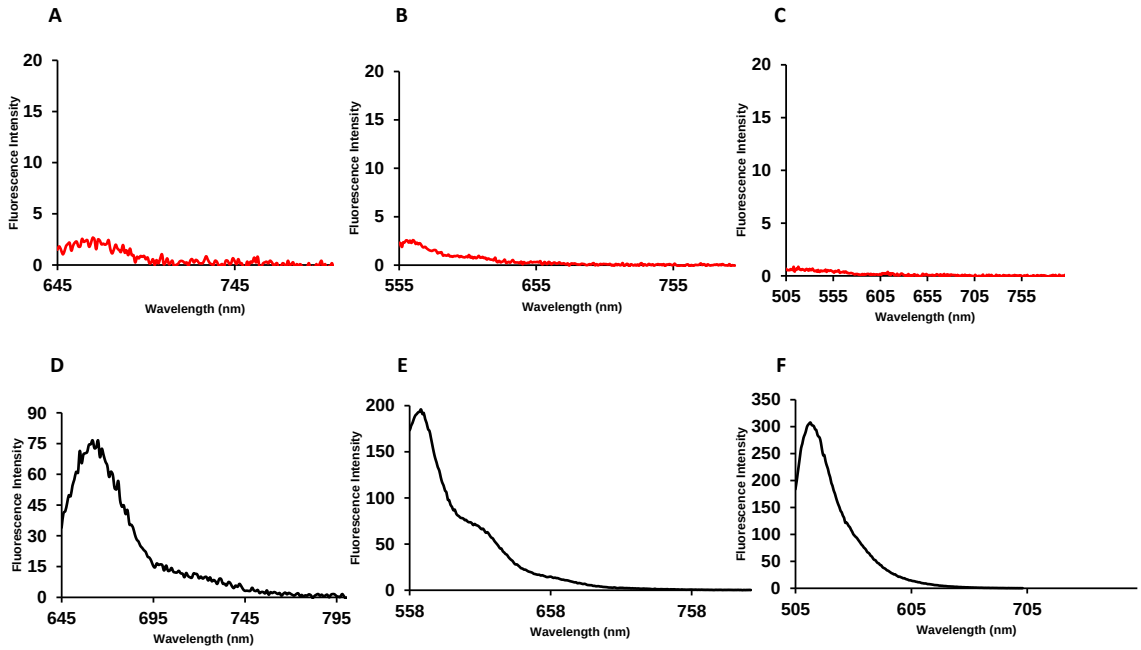

Figure A.B 3 Fluorescent spectra of i) dye-functionalized oligonucleotides attached to a 15 ± 1 nm AuNP surface (A-C) and ii) free dye-functionalized oligonucleotides in solution after release from the nanoparticle by a target sequence (D-F). Cy5 is used at A and D, Cy3 at B and E and FAM at C and F.

B.2.4 Supporting data for nuclease assays

As discussed in **section 5.2**, the stability of ligated AuNP dimers was evaluated in the presence of DNase I and DNase II. The percentage degradation as shown in Figure 5.6 and Figure 5.8 was calculated by monitoring the fluorescence output from the 5' FAM dye on the sense strand over 24 h as shown in Figure A.B 4. Degradation would result in an

increase in the fluorescence intensity of FAM as it would no longer be quenched by the AuNP core.

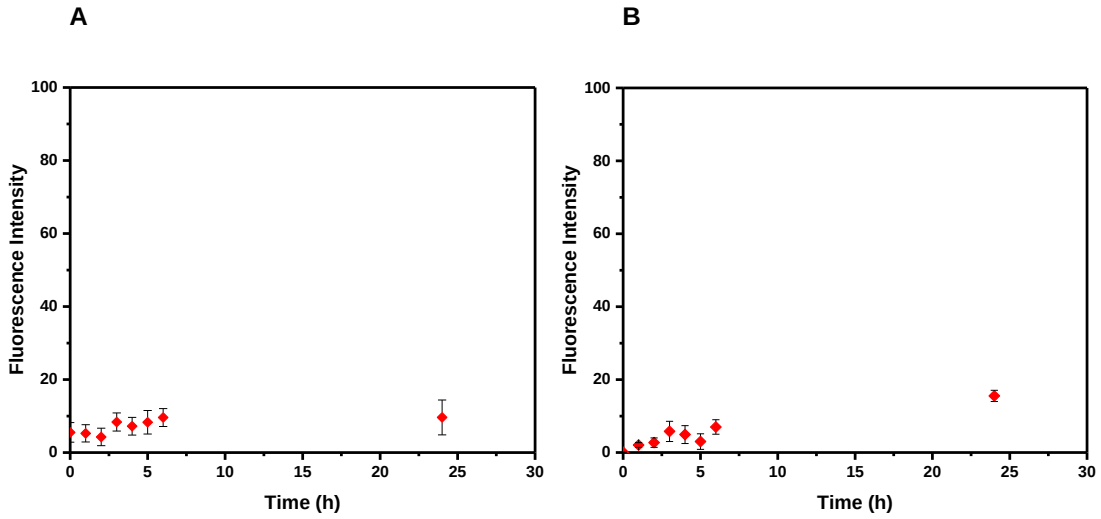

Figure A.B 4 Data showing the fluorescence intensity from the 5' dye modified sense strand on AuNPs upon incubation with DNase I (A) and DNase II (B)

By using the fluorescence data presented in Figure A.B 4 the % of oligonucleotide degradation could be determined. An analytical experimental protocol can be found in **section 3.4.2.2.1**.

B.2.5 Supporting data for the stability of drug intercalation

As discussed in **section 5.5.1.2** ligated AuNP dimers could retail a high percentage of their drug payload. This was assessed by monitoring the fluorescence output of DOX and MTX over a 24 h period. When intercalated within the sense/flare duplex fluorescence is quenched. Therefore

potential drug leaking would be observed as a corresponding increase in the fluorescence signature of the drug. The fluorescence data is presented below in Figure A.B 5.

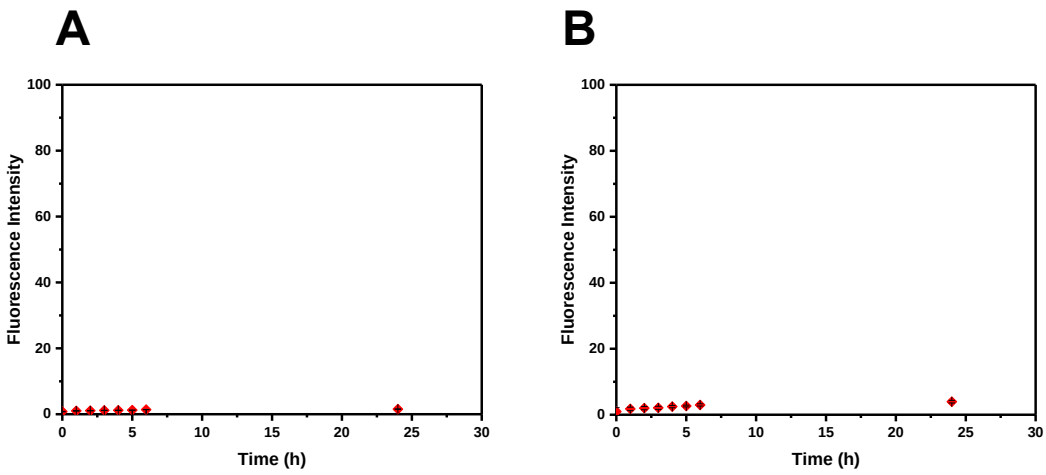

Figure A.B 5 Fluorescence intensity of DOX (A) and MTX (B) monitored over a 24 h period

B.2.6 Additional controls

Apart from scramble nanoparticle dimers, single scramble nanoprobes (using scramble sense 1 and scramble flare 1 sequences in each case, see Table 3.2) were also used as controls to ensure specific mRNA detection and targeted drug delivery in 16 HBEs, MRC 5s and A 549s.

The same protocol as outlined in **section 3.5.6.1**, was followed for the incubation and imaging of mRNA detection using single scramble nanoprobes in 16 HBE, MRC 5 and A 549 cells.

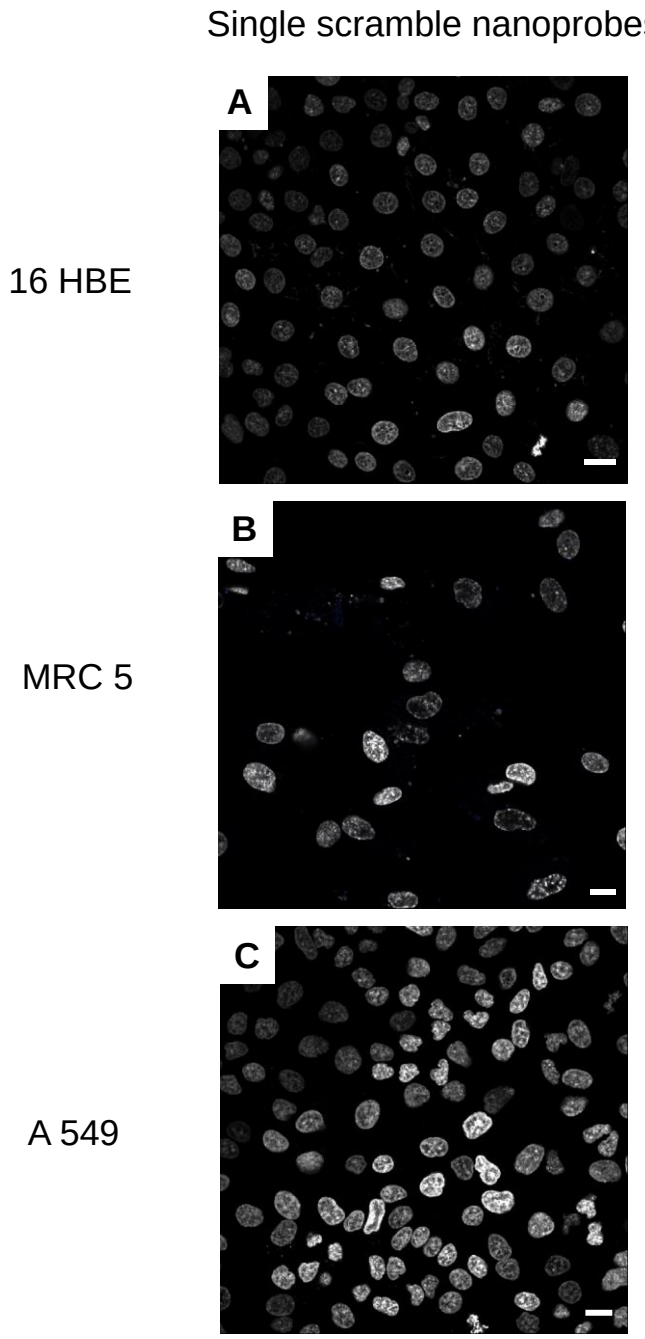

Figure A.B 6 Single scramble nanoprobes incubated with 16 HBE (A), MRC 5 (B) and A 549 (C) cells for 18 h prior to confocal imaging Colour guide: nuclear counterstain – white, FAM – blue, Cy3 – green. Scale bar is 15 μm.

As seen in Figure A.B 6, no fluorescence corresponding to flare release was observed indicating once more that unless the specific mRNA target is present, the flare strand remains bound to the sense strand and no fluorescence is detectable.

Both DOX and MTX were intercalated into separate single scramble nanoprobes and their efficiency to retain their drug payload in the absence of the specific target was tested *via* confocal microscopy as well as by measuring their effect on the cell viability of all three cell lines.

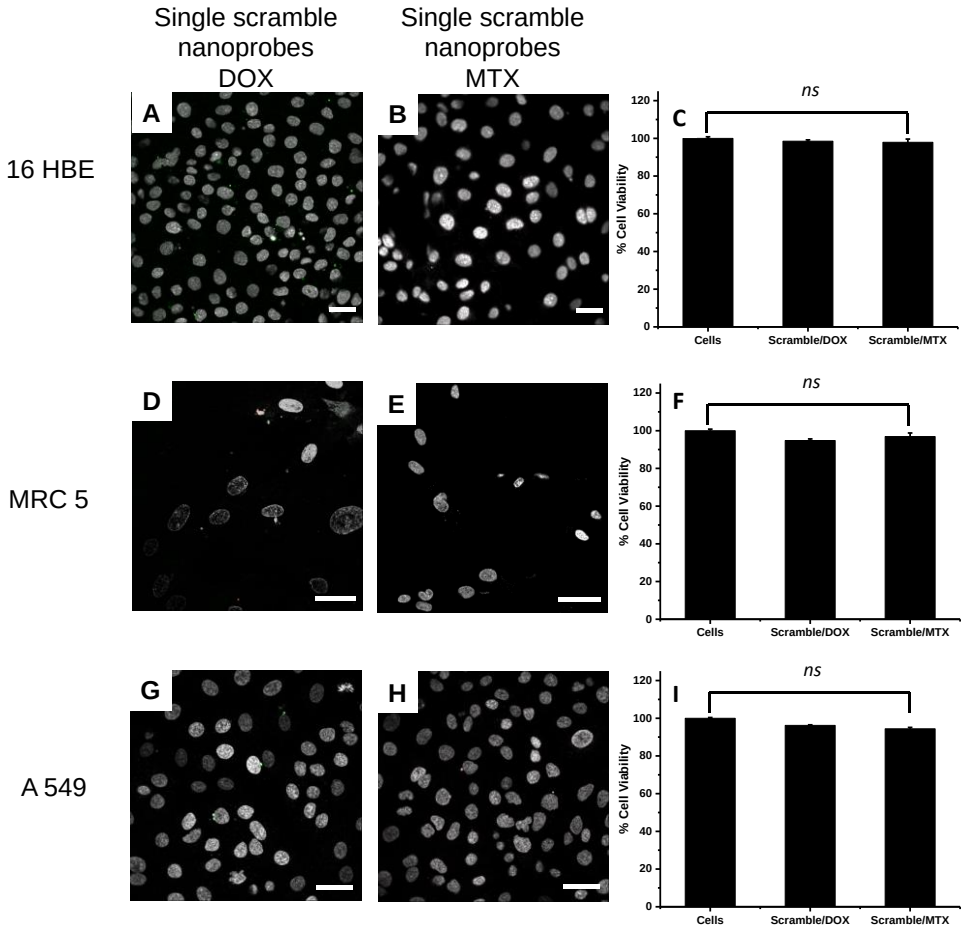

Figure A.B 7 Confocal microscopy images of live cells incubated with single scramble nanoprobes intercalated with DOX or MTX as well as the respective viability assay for each cell line. Scale bar is 15 µm. Cell viability data are shown as mean ± SEM (n=3). P-values were determined by a one-way ANOVA

The absence of a fluoresce signal in confocal images A – H of Figure A.B 7 is a strong indication that the single scramble nanoprobes were able to retain their payload over an 18 h incubation period and showed no significant effect on the cell viability of 16 HBEs, MRC 5s and A 549s.

B.3 Additional confocal images

B.3.1 Separated confocal channels

Fluorescence confocal channels for A549 cells were separated and presented below in Figure A.B 8. As A 549 cells express both vimentin and keratin 8 two fluorescence signals from both flare and drug release were observed. Channels were therefore presented separately for clarity.

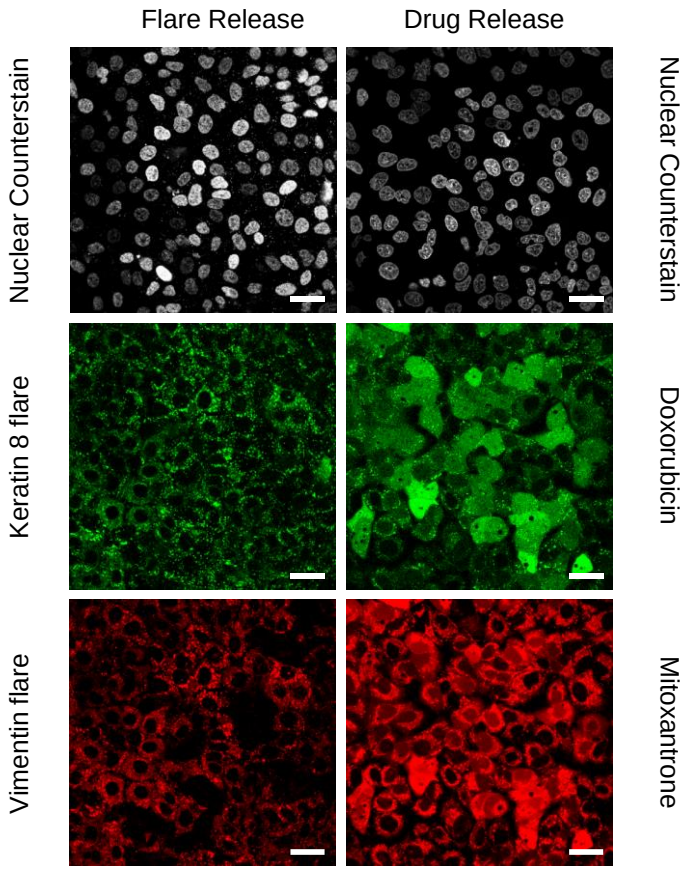

Figure A.B 8 Confocal images of A 549 cells showing the separate channels for the nuclear counterstain, keratin 8 and vimentin flare release as well as separate channels for endocellular drug release of doxorubicin and mitoxantrone. Scale bars are 15 μm.

B.3.2 z-stack confocal images

z stack confocal imaging was also performed when investigating the location of mRNA detection as discussed in **section 6.2.2.** It was found that the fluorescence signal corresponding to mRNA detection showed strong co-localization with mitochondria (imaged using organelle stains) as the fluorescence signal from both the flare and the organelle stain overlapped. However, no significant co-localization was observed with early or late endosomes in a 2D image. Cells were therefore also imaged in the z plane as shown below in Figure A.B 9.

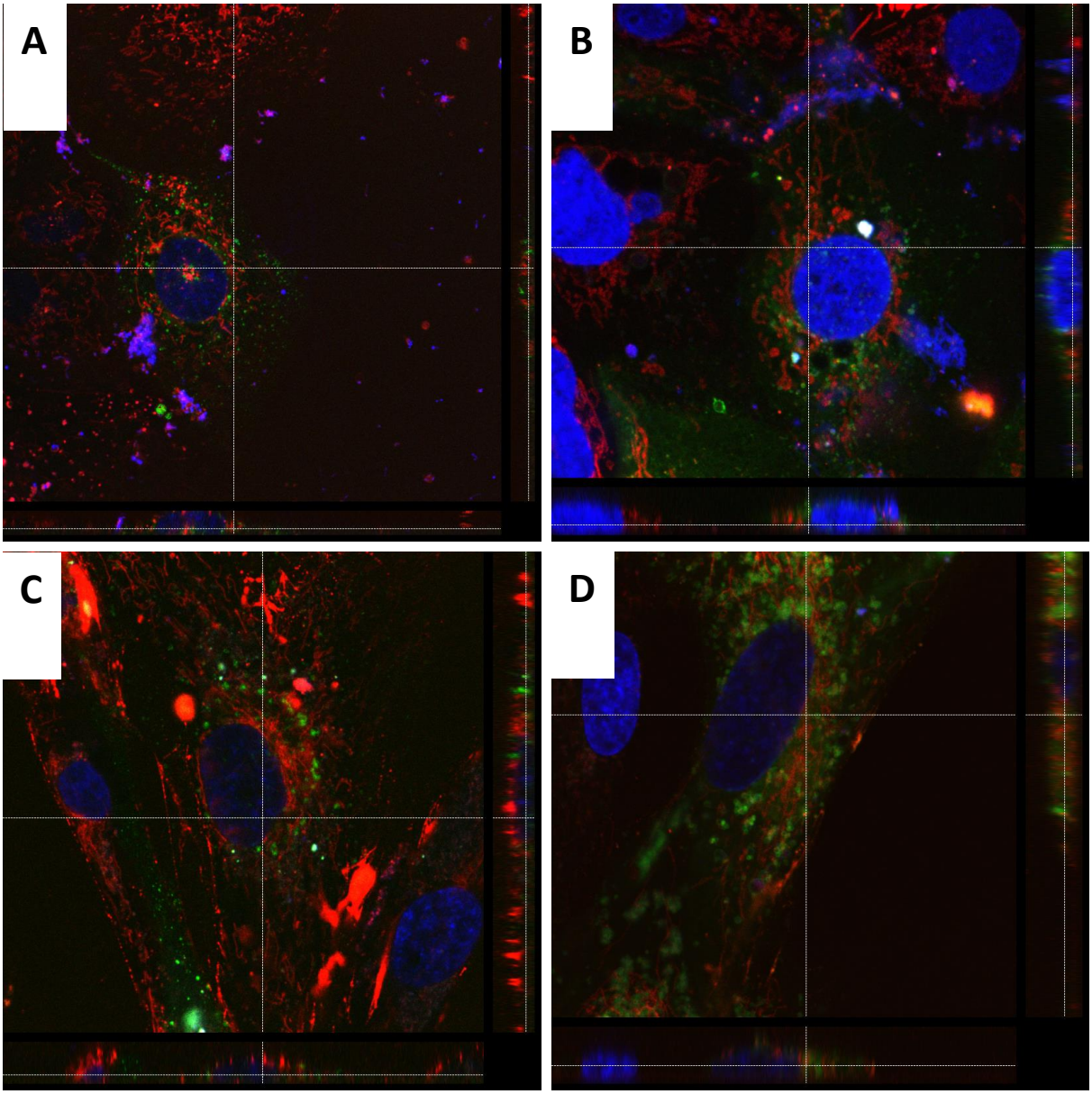

Figure A.B 9 Confocal microscopy z-stack images of 16 HBE (A and B) and MRC 5 cells (C and D). Early (A and C) and late (B and D) endosomes are stained and imaged in conjunction with flare release due to mRNA detection.

Figure A.B 9 shows that even when imaged in the z plane no co-localization and overlap of fluorescence signal is observed. This is a strong

indication that mRNA detection and subsequent flare release does not occur in the early or late endosome.

References

1. Heuer-Jungemann, A., et al., *Gold nanoparticles and fluorescently-labelled DNA as a platform for biological sensing.* Nanoscale, 2013. **5**(20): p. 9503-9510.

2. Giljohann, D.A., et al., *Gold Nanoparticles for Biology and Medicine.* Angewandte Chemie-International Edition, 2010. **49**(19): p. 3280-3294.

3. Chinen, A.B., et al., *Nanoparticle Probes for the Detection of Cancer Biomarkers, Cells, and Tissues by Fluorescence.* Chemical Reviews, 2015. **115**(19): p. 10530-10574.

4. *Bio-Applications of Nanoparticles.* Bio-Applications of Nanoparticles, 2007. **620**.

5. Quidant, R., C. Louis, and O. Pluchery, *Optical and Thermal Properties of Gold Nanoparticles for Biology and Medicine.* Gold Nanoparticles for Physics, Chemistry and Biology, 2012: p. 273-298.

6. Myroshnychenko, V., et al., *Modelling the optical response of gold nanoparticles.* Chemical Society Reviews, 2008. **37**(9): p. 1792-1805.

7. Huang, X., et al., *Gold nanoparticles: interesting optical properties and recent applications in cancer diagnostic and therapy.* Nanomedicine, 2007. **2**(5): p. 681-693.

8. Li, F., et al., *Thermal Stability of DNA Functionalized Gold Nanoparticles.* Bioconjugate Chemistry, 2013. **24**(11): p. 1790-1797.

9. Alivisatos, A.P., et al., *Organization of 'nanocrystal molecules' using DNA.* Nature, 1996. **382**(6592): p. 609-611.

10. Mirkin, C.A., et al., *A DNA-based method for rationally assembling nanoparticles into macroscopic materials.* Nature, 1996. **382**(6592): p. 607-609.

11. Cutler, J.I., E. Auyeung, and C.A. Mirkin, *Spherical Nucleic Acids.* Journal of the American Chemical Society, 2012. **134**(3): p. 1376-1391.

12. Mulvaney, P., *Surface plasmon spectroscopy of nanosized metal particles.* Langmuir, 1996. **12**(3): p. 788-800.

13. Kelly, K.L., et al., *The optical properties of metal nanoparticles: The influence of size, shape, and dielectric environment.* Journal of Physical Chemistry B, 2003. **107**(3): p. 668-677.

14. Liz-Marzan, L.M., *Nanometals formation and color.* Materials Today, 2004. **7**(2): p. 26-31.

15. Faraday, M., *The Bakerian Lecture: Experimental Relations of Gold (and Other Metals) to Light.* Philosophical Transactions of the Royal Society of London, 1857(147): p. 145-181.

16. Turkevich, J., P.C. Stevenson, and J. Hillier, *A study of the nucleation and growth processes in the synthesis of colloidal gold* Discussions of the Faraday Society 1951. **11**(0): p. 20.

17. Turkevich, J., P.C. Stevenson, and J. Hillier, *The Formation of Colloidal Gold.* The Journal of Physical Chemistry, 1953. **57**(7): p. 3.

18. Frens, G., *Controlled nucleation for regulation of particle-size in monodisperse gold suspensions.* Nature-Physical Science, 1973. **241**(105): p. 20-22.

19. Ji, X.H., et al., *Size control of gold nanocrystals in citrate reduction: The third role of citrate.* Journal of the American Chemical Society, 2007. **129**(45): p. 13939-13948.

20. Schulz, F., et al., *Little Adjustments Significantly Improve the Turkevich Synthesis of Gold Nanoparticles.* Langmuir, 2014. **30**(35): p. 10779-10784.

21. Tyagi, H., et al., *A Facile pH Controlled Citrate-Based Reduction Method for Gold Nanoparticle Synthesis at Room Temperature.* Nanoscale Research Letters, 2016.

22. Kumar, S., K.S. Gandhi, and R. Kumar, *Modeling of formation of gold nanoparticles by citrate method.* Industrial & Engineering Chemistry Research, 2007. **46**(10): p. 3128-3136.

23. Xia, H.B., et al., *Synthesis of Monodisperse Quasi-Spherical Gold Nanoparticles in Water via Silver(I)-Assisted Citrate Reduction.* Langmuir, 2010. **26**(5): p. 3585-3589.

24. Privman, V., et al., *Mechanism of formation of monodispersed colloids by aggregation of nanosize precursors.* Journal of Colloid and Interface Science, 1999. **213**(1): p. 36-45.

25. Frens, G., *PARTICLE-SIZE AND SOL STABILITY IN METAL COLLOIDS.* Kolloid-Zeitschrift and Zeitschrift Fur Polymere, 1972. **250**(7): p. 736-+.

26. Bastus, N.G., J. Comenge, and V. Puntes, *Kinetically Controlled Seeded Growth Synthesis of Citrate-Stabilized Gold Nanoparticles of up to 200 nm: Size Focusing versus Ostwald Ripening.* Langmuir, 2011. **27**(17): p. 11098-11105.

27. Brown, K.R., D.G. Walter, and M.J. Natan, *Seeding of colloidal Au nanoparticle solutions. 2. Improved control of particle size and shape.* Chemistry of Materials, 2000. **12**(2): p. 306-313.

28. Ziegler, C. and A. Eychmuller, *Seeded Growth Synthesis of Uniform Gold Nanoparticles with Diameters of 15-300 nm.* Journal of Physical Chemistry C, 2011. **115**(11): p. 4502-4506.

29. Brown, K.R., et al., *Hydroxylamine seeding of colloidal au nanoparticles. 3. Controlled formation of conductive Au films.* Chemistry of Materials, 2000. **12**(2): p. 314-323.

30. Brown, K.R. and M.J. Natan, *Hydroxylamine seeding of colloidal Au nanoparticles in solution and on surfaces.* Langmuir, 1998. **14**(4): p. 726-728.

31. Jana, N.R., L. Gearheart, and C.J. Murphy, *Seeding growth for size control of 5-40 nm diameter gold nanoparticles.* Langmuir, 2001. **17**(22): p. 6782-6786.

32. Rodriguez-Fernandez, J., et al., *Seeded growth of submicron Au colloids with quadrupole plasmon resonance modes.* Langmuir, 2006. **22**(16): p. 7007-7010.

33. John, C.L., et al., *Reproducibly synthesize gold nanorods and maintain their stability.* Rsc Advances, 2013. **3**(27): p. 10909-10918.

34. Jana, N.R., L. Gearheart, and C.J. Murphy, *Seed-mediated growth approach for shape-controlled synthesis of spheroidal and rod-like gold nanoparticles using a surfactant template.* Advanced Materials, 2001. **13**(18): p. 1389-1393.

35. Gole, A. and C.J. Murphy, *Seed-mediated synthesis of gold nanorods: Role of the size and nature of the seed.* Chemistry of Materials, 2004. **16**(19): p. 3633-3640.

36. Liu, M.Z. and P. Guyot-Sionnest, *Mechanism of silver(I)-assisted growth of gold nanorods and bipyramids.* Journal of Physical Chemistry B, 2005. **109**(47): p. 22192-22200.

37. Murphy, C.J., et al., *One-dimensional colloidal gold and silver nanostructures.* Inorganic Chemistry, 2006. **45**(19): p. 7544-7554.

38. Orendorff, C.J. and C.J. Murphy, *Quantitation of metal content in the silver-assisted growth of gold nanorods.* Journal of Physical Chemistry B, 2006. **110**(9): p. 3990-3994.

39. Nikoobakht, B. and M.A. El-Sayed, *Preparation and growth mechanism of gold nanorods (NRs) using seed-mediated growth method.* Chemistry of Materials, 2003. **15**(10): p. 1957-1962.

40. Guerrero-Martinez, A., et al., *Nanostars shine bright for you Colloidal synthesis, properties and applications of branched metallic nanoparticles.* Current Opinion in Colloid & Interface Science, 2011. **16**(2): p. 118-127.

41. Hao, F., et al., *Plasmon resonances of a gold nanostar.* Nano Letters, 2007. **7**(3): p. 729-732.

42. Cheng, K., et al., *Construction and Validation of Nano Gold Tripods for Molecular Imaging of Living Subjects.* Journal of the American Chemical Society, 2014. **136**(9): p. 3560-3571.

43. Chen, S.H., et al., *Monopod, bipod, tripod, and tetrapod gold nanocrystals.* Journal of the American Chemical Society, 2003. **125**(52): p. 16186-16187.

44. Xie, J.P., et al., *The Synthesis of SERS-Active Gold Nanoflower Tags for In Vivo Applications.* Acs Nano, 2008. **2**(12): p. 2473-2480.

45. Barbosa, S., et al., *Tuning Size and Sensing Properties in Colloidal Gold Nanostars.* Langmuir, 2010. **26**(18): p. 14943-14950.

46. Sau, T.K. and C.J. Murphy, *Room temperature, high-yield synthesis of multiple shapes of gold nanoparticles in aqueous solution.* Journal of the American Chemical Society, 2004. **126**(28): p. 8648-8649.

47. Day, H.A., et al., *Controlling the three-dimensional morphology of nanocrystals.* Crystengcomm, 2010. **12**(12): p. 4312-4316.

48. Kuo, C.H. and M.H. Huang, *Synthesis of branched gold nanocrystals by a seeding growth approach.* Langmuir, 2005. **21**(5): p. 2012-2016.

49. Pastoriza-Santos, I. and L.M. Liz-Marzan, *N,N-Dimethylformamide as a Reaction Medium for Metal Nanoparticle Synthesis.* Advanced Functional Materials, 2009. **19**(5): p. 679-688.

50. Kumar, P.S., et al., *High-yield synthesis and optical response of gold nanostars.* Nanotechnology, 2008. **19**(1).

51. Yuan, H., et al., *Shape and SPR evolution of thorny gold nanoparticles promoted by silver ions.* Chemistry of Materials, 2007. **19**(7): p. 1592-1600.

52. Zou, X.Q., E.B. Ying, and S.J. Dong, *Seed-mediated synthesis of branched gold nanoparticles with the assistance of citrate and their surface-enhanced Raman scattering properties.* Nanotechnology, 2006. **17**(18): p. 4758-4764.

53. Yang, X., et al., *Gold Nanomaterials at Work in Biomedicine.* Chem. Revi., 2015. **115**(19): p. 10410-10488.

54. Cobley, C.M., et al., *Gold nanostructures: a class of multifunctional materials for biomedical applications.* Chemical Society Reviews, 2011. **40**(1): p. 44-56.

55. Dreaden, E.C., et al., *The golden age: gold nanoparticles for biomedicine.* Chemical Society Reviews, 2012. **41**(7): p. 2740-2779.

56. Willets, K.A. and R.P. Van Duyne, *Localized surface plasmon resonance spectroscopy and sensing.* Annual Review of Physical Chemistry, 2007. **58**: p. 267-297.

57. Yang, X., et al., *Gold Nanomaterials at Work in Biomedicine.* Chem. Rev., 2015. **115**(19): p. 10410-10488.

58. Ghosh, S.K. and T. Pal, *Interparticle coupling effect on the surface plasmon resonance of gold nanoparticles: From theory to applications.* Chemical Reviews, 2007. **107**(11): p. 4797-4862.

59. Louis, C. and O. Pluchery, *Gold Nanoparticles for Physics, Chemistry and Biology.* Gold Nanoparticles for Physics, Chemistry and Biology, 2012: p. 1-395.

60. Link, S. and M.A. Ei-Sayed, *Optical properties and ultrafast dynamics of metallic nanocrystals.* Annual Review of Physical Chemistry, 2003. **54**: p. 331-366.

61. Link, S., M.A. El-Sayed, and M.B. Mohamed, *Simulation of the optical absorption spectra of gold nanorods as a function of their aspect ratio and the effect of the medium dielectric constant (vol 103B, pg 3073, 1999).* Journal of Physical Chemistry B, 2005. **109**(20): p. 10531-10532.

62. Shao, L., et al., *Plasmonic Properties of Single Multispiked Gold Nanostars: Correlating Modeling with Experiments.* Langmuir, 2012. **28**(24): p. 8979-8984.

63. Nehl, C.L. and J.H. Hafner, *Shape-dependent plasmon resonances of gold nanoparticles.* Journal of Materials Chemistry, 2008. **18**(21): p. 2415-2419.

64. Mohamed, M.B., et al., *The 'lightning' gold nanorods: fluorescence enhancement of over a million compared to the gold metal.* Chemical Physics Letters, 2000. **317**(6): p. 517-523.

65. Wang, H.F., et al., *In vitro and in vivo two-photon luminescence imaging of single gold nanorods.* Proceedings of the National Academy of Sciences of the United States of America, 2005. **102**(44): p. 15752-15756.

66. Durr, N.J., et al., *Two-photon luminescence imaging of cancer cells using molecularly targeted gold nanorods.* Nano Letters, 2007. **7**(4): p. 941-945.

67. Gao, N.Y., et al., *Shape-Dependent Two-Photon Photoluminescence of Single Gold Nanoparticles.* Journal of Physical Chemistry C, 2014. **118**(25): p. 13904-13911.

68. Au, L., et al., *Quantifying the Cellular Uptake of Antibody-Conjugated Au Nanocages by Two-Photon Microscopy and Inductively Coupled Plasma Mass Spectrometry.* Acs Nano, 2010. **4**(1): p. 35-42.

69. Jiang, Y.Q., et al., *Bioimaging with Two-Photon-Induced Luminescence from Triangular Nanoplates and Nanoparticle Aggregates of Gold.* Advanced Materials, 2009. **21**(22): p. 2309-+.

70. Wu, X., et al., *High-Photoluminescence-Yield Gold Nanocubes: For Cell Imaging and Photothermal Therapy.* Acs Nano, 2010. **4**(1): p. 113-120.

71. G.M., B., et al., *Chapter 2 DNA and RNA Structure*. 2006: Cambridge: The Royal Society if Chemistry.

72. D., W.J. and C.F.H. C., *Molecular Structure of Nucleic Acids: A Structure for Deoxyribose Nucleic Acid.* Nature, 1953. **171**(4356): p. 737-738.

73. T., B. *Nucleic Acids Book*. 2005 [cited 2018; Available from: https://www.atdbio.com/nucleic-acids-book.

74. Kool, E.T., *Hydrogen bonding, base stacking, and steric effects in DNA replication.* Annual Review of Biophysics and Biomolecular Structure, 2001. **30**: p. 1-22.

75. Owczarzy, R., et al., *Predicting stability of DNA duplexes in solutions containing magnesium and monovalent cations.* Biochemistry, 2008. **47**(19): p. 5336-5353.

76. Ansevin, A.T., et al., *HIGH-RESOLUTION THERMAL DENATURATION OF DNA .1. THEORETICAL AND PRACTICAL CONSIDERATIONS FOR RESOLUTION OF THERMAL SUBTRANSITIONS.* Biopolymers, 1976. **15**(1): p. 153-174.

77. D'Abramo, M., et al., *On the Nature of DNA Hyperchromic Effect.* Journal of Physical Chemistry B, 2013. **117**(29): p. 8697-8704.

78. Kibbe, W.A., *OligoCalc: an online oligonucleotide properties calculator.* Nucleic Acids Research, 2007. **35**: p. W43-W46.

79. Pon, R.T., N. Usman, and K.K. Ogilvie, *DERIVATIZATION OF CONTROLLED PORE GLASS-BEADS FOR SOLID-PHASE OLIGONUCLEOTIDE SYNTHESIS.* Biotechniques, 1988. **6**(8): p. 768-775.

80. Damha, M.J., P.A. Giannaris, and S.V. Zabarylo, *AN IMPROVED PROCEDURE FOR DERIVATIZATION OF CONTROLLED-PORE GLASS-BEADS FOR SOLID-PHASE OLIGONUCLEOTIDE SYNTHESIS.* Nucleic Acids Research, 1990. **18**(13): p. 3813-3821.

81. Caruthers, M.H., *GENE SYNTHESIS MACHINES - DNA CHEMISTRY AND ITS USES.* Science, 1985. **230**(4723): p. 281-285.

82. Hall, L.M., M. Gerowska, and T. Brown, *A highly fluorescent DNA toolkit: synthesis and properties of oligonucleotides containing new Cy3, Cy5 and Cy3B monomers.* Nucleic Acids Research, 2012. **40**(14).

83. Shelbourne, M., et al., *Fast copper-free click DNA ligation by the ring-strain promoted alkyne-azide cycloaddition reaction.* Chemical Communications, 2011. **47**(22): p. 6257-6259.

84. Cutler, J.I., E. Auyeung, and C.A. Mirkin, *Spherical Nucleic Acids.* J. Am. Chem. Soc., 2012. **134**(3): p. 1376-1391.

85. Macfarlane, R.J., et al., *Nanoparticle superlattice engineering with DNA.* Abstracts of Papers of the American Chemical Society, 2012. **243**.

86. Halo, T.L., et al., *NanoFlares for the detection, isolation, and culture of live tumor cells from human blood.* Proc. Natl. Acad. Sci. U.S.A., 2014. **111**(48): p. 17104-17109.

87. Giljohann, D.A., et al., *Gold Nanoparticles for Biology and Medicine.* Angew. Chem. Int. Ed., 2010. **49**(19): p. 3280-3294.

88. Nykypanchuk, D., et al., *DNA-guided crystallization of colloidal nanoparticles.* Nature, 2008. **451**(7178): p. 549-552.

89. Vives, E., J. Schmidt, and A. Pelegrin, *Cell-penetrating and cell-targeting peptides in drug delivery.* Biochimica Et Biophysica Acta-Reviews on Cancer, 2008. **1786**(2): p. 126-138.

90. de la Fuente, J.M. and C.C. Berry, *Tat peptide as an efficient molecule to translocate gold nanoparticles into the cell nucleus.* Bioconjugate Chemistry, 2005. **16**(5): p. 1176-1180.

91. Oyelere, A.K., et al., *Peptide-conjugated gold nanorods for nuclear targeting.* Bioconjugate Chemistry, 2007. **18**(5): p. 1490-1497.

92. El-Sayed, I.H., X.H. Huang, and M.A. El-Sayed, *Surface plasmon resonance scattering and absorption of anti-EGFR antibody*

conjugated gold nanoparticles in cancer diagnostics: Applications in oral cancer. Nano Letters, 2005. **5**(5): p. 829-834.

93. Rosi, N.L., et al., *Oligonucleotide-modified gold nanoparticles for intracellular gene regulation.* Science, 2006. **312**(5776): p. 1027-1030.

94. Lytton-Jean, A.K.R. and C.A. Mirkin, *A thermodynamic investigation into the binding properties of DNA functionalized gold nanoparticle probes and molecular fluorophore probes.* Journal of the American Chemical Society, 2005. **127**(37): p. 12754-12755.

95. Jin, R.C., et al., *What controls the melting properties of DNA-linked gold nanoparticle assemblies?* Journal of the American Chemical Society, 2003. **125**(6): p. 1643-1654.

96. Elghanian, R., et al., *Selective colorimetric detection of polynucleotides based on the distance-dependent optical properties of gold nanoparticles.* Science, 1997. **277**(5329): p. 1078-1081.

97. Park, J.W. and J.S. Shumaker-Parry, *Strong Resistance of Citrate Anions on Metal Nanoparticles to Desorption under Thiol Functionalization.* Acs Nano, 2015. **9**(2): p. 1665-1682.

98. Pensa, E., et al., *The Chemistry of the Sulfur-Gold Interface: In Search of a Unified Model.* Accounts of Chemical Research, 2012. **45**(8): p. 1183-1192.

99. Hill, H.D., et al., *The Role Radius of Curvature Plays in Thiolated Oligonucleotide Loading on Gold Nanoparticles.* Acs Nano, 2009. **3**(2): p. 418-424.

100. Hurst, S.J., A.K.R. Lytton-Jean, and C.A. Mirkin, *Maximizing DNA loading on a range of gold nanoparticle sizes.* Anal. Chem., 2006. **78**(24): p. 8313-8318.

101. Giljohann, D.A., et al., *Oligonucleotide loading determines cellular uptake of DNA-modified gold nanoparticles.* Nano Lett., 2007. **7**(12): p. 3818-3821.

102. Kanaras, A.G., et al., *Towards multistep nanostructure synthesis: Programmed enzymatic self-assembly of DNA/gold systems.* Angewandte Chemie-International Edition, 2003. **42**(2): p. 191-+.

103. Zhang, X., M.R. Servos, and J. Liu, *Instantaneous and Quantitative Functionalization of Gold Nanoparticles with Thiolated DNA Using a pH-Assisted and Surfactant-Free Route.* Journal of the American Chemical Society, 2012. **134**(17): p. 7266-7269.

104. Wen, Y.Q., et al., *Stable Gold Nanoparticle Conjugation to Internal DNA Positions: Facile Generation of Discrete Gold Nanoparticle-DNA Assemblies.* Bioconjugate Chemistry, 2010. **21**(8): p. 1413-1416.

105. Parak, W.J., et al., *Biological applications of colloidal nanocrystals.* Nanotechnology, 2003. **14**(7): p. R15-R27.

106. Pellegrino, T., et al., *Gel electrophoresis of gold-DNA nanoconjugates.* Journal of Biomedicine and Biotechnology, 2007.

107. Claridge, S.A., et al., *Isolation of discrete nanoparticle - DNA conjugates for plasmonic applications.* Nano Letters, 2008. **8**(4): p. 1202-1206.

108. Zanchet, D., et al., *Electrophoretic isolation of discrete Au nanocrystal/DNA conjugates.* Nano Letters, 2001. **1**(1): p. 32-35.

109. Busson, M.P., et al., *Optical and Topological Characterization of Gold Nanoparticle Dimers Linked by a Single DNA Double Strand.* Nano Letters, 2011. **11**(11): p. 5060-5065.

110. Seferos, D.S., et al., *Nano-flares: Probes for transfection and mRNA detection in living cells.* J. Am. Chem. Soc., 2007. **129**(50): p. 15477-+.

111. Prigodich, A.E., et al., *Nano-flares for mRNA Regulation and Detection.* Acs Nano, 2009. **3**(8): p. 2147-2152.

112. Shi, J., et al., *Fluorescence Lifetime Imaging of Nanoflares for mRNA Detection in Living Cells.* Anal. Chem., 2016. **88**(4): p. 1979-1983.

113. Pan, W., et al., *Multiplexed Detection and Imaging of Intracellular mRNAs Using a Four-Color Nanoprobe.* Anal. Chem., 2013. **85**(21): p. 10581-10588.

114. Li, N., et al., *A Multicolor Nanoprobe for Detection and Imaging of Tumor-Related mRNAs in Living Cells.* Angew. Chem. Int. Ed., 2012. **51**(30): p. 7426-7430.

115. Tyagi, S. and F.R. Kramer, *Molecular beacons: Probes that fluoresce upon hybridization.* Nature Biotechnology, 1996. **14**(3): p. 303-308.

116. Sokol, D.L., et al., *Real time detection of DNA RNA hybridization in living cells.* Proceedings of the National Academy of Sciences of the United States of America, 1998. **95**(20): p. 11538-11543.

117. Santangelo, P.J., et al., *Dual FRET molecular beacons for mRNA detection in living cells.* Nucleic Acids Research, 2004. **32**(6).

118. Chithrani, B.D., A.A. Ghazani, and W.C.W. Chan, *Determining the size and shape dependence of gold nanoparticle uptake into mammalian cells.* Nano Letters, 2006. **6**(4): p. 662-668.

119. Narayan, S.P., et al., *The Sequence-Specific Cellular Uptake of Spherical Nucleic Acid Nanoparticle Conjugates.* Small, 2015. **11**(33): p. 4173-4182.

120. Choi, C.H.J., et al., *Mechanism for the endocytosis of spherical nucleic acid nanoparticle conjugates.* Proc. Natl. Acad. Sci. U.S.A., 2013. **110**(19): p. 7625-7630.

121. Kewalramani, S., et al., *Counterion Distribution Surrounding Spherical Nucleic Acid-Au Nanoparticle Conjugates Probed by Small-Angle X-ray Scattering.* Acs Nano, 2013. **7**(12): p. 11301-11309.

122. Lee, O.S. and G.C. Schatz, *Molecular Dynamics Simulation of DNA-Functionalized Gold Nanoparticles.* Journal of Physical Chemistry C, 2009. **113**(6): p. 2316-2321.

123. Zwanikken, J.W., et al., *Local Ionic Environment around Polyvalent Nucleic Acid-Functionalized Nanoparticles.* Journal of Physical Chemistry C, 2011. **115**(33): p. 16368-16373.

124. Barnaby, S.N., et al., *Design Considerations for RNA Spherical Nucleic Acids (SNAs).* Bioconjugate Chemistry, 2016. **27**(9): p. 2124-2131.

125. Seferos, D.S., et al., *Polyvalent DNA Nanoparticle Conjugates Stabilize Nucleic Acids.* Nano Lett., 2009. **9**(1): p. 308-311.

126. Pan, C.Q. and R.A. Lazarus, *Ca2+-dependent activity of human DNase I and its hyperactive variants.* Protein Science, 1999. **8**(9): p. 1780-1788.

127. Altieri, D.C., *Survivin, versatile modulation of cell division and apoptosis in cancer.* Oncogene, 2003. **22**(53): p. 8581-8589.

128. Seferos, D.S., et al., *Nano-flares: Probes for transfection and mRNA detection in living cells.* Journal of the American Chemical Society, 2007. **129**(50): p. 15477-+.

129. McClellan, S., et al., *mRNA detection in living cells: A next generation cancer stem cell identification technique.* Methods, 2015. **82**: p. 47-54.

130. Seftor, E.A., et al., *Melanoma Tumor Cell Heterogeneity: A Molecular Approach to Study Subpopulations Expressing the Embryonic Morphogen Nodal.* Seminars in Oncology, 2014. **41**(2): p. 259-266.

131. Li, B.J., et al., *Monitoring live human mesenchymal stromal cell differentiation and subsequent selection using fluorescent RNA-based probes (vol 6, 26014, 2016).* Scientific Reports, 2016. **6**.

132. Lahm, H., et al., *Live Fluorescent RNA-Based Detection of Pluripotency Gene Expression in Embryonic and Induced Pluripotent Stem Cells of Different Species.* Stem Cells, 2015. **33**(2): p. 392-402.

133. Shi, J., et al., *Fluorescence Lifetime Imaging of Nanoflares for mRNA Detection in Living Cells.* Analytical Chemistry, 2016. **88**(4): p. 1979-1983.

134. Xue, J., et al., *Visual detection of STAT5B gene expression in living cell using the hairpin DNA modified gold nanoparticle beacon.* Biosensors & Bioelectronics, 2013. **41**: p. 71-77.

135. Yang, Y.J., et al., *FRET Nanoflares for Intracellular mRNA Detection: Avoiding False Positive Signals and Minimizing Effects of System Fluctuations.* Journal of the American Chemical Society, 2015. **137**(26): p. 8340-8343.

136. Yang, X.J., et al., *Reliable Forster Resonance Energy Transfer Probe Based on Structure-Switching DNA for Ratiometric Sensing of Telomerase in Living Cells.* Analytical Chemistry, 2017. **89**(7): p. 4216-4222.

137. Prigodich, A.E., et al., *Multiplexed Nanoflares: mRNA Detection in Live Cells.* Analytical Chemistry, 2012. **84**(4): p. 2062-2066.

138. Pan, W., et al., *Multiplexed Detection and Imaging of Intracellular mRNAs Using a Four-Color Nanoprobe.* Analytical Chemistry, 2013. **85**(21): p. 10581-10588.

139. Li, N., et al., *A Multicolor Nanoprobe for Detection and Imaging of Tumor-Related mRNAs in Living Cells.* Angewandte Chemie-International Edition, 2012. **51**(30): p. 7426-7430.

140. Briley, W.E., et al., *Quantification and real-time tracking of RNA in live cells using Sticky-flares.* Proceedings of the National Academy of Sciences of the United States of America, 2015. **112**(31): p. 9591-9595.

141. Tu, Y.Q., et al., *Fluorescence quenching of gold nanoparticles integrating with a conformation-switched hairpin oligonucleotide probe for microRNA detection.* Chemical Communications, 2012. **48**(87): p. 10718-10720.

142. J., L., et al., *Two-Color-Based Nanoflares for Multiplexed MicroRNAs Imaging in Live Cells.* Nanotheranostics, 2018. **2**(1): p. 96-105.

143. Zheng, D., et al., *Topical delivery of siRNA-based spherical nucleic acid nanoparticle conjugates for gene regulation.* Proceedings of the National Academy of Sciences of the United States of America, 2012. **109**(30): p. 11975-11980.

144. Nemati, H., et al., *Using siRNA-based spherical nucleic acid nanoparticle conjugates for gene regulation in psoriasis.* Journal of Controlled Release, 2017. **268**: p. 259-268.

145. Barnaby, S.N., A. Lee, and C.A. Mirkin, *Probing the inherent stability of siRNA immobilized on nanoparticle constructs.* Proceedings of the National Academy of Sciences of the United States of America, 2014. **111**(27): p. 9739-9744.

146. Jensen, S.A., et al., *Spherical Nucleic Acid Nanoparticle Conjugates as an RNAi-Based Therapy for Glioblastoma.* Science Translational Medicine, 2013. **5**(209).

147. Sita, T.L., et al., *Dual bioluminescence and near-infrared fluorescence monitoring to evaluate spherical nucleic acid nanoconjugate activity in vivo.* Proceedings of the National Academy of Sciences of the United States of America, 2017. **114**(16): p. 4129-4134.

148. Randeria, P.S., et al., *siRNA-based spherical nucleic acids reverse impaired wound healing in diabetic mice by ganglioside GM3 synthase knockdown.* Proceedings of the National Academy of Sciences of the United States of America, 2015. **112**(18): p. 5573-5578.

149. Radovic-Moreno, A.F., et al., *Immunomodulatory spherical nucleic acids.* Proceedings of the National Academy of Sciences of the United States of America, 2015. **112**(13): p. 3892-3897.

150. Heuer-Jungemann, A., et al., *Selective killing of cells triggered by their mRNA signature in the presence of smart nanoparticles.* Nanoscale, 2016. **8**(38): p. 16857-16861.

151. Lee, C.S., et al., *Doxorubicin-loaded oligonucleotide conjugated gold nanoparticles: A promising in vivo drug delivery system for colorectal cancer therapy.* European Journal of Medicinal Chemistry, 2017. **142**: p. 416-423.

152. Dhar, S., et al., *Polyvalent Oligonucleotide Gold Nanoparticle Conjugates as Delivery Vehicles for Platinum(IV) Warheads.* Journal of the American Chemical Society, 2009. **131**(41): p. 14652-+.

153. Zhang, X.Q., et al., *Strategy for Increasing Drug Solubility and Efficacy through Covalent Attachment to Polyvalent DNA - Nanoparticle Conjugates.* Acs Nano, 2011. **5**(9): p. 6962-6970.

154. van den Broek, B., et al., *Parallel Nanometric 3D Tracking of Intracellular Gold Nanorods Using Multifocal Two-Photon Microscopy.* Nano Letters, 2013. **13**(3): p. 980-986.

155. Tong, L., et al., *Gold Nanorods as Contrast Agents for Biological Imaging: Optical Properties, Surface Conjugation and Photothermal Effects.* Photochemistry and Photobiology, 2009. **85**(1): p. 21-32.

156. Liu, Y., et al., *A Plasmonic Gold Nanostar Theranostic Probe for In Vivo Tumor Imaging and Photothermal Therapy.* Theranostics, 2015. **5**(9): p. 946-960.

157. Rane, T.D. and A.M. Armani, *Two-Photon Microscopy Analysis of Gold Nanoparticle Uptake in 3D Cell Spheroids.* Plos One, 2016. **11**(12).

158. Hurst, S.J., H.D. Hill, and C.A. Mirkin, "*Three-Dimensional Hybridization*" *with polyvalent DNA-gold nanoparticle conjugates.* Journal of the American Chemical Society, 2008. **130**(36): p. 12192-12200.

159. Jones, M.R., et al., *DNA-nanoparticle superlattices formed from anisotropic building blocks.* Nature Materials, 2010. **9**(11): p. 913-917.

160. Park, S.Y., et al., *DNA-programmable nanoparticle crystallization.* Nature, 2008. **451**(7178): p. 553-556.

161. Park, S.J., et al., *The structural characterization of oligonucleotide-modified gold nanoparticle networks formed by DNA hybridization.* Journal of Physical Chemistry B, 2004. **108**(33): p. 12375-12380.

162. Heuer-Jungemann, A., et al., *Copper-free click chemistry as an emerging tool for the programmed ligation of DNA-functionalised gold nanoparticles.* Nanoscale, 2013. **5**(16): p. 7209-7212.

163. Kolb, H.C., M.G. Finn, and K.B. Sharpless, *Click chemistry: Diverse chemical function from a few good reactions.* Angewandte Chemie-International Edition, 2001. **40**(11): p. 2004-+.

164. Harimech, P.K., et al., *Reversible Ligation of Programmed DNA-Gold Nanoparticle Assemblies.* Journal of the American Chemical Society, 2015. **137**(29): p. 9242-9245.

165. Xu, L.G., et al., *Regiospecific Plasmonic Assemblies for in Situ Raman Spectroscopy in Live Cells.* Journal of the American Chemical Society, 2012. **134**(3): p. 1699-1709.

166. Chou, L.Y.T., K. Zagorovsky, and W.C.W. Chan, *DNA assembly of nanoparticle superstructures for controlled biological delivery and elimination.* Nature Nanotechnology, 2014. **9**(2): p. 148-155.

167. Ohta, S., D. Glancy, and W.C.W. Chan, *NANOMATERIALS DNA-controlled dynamic colloidal nanoparticle systems for mediating cellular interaction.* Science, 2016. **351**(6275): p. 841-845.

168. Raeesi, V., L.Y.T. Chou, and W.C.W. Chan, *Tuning the Drug Loading and Release of DNA-Assembled Gold-Nanorod Superstructures.* Advanced Materials, 2016. **28**(38): p. 8511-8518.

169. Murphy, C.J., et al., *Anisotropic metal nanoparticles: Synthesis, assembly, and optical applications.* Journal of Physical Chemistry B, 2005. **109**(29): p. 13857-13870.

170. Kawamura, G., et al., *Shape control synthesis of multi-branched gold nanoparticles.* Materials Chemistry and Physics, 2009. **115**(1): p. 229-234.

171. Wu, W.-C. and J.B. Tracy, *Large-Scale Silica Overcoating of Gold Nanorods with Tunable Shell Thicknesses.* Chemistry of Materials, 2015. **27**(8): p. 2888-2894.

172. Zhang, Z., et al., *Mesoporous Silica-Coated Gold Nanorods as a Light-Mediated Multifunctional Theranostic Platform for Cancer Treatment.* Advanced Materials, 2012. **24**(11): p. 1418-1423.

173. Abadeer, N.S. and C.J. Murphy, *Recent Progress in Cancer Thermal Therapy Using Gold Nanoparticles.* Journal of Physical Chemistry C, 2016. **120**(9): p. 4691-4716.

174. Blake, R.D. and S.G. Delcourt, *Thermodynamic effects of formamide on DNA stability.* Nucleic Acids Research, 1996. **24**(11): p. 2095-2103.

175. Lee, P.Y., et al., *Agarose Gel Electrophoresis for the Separation of DNA Fragments.* Jove-Journal of Visualized Experiments, 2012(62).

176. Hanauer, M., et al., *Separation of nanoparticles by gel electrophoresis according to size-and shape.* Nano Letters, 2007. **7**(9): p. 2881-2885.

177. Bonilla, J.V. and G.S. Srivatsa, *Handbook of Analysis of Oligonucleotides and Related Products*. 2011: Taylor & Francis.

178. Haiss, W., et al., *Determination of size and concentration of gold nanoparticles from UV-Vis spectra.* Analytical Chemistry, 2007. **79**(11): p. 4215-4221.

179. Liu, X.O., et al., *Extinction coefficient of gold nanoparticles with different sizes and different capping ligands.* Colloids and Surfaces B-Biointerfaces, 2007. **58**(1): p. 3-7.

180. Cho, E.C., et al., *Understanding the Role of Surface Charges in Cellular Adsorption versus Internalization by Selectively Removing Gold Nanoparticles on the Cell Surface with a I-2/KI Etchant.* Nano Letters, 2009. **9**(3): p. 1080-1084.

181. Pelfrene, A., et al., *In Vitro Investigations of Human Bioaccessibility from Reference Materials Using Simulated Lung Fluids.* International Journal of Environmental Research and Public Health, 2017. **14**(2).

182. Chen, C.L., et al., *Kinetics and thermodynamics of DNA hybridization on gold nanoparticles.* Nucleic Acids Research, 2009. **37**(11): p. 3756-3765.

183. Zheng, T.Y., S. Bott, and Q. Huo, *Techniques for Accurate Sizing of Gold Nanoparticles Using Dynamic Light Scattering with Particular Application to Chemical and Biological Sensing Based on Aggregate Formation.* Acs Applied Materials & Interfaces, 2016. **8**(33): p. 21585-21594.

184. Pfaffl, M.W., *A new mathematical model for relative quantification in real-time RT-PCR.* Nucleic Acids Research, 2001. **29**(9).

185. Strober, W., *Trypan blue exclusion test of cell viability.* Current protocols in immunology, 2001.

186. Clayden, J., et al., *Organic Chemistry*

1st ed. 2001, New York: Oxford University Press. 1512.

187. Barreto, A., et al., *Behavior of colloidal gold nanoparticles in different ionic strength media.* Journal of Nanoparticle Research, 2015. **17**(12).

188. Loweth, C.J., et al., *DNA-based assembly of gold nanocrystals.* Angewandte Chemie-International Edition, 1999. **38**(12): p. 1808-1812.

189. Schmid, G. and A. Lehnert, *THE COMPLEXATION OF GOLD COLLOIDS.* Angewandte Chemie-International Edition in English, 1989. **28**(6): p. 780-781.

190. Kimling, J., et al., *Turkevich method for gold nanoparticle synthesis revisited.* Journal of Physical Chemistry B, 2006. **110**(32): p. 15700-15707.

191. Jain, P.K., et al., *Calculated absorption and scattering properties of gold nanoparticles of different size, shape, and composition: Applications in biological imaging and biomedicine.* Journal of Physical Chemistry B, 2006. **110**(14): p. 7238-7248.

192. Berciaud, S., et al., *Observation of intrinsic size effects in the optical response of individual gold nanoparticles.* Nano Letters, 2005. **5**(3): p. 515-518.

193. El-Sayed, M. and X. Huang, *Gold nanoparticles: Optical properties and implementations in cancer diagnosis and photothermal therapy.* Journal of Advanced Research, 2010. **1**(1): p. 13-28.

194. Link, S. and M.A. El-Sayed, *Size and temperature dependence of the plasmon absorption of colloidal gold nanoparticles.* Journal of Physical Chemistry B, 1999. **103**(21): p. 4212-4217.

195. Wu, H.L., C.H. Chen, and M.H. Huang, *Seed-Mediated Synthesis of Branched Gold Nanocrystals Derived from the Side Growth of Pentagonal Bipyramids and the Formation of Gold Nanostars.* Chemistry of Materials, 2009. **21**(1): p. 110-114.

196. Xia, Y.N., et al., *Shape-Controlled Synthesis of Metal Nanocrystals: Simple Chemistry Meets Complex Physics?* Angewandte Chemie-International Edition, 2009. **48**(1): p. 60-103.

197. Evcimen, N.I., et al., *Growth of branched gold nanoparticles on solid surfaces and their use as surface-enhanced Raman scattering substrates.* Rsc Advances, 2015. **5**(123): p. 101656-101663.

198. Tornblom, M. and U. Henriksson, *Effect of solubilization of aliphatic hydrocarbons on size and shape of rodlike C(16)TABr micelles studied by H-2 NMR relaxation.* Journal of Physical Chemistry B, 1997. **101**(31): p. 6028-6035.

199. Tong, W.M., et al., *Control of Symmetry Breaking Size and Aspect Ratio in Gold Nanorods: Underlying Role of Silver Nitrate.* Journal of Physical Chemistry C, 2017. **121**(6): p. 3549-3559.

200. Shenashen, M.A., S.A. El-Safty, and E.A. Elshehy, *Synthesis, Morphological Control, and Properties of Silver Nanoparticles in Potential Applications.* Particle & Particle Systems Characterization, 2014. **31**(3): p. 293-316.

201. Kooij, E.S. and B. Poelsema, *Shape and size effects in the optical properties of metallic nanorods.* Physical Chemistry Chemical Physics, 2006. **8**(28): p. 3349-3357.

202. Li, J.X., et al., *Synergetic Approach for Simple and Rapid Conjugation of Gold Nanoparticles with Oligonucleotides.* Acs Applied Materials & Interfaces, 2014. **6**(19): p. 16800-16807.

203. Hakkinen, H., *The gold-sulfur interface at the nanoscale.* Nature Chemistry, 2012. **4**(6): p. 443-455.

204. Liu, B. and J.W. Liu, *Methods for preparing DNA-functionalized gold nanoparticles, a key reagent of bioanalytical chemistry.* Analytical Methods, 2017. **9**(18): p. 2633-2643.

205. Pakiari, A.H. and Z. Jamshidi, *Nature and Strength of M-S Bonds (M = Au, Ag, and Cu) in Binary Alloy Gold Clusters.* Journal of Physical Chemistry A, 2010. **114**(34): p. 9212-9221.

206. Claridge, S.A., et al., *Enzymatic ligation creates discrete multinanoparticle building blocks for self-assembly.* Journal of the American Chemical Society, 2008. **130**(29): p. 9598-9605.

207. Kim, J.W., J.H. Kim, and R. Deaton, *DNA-Linked Nanoparticle Building Blocks for Programmable Matter.* Angewandte Chemie-International Edition, 2011. **50**(39): p. 9185-9190.

208. Parak, W.J., et al., *Conformation of oligonucleotides attached to gold nanocrystals probed by gel electrophoresis.* Nano Letters, 2003. **3**(1): p. 33-36.

209. Hurst, S.J., A.K.R. Lytton-Jean, and C.A. Mirkin, *Maximizing DNA loading on a range of gold nanoparticle sizes.* Analytical Chemistry, 2006. **78**(24): p. 8313-8318.

210. Ding, Y., et al., *Gold Nanoparticles for Nucleic Acid Delivery.* Molecular Therapy, 2014. **22**(6): p. 1075-1083.

211. Li, X., et al., *Localized surface plasmon resonance (LSPR) of polyelectrolyte-functionalized gold-nanoparticles for bio-sensing.* Colloids and Surfaces a-Physicochemical and Engineering Aspects, 2009. **332**(2-3): p. 172-179.

212. Demers, L.M., et al., *A fluorescence-based method for determining the surface coverage and hybridization efficiency of thiol-capped oligonucleotides bound to gold thin films and nanoparticles.* Analytical Chemistry, 2000. **72**(22): p. 5535-5541.

213. Wu, X.A., et al., *Intracellular Fate of Spherical Nucleic Acid Nanoparticle Conjugates.* Journal of the American Chemical Society, 2014. **136**(21): p. 7726-7733.

214. Baldock, B.L. and J.E. Hutchison, *UV-Visible Spectroscopy-Based Quantification of Unlabeled DNA Bound to Gold Nanoparticles.* Analytical Chemistry, 2016. **88**(24): p. 12072-12080.

215. Chegel, V., et al., *Gold Nanoparticles Aggregation: Drastic Effect of Cooperative Functionalities in a Single Molecular Conjugate.* Journal of Physical Chemistry C, 2012. **116**(4): p. 2683-2690.

216. Takahashi, H., et al., *Modification of gold nanorods using phospatidylcholine to reduce cytotoxicity.* Langmuir, 2006. **22**(1): p. 2-5.

217. Pierrat, S., et al., *Self-assembly of small gold colloids with functionalized gold nanorods.* Nano Letters, 2007. **7**(2): p. 259-263.

218. Gorelikov, I. and N. Matsuura, *Single-step coating of mesoporous silica on cetyltrimethyl ammonium bromide-capped nanoparticles.* Nano Letters, 2008. **8**(1): p. 369-373.

219. Sendroiu, I.E., M.E. Warner, and R.M. Corn, *Fabrication of Silica-Coated Gold Nanorods Functionalized with DNA for Enhanced Surface Plasmon Resonance Imaging Biosensing Applications.* Langmuir, 2009. **25**(19): p. 11282-11284.

220. Liz-Marzan, L.M., M. Giersig, and P. Mulvaney, *Synthesis of nanosized gold-silica core-shell particles.* Langmuir, 1996. **12**(18): p. 4329-4335.

221. Obare, S.O., N.R. Jana, and C.J. Murphy, *Preparation of polystyrene- and silica-coated gold nanorods and their use as templates for the synthesis of hollow nanotubes.* Nano Letters, 2001. **1**(11): p. 601-603.

222. Pastoriza-Santos, I., J. Perez-Juste, and L.M. Liz-Marzan, *Silica-coating and hydrophobation of CTAB-stabilized gold nanorods.* Chemistry of Materials, 2006. **18**(10): p. 2465-2467.

223. Stober, W. and A. Fink, *Controlled Growth of Monodisperse Silica Spheresin the Micron Size Range.* JOURNAL OF COLLOID AND INTERFACE SCIENCE, 1968. **26**: p. 62-69.

224. Bhakta, S., et al., *Sodium hydroxide catalyzed monodispersed high surface area silica nanoparticles.* Materials Research Express, 2016. **3**(7).

225. Lee, K.S. and M.A. El-Sayed, *Gold and silver nanoparticles in sensing and imaging: Sensitivity of plasmon response to size, shape, and metal composition.* Journal of Physical Chemistry B, 2006. **110**(39): p. 19220-19225.

226. Zhang, J.J., et al., *Synthesis, characterizations of silica-coated gold nanorods and its applications in electroanalysis of hemoglobin.* Electrochemistry Communications, 2008. **10**(3): p. 355-358.

227. Kang, K.A., et al., *Fluorescence Manipulation by Gold Nanoparticles: From Complete Quenching to Extensive Enhancement.* Journal of Nanobiotechnology, 2011. **9**.

228. Wu, Z.S., et al., *Optical detection of DNA hybridization based on fluorescence quenching of tagged oligonucleotide probes by gold nanoparticles.* Analytical Biochemistry, 2006. **353**(1): p. 22-29.

229. Zheng, D., et al., *Aptamer Nano-flares for Molecular Detection in Living Cells.* Nano Letters, 2009. **9**(9): p. 3258-3261.

230. Khandelwal, G. and J. Bhyravabhotla, *A Phenomenological Model for Predicting Melting Temperatures of DNA Sequences.* Plos One, 2010. **5**(8).

231. Giljohann, D.A., et al., *Oligonucleotide loading determines cellular uptake of DNA-modified gold nanoparticles.* Nano Letters, 2007. **7**(12): p. 3818-3821.

232. Mergny, J.L., et al., *FLUORESCENCE ENERGY-TRANSFER AS A PROBE FOR NUCLEIC-ACID STRUCTURES AND SEQUENCES.* Nucleic Acids Research, 1994. **22**(6): p. 920-928.

233. Leskovac, V., *Comprehensive Enzyme Kinetics*. 2003, New York: Academic/Plenum Pub.

234. Seferos, D.S., et al., *Polyvalent DNA Nanoparticle Conjugates Stabilize Nucleic Acids.* Nano Letters, 2009. **9**(1): p. 308-311.

235. Suck, D. and C. Oefner, *STRUCTURE OF DNASE-I AT 2.0 A RESOLUTION SUGGESTS A MECHANISM FOR BINDING TO AND CUTTING DNA.* Nature, 1986. **321**(6070): p. 620-625.

236. Townend, R. and G. Bernardi, *STUDIES ON ACID DEOXYRIBONUCLEASE .10. MOLECULAR WEIGHT IN DENATURING SOLVENTS.* Archives of Biochemistry and Biophysics, 1971. **147**(2): p. 728-&.

237. Ehrlich, S.D. and G. Bernardi, *STUDIES ON ACID DEOXYRIBONUCLEASE .9. 5'-HYDROXY-TERMINAL AND PENULTIMATE NUCLEOTIDES OF OLIGONUCLEOTIDES OBTAINED FROM CALF THYMUS DEOXYRIBONUCLEIC ACID.* Biochemistry, 1971. **10**(11): p. 2000-&.

238. Evans, C.J. and R.J. Aguilera, *DNase II: genes, enzymes and function.* Gene, 2003. **322**: p. 1-15.

239. Liu, C.Y., et al., *Vimentin contributes to epithelial-mesenchymal transition cancer cell mechanics by mediating cytoskeletal organization and focal adhesion maturation.* Oncotarget, 2015. **6**(18): p. 15966-15983.

240. Katsumoto, T., A. Mitsushima, and T. Kurimura, *THE ROLE OF THE VIMENTIN INTERMEDIATE FILAMENTS IN RAT 3Y1-CELLS ELUCIDATED BY IMMUNOELECTRON MICROSCOPY AND COMPUTER-GRAPHIC RECONSTRUCTION.* Biology of the Cell, 1990. **68**(2): p. 139-146.

241. Buccheri, G. and D. Ferrigno, *Lung tumor markers of cytokeratin origin: an overview.* Lung Cancer, 2001. **34**: p. S65-S69.

242. Karantza, V., *Keratins in health and cancer: more than mere epithelial cell markers.* Oncogene, 2011. **30**(2): p. 127-138.

243. A., R., S. C., and S. P., *Comparative Proteomic Analysis of Lung Cancer Cell Line and Lung Fibroblast Cell Line*

Cancer Genomics and Proteomics, 2009. **6**(4): p. 229-237.

244. Satelli, A. and S. Li, *Vimentin in cancer and its potential as a molecular target for cancer therapy.* Cellular and Molecular Life Sciences, 2011. **68**(18): p. 3033-3046.

245. Dauphin, M., et al., *Vimentin expression predicts the occurrence of metastases in non small cell lung carcinomas.* Lung Cancer, 2013. **81**(1): p. 117-122.

246. Di Pietro, P., et al., *Gold and Silver Nanoparticles for Applications in Theranostics.* Current Topics in Medicinal Chemistry, 2016. **16**(27): p. 3069-3102.

247. Zhao, J., et al., *Gold Nanoparticles in Cancer Therapy: Efficacy, Biodistribution, and Toxicity.* Current Pharmaceutical Design, 2015. **21**(29): p. 4240-4251.

248. Jain, S., D.G. Hirst, and J.M. O'Sullivan, *Gold nanoparticles as novel agents for cancer therapy.* British Journal of Radiology, 2012. **85**(1010): p. 101-113.

249. Patra, C.R., et al., *Fabrication of gold nanoparticles for targeted therapy in pancreatic cancer.* Advanced Drug Delivery Reviews, 2010. **62**(3): p. 346-361.

250. Brown, S.D., et al., *Gold Nanoparticles for the Improved Anticancer Drug Delivery of the Active Component of Oxaliplatin.* Journal of the American Chemical Society, 2010. **132**(13): p. 4678-4684.

251. Ma, P.A., et al., *Inorganic nanocarriers for platinum drug delivery.* Materials Today, 2015. **18**(10): p. 554-564.

252. Prabaharan, M., et al., *Gold nanoparticles with a monolayer of doxorubicin-conjugated amphiphilic block copolymer for tumor-targeted drug delivery.* Biomaterials, 2009. **30**(30): p. 6065-6075.

253. Swiech, O.A., et al., *Doxorubicin carriers based on Au nanoparticles - effect of shape and gold-drug linker on the carrier toxicity and therapeutic performance.* Rsc Advances, 2016. **6**(38): p. 31960-31967.

254. Newell, B.B., Y.L. Wang, and J. Irudayaraj, *Multifunctional gold nanorod theragnostics probed by multi-photon imaging.* European Journal of Medicinal Chemistry, 2012. **48**: p. 330-337.

255. Xiao, Y.L., et al., *Gold Nanorods Conjugated with Doxorubicin and cRGD for Combined Anticancer Drug Delivery and PET Imaging.* Theranostics, 2012. **2**(8): p. 757-768.

256. Lee, J.M., et al., *The epithelial-mesenchymal transition: new insights in signaling, development, and disease.* Journal of Cell Biology, 2006. **172**(7): p. 973-981.

257. Perez-Arnaiz, C., et al., *New Insights into the Mechanism of the DNA/Doxorubicin Interaction.* Journal of Physical Chemistry B, 2014. **118**(5): p. 1288-1295.

258. Hajihassan, Z. and A. Rabbani-Chadegani, *Studies on the binding affinity of anticancer drug mitoxantrone to chromatin, DNA and histone proteins.* Journal of Biomedical Science, 2009. **16**.

259. Agudelo, D., et al., *Intercalation of antitumor drug doxorubicin and its analogue by DNA duplex: Structural features and biological implications.* International Journal of Biological Macromolecules, 2014. **66**: p. 144-150.

260. Box, V.G.S., *The intercalation of DNA double helices with doxorubicin and nagalomycin.* Journal of Molecular Graphics & Modelling, 2007. **26**(1): p. 14-19.

261. Yang, F., et al., *Doxorubicin, DNA torsion, and chromatin dynamics.* Biochimica Et Biophysica Acta-Reviews on Cancer, 2014. **1845**(1): p. 84-89.

262. Li, N., et al., *Interaction of anticancer drug mitoxantrone with DNA analyzed by electrochemical and spectroscopic methods.* Biophysical Chemistry, 2005. **116**(3): p. 199-205.

263. Koeller, J. and M. Eble, *MITOXANTRONE - A NOVEL ANTHRACYCLINE DERIVATIVE.* Clinical Pharmacy, 1988. **7**(8): p. 574-581.

264. Ohnuma, T., et al., *Enhanced sensitivity of A549 cells to the cytotoxic action of anticancer drugs via suppression of Nrf2 by procyanidins from Cinnamomi Cortex extract.* Biochemical and Biophysical Research Communications, 2011. **413**(4): p. 623-629.

265. Momparler, R.L., et al., *EFFECT OF ADRIAMYCIN ON DNA, RNA, AND PROTEIN-SYNTHESIS IN CELL-FREE SYSTEMS AND INTACT-CELLS.* Cancer Research, 1976. **36**(8): p. 2891-2895.

266. Kim, J.H., *Lethal effect of adriamycin on the division cycle of HeLa cells.* Cancer Research, 1972. **32**(2): p. 323-325.

267. Bachur, N.R., S.L. Gordon, and M.V. Gee, *ANTHRACYCLINE ANTIBIOTIC AUGMENTATION OF MICROSOMAL ELECTRON-TRANSPORT AND FREE-RADICAL FORMATION.* Molecular Pharmacology, 1977. **13**(5): p. 901-910.

268. Berlin, V. and W.A. Haseltine, *REDUCTION OF ADRIAMYCIN TO A SEMIQUINONE-FREE RADICAL BY NADPH CYTOCHROME-P-450 REDUCTASE PRODUCES DNA CLEAVAGE IN A REACTION MEDIATED BY MOLECULAR-OXYGEN.* Journal of Biological Chemistry, 1981. **256**(10): p. 4747-4756.

269. Gerwitz, D., *A Critical Evaluation of the Mechanisms of Action*

Proposed for the Antitumor Effects of the

Anthracycline Antibiotics Adriamycin

and Daunorubicin. Biochemical Pharmacology, 1999. **57**: p. 727-741.

270. Nitiss, J.L., *Targeting DNA topoisomerase II in cancer chemotherapy.* Nature Reviews Cancer, 2009. **9**(5): p. 338-350.

271. White, R.J. and F.E. Durr, *DEVELOPMENT OF MITOXANTRONE.* Investigational New Drugs, 1985. **3**(2): p. 85-93.

272. Evison, B.J., et al., *Mitoxantrone, More than Just Another Topoisomerase II Poison.* Medicinal Research Reviews, 2016. **36**(2): p. 248-299.

273. Gilleron, J., et al., *Image-based analysis of lipid nanoparticle-mediated siRNA delivery, intracellular trafficking and endosomal escape.* Nature Biotechnology, 2013. **31**(7): p. 638-U102.

274. Blanco, E., H. Shen, and M. Ferrari, *Principles of nanoparticle design for overcoming biological barriers to drug delivery.* Nature Biotechnology, 2015. **33**(9): p. 941-951.

275. Bartczak, D., et al., *Interactions of Human Endothelial Cells with Gold Nanoparticles of Different Morphologies.* Small, 2012. **8**(1): p. 122-130.

276. Chithrani, B.D. and W.C.W. Chan, *Elucidating the mechanism of cellular uptake and removal of protein-coated gold nanoparticles of different sizes and shapes.* Nano Letters, 2007. **7**(6): p. 1542-1550.

277. Bartczak, D., et al., *Receptor-Mediated Interactions between Colloidal Gold Nanoparticles and Human Umbilical Vein Endothelial Cells.* Small, 2011. **7**(3): p. 388-394.

278. Albanese, A., P.S. Tang, and W.C.W. Chan, *The Effect of Nanoparticle Size, Shape, and Surface Chemistry on Biological Systems.* Annual Review of Biomedical Engineering, Vol 14, 2012. **14**: p. 1-16.

279. Nativo, P., I.A. Prior, and M. Brust, *Uptake and intracellular fate of surface-modified gold nanoparticles.* Acs Nano, 2008. **2**(8): p. 1639-1644.

280. Saha, K., et al., *Surface Functionality of Nanoparticles Determines Cellular Uptake Mechanisms in Mammalian Cells.* Small, 2013. **9**(2): p. 300-305.

281. Zheng-Jiang, Z., et al., *The Interplay of Monolayer Structure and Serum Protein Interactions on the Cellular Uptake of Gold Nanoparticles.* Small, 2012. **8**(17): p. 2659-63.

282. Brandenberger, C., et al., *Quantitative Evaluation of Cellular Uptake and Trafficking of Plain and Polyethylene Glycol-Coated Gold Nanoparticles.* Small, 2010. **6**(15): p. 1669-1678.

283. Van Hoecke, K., et al., *Ecotoxicity and uptake of polymer coated gold nanoparticles.* Nanotoxicology, 2013. **7**(1): p. 37-47.

284. Patel, P.C., et al., *Scavenger Receptors Mediate Cellular Uptake of Polyvalent Oligonucleotide-Functionalized Gold Nanoparticles.* Bioconjugate Chemistry, 2010. **21**(12): p. 2250-2256.

285. Choi, C.H.J., et al., *Mechanism for the endocytosis of spherical nucleic acid nanoparticle conjugates.* Proceedings of the National Academy of Sciences of the United States of America, 2013. **110**(19): p. 7625-7630.

286. Fernando, L.P., et al., *Mechanism of Cellular Uptake of Highly Fluorescent Conjugated Polymer Nanoparticles.* Biomacromolecules, 2010. **11**(10): p. 2675-2682.

287. Vranic, S., et al., *Deciphering the mechanisms of cellular uptake of engineered nanoparticles by accurate evaluation of internalization using imaging flow cytometry.* Particle and Fibre Toxicology, 2013. **10**.

288. Wu, X.A., et al., *Intracellular Fate of Spherical Nucleic Acid Nanoparticle Conjugates.* J. Am. Chem. Soc., 2014. **136**(21): p. 7726-7733.

289. Rhee, W.J. and G. Bao, *Slow non-specific accumulation of 2'-deoxy and 2'-O-methyl oligonucleotide probes at mitochondria in live cells.* Nucleic Acids Research, 2010. **38**(9).

290. Zheng, D., et al., *Aptamer Nano-flares for Molecular Detection in Living Cells.* Nano Lett., 2009. **9**(9): p. 3258-3261.

291. Noguez, C., *Surface Plasmons on Metal Nanoparticles: The Influence of Shape and Physical Environment.* Journal of Physical Chemistry C, 2007. **111**(10): p. 3806-3819.

292. Rubart, M., *Two-photon microscopy of cells and tissue.* Circulation Research, 2004. **95**(12): p. 1154-1166.

293. Helmchen, F. and W. Denk, *Deep tissue two-photon microscopy (vol 2, pg 932, 2005).* Nature Methods, 2006. **3**(3): p. 235-235.

294. Garai, M., et al., *Single Particle Studies on Two-Photon Photoluminescence of Gold Nanorod-Nanosphere Heterodimers.* Journal of Physical Chemistry C, 2016. **120**(21): p. 11621-11630.

295. Jiang, X.-F., et al., *Excitation Nature of Two-Photon Photoluminescence of Gold Nanorods and Coupled Gold Nanoparticles Studied by Two-Pulse Emission Modulation Spectroscopy.* Journal of Physical Chemistry Letters, 2013. **4**(10): p. 1634-1638.

296. Imura, K., T. Nagahara, and H. Okamoto, *Near-field two-photon-induced photoluminescence from single gold nanorods and imaging of plasmon modes.* Journal of Physical Chemistry B, 2005. **109**(27): p. 13214-13220.

297. Biagioni, P., et al., *Dependence of the two-photon photoluminescence yield of gold nanostructures on the laser pulse duration.* Physical Review B, 2009. **80**(4).

298. Nehl, C.L., H.W. Liao, and J.H. Hafner, *Optical properties of star-shaped gold nanoparticles.* Nano Letters, 2006. **6**(4): p. 683-688.

299. Lee, Y.H., et al., *Refractive Index Sensitivities of Noble Metal Nanocrystals: The Effects of Multipolar Plasmon Resonances and the Metal Type.* Journal of Physical Chemistry C, 2011. **115**(16): p. 7997-8004.

300. Yasun, E., et al., *BSA modification to reduce CTAB induced nonspecificity and cytotoxicity of aptamer-conjugated gold nanorods.* Nanoscale, 2015. **7**(22): p. 10240-10248.